INVESTIGATION OF ELECTRIC ARCS IN SELF-GENERATED FLOW

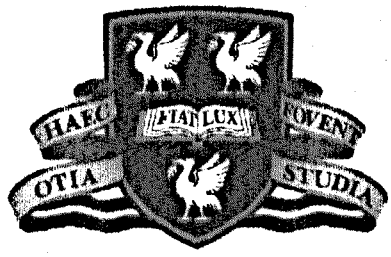

THE UNIVERSITY
of LIVERPOOL

Thesis submitted in accordance with the requirements of the University of Liverpool for the Degree of Doctor in Philosophy by

Jiu Dun Yan

December 1997

Department of Electrical Engineering and Electronics
The University of Liverpool

ACKNOWLEDGEMENTS

I wish first of all to express my deep appreciation to my supervisor, Professor M. T. C. Fang, for his guidance, encouragement and support during my study.

I would like to thank Dr. Bill Hall and Chris Dixon at Rolls Royce Reyrolle for their friendly corporation and tremendous help. I am very grateful to Jim Humphries and Les Issac in the Arc Research Group, who assisted me in the experiments. Thanks are due also to Professor Gordon Jones and Mr. David Turner for their useful suggestions, and to my colleague Dr. Bob Blundell for the inspirational discussions.

I have been financially supported by Rolls Royce Reyrolle. This is gratefully acknowledged.

Finally, I wish to express my sincere appreciation to my wife, for her forbearance, encouragement and support over the years.

ABSTRACT

The utilisation of an arc's energy to generate the flow conditions required for current interruption has given rise to a new generation of circuit breakers, the auto-expansion circuit-breaker. The design of such a circuit breaker depends on a large number of inter-related design parameters. This thesis is aimed at a quantitative understanding of the physical processes occurring in such a device and at developing computer simulation tools which can be beneficially used by circuit breaker designers.

In order to gain an understanding of the first stage (immediately following contact separation) of arcing in an auto-expansion circuit breaker, experiments have been conducted on a free burning arc in a confined pot. Arc voltage, current and pressure at several positions have been measured for a number of discharge conditions. A simplified arc model based on the radially integrated conservation equations has been used to predict the arc behaviour and the pressure in the pot. The arc motion is driven by the Lorentz force and the velocity profile is assumed to be of a known shape. In addition, the simplified model assumes a top-hat radial temperature profile in the arc region and uniform temperature and pressure in the arc's surrounding region. These simplifications are valid provided that the arcing current is above 1kA and that the volume of the surrounding region is much bigger than that of the arc. The predicted arc voltage and pressure agree reasonably well with the experiments.

When the current is high and the arc occupies a large proportion of the arcing chamber, the surrounding gas can no longer be assumed stationary and with uniform temperature and pressure. The assumption of top-hat radial temperature profile departs severely from the actual temperature profile when the current is below 1kA. Under these circumstances, simplified model can no longer give reasonable predictions. Improvement of arc modelling necessitates the numerical solution of highly non-linear arc conservation equations. The solution of these equations is based on a commercial computational fluid dynamics package, PHOENICS.

Before attempting to use PHOENICS to simulate the operation of an auto-expansion circuit breaker some fundamental problems need to be resolved. These are concerned with the choice of turbulence model, the computational domain size for electric field, which is a long range force, the influence of the Lorentz force, and the arc-shock interaction. In order to gain an understanding of these problems and to verify PHOENICS's results, an arc burning in a supersonic nozzle with known stagnation pressure and exit pressure has been used.

The two most commonly used turbulence models, the Prandtl mixing length model and the K-ε model, have been applied to the Aachen nozzle [45]. The relevant turbulence parameters are adjusted according to the measured temperature profiles. It has been found that the turbulence parameters of the Prandtl mixing length model is not sensitive to the absolute value of the current while for the K-ε model, agreement with experimental results

can only be achieved if the turbulence parameters are adjusted according to the current. Thus, the Prandtl mixing length model is adopted.

The accurate computation of the electric field requires a computational domain which is considerably larger than that of the fluid. This enables the Lorentz force to be computed accurately. Although the Lorentz force has a large influence on the flow fields the current-voltage characteristics of the arc are not much affected. The understanding of arc-shock interaction is important to the operation of puffer and auto-expansion circuit-breakers as the presence of the shock cannot be avoided in these devices. The major influence of the shock is the generation of circulating flow, which has adverse effects on thermal and dielectric recovery.

Successful resolution of these fundamental problems results in the establishment of a computer model for the operation of a 245kV auto-expansion circuit breaker. Appropriate boundary conditions are imposed at the moving contact as well as at the gas exits. Radiation induced ablation of the nozzle inner surface is extremely important in building up the pressure in the gas storage volume of the breaker. Simulation has been carried out for the whole arcing period which reveals in detail the generation of reverse flow by ablation, the flow circulation generated by the shock, the generation of a flow stagnation point away from the downstream solid electrode just before current zero and the role of the storage volume in shaping the flow conditions in the interrupter during the current zero period. The computed pressure in the storage volume has been found to be in good agreement with that measured at the Reyrolle Short Circuit Test Station. The reported work clearly demonstrates that PC based PHOENICS, when coded with the correct arc physics and with the appropriate boundary conditions, can be used as a design tool to aid the development of auto-expansion circuit breakers.

TABLE OF CONTENTS

CHAPTER ONE INTRODUCTION

1.1 History and Recent Development of High Voltage Circuit Breakers

High voltage circuit breakers are an important link in a power system. They perform both operational and safety functions. During normal operation, they carry load current for most of the time and can be called on by a controller to switch off/on a circuit. In the event of a line fault, a circuit breaker has to interrupt short-circuit current and acts as an insulating point in the power network.

1.1.1 History

The basic idea of a mechanical circuit breaker is to disconnect two metallic contacts which are normally in a closed position, or to close them from an open position. When the two contacts are drawn apart while carrying a current, the gap between them is dielectrically broken down and an electric arc is subsequently developed. The development of high voltage circuit breakers was closely related to the availability of good insulating material [1,2,3,4]. The simplest principle used to interrupt a circuit is by separating two contacts as in a plain breaker in oil. Oil molecules dissociate under the high temperature of an arc. Hydrogen is the main product of the dissociation. The high pressure hydrogen gas bubbles created by the arc

energy is advantageously used to confine, compress and cool the arc so that the arc is extinguished at a natural ac current zero. Since there is no artificial control of the arc, the plain breaker has a low interruption capacity and was soon replaced by an arc control system employing explosion pots and cross flow baffles. Oil circuit breakers, which include the bulk oil and minimum oil designs, have proved a very successful circuit interrupting technology with voltage ratings per break between 3.3kV to 33kV for the former and 11kV to 170kV for the latter [1]. They still remain in service to this day.

Airbreak circuit breakers were first developed in 1929 by Slepian at Westinghouse [2]. Arc extinction in this kind of circuit breaker is achieved by magnetically forcing the arc into a chute where the arc is lengthened and cooled. The cooling of the arc by the surface of the chute and the increase in the arc length result in a high arc voltage (high arc resistance), which leads to favourable conditions for arc extinction at a natural current zero. For current interruption at voltage levels higher than 15kV [4], airbreak circuit breakers demand an arc chute of formidable size and were replaced in 1930's by air-blast circuit breakers where the switching arc is confined and cooled by the high speed air flow through an insulating nozzle. Air-blast circuit breakers have several advantages over their predecessors. They are suitable for frequent switching duties, provide high speed operation, have short and consistent arcing and total breaking time, and require minimum maintenance. Air-blast circuit breakers were predominantly used for voltages higher than 100kV before the adoption of SF_6 as a main switching medium.

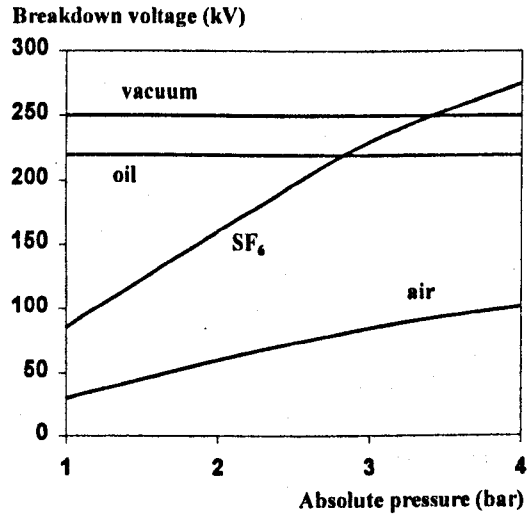

Figure 1.1 Comparison of the 50Hz rms breakdown voltage of oil, air and SF_6 for a 10^{-2} metre uniform gap as a function of the absolute pressure.

The discovery in the 1950's of the excellent dielectric and arc quenching properties of Sulfurhexafluoride (SF_6) [5] led to a new generation of SF_6-blast circuit breakers. SF_6 is a very stable, odourless, non-toxic and non-flammable gas. Its dielectric strength is higher than that of oil at an absolute pressure above 3 bar and is at least twice that of air (figure 1.1) owing to its electro-negative property. The adoption of SF_6 resulted in a considerable increase in voltage and current ratings without resorting to extreme gas pressures or large number of breaks in series.

The first generation of SF_6 gas-blast circuit breakers required part of the working gas to be stored permanently at a high pressure (typically 16bar) which generates a high speed flow for arc quenching. However SF_6 has a high boiling point, typically 20°C at 24bar (figure 1.2). Heating facilities are thus necessary to prevent liquefaction of pressurised SF_6 in low temperature environment. A method to overcome this problem is to use the so-called puffer principle: The high speed flow in the nozzle can be generated by compressing the gas in a moving cylinder against a stationary piston during the operation of the circuit breaker. SF_6 puffer circuit breakers first appeared in 1964 [6] and have become the most successful technology in current interruption at transmission voltage levels in the last two decades. The interrupting capacity per break has increased from 72kV/25kA in 1970 to 550kv/63kA in 1993 [7]. However, the necessary gas compression in the puffer cylinder requires a very powerful operating mechanism such as the very costly hydraulic system.

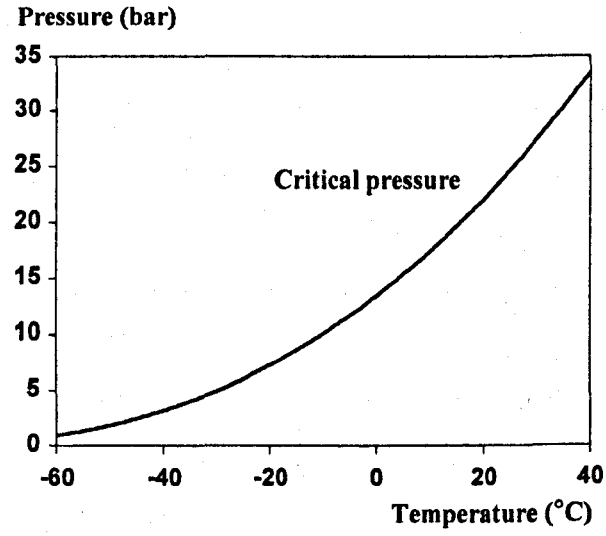

Figure 1.2 Vapour pressure curve for SF_6 as a function of temperature [2].

Vacuum circuit breakers are a special type of switching device. They are self contained and maintenance free. Arcs generated during the operation are burning in the metallic vapour produced by contact erosion. Vacuum circuit breakers are mainly used in distribution voltage level up to 36kV, although much work has been done to raise the voltage ratings [3]. Vacuum circuit breakers at 132kV are already in service in some outdoor stations [1].

1.1.2 Recent Development

SF_6 puffer circuit breakers have almost exclusively been used in extra high voltage (EHV) power systems nowadays for their excellent performance and their well established technology. The interruption of a small capacitive current requires an operating mechanism which is able to drive the moving contact sufficiently fast so that the gap length between the two contacts after current zero can withstand the high recovery voltage in terms of rated values imposed by the power system. The operating mechanism must also be able to overcome the high pressure in the puffer cylinder during high current phase. The combination of these two requirements demands a powerful operating system which is very costly. Recent development on high voltage circuit breakers has been focused on the reduction of operating energy by advantageously exploiting part of the arc energy to establish a gas flow in the nozzle for current interruption. This is the basic principle of an auto-expansion circuit breaker, a new generation of circuit breaker.

It is certainly not a new idea to extinguish an arc by exploiting part of its energy. In an early design of oil circuit breakers [1], an explosion pot system had been used to force the gas which is generated by the dissociation of oil flowing through a hole in the pot so that the switching arc running in the hole could be efficiently blown out. Extension of the principle of explosion pot system to SF_6 circuit breakers was, to the author's knowledge, first carried out by Reyrolle Switchgear [8] in 1973. Renewed interest in auto-expansion principle was first reported in 1981 by Ueda et al [9]. The Japanese group studied the self-flow generation phenomenon in a puffer circuit breaker with the help of pressure and arc voltage measurement and optical observation [9-15]. A compact 7.2kV/63kA circuit breaker, with reduced volume of the puffer cylinder and low energy driving mechanism, was then developed in 1982 [13]. To help the interruption of small current without any puffer action, a ring-shaped permanent

magnet attached co-axially to the nozzle was used to rotate the arc over the surface of the hollow contact. In 1990, they developed a magnet-assisted auto-expansion circuit breaker rated at 24kV/25kA. In Europe, Bernard et al at Merlin Gerin (France) and at the University of Liege (Belgium) [16,17,18] reported in 1988 the development of a similar magnet-assisted auto-expansion circuit breaker rated at 15kV/25kA. Recent developmental work on auto-expansion circuit breakers with voltage ratings of 45kV and above has been reported by ABB [19], AEG [20] and GEC-Alsthom[21]. Since 1984, GEC- has been actively involved in the research and development of auto-expansion circuit breakers in the voltage range from 52 to 245kV without any magnet-assistance [21]. Products (FXT range) operated by BLRXE spring control mechanism have been available for voltage ratings 52, 72.5, 100 and 123kV. Auto-expansion circuit breakers in the range from 145kV to 245kV, which are fitted with a device called a "back-piston" to accelerate the contact separation, were under test in 1991.

1.2 Review of Basic Arc Physics

1.2.1 Electric arcs as switching medium

Electric arcs are gaseous plasma maintained by an externally imposed electric current between two electrodes. They are unavoidable in the operation of mechanical circuit breakers as long as gas, oil or vacuum (strictly speaking, electrode vapour) is used as the working medium. That people willingly accept electric arcs as an efficient switching medium is because they are able to change quickly from an excellent conductor at high temperature into a very good insulating medium after current zero. Improvement in our knowledge of arc physics has, however, proved a slow process. It has been almost sixty years since the introduction of the first black box arc model. Advances in both experimental technique and theoretical modelling in the past sixty years have greatly enhanced our understanding of the important mechanisms in switching arcs, such as the role of heat conduction, the role of radiation and turbulent mixing, and the effects of arc-flow interaction on the performance of a circuit breaker. Nevertheless, our knowledge in switching arc physics is still very limited. Taking turbulence as an example, solution of the Navier-Stokes equations with temporal and spatial resolutions consistent with the turbulent fluctuation is beyond the computational power

of modern computers. We have also no rigorous model specially designed to describe the behaviour of turbulence in circuit breaker arcs.

Physically, the thermal and electrical properties of the arcing gas undergo rapid change during a circuit breaker operation, especially at the current zero period. To achieve a quantitative description of the evolution of all important parameters in a domain of interest, we need to solve a set of equations governing the important physical processes in circuit breaker arcs with appropriate initial and boundary conditions. Approximations, usually in the form of assumptions or simplified models based on experience, need to be introduced in situations where there is a lack of rigorous knowledge of a physical process.

1.2.2 Basic equations

1.2.2.1 Local thermal equilibrium (LTE)

Complete thermodynamic equilibrium (CTE) state is said to exist in a system of gas particles only if the following criteria are satisfied [22]:

(1) The velocity distribution of all particle species can be described by Maxwell's equation with a single temperature:

$$dn_r = n_r f(v_r) dv_r \qquad (1.1.a)$$

$$f(v_r) = \frac{4v_r^2}{\sqrt{\pi(2kT/m_r)^3}} \exp(-\frac{m_r v_r^2}{2kT}) \qquad (1.1.b)$$

where v_r is the magnitude of the velocity vector, n_r the number density of species r, m_r the mass per particle, T the common temperature for all particle species and k is the Boltzmann constant.

(2) The population density of excited states for each particle species follows the Boltzmann distribution:

$$n_{r,s} = n_r \frac{g_{r,s}}{Z_r} \exp(-\frac{E_{r,s}}{kT}) \qquad (1.2)$$

where $n_{r,s}$ is the number of particles of species r at an excited state s. $g_{r,s}$ is the statistical weight of the state s, $E_{r,s}$ its energy and Z_r is the partition function of species r.

(3) The number densities of charged particle species are related through the Saha equation:

$$\frac{n_{r+1}n_e}{n_r} = \frac{2Z_{r+1}}{Z_r}\frac{(2\pi m_e kT)^{\frac{3}{2}}}{h^3}\exp(-\frac{\chi_{r+1}}{kT}) \qquad (1.3)$$

where n_r and n_{r+1} are the number density of ion species in the (r)th and (r+1)th ionisation state respectively. n_e is the electron number density, χ_{r+1} the ionisation energy which is required to produce an ion in the (r+1)th state from the (r)th state, m_e the electronic mass and h the Planck constant.

(4) Radiation field within the arc obeys Planck's law for black body:

$$B_\nu d\nu = \frac{2h\nu^3}{c^2}\frac{d\nu}{\exp[h\nu/(kT)]-1} \qquad (1.4)$$

where ν is the frequency, c the speed of light and B_ν is the radiation intensity of Black body in $W/(m^3\ ster)$.

CTE does not exist in practical arcing situations. Deviations from CTE can originate from several sources, such as radiation escaping from the arc, mass and energy exchange due to spatial inhomogeneity of arc parameters, and the rapid change of arcing conditions. Since arcs burning in high voltage circuit breakers are usually at or above atmospheric pressure, collisions between electrons and other particles (including electrons) are expected to dominate the microscopic momentum and energy exchange processes in the arc plasma. For SF_6 arcs in the high current phase the number density of electrons is of the order of $10^{24}/m^3$ (20,000K, 5 bar). Local Thermal Equilibrium (LTE), which is defined by equations (1.1), (1.2) and (1.3), is a good approximation of the plasma state. For arcs at current zero in a gas blast circuit breaker, the temperature of the gas is around 10,000K. Lewis et al [23] carried out a spectroscopic study of the plasma state of an SF_6 arc at current zero in a nozzle with a upstream pressure of 7.8bar and a downstream pressure of 1bar. Their results indicated that the electron number density ($3\sim8\times10^{23}/m^3$) immediately before and at the current zero of a transient arc is sufficient for LTE state to exist in the di/dt range of 13~24A/μs. The effect of particle demixing on the statistic equilibrium of SF_6 arc plasmas due to spatial inhomogenity has been studied by Gleizes et al [24]. Deviation from Saha equilibrium for atomic fluorine, which accounts 90% of the particle density of SF_6 plasma at 10,000K, can be neglected when

the electron number density is higher than $5\times10^{22}/m^3$ at 1bar which is much lower than the measured electron number density of $3\sim8\times10^{23}/m^3$ by Lewis [23].

In our case, we are also interested in the first five to ten microseconds after current zero, during which the thermal recovery process of a circuit breaker takes place. The contact gap of a circuit breaker is electrically stressed after current zero by the fast rising recovery voltage from the power system. The value of dv/dt is usually around 2~5kV/μs. At a temperature of 10,000K, atomic fluorine accounts 90% of the plasma particle density which is around $3\times10^{24}/m^3$ at 5bar. The elastic collision cross section of electrons with atomic fluorine is 1.2×10^{-20} m^2 [25]. The collision frequency of an electron with atomic fluorine is thus $3\times10^{10}/s$. It takes about 0.27μs (8100 collisions) for an electron to transfer its thermal energy to atomic fluorine by elastic collisions, which implies that the time scale for energy relaxation between electrons and heavy particles in the arc plasma is much shorter than that of the thermal recovery process. Under the effect of an applied electric field, the temperature of electrons is higher than that of heavy particles. This temperature difference can be calculated with a knowledge of the mean free path of electrons [26] which can be estimated from the electrical conductivity of the arc plasma. With a dv/dt of 2kV/μs, the electron temperature at 10μs after current zero is higher than that of heavy particles by only a very small fraction. Based on the preceding experimental evidence [23,24] and the theoretical estimates, we assume LTE state existing in the high current phase, during the current zero period and in the thermal recovery period of an auto-expansion circuit breaker.

1.2.2.2 Basic equations

The electrical and aerodynamic behaviour of arcs under LTE can be fully described by the conservation equations of mass, momentum and energy of the arcing gas together with the Maxwell equations. These equations are supplemented by the appropriate initial and boundary conditions. For an electrically quasi-neutral arc-flow system, the conservation equations can be written as [27-30]

Continuity equation

$$\frac{\partial \rho}{\partial t} + \nabla \bullet (\rho \vec{V}) = 0 \qquad (1.5)$$

Momentum equation

$$\rho \frac{D\vec{V}}{Dt} = \rho \vec{g} + \nabla \bullet \Pi_{ij} + \vec{J} \times \vec{B} \qquad (1.6)$$

Energy equation

$$\frac{\partial}{\partial t}[\rho(e + \frac{\vec{V}^2}{2})] + \nabla \bullet [\rho(e + \frac{\vec{V}^2}{2})\vec{V}] = \rho \vec{g} \bullet \vec{V} - \nabla \bullet (P\vec{V}) + \nabla \bullet (k\nabla T) + \vec{J} \bullet \vec{E} - q + \Phi \qquad (1.7)$$

where t is the time, ρ the density, e the internal energy, P the static pressure, k the thermal conductivity, T the temperature, $\vec{V}$ the velocity vector and $\vec{g}$ the gravitational acceleration. Other symbols will be explained below. The stress tensor in equation (1.6) for a Newtonian fluid is given by

$$\Pi_{ij} = -P\delta_{ij} + \mu(\frac{\partial u_i}{\partial x_j} + \frac{\partial u_j}{\partial x_i}) + \delta_{ij}\mu' \frac{\partial u_k}{\partial x_k}, \quad i, j, k = 1, 2, 3 \qquad (1.8a)$$

where δ_{ij} is the Kronecker delta and u the velocity component. μ and μ' are respectively the dynamic viscosity and the second coefficient of viscosity which are related through the bulk viscosity

$$\eta = \frac{2}{3}\mu + \mu'$$

Following Stokes' hypothesis (η=0) equation (1.8a) becomes

$$\Pi_{ij} = -P\delta_{ij} + \tau_{ij} \qquad (1.8b)$$

where τ_{ij} is the viscous stress tensor given by

$$\tau_{ij} = \mu[(\frac{\partial u_i}{\partial x_j} + \frac{\partial u_j}{\partial x_i}) - \frac{2}{3}\delta_{ij}\frac{\partial u_k}{\partial x_k}], \quad i, j, k = 1, 2, 3 \qquad (1.8c)$$

The viscous dissipation term in equation (1.7) can thus be expressed as

$$\Phi = \tau_{ij}\frac{\partial u_i}{\partial x_j}, \quad i, j, k = 1, 2, 3 \qquad (1.9)$$

The closure of equations (1.5) to (1.7) requires a knowledge of the material properties of the arcing gas, the radiation source term q, the equation of state, the current density $\vec{J}$, the magnetic flux density $\vec{B}$ and the electric field $\vec{E}$. The last three vectors are coupled through the following equations

Ohm's law

$$\vec{J} = \sigma(\vec{E} + \vec{V} \times \vec{B}) \tag{1.10}$$

Ampere's law

$$\nabla \times (\frac{\vec{B}}{\mu_0}) = \frac{\partial(\varepsilon\vec{E})}{\partial t} + \vec{J} \tag{1.11}$$

Faraday's law

$$\nabla \times \vec{E} = -\frac{\partial \vec{B}}{\partial t} \tag{1.12}$$

and

$$\nabla \cdot (\varepsilon\vec{E}) = \rho_c \tag{1.13}$$

$$\nabla \cdot \vec{B} = 0 \tag{1.14}$$

where σ is the electrical conductivity, μ_0 the permeability of vacuum, and ε the permittivity of the medium. $\vec{V}$ is the velocity of the arcing gas and ρ_c is the density of space charges.

1.2.3 Turbulence

It is well known that arcs in a supersonic nozzle can become turbulent, especially at low currents [31,32]. Turbulence is three dimensional and rotational in nature. The large scale eddies, whose size is comparable with the scale of the flow, extract energy from the mean flow. The small eddies, in which the viscous effect is important, dissipate the turbulent energy by vortex stretching.

Turbulent momentum and energy exchange plays a very important part in determining the breaking capacity of SF_6-blast circuit breakers. Since direct simulation of turbulence by solving Navier-Stokes equations is impossible with available computing power, the statistical behaviour of a turbulent flow is conventionally described by the time-averaged values of the flow and thermodynamic properties:

$$\bar{\phi} = \frac{1}{T}\int_{t_0}^{t_0+T} \phi dt \qquad (1.15a)$$

$$\phi = \bar{\phi} + \phi' \qquad (1.15b)$$

where t_0 is the time when the average is performed. The duration of integration, T, should be much bigger than the time scale of turbulent fluctuation but be much smaller than that of the physical problem. The average of the fluctuating component, ϕ', is by definition equal to zero.

Substituting equation (1.15b) into equations (1.5), (1.6) and (1.7) results in various time-averaged terms of the correlated fluctuating components. For small density fluctuation, the most important terms are the Reynolds stress $-\rho\overline{u_i'u_j'}$ (i and j denote the coordinates) in the momentum equation and the term $-\rho\overline{u_i'e'}$ in the energy equation. It is therefore necessary to introduce additional relations to relate these two terms to the main (averaged) turbulent quantities, which is the task of all turbulence models.

The two most popular turbulence models, namely the Prandtl mixing length model and the two equation K-epsilon model, are all based on the assumption of negligible density fluctuation. The concept of eddy viscosity has long been used to model the turbulent viscous effect in analogue to its molecular counterpart. For example, in an axially dominant flow (in the i direction) the Reynolds stress and the turbulent energy exchange term $-\rho\overline{u_i'e'}$ can be modelled by

$$-\rho\overline{u_i'u_j'} = \mu_t\left|\frac{\partial u_i}{\partial x_j}\right| \qquad (1.16a)$$

$$-\rho\overline{u_j'e'} = k_t\frac{\partial T}{\partial x_j} \qquad (1.16b)$$

where μ_t is the eddy viscosity which has the same dimension as the molecular dynamic viscosity, and k_t is an equivalent turbulent thermal conductivity which is correlated to the eddy viscosity by the turbulent Prandtl number P_{rt}

$$P_{rt} = \frac{\mu_t}{k_t / c_p} \qquad (1.17)$$

Application of the existing turbulence models to circuit breaker arcs has shown that theoretical predictions are in agreement with experimental results although turbulent parameters need to be adjusted to fit one set of test results. In the early work of arc modelling by Swanson and Roidt [33-39], turbulent energy transport based on the Prandtl mixing length theory has

been assumed to be important in the cooling of arc. However, the behaviour of a turbulent circuit breaker arc was poorly understood. Hermann and Ragaller [40] found that it was necessary to introduce turbulence for SF_6 arcs in double-nozzle gas-blast circuit breakers. Although Mitchell et al [41] argued that the energy loss by convection and laminar thermal conduction is sufficient to cool the decaying arc under the same conditions as in [40], his results of radial temperature profiles up to 200μs after current zero (figure 8 in [41]) seem to be similar to those of Hermann and Ragaller based on laminar flow (figure 2 in[40]). Fang et al [42] has successfully predicted the critical rate of rise of recovery voltage (RRRV) in a puffer circuit breaker [43] with the Prandtl mixing length model. Recently, a preliminary comparative study by Kwan [44] has shown that the popular two equation K-epsilon model has no advantage over the Prandtl mixing length model in that one of the five constants in the former needs to be adjusted in order to achieve agreement between the predicted and measured radial temperature profiles in a supersonic nozzle [45]. The behaviour of these two turbulence models will be compared in Chapter Three.

1.2.4 Radiation

Radiation transfer in an arc-flow system is an extremely complex phenomenon. For molecular gases there may be several hundred or more spectral lines superimposed on the continuum spectrum of the radiation in an arc column. The radiation flux at a particular position is not only a function of the local gas properties but also dependent on the temperature and pressure field in the whole domain of interest.

It has long been recognised that the energy transport at the centre of a high current arc is radiation dominated. The local energy loss by radiation at the arc centre is approximately equal to the local Ohmic heating. Liebermann and Lowke [46] calculated the net emission coefficient of SF_6 at the centre of an isothermal and cylindrical arc column under uniform pressure. The results showed that the net radiation emission coefficient (emission-absorption) is sensitive to the column radius and is approximately proportional to pressure in the range 1 to 10 bar (figure 1.3).

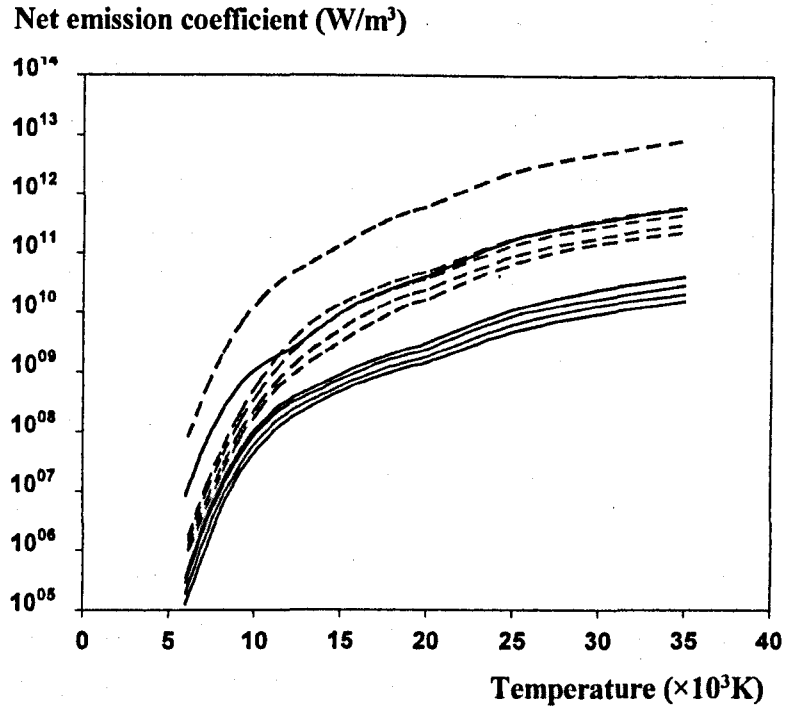

Figure 1.3 Net emission coefficient of isothermal and cylindrical SF_6 arc column of infinite length at uniform pressure, calculated by Liebermann and Lowke [46]. Solid curves are for the pressure of 1bar and the broken curves for 10bar. In each of the two groups, the column radius from top to bottom is: 0, 1mm, 2mm, 5mm and 10mm.

However, as the radiation from the arc centre is mainly in the ultra-violet region, most of the radiation is re-absorbed at the edge of the arc which is at a lower temperature. Calculation of the exact amount of radiation which escapes from an arc column by solving the radiation transport equation is not practical in terms of computational cost. Experimental investigation by Strachan et al [47] indicated that, depending on the material of upstream electrode, up to 50% of the electrical power input in a free burning arc could be lost to its surroundings by radiation, and contamination of the arcing gas by electrode erosion has strong influence on the radiation behaviour. For arcs free from electrode vapour contamination, a common practice is to calculate the radiation emission from the arc core by a net emission coefficient, and calculate the radiation absorption outside the arc core by prescribing a local absorption coefficient as a function of the local temperature [48,49].

The partial characteristics method developed by Sevast'yanenko [50,51] has recently been applied to SF_6 arcs [52,53,54,55]. The basic idea of this method is to approximate the calculation of the radiation flux in a specific direction (one-dimensional calculation) and its

divergence by introducing two sets of tabulated coefficients which depend on the arcing gas. Results based on the partial characteristics method are very close to those of exact calculations [55]. The application of this method has so far been limited to uniform pressure situations. We will make no effort to extend its application to auto-expansion circuit breakers where large pressure gradient exists in the nozzle.

1.3 Review of Arc Modelling

1.3.1 Early arc models

Although the discovery of arc can be dated back to the beginning of last century, investigation of the underlying physical processes in an electric arc only started in this century. Slepian [56] was probably the first person to propose a theory for arc interruption: The race between the reapplication of voltage across the contacts of a circuit breaker and the recovery of dielectric strength of the contact gap determines the arc behaviour.

The first mathematical description of a dynamic arc was given in 1939 by Cassie [57], who assumed constant and uniform temperature in the arc column. This is virtually an approximation for radiation controlled, optically thin arc at very high current. The diameter of the arc responds proportionally to the variation of the electric current. Since the energy loss is proportional to arc's volume, we have

$$P_{loss} = \frac{\text{energy loss at steady state}}{\text{volume at steady state}} \times (\text{volume at transient state})$$
$$= \frac{E_0 I_0}{(1/R_0)}(1/R) = \frac{E_0^2}{R} \qquad (1.18)$$

where P_{loss} is the energy loss in a transient arc, E the electric field strength, I the current and R the resistance per unit length. The subscript 0 refers to a steady state at the same temperature. Based on the overall energy balance in the arc column, Cassie arrived at the following equation:

$$R\frac{d}{dt}(\frac{1}{R}) = \frac{1}{\tau}\left[(\frac{E}{E_0})^2 - 1\right] \qquad (1.19)$$

where $\tau = Q_0 R_0 / E_0^2$ is a time constant with Q_0 being the heat content at a steady state.

Four years late in 1943, Mayr [58] proposed a model for low current arc. He assumed that the arc radius and the energy loss per unit length remain constant. By relating the resistance of the arc, R, to its heat content, Q, in the form $R \propto \exp(-Q/Q_0)$ with Q_0 being the heat content at a steady state, Mayr expressed the energy conservation equation in a differential form:

$$R\frac{d}{dt}(\frac{1}{R}) = \frac{1}{\tau}\left[\frac{EI}{P_0} - 1\right] \tag{1.20}$$

where P_0 is the energy loss at a steady state and $\tau = Q_0/P_0$ is again a time constant.

The models of Cassie and Mayr are only for extreme cases in circuit interruption. Although Browne [59] in 1948 combined these two models by using Cassie's equation before current zero and that of Mayr for post zero period, the performance of these "black box" models depends on the availability of test results since the fundamental physical processes inside the arc were not represented at all.

Elenbaas [60] in 1946 first started the work to describe the arc's behaviour in terms of its thermal and electrical properties:

$$\frac{1}{r}\frac{d}{dr}(rk\frac{dT}{dr}) + \sigma E^2 = 0 \tag{1.21}$$

where the variables have their conventional meaning. Equation (1.21) is obviously oversimplified in that some of the important processes such as radiation and convection are excluded from the energy balance. Subsequent applications of Elenbaas' equation by Frind [61] and Phillips [62] to transient wall stabilised arcs established for the first time how arc's time constant is related to the gas properties and the system dimension.

1.3.2 Models for arcs in gas flow

The models, which we discussed so far, did not consider the effects of radiation and gas flow on arc behaviour. In 1964, Weber [63] studied the axial growth of an arc column (radius) in tubular flow under steady state conditions. He used the mass, momentum and energy conservation equations for laminar boundary layer flow. It was not until the beginning of the 1970's that vigorous research into arc physics took place. However, because of the complexity of the conservation equations and a lack of efficient numerical method for highly non-linear partial differential equations, the integral approach was generally adopted in the 1970's. With the availability of fast computers at reduced cost in the last decade, numerical

modelling of switching arcs based on the solution of mass, momentum and energy conservation equations in their full differential form began to dominate circuit breaker research.

1.3.2.1 Integral method

A series of seven papers on arc modelling were published by Swanson and Roidt [33-39] between 1970 and 1977, which, together with the work of Topham [64], marked a turning point in gas blast arc modelling. The similarity between an arc in an axial flow and a hot boundary layer was clearly recognised and used to simplify the arc conservation equations. However, their starting conservation equation for energy [33] is in general not correct, as pointed out by Fang [65]. The treatment of the terms in the radially integrated energy equation was not physically justified.

In 1975, Lowke and Ludwig [66] developed a simple arc model for convection stabilised arcs that is only applicable to a certain current range. The current must first be large enough so that thermal conduction and turbulent loss do not influence the central arc temperature. The current must not cause blocking in the nozzle. Tuma and Lowke [67] applied this model to analyse the data of Hermann et al [68]. El-Akari and Tuma [69] later extended this channel model to transient arcs.

At the same time, extensive investigations on arcs in gas flow were undertaken by BBC (Brown Boveri) [68,70,71,72,73,74]. Their work on arc radiation and turbulence has greatly enhanced our understanding. A two-zone model including turbulent momentum and heat transfer was successfully employed in elucidating the physics of a 2kA nitrogen nozzle arc [70]. A similar arc model neglecting the axial variation of thermodynamic quantities was used to study the arc behaviour during the current zero period [72]. In spite of the drastic simplifications introduced, the model has achieved remarkable success when compared with test results. However, the application of this arc model requires the input of six parameters, the value of which cannot be determined by a consideration of physics or system dimension.

Following the same lines as those of Hermann and Ragaller [68], Tuma and his co-workers [75,76] studied the free recovery and current zero behaviour of a gas blast arc. Parameters, which control the turbulence strength and the radial profiles of temperature and axial velocity component, have to be adjusted so that the interruption capability agrees with experiment.

An important step in the development of a simplified method of arc analysis, the boundary layer integral method, was taken in 1974 by Cowley [77] in that the arc conservation equations in general form, together with the external flow equations, were rigorously formulated. In a later paper [78] Chan et al extended Cowley's formulation to include an energy integral equation for the arc conducting zone. Thus, the models discussed above are all special cases of this general formulation. The Liverpool-Cambridge arc model has achieved considerable success in elucidating experimental [79,80,81] and computer simulated arcs [82,83]. Recently, this method has been used to investigate the effects of nozzle ablation [84,85,86].

1.3.2.2 Differential method

During the last decade, the rapid increase in computing power and the availability of reliable numerical method for solving the partial differential flow conservation equations [87] have made arc modelling in full differential form practical. The basic idea of the differential approach is to solve the conservation equations of mass, momentum and energy with appropriate initial and boundary conditions of the physical domain. Since some of the important physical mechanisms in switching arcs, such as radiation transfer, turbulent mixing and electrode sheath interaction, are still too complex, simplifications and approximations must be made. This gives rise to various models devised for different arcing situations.

Ragaller et al [40] at BBC proposed a model in 1982 for predicting the dielectric recovery of a gas blast arc after current zero. Viscous dissipation and axial heat conduction are neglected in the energy equation. To simplify the problem, the radial momentum equation is reduced to a uniform radial pressure distribution. Thus the surrounding cold flow solely determines the axial pressure distribution. Their numerical solution involves an isothermal transformation of the differential equations. Strong turbulent energy exchange needs to be introduced in their model in order to bring the numerical prediction close to the measured dielectric recovery characteristics [88]. Turbulence starts to play an important role in the cooling of the residual hot gas at the stagnation point from about 30μs after current zero. Flow downstream of the nozzle throat becomes turbulent before current zero.

Mitchell et al [41] investigated the dielectric behaviour after current zero assuming laminar flow. Radiation from the high temperature core is assumed to be fully absorbed in a single layer of one-cell thickness at the arc edge. Adaptive grids are used in the solution

because of the very high radial temperature gradient. The solution at the stagnation point is first obtained. The conservation equations are then solved in the downstream region. The boundary condition for the energy equation at the upstream stagnation point is obtained by solving the mass and energy conservation equations at z=0, with the axial gradient of the axial velocity extrapolated from the cell downstream. Although Mitchell et al [41] argued that the energy loss by convection and laminar thermal conduction is sufficient to cool the residual plasma under the same conditions as in [40], their results of radial temperature profiles (figure 8 in [41]) are clearly similar to those of Hermann and Ragaller based on laminar flow (figure 2 in[40]) for the period up to 200μs after current zero. The results given by Mitchell et al [41] of a steady state SF_6 arc at 1200A and 3.6bar indicated that the net emission coefficient given by Liebermann and Lowke [46] should be increased by a factor of 4.

Lowke and Lee [89] investigated the thermal recovery process of a gas blast circuit breaker. They start the transient simulation from a steady state at 2kA before current zero. However, their laminar flow results showed that the predicted critical RRRV for both nitrogen and SF_6 is more than one order of magnitude lower than that given by Hermann and Ragaller [71].

Since the middle of the 1980's Fang and his co-workers [42,90,91] at the University of Liverpool have been at the forefront of gas blast arc modelling. They have shown that for nitrogen arcs theory based on laminar flow can give a reasonable prediction of the thermal interruption capability [90] but not for SF_6 [42,91]. Introduction of turbulence has been found necessary for SF_6 arcs. Shock waves are unavoidable during the operation of gas-blast circuit breakers. The behaviour of SF_6 arcs under shock conditions has been investigated by Fang et al [86].

1.3.3 Free burning arcs

Differential method has been used to investigate arcs in gas-blast and puffer circuit breakers. Unlike the puffer circuit breaker where the flow in the nozzle is generated by the compression of a piston, the flow in an auto-expansion circuit breaker is indirectly caused by the presence of the arc in the quenching chamber. The arc shortly after contact separation is freely burning in a confined space although the volume of which may be very large. A model for free burning arcs in a confined space is thus necessary.

The concept of free burning arc is commonly referred to a situation where there is no externally imposed flow and the arc is free from any influence of solid surface except at the two electrodes. The boundary conditions away from the electrode can thus be set at fixed pressure and temperature with mass exchange across the boundary left free.

Free burning arcs have been used in many industrial applications such as welding, arc lamps, arc furnaces, plasma cutting and plasma heating for mineral processing. Successful simulation of free burning arcs has so far been based on the work of Maecker [93] who first explained the generation of arc flow on the basis of self-magnetic compression on the arc column.

A simplified model was developed by Ramakrishnan et al [94] in 1978 and was applied to free burning air arcs in the range of 520A to 10.8kA. The radial distribution of temperature inside the arc column was assumed to be uniform and that of the axial velocity was prescribed by a given function of axis velocity and arc radius. Their results showed that turbulent momentum exchange are important for current higher than 500A. Reasonable agreement was obtained between the experimental results and the theoretical predictions of axial velocity and of axial variations of temperature, arc radius and electric field.

Extensive investigation into free burning arcs in the last fifteen years has been following the differential approach. The solution of the conservation equations of mass, momentum and energy requires a knowledge of the electric current density and magnetic flux density distributions which in turn are calculated from the current continuity equation and Ampere's law. Models differ from each other mainly in two aspects: the current density distribution over the cathode surface and the calculation of radiation transfer. Predictions based on laminar flow theory and the assumption of optical thin arc column agreed well with measured temperature field [48,95,96,97,98,99] for 200A steady state argon arcs.

The behaviour of free burning arcs is not sensitive to the cathode sheath phenomenon, but is to the current density distribution at the arc root. Most of the models for free burning arcs neglect this sheath layer and assume a distribution of current density over the cathode surface. The current density over the axis-symmetrical cathode is usually described by an exponentially decaying function of the distance from the axis of the cathode surface [95,96] or of the square of the distance from the centre [99]. There are also models assuming uniform current density in a circular spot on the cathode surface [48]. In recent years effort has been initiated to calculate the current density distribution and heat conduction at the cathode

surface by introducing one dimensional conservation equations of electron number density and energy and a generalised Ohm's law in the cathode sheath layer [97,98].

A free burning arc in a confined space approximates the initial arcing stage in an auto-expansion circuit breaker during which ablation of the wall material is negligible and there is no substantial pressure difference in the system. The arcing process is basically of a transient nature as the pressure and temperature in the region which surrounds the arc cannot remain constant. Despite the considerable success in numerical modelling of steady state free burning arcs, there are still substantial difficulties in developing a differential model for transient free burning arcs in a confined space, especially the associated software to solve the highly non-linear governing equations. With the available computing power at the time when the work on auto-expansion circuit breakers started (The typical speed of fast PCs is 100MHz in 1994), it was recognised that success in modelling auto-expansion arcs by a two-dimensional differential model could not be guaranteed in a time of three years. We thus decided to start the work with a simplified model for the initial arcing stage in an auto-expansion circuit breaker, which is characterised by a free burning arc in a confined space.

1.3.4 Ablation controlled arcs

Ablation controlled arcs are a special type of convectively cooled arcs where the cooling flow is supplied by nozzle wall evaporation due to the strong heating by arc radiation. Modern auto-expansion circuit breakers take advantage of the nozzle ablation to help build up a high pressure in their storage volume. The high pressure accumulated during the high current phase maintains a high speed flow through the nozzle when the arc approaches current zero before extinction.

The radiation from the arc column can directly destroy the material commonly used for circuit breaker nozzles if the arcing current exceeds a certain threshold as indicated by Jones et al [100]. For circuit breaker arcs, radiation emission is the main source of the ablating energy [101,102]. Radiation induced ablation of nozzle material is a very complicated process and so far there is no rigorous theory for it or reliable experimental data. Thermal pyrolysis of PTFE, which is basically a chemical reaction, occurs above 600K [103] and produce pure C_2F_4 gas at 1,000K [102,104]. However, there is indirect evidence that the temperature of the ablated PTFE vapour generated by a switching arc is as high as 3,500K [101]. Ruchti and Niemeyer [102] suggested a threshold wavelength of 220nm in the radiation spectrum: the

photons with wavelength longer than the threshold penetrate into the depth of and heat up the PTFE, while the photons with shorter wavelengths are able to directly break the C-C bond and generate excited CF_2 radicals which thermalise themselves through collisions to a temperature of 3400K. The total energy to change the solid PTFE at room temperature into ablated vapour at 3,400K, which includes the depolymerisation energy, is estimated to be 1.19×10^7 J/kg.

A common practice in modelling of the ablation of PTFE by nozzle arcs is to assume a total energy which is required to change the solid PTFE into a vapour at a temperature above 3400K. Experimental results of Muller [104] indicated that the vapour temperature depends on the nozzle material and is a slowly increasing function of a nominal current density (the ratio of the arcing current to the nozzle cross section). Claessens et al [105] used the following relation to fit the data in [104]:

$$T_v = 3555 + 0.1189\sqrt{J_n} \qquad (1.22)$$

where J_n is the nominal current density defined above.

The amount of radiation emitted by an arc column is usually not known. An empirical coefficient has to be introduced to relate the amount of radiation reaching the nozzle wall to the local electrical power input [85,104-109]. However, this coefficient can vary from 0.15 [100] to 0.6 [104] depending on the arcing situation. A value of 0.5 gives good agreement between the predicted and measured pressure evolution [105] during the high current phase of an auto-expansion circuit breaker. The details of the ablation model, which will be used in the present work, will be discussed in Chapter 3.

1.4 Arc Modelling Based on Commercial CFD (Computational Fluid Dynamics) Package

Commercially available general-purpose CFD packages have increasingly been used in recent years to help the simulation of circuit breakers [21,105]. The first published attempt in this area was that of Rutten [110] who modelled a puffer arc up to 1kA. The use of commercial CFD packages has proven not an easy task. The difficulties encountered are summarised below:

- Generation of grids, which are usually non-uniform and non-orthogonal with moving boundaries. Ideally, these grids should be adaptive.
- The correct specifications of boundary conditions and correct description of arc physics.

- Problems associated with very steep density gradients at the edge of the arc core and highly compressible nature of the flow encountered in a circuit-breaker (flow speeds in the solution domain vary from nearly zero to supersonic).
- The calculation for electromagnetic fields often requires a calculation domain bigger than that of the fluid field.
- Transition from laminar flow to turbulent region and the appropriate turbulence model in the presence of an arc and in the region of low Reynolds number.
- Verification of CFD solutions.

It appears that the majority of commercially available CFD packages are based on the finite volume method of Spalding and Pantakar [87]. PHOENICS [111] has, perhaps, the longest history. Successful application of commercial CFD packages to circuit breaker arcs will greatly reduce the cost and effort which need to be spent on the development of purpose-oriented CFD code, including the software for visualisation of the computational results. PHOENICS has been used at the University of Liverpool for the past five years. Sufficient experience with PHOENICS has been accumulated. The arc results from PHOENICS have been verified by comparison with experimental results or numerical solutions obtained by the software developed at Liverpool [44]. The arc model developed in this thesis will be implemented into PHOENICS to investigate the behaviour of electric arcs in an auto-expansion circuit breaker.

1.5 The Objective and Organisation of the Thesis

The work in this thesis, which is supported by Rolls-Royce Reyrolle, a major switchgear manufacturer in the United Kingdom, will concentrate on the investigation of electric arcs related to auto-expansion circuit breakers although the research approach is also suitable for other arcing devices. A diagram of a high voltage auto-expansion circuit breaker is shown in figure 1.4.

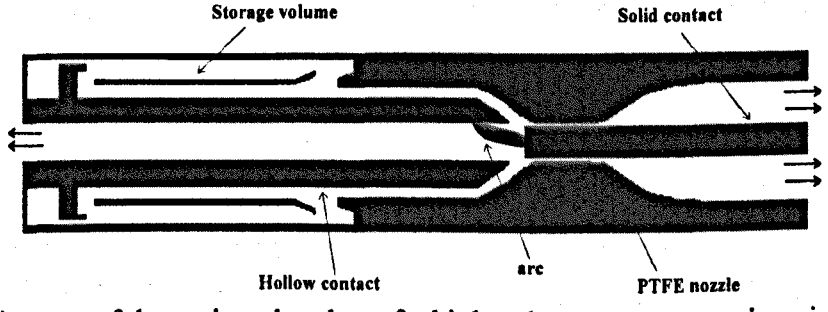

Figure 1.4 Diagram of the arcing chamber of a high voltage auto-expansion circuit breaker.

The arc in the arcing chamber is burning in the flow established by the arc itself, which differs from a puffer circuit breaker where the nozzle flow is solely imposed by the action of a puffer piston. The flow in an auto-expansion circuit breaker originates from two sources. The interaction between the arcing current and its magnetic field exerts an electromagnetic force which is perpendicular to the local current density vector and the local magnetic field vector, the so called $\vec{J} \times \vec{B}$ force. The arc shortly after contact separation in an auto-expansion circuit breaker is freely burning in the arcing chamber before the onset of nozzle ablation. It is well known that the flow in a free burning arc is determined by the $\vec{J} \times \vec{B}$ force. Secondly, when the arc column extends into the nozzle section of an auto-expansion circuit breaker due to the moving contact, strong radiation from the arc column ablates the nozzle thus forming a mass source. This mass source builds up a vapour flow of the ablated nozzle material towards both ends of the nozzle. The arc is subsequently burning in an ablation dominated environment. A mixture of the ablated vapour and the working gas can be accumulated in a storage volume during the high current phase thus producing a high pressure source. When the arc approaches a natural current zero, ablation and the $\vec{J} \times \vec{B}$ force become negligible. The arc will be burning in the established flow field which is maintained by the high pressure in the storage volume. The behaviour of the arc at current zero in an auto-expansion circuit breaker therefore depends on the arcing history (current waveform), the geometry and size of the arcing chamber, the nozzle material and size, and the speed of the moving contact. The performance of an auto-expansion circuit breaker depends on a large number of factors. It is difficult to predict the influence of changing one parameter on the breaker performance. Development cost, if relying solely on test, is extremely high.

The objective of the present work is to investigate the behaviour of arcs burning in auto-expansion circuit breakers over the whole arcing period, and to develop an arc model which can be used to help the optimum design of high voltage auto-expansion circuit breakers. Since electromagnetic force plays an important role in an auto-expansion circuit breaker, especially at the initial stage of the arcing process, we start our work by investigating a free burning arc in a confined space where ablation of wall material is negligible. Initially, it would be extremely difficult to develop a differential arc model for auto-expansion circuit breakers and the corresponding software for arc modelling, a simplified model based on that of Ramakrishnan et al [94] was used to study free burning arcs in a confined space which are

basically of a transient nature (Chapter Two). Experiments were also carried out on an auto-expansion arcing device for the verification of the simplified model.

The successful application of PHOENICS to the simulation of puffer circuit breaker arcs by Kwan [44] has greatly reduced the difficulties to investigate the arcing phenomena in an auto-expansion circuit breaker by a differential arc model. Kwan has shown that PHOENICS can be reliably used to model the arc. A differential arc model for auto-expansion arcs, which has been implemented into PHOENICS, is described in Chapter Three which includes the following aspects: the conservation equations and their boundary conditions, the radiation model, turbulence and ablation, and the modelling of moving contact. The basic mechanisms operating in auto-expansion circuit breaker arcs, such as the effect of the $\vec{J} \times \vec{B}$ force in high current arcs and the electrical and aerodynamic behaviour of arcs under shock conditions, were also studied in Chapter Three. Chapter Four presents the computational simulation of the whole arcing process of an auto-expansion circuit breaker. Predicted arc voltage and pressure evolution in the storage volume are compared with the test results which are supplied by Rolls-Royce Reyrolle. The current zero period and the calculation of the critical RRRV in an auto-expansion circuit breaker is discussed. The work is summarised in Chapter Five, which also includes a proposal for possible future work.

CHAPTER TWO THEORETICAL AND EXPERIMENTAL INVESTIGATION OF FREE BURNING ARCS IN A CONFINED SPACE

2.1 Introduction

A free burning arc in a confined space approximates the initial arcing stage in an auto-expansion circuit breaker during which ablation of the wall material is negligible and there is no substantial pressure difference in the system. The arcing process is basically of a transient nature as the pressure and temperature in the region which surrounds the arc cannot remain constant. Despite the considerable success in numerical modelling of steady state free burning arcs (in the electric current range from 100A to 500A in argon) over the last fifteen years [48,95,96,97,98], there are still substantial difficulties in developing a differential model for

transient free burning arcs in a confined space, especially with the software to solve the highly non-linear governing equations. In high voltage auto-expansion circuit breakers the arcing current can vary from several hundred amperes to several kA or even several tens of kA, and the size of the arc column undergoes rapid change. Numerically a huge number of cells must be used to catch the steep temperature gradient at the arc edge whose position is moving during the arcing process, or an adaptive grid system has to be employed in the solution procedure which is computationally costly. With the available computing power at the time when the work on auto-expansion circuit breakers started (The typical speed of fast PCs was 100MHz in 1994), it was recognised that success in modelling auto-expansion arcs by a two-dimensional differential model could not be guaranteed in a time of three years. We thus decided to start the work with a simplified model for the initial arcing stage in an auto-expansion circuit breaker, which is characterised by a free burning arc in a confined space.

The development of the simplified model is presented in Section 2.2, which is followed by an experimental investigation in Section 2.3 of free burning arcs in a cylindrical chamber. Measurements of arc voltage and pressure variation in the arcing chamber are taken under various conditions. The performance of the simplified model is examined in Section 2.4 where comparison has been made of the predicted and measured pressure and arc voltage under the experimental conditions investigated. Conclusions, which include a discussion of the limitations of the simplified model, is finally given in Section 2.5.

2.2 Simplified Model for Free Burning Arcs in a Confined Space

2.2.1 Basic equations

The size of the free burning arc is assumed to be small in comparison with the confining space, the gas in the surrounding region is thus rather stagnant. We divide the whole space into two regions, namely the arc column and the surrounding cold gas region (figure 2.1). The arc is burning in Volume V_1 which is connected to Volume V_2 through a gap. The flow in the arc column is axially dominant and is driven by the $\vec{J} \times \vec{B}$ force generated by the arcing current and its magnetic field. We solve the mass, momentum and energy conservation equations in integral form. In the surrounding region where gas remains stagnant, uniform pressure and temperature

are assumed and the momentum equation is redundant. The equation of state for ideal gas is assumed in the surrounding region.

For high current free burning arcs, the radial inertia and viscous terms are small in comparison with the $\vec{J} \times \vec{B}$ force, and the flow is in turbulent state [94]. The viscous dissipation and the axial thermal conduction in the energy equation can also be neglected. For an electrically quasi-neutral arc the conservation equations in a cylindrical polar coordinate system are

Conservation of mass:

$$\frac{\partial \rho}{\partial t} + \frac{1}{r}\frac{\partial}{\partial r}(r\rho v) + \frac{\partial}{\partial z}(\rho w) = 0 \tag{2.1}$$

Radial momentum conservation:

$$\frac{\partial P}{\partial r} = (\vec{J} \times \vec{B})_r \tag{2.2}$$

Axial momentum conservation:

$$\frac{\partial \rho w}{\partial t} + \frac{1}{r}\frac{\partial}{\partial r}(r\rho w v) + \frac{\partial}{\partial z}(\rho w^2) = -\frac{\partial P}{\partial z} + (\vec{J} \times \vec{B})_z + \frac{1}{r}\frac{\partial}{\partial r}[r(\mu + \mu_t)\frac{\partial w}{\partial r}] \tag{2.3}$$

Energy conservation:

$$\begin{aligned} &\frac{\partial}{\partial t}([\rho(h + \frac{w^2}{2})] + \frac{1}{r}\frac{\partial}{\partial r}[r\rho(h + \frac{w^2}{2})v] + \frac{\partial}{\partial z}[\rho(h + \frac{w^2}{2})w] = \\ &\frac{\partial P}{\partial t} + \frac{1}{r}\frac{\partial}{\partial r}(r\frac{k + k_t}{c_p}\frac{\partial h}{\partial r}) + \sigma E^2 - q \end{aligned} \tag{2.4}$$

where w is the axial velocity component, v the radial velocity component, $\vec{J}$ the local current density, $\vec{B}$ the local magnetic flux density, σ the electrical conductivity, E the electric field, μ the laminar viscosity, k the thermal conductivity and q is a radiative energy source. μ_t and k_t are respectively the turbulent eddy viscosity and the turbulent energy exchange coefficient, which are defined by equations (1.16a) and (1.16b). Other symbols have their conventional meaning.

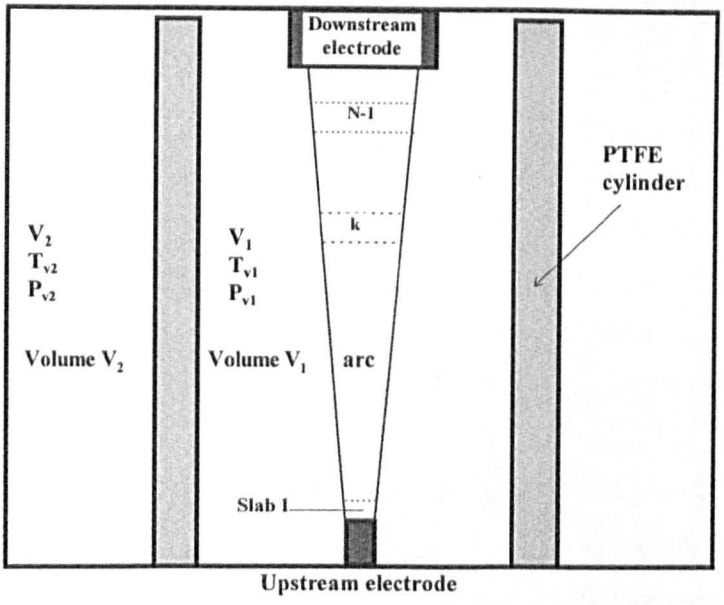

Figure 2.1 Schematic diagram of a free burning arc in a confined space. V stands for volume, T temperature and P pressure. Volume V_2 is intended to simulate the gas flow from the arcing chamber to the low pressure exhaust volume in an auto-expansion circuit breaker.

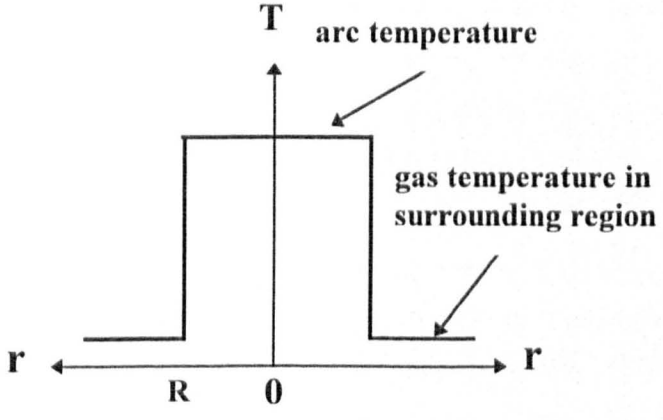

Figure 2.2 Top-hat approximation of the radial temperature profile for free burning arcs in a confined space.

2.2.2 Simplifications and shape factors

There is experimental evidence that the radial temperature distribution of high current free burning arcs can be approximated by a "top-hat" profile [112,113] as shown in figure 2.2. The arc radius, R, is defined at the radial position where there is a discontinuity of temperature.

When the diameter of an arc is small in comparison with its length, the electric field is almost axial, which can be calculated from Ohm's law:

$$E_z = \frac{I}{\int_0^R \sigma 2\pi r dr} \tag{2.5.a}$$

where E_z is the electric field in the longitudinal direction of the arc column and I is the current. Since electrical conductivity is radially uniform, equation(2.5.a) becomes

$$E_z = \frac{I}{\sigma \pi R^2} \tag{2.5.b}$$

The azimuthal magnetic flux density inside the arc column (r<=R) is

$$B = \frac{\mu_0 I r}{2\pi R^2} \tag{2.6}$$

where μ_0 is the permeability of free space. The role of magnetic flux density in the momentum balance can be represented by a tensile stress B^2/μ_0 in the direction of the magnetic field lines and an isotropic compressive stress $B^2/(2\mu_0)$. Neglecting the radial viscous and inertia forces, the radial pressure gradient is solely balanced by the magnetic stress system. Following Cowley [77] the radial momentum equation (2.2) is reduced to

$$\frac{\partial}{\partial r}\left(P + \frac{B^2}{2\mu_0}\right) = -\frac{B^2}{\mu_0 r} \tag{2.7}$$

which can be further simplified with the help of equation (2.6)

$$P = P_0 - \frac{\mu_0 I^2}{4\pi^2 R^2}\frac{r^2}{R^2} \tag{2.8}$$

where P_0 is the pressure on the axis (r=0). The first and second term on the RHS of equation (2.3) become

$$-\frac{\partial P}{\partial z} + (\vec{J} \times \vec{B})_z = -\frac{\partial}{\partial z}\left(P + \frac{B^2}{2\mu_0}\right) \tag{2.9}$$

Ramakrishnan et al [94] assumed that the radial profile of the axial velocity component in high current free burning arcs can be represented by the following expression

$$w = w_0\left[1 - \left(\frac{r}{R}\right)^2\right]^n \tag{2.10}$$

where w_0 is the velocity on the axis and n is a variable factor which determines the shape of the radial profile of the axial velocity. The radial variation of pressure and density in the arc column needs to be taken into account when the conservation equations (2.1), (2.3) and (2.4) are integrated from r = 0 to r = R. Since enthalpy is a weak function of pressure, it is assumed to be radially uniform inside the arc column under the top-hat temperature profile. Taking

density to be proportional to pressure at a fixed temperature, the radial integration of the conservation equations can be performed analytically and the problem reduced to numerically one-dimensional. The terms in the first column of Table 2.1 are involved during the integration, which can be expressed in terms of density, ρ_0 , and velocity, w_0 , on the axis and the shape factors as listed in the third column of Table 2.1.

Table 2.1

integration	results	shape factor
$\int_0^R \rho 2\pi r dr$	$\rho_0 \pi R^2 \xi_\rho$	$\xi_\rho = 1 - \frac{\xi_0}{2}$
$\int_0^R \rho w 2\pi r dr$	$\rho_0 \pi R^2 w_0 \xi_{v1}$	$\xi_{v1} = \frac{1}{n+1}(1 - \frac{\xi_0}{n+2})$
$\int_0^R \rho w^2 2\pi r dr$	$\rho_0 \pi R^2 w_0^2 \xi_{v2}$	$\xi_{v2} = \frac{1}{2n+1}(1 - \frac{\xi_0}{2n+2})$
$\int_0^R \rho w^3 2\pi r dr$	$\rho_0 \pi R^2 w_0^3 \xi_{v3}$	$\xi_{v3} = \frac{1}{3n+1}(1 - \frac{\xi_0}{3n+2})$
$\xi_0 = (1 + \frac{4\pi^2 P_{v1} R^2}{\mu_0 I^2})^{-1}$, where P_{v1} is the pressure in Volume V_1 , R the arc radius, and I the current.		

2.2.3 Governing equations of the simplified model

The approximations made in Section 2.2.2 enable equations (2.1), (2.3) and (2.4) be radially integrated from r = 0 to r = R and expressed in terms of the shape factors which are listed in Table 2.1. The Continuity equation for the arc column is

$$\frac{\partial}{\partial t}(\rho_0 \pi R^2 \xi_\rho) + \frac{\partial}{\partial z}(\rho_0 \pi R^2 w_0 \xi_{v1}) = m \qquad (2.11)$$

where m is the radial mass inflow rate per unit length across the arc boundary at r = R. The axial momentum equation for the arc column takes the form

$$\frac{\partial}{\partial t}(\rho_0 \pi R^2 w_0 \xi_{v1}) + \frac{\partial}{\partial z}(\rho_0 \pi R^2 w_0^2 \xi_{v2}) = \frac{\mu_0 I^2}{4\pi R}\frac{\partial R}{\partial z} \qquad (2.12)$$

where the first term on the LHS is the rate of change of momentum storage per unit length of the arc column, and the second term is the momentum taken away by axial convection. The term on the RHS results from the electromagnetic forces. The energy equation for the arc column can be written as

$$(h_0 - h_{v1})\frac{\partial}{\partial t}(\rho_0 \pi R^2 \xi_\rho) = -\rho_0 \pi R^2 \xi_\rho \frac{\partial h_0}{\partial t} - \frac{\partial}{\partial t}(\rho_0 \pi R^2 \xi_{v2} \frac{w_0^2}{2})$$
$$- \frac{\partial}{\partial z}[\rho_0 \pi R^2 w_0 \xi_{v1}(h_0 - h_{v1}) + \rho_0 \pi R^2 w_0 \xi_{v3} \frac{w_0^2}{2}] \qquad (2.13)$$
$$+ \pi R^2 \frac{\partial P_{v1}}{\partial t} + \frac{\mu_0}{8\pi}\frac{\partial}{\partial t}(I^2) + E_z I - c_t u \pi R^2$$

where h_{v1} is the enthalpy of gas in volume V_1, h_0 the enthalpy on the axis, u the net radiation emission coefficient of an isothermal cylindrical column of radius R and c_t is a dimensionless parameter which accounts for the radiation loss from the arc column to its surroundings. The term on the LHS is the rate of change of enthalpy storage per unit length of the arc column due to variation of the mass storage with respect to time and the first term on the RHS is that due to variation of the axis enthalpy. The second term on the RHS is the rate of change of kinetic energy storage per unit length of the arc column. The third to fifth terms on the RHS are respectively the convective term, the rate of change of enthalpy storage per unit length of the arc column due to pressure variation in the surrounding cold region, and that due to variation of the electric current which influences the axis pressure through equation (2.8). The last two terms are respectively the Ohmic heating and the radiation loss per unit arc length. The net emission coefficient, u in equation (2.13), is assumed to be radially uniform in the arc column and can be expressed as

$$u = u(T_0, P_0, R) \qquad (2.14)$$

where T_0 and P_0 are respectively the temperature and pressure on the axis.

Equations (2.11), (2.12) and (2.13) are for the whole arc cross section. They will respectively determine the radial mass inflow rate per unit length across the arc boundary, the variable factor, n, in equation (2.10), and the arc radius in the simplified model. The axial velocity on the axis, w_0, the axis enthalpy, h_0, and the axis density ρ_0 are respectively determined by the momentum equation, the energy equation and the equation of state on the axis. The axial momentum equation on the axis is

$$\rho_0 \frac{\partial w_0}{\partial t} + \rho_0 w_0 \frac{\partial w_0}{\partial z} = \frac{\mu I^2}{2\pi^2 R^3} \frac{\partial R}{\partial z} + \frac{1}{r} \frac{\partial}{\partial r}[r(\mu + \mu_t) \frac{\partial w}{\partial r}]_{r=0} \quad (2.15)$$

where the first term on the RHS is the electromagnetic force due to axial variation of the arc radius. The energy equation on the axis reads

$$\rho_0 \frac{\partial}{\partial t}(h_0 + \frac{w_0^2}{2}) + \rho_0 w_0 \frac{\partial}{\partial z}(h_0 + \frac{w_0^2}{2}) = \frac{\partial P_{v1}}{\partial t} + \frac{\mu_0}{4\pi^2} \frac{\partial}{\partial t}(\frac{I^2}{R^2}) + \sigma E_z^2 - u \quad (2.16)$$

and the equation of state on the axis is

$$f(h_0, P_0, \rho_0) = 0 \quad (2.17)$$

where the axis pressure P_0 can be calculated by

$$P_0 = P_{v1} + \frac{\mu_0 I^2}{4\pi^2 R^2} \quad (2.18)$$

Volume V_1 in figure 2.1 exchanges mass by convection and energy by convection and radiation with the arc column. The axial velocity at the surface of the upstream electrode is zero. Gas is drawn from Volume V_1 into the arc column. The mass flux hitting the downstream electrode is fully returned to volume V_1 , while part of the energy flux hitting the downstream electrode is absorbed by the electrode. The mass conservation equation for volume V_1 is thus

$$\frac{\partial M_{v1}}{\partial t} = -\int_0^{d_{N-1}} m dz + (\rho_0 \pi R^2 w_0 \xi_{v1})_{z=d_{N-1}} - F_m \quad (2.19)$$

where d_{N-1} is the axial distance of the downstream side of slab N-1 from the upstream electrode. The second term on the RHS approximates the radial mass flow rate across the arc boundary in slab N. F_m is the mass flow rate from volume V_1 to volume V_2, which can be calculated by assuming isentropic flow between the two volumes. When the flow is subsonic F_m can be calculated by

$$F_m = A_m (\frac{P_{v2}}{P_{v1}})^{\frac{1}{\gamma}} \sqrt{\frac{2\gamma}{\gamma - 1} \frac{P_{v1}^2}{R_g T_{v1}} [1 - (\frac{P_{v2}}{P_{v1}})^{\frac{\gamma-1}{\gamma}}]} \quad \text{for } P_{v1} \geq P_{v2}$$

$$F_m = -A_m (\frac{P_{v1}}{P_{v2}})^{\frac{1}{\gamma}} \sqrt{\frac{2\gamma}{\gamma - 1} \frac{P_{v2}^2}{R_g T_{v2}} [1 - (\frac{P_{v1}}{P_{v2}})^{\frac{\gamma-1}{\gamma}}]} \quad \text{for } P_{v1} < P_{v2} \quad (2.20)$$

where A_m is the area of the flow passage which is assumed to be constant along the flow, P_{v1} the pressure in volume V_1, P_{v2} the pressure in volume V_2, T_{v1} the temperature in Volume V_1, T_{v2} the temperature in Volume V_2, R_g the gas constant, and γ is the ratio of the specific heat at constant pressure to the specific heat at constant volume of the cold gas in Volume V_1 and

Volume V_2. When the flow from Volume V_1 to Volume V_2 approaches sonic speed, F_m reaches its maximum, which is

$$F_m = A_m \frac{P_{v1}}{R_g}\left(\frac{2}{\gamma-1}\right)^{\frac{1}{\gamma}}\sqrt{\frac{2c_p}{T_{v1}}\left[1-\left(\frac{2}{\gamma+1}\right)^{\frac{\gamma+1}{\gamma-1}}\right]} \tag{2.21}$$

where c_p is the specific heat at constant pressure. Volume V_1 is bounded by the PTFE cylinder and two metallic plates. The thermal energy absorbed by the wall is neglected. The energy conservation equation for volume V_1 is

$$\begin{aligned}\frac{\partial}{\partial t}(M_{v1}e_{v1}) &= (1-c_e)(\rho_0\pi R^2 w_0 \xi_{v1} h_0 + \rho_0\pi R^2 w_0 \xi_{v3} w_0^{\,2}/2)_{z=d_{N-1}} \\ &- \int_0^{d_{N-1}} m h_{v1} dz + \int_0^{d} \pi R^2 c_t c_a u dz - F_h\end{aligned} \tag{2.22}$$

where $e_{v1} = c_v T_{v1}$ (c_v is the specific heat at constant volume) is the internal energy of gas and d is the gap length between the two electrodes. c_a is a dimensionless parameter which determines the radiation absorption in volume V_1 and c_e is a dimensionless parameter accounting for the energy loss to the downstream electrode. F_c is the energy flow rate from volume V_1 to volume V_2 which can be calculated by

$$\begin{aligned} F_h &= c_p T_{v1} F_m \quad \text{for } P_{v1} \geq P_{v2} \\ F_h &= c_p T_{v2} F_m \quad \text{for } P_{v1} < P_{v2}\end{aligned} \tag{2.23}$$

The pressure in volume V_1 is determined by the equation of state for an ideal gas:

$$P_{v1}\left(V_1 - \int_0^{d}\pi R^2 dz\right) = M_{v1} R_g T_{v1} \tag{2.24}$$

where R_g is the gas constant and d is the gap length between the electrodes. The mass and energy conservation equations, and the equation of state for volume V_2 are

$$\frac{\partial M_{v2}}{\partial t} = F_m \tag{2.25}$$

$$\frac{\partial}{\partial t}(M_{v2}e_{v2}) = F_h \tag{2.26}$$

where $e_{v2}=c_v T_{v2}$ and

$$P_{v2}V_2 = M_{v2} R_g T_{v2} \tag{2.27}$$

We have altogether 13 independent equations, namely equations (2.11) to (2.13), (2.15) to (2.19), (2.22) and (2.24) to (2.27), to solve the 13 variables P_0 , h_0 , ρ_0 , w_0 , m , R , n , P_{v1} , M_{v1} , h_{v1} , P_{v2} , M_{v2} and e_{v2} . This set of equations are supplemented by equations (2.20), (2.21) and (2.23) for calculating F_m and F_h , and equation (2.5) for the axial electric field. Full closure of the 13 independent equations requires the radiation model and the turbulence model.

SF_6 is used as the arcing gas. When the temperature is below 1000K, the equation of state for an ideal gas can be assumed with a gas constant of 56 N•m/(kg•K). The specific heat of SF_6 at constant pressure is 575 J/(kg•K) and that at constant volume is 530 J/(kg•K). The equation of state of SF_6 at high temperatures no long obeys the form for an ideal gas. The data used in this simplified model are those given by Frost and Liebermann [114]. The calculation of the net radiation emission coefficient, u, in equation (2.16) is based on the results of Liebermann and Lowke [46]. Gleizes et al [115] investigated the influence of radiation on the temperature of SF_6 arcs. His results indicated that the net emission coefficient of Libermann and Lowke [114] gives too high temperatures on the axis for circuit breaker arcs. Mitchell et al [41] reached a similar conclusion on the net emission coefficient of [114]. They suggested that the data in [114] should be multiplied by a factor between 2.5 and 4. A factor of 3 is used in our simplified model.

Ramakrishnan et al [94] have shown that turbulent mixing is responsible for the decaying axial velocity on the axis of high current free burning arcs. The turbulent eddy viscosity is related to the local velocity and arc length scale by

$$\mu_t = \rho_0 c_1 R w_0 \qquad (2.28)$$

where c_1 is a dimensionless parameter. Since we assume a top-hat radial temperature profile, turbulent energy exchange is not considered in the simplified model.

2.2.4 Boundary conditions and adjustable parameters in the model

The axial coordinate in the arc column is assumed one-way [87] (i.e. conditions downstream of the flow do not affect upstream). The solution of the governing equations of the simplified model requires the upstream boundary conditions for temperature (enthalpy), arc radius and axial velocity for a given current. In a region close to the upstream electrode where LTE does not hold, the plasma state depends on the sheath-electrode interaction. This region, the thickness of which is of the order of 10^{-4}m [95,116] is not included in our model. We specify boundary conditions for the arc column at the interface (the arc root) between the sheath

layer and the arc column, where we define z=0. The plasma temperature at this interface, where LTE becomes valid, must be high enough to ensure sufficient electrical conductivity. It will be shown in Section 2.2.7.2 that the solution of the governing equations is not sensitive to the temperature at the arc root. We set it at 15000K in our model. The axial velocity at z=0 is set at zero. The radius at the arc root is determined by an average current density. Experiments [95] indicated that this average current density at the arc root is around $10^8 A/m^2$.

It is necessary to introduce adjustable parameters in the simplified model. Apart from the temperature and electric current density at the arc root, there are another four adjustable parameters in the model which will be discussed below.

c_e in equation (2.22) is a dimensionless factor which determines the percentage of the energy flux hitting the downstream electrode that is absorbed by the electrode. Gleizes et al [117] reviewed the overall energy balance in SF_6 arcs. The energy loss to electrodes was estimated to be 20% to 30% of the total electrical power input. However, the arc voltage in their energy balance analysis includes the voltage drop across the electrodes and the electrode-sheath layers, and they further assumed that Ohmic heating by this voltage drop solely balances the energy loss to the electrodes. In our case where we only consider the voltage drop across the arc column which excludes the electrode-sheath layers, the percentage of the electrical power input which will be lost to the electrodes should be very low. We have found that a value of 0.35 for c_e produces good agreement between predicted and measured pressure variation in the confining space for all cases investigated. As will be shown in Section 2.2.7.3 the predicted energy flux which hits the downstream electrode accounts for typically 30% to 35% of the total power input in the current range 500A to 5kA, which means that only about 12% of the total power input in the arc column is lost to the electrodes.

The top-hat radial temperature profile in our model implies that any cold gas which is brought into the arc column by the radial mass flow across the arc boundary will be immediately heated up to the arc temperature. Radiation re-absorption at the arc edge is partially responsible for this heating-up process. The radiation loss from high current free burning arcs between copper electrodes was investigated by Strachan [118]. His results indicated that the average radiation loss in a duration of 10ms is between 0.3 to 0.5 of the electrical power input. Different from the case which Strachan investigated, the effect of electrode vapour contamination on radiation emission of the arc is not considered here. We use a net emission coefficient to calculate the radiation loss from the arc column instead of directly

relating the radiation loss to the electrical power input. Radiation re-absorption in cold SF_6 has recently been studied by Bouaziz et al [119]. Their results indicated that about 35% of the net radiation emission of an isothermal arc column can penetrate the cold SF_6 gas and reach the radiation detector. We assume that 40% of the net radiation emission ($\pi R^2 u$ per unit arc length) leaves the radially isothermal arc column (c_t in equations (2.13) and (2.22) = 0.4) and that 25% of the radiation which leaves the arc column (c_a in equation (2.22) = 0.25) is re-absorbed in the cold surrounding volume V_1 (See figure 2.1). Thus we are assuming that 30% of the radiation from an isothermal arc column is lost to the wall. Radiation emission on the axis can be stronger than the local Ohmic heating under certain flow conditions. The results predicted by our simplified model (presented in Section 2.2.7.3) will show that the radiation which leaves the whole arc column accounts for 65% to 70% of the total electrical power input. Since 25% of the radiation which leaves the arc column is absorbed in the surrounding cold gas, about 50% of the total power input into the arc column is lost to the wall of the confining space in the form of radiation.

C_1 in equation (2.28) is a dimensionless turbulent parameter. A value of 0.012 has been found acceptable for free burning arcs in air [94]. This value is used for free burning SF_6 arcs due a lack of information for SF_6. We will show in Section 2.2.7.4 that c_1 only affects the axial velocity and its influence on temperature and arc radius is negligible.

2.2.5 Discretisation of the governing equations

An explicit algorithm is used to solve the governing equations. All the convective terms are discretised by upwind difference. Referring to figure 2.1, the whole arc length is divided into N uniformly distributed slabs. All the physical quantities are defined at the downstream side of a slab. Thus the upstream boundary conditions will be denoted in the discretised equations by the subscript '$_k$' = 0 . The continuity equation calculates the radial mass flow rate per unit length of the arc column at the end of each time step. At the (k)th slab,

$$m_k = \frac{1}{\Delta t}[\rho_{0,k}{}^{*}\pi(R_k{}^{*})^2\xi_{\rho,k}{}^{*} - \rho_{0,k}\pi(R_k)^2\xi_{\rho,k}] + \frac{1}{\Delta z_k}[\rho_{0,k}\pi(R_k)^2 w_{0,k}\xi_{v1,k} - \rho_{0,k-1}\pi(R_{k-1})^2 w_{0,k-1}\xi_{v1,k-1} \tag{2.29}$$

where Δt is the time step and Δz_k is the thickness of slabs k (figure 2.1). The starred variables are the values at the end of the present time step. The momentum equation on the axis determines the axial velocity. Since turbulent momentum exchange is much stronger than molecular diffusion, the momentum equation on the axis takes the form

$$w_{0,k}^{*} = w_{0,k} - \frac{\Delta t}{\Delta z_k}[w_{0,k}(w_{0,k} - w_{0,k-1}) - \frac{\mu_0 I^2}{2\pi^2 R_k^{\,3} \rho_{0,k}}(R_k - R_{k-1})] - \frac{4c_1 n_k w_{0,k}^{\,2}}{R_k}\Delta t \tag{2.30}$$

The energy equation on the axis is used to calculate the enthalpy of the arc:

$$h_{0,k}^{*} = h_{0,k} - [(w_{0,k}^{*})^2 - (w_{0,k})^2]/2 - \frac{\Delta t}{\Delta z_k} w_{0,k}[h_{0,k} + (w_{0,k})^2/2 - h_{0,k-1} - (w_{0,k-1})^2/2] + \frac{1}{\rho_{0,k}}(P_{v1}^{*} - P_{v1}) + \frac{\mu_0}{4\pi^2 R_k^{\,2} \rho_{0,k}}[(I^{*})^2 - I^2] - \frac{\mu_0 I^2}{2\pi^2 R_k^{\,3} \rho_{0,k}}(R_k^{*} - R_k) + \frac{\Delta t}{\rho_{0,k}}(\sigma_k E_{z,k}^{\,2} - u_k) \tag{2.31}$$

The variable factor n in the radial profile of the axial velocity which is given by equation (2.10) is calculated from the axial momentum equation for the whole arc column:

$$(\rho_{0,k}\pi R_k^{\,2} w_{0,k}\xi_{v1,k})^{*} = \rho_{0,k}\pi R_k^{\,2} w_{0,k}\xi_{v1,k} - \frac{\Delta t}{\Delta z_k}[\rho_{0,k}\pi R_k^{\,2}(w_{0,k})^2\xi_{v2,k} - \rho_{0,k-1}\pi R_{k-1}^{\,2}(w_{0,k-1})^2\xi_{v2,k-1} - \frac{\mu_0 I^2}{4\pi R_k}(R_k - R_{k-1})] \tag{2.32}$$

The energy equation for the arc column determines the change of the arc radius. The convective term, which is the third term on the RHS of equation (2.13) can be discretised as

$$CONV_k = \frac{\Delta t}{\Delta z_k}[\rho_{0,k}\pi R_k^{\,2} w_{0,k}\xi_{v1,k}(h_{0,k} - h_{v1}) - \rho_{0,k-1}\pi R_{k-1}^{\,2} w_{0,k-1}\xi_{v1,k-1}(h_{0,k-1} - h_{v1}) + \rho_{0,k}\pi R_k^{\,2} w_{0,k}\xi_{v3,k} w_{0,k}^{\,2}/2 - \rho_{0,k-1}\pi R_{k-1}^{\,2} w_{0,k-1}\xi_{v3,k-1} w_{0,k-1}^{\,2}/2] \tag{2.33}$$

The last four terms in equation (2.13) is regarded as a source term:

$$SOU_k = \pi R_k^2 (P_{v1}^* - P_{v1}) + \frac{\mu_0}{8\pi}(I^{*2} - I^2) + \Delta t(E_{z,k} I - c_t u_k \pi R_k^2) \qquad (2.34)$$

The temporal change of kinetic energy which is the second term on the RHS of equation (2.13) is

$$KIC_k = \rho_{0,k}^* \pi (R_k^*)^2 \xi_{v2,k}^* (w_{0,k}^*)^2 / 2 - \rho_{0,k} \pi R_k^2 \xi_{v2,k} (w_{0,k})^2 / 2 \qquad (2.35)$$

The discretised energy equation for the arc column can thus be written in the form

$$(\rho_{0,k} \pi R_k^2 \xi_{\rho,k})^* = \rho_{0,k} \pi R_k^2 \xi_{\rho,k} + \frac{1}{H_k}[-\rho_{0,k} \pi R_k^2 \xi_{\rho,k} (h_{0,k}^* - h_{0,k}) - KIC_k - CONV_k + SOU_k] \qquad (2.36)$$

where $H_k = h_{0,k} - h_{v1}$ and h_{v1} is the enthalpy in Volume V_1 . The radial momentum equation determines the pressure on the axis

$$P_{0,k} = P_{v1} + \frac{\mu_0 I^2}{4\pi^2 R_k^2} \qquad (2.37)$$

The equation of state on the axis has the form

$$F(\rho_{0,k}, h_{0,k}, P_{0,k}) = 0 \qquad (2.38)$$

Ohm's law is used to calculate the electric field in the (k)th slab

$$E_{z,k} = \frac{I}{\sigma_k \pi R_k^2} \qquad (2.39)$$

The discretised equation for the mass in volume V_1 is given by

$$M_{v1}^* = M_{v1} - \Delta t [\sum_{k=1}^{N-1} m_k \Delta z_k - (\rho_0 \pi R^2 w_0 \xi_{v1})_{N-1} + F_m] \qquad (2.40)$$

where N is the total number of slabs. The equation of state for Volume 1 is written as

$$p_{v1}(V_1 - \sum_{k=1}^{N} \pi R_k^2 \Delta z_k) = M_{v1} R_g T_{v1} \qquad (2.41)$$

The discretised energy equation for volume V_1 takes the following form

$$T_{v1}^{*} = T_{v1} - \frac{T_{v1}}{M_{v1}}(M_{v1}^{*} - M_{v1}) - \frac{h_{v1}\Delta t}{c_v M_{v1}}\sum_{k=1}^{N-1} m_k \Delta z_k$$
$$+ \frac{\Delta t}{c_v M_{v1}}\sum_{k=1}^{N}(c_a c_t u_k \pi R_k^2 \Delta z_k) - \frac{F_h}{c_v M_{v1}}\Delta t \qquad (2.42)$$
$$+ \frac{\Delta t}{c_v M_{v1}}(1-c_e)(\rho_0 \pi R^2 w_0 \xi_{v1} h_0 + \rho_0 \pi R^2 w_0 \xi_{v3} w_0^2/2)_{N-1}$$

Mass equation for volume V_2 is

$$M_{v2}^{*} = M_{v2} + F_m \Delta t \qquad (2.43)$$

and the energy equation for volume V_2 becomes

$$T_{v2}^{*} = T_{v2} + \frac{\Delta t}{c_v M_{v2}}(F_h - c_v T_{v2} F_m) \qquad (2.44)$$

2.2.6 The Solution procedure and the associated software

The numerical algorithm used to solve the governing equations is explicit. The time step must be well controlled to ensure numerical stability and the accuracy of the results. The maximum time step in the simplified model is determined by the axial velocity, the slab thickness and the magnitude of the source terms in the energy equations. Taking the energy equation, equation (2.16) on the axis, as an example, the maximum time step based on this equation should be much smaller than the minimum of following two terms over all the slab. The first term is related to the velocity and slab thickness, $\left|\frac{\Delta z_k}{w_{0,k}}\right|$, where k =1 to N. The second term is to related to the Ohmic heating and net radiation emission, $\frac{\rho_{0,k} h_{0,k}}{\sigma_k E_{z,k}^{\ 2} + u_k}$, where k = 1 to N. The hierarchical chart of the program is shown in figure 2.3. The solution procedure is shown in figure 2.4. There is one main program and seventeen subroutines:

MAIN.F:	main program
RUNSTEDY:	solve a steady state arc
RUNTRANS:	solve a transient arc
STEPON:	solution at a new time step
SOLVARC:	solves equations in the arc column
SOLVCOL:	solves equations in the two cool volumes
INITIAL:	initialise the computation

RADIUS:	calculates the arc radius
ENTHALPY:	calculated the enthalpy on axis
VELOCITY:	calculates velocity on axis
WFLUX:	calculates the momentum flux from equation (2.29)
WSHAPE:	calculated n in equation (2.10)
READINTE:	read in intermediate results for RESTART
TIMESTEP:	calculated the time step
FINDI:	calculates the current
TEMPFIND:	calculates the temperature from enthalpy
SIGMFIND:	calculates electrical conductivity
RECORDER:	write computational results on disk files

The solution of a steady state free burning arc in an open space is used as the initial condition for a transient free burning arc. The pressure and temperature in the open space is equal to those in the confining space at time zero of the transient case. The current of the steady state free burning arc is about one-tenth of the peak current of the transient case. The arcing conditions, the name of the data files which are used to store the results, and an integer variable which can switch the program between "steady state simulation (for initial condition)" and "transient simulation" are specified in three special data files of ".DDD" type, a list of which is shown in Appendix 1.

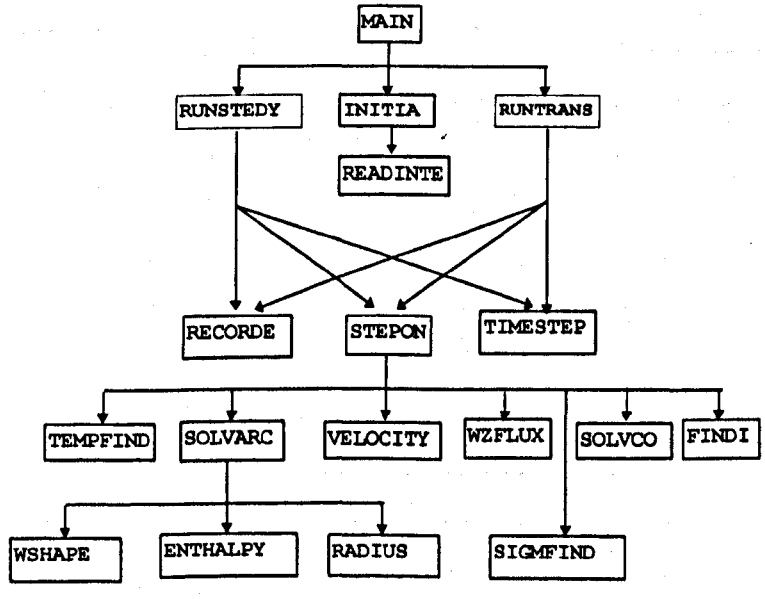

Figure 2.3 Hierarchical chart of the FORTRAN 77 program for simulation of free burning arcs in a confined space.

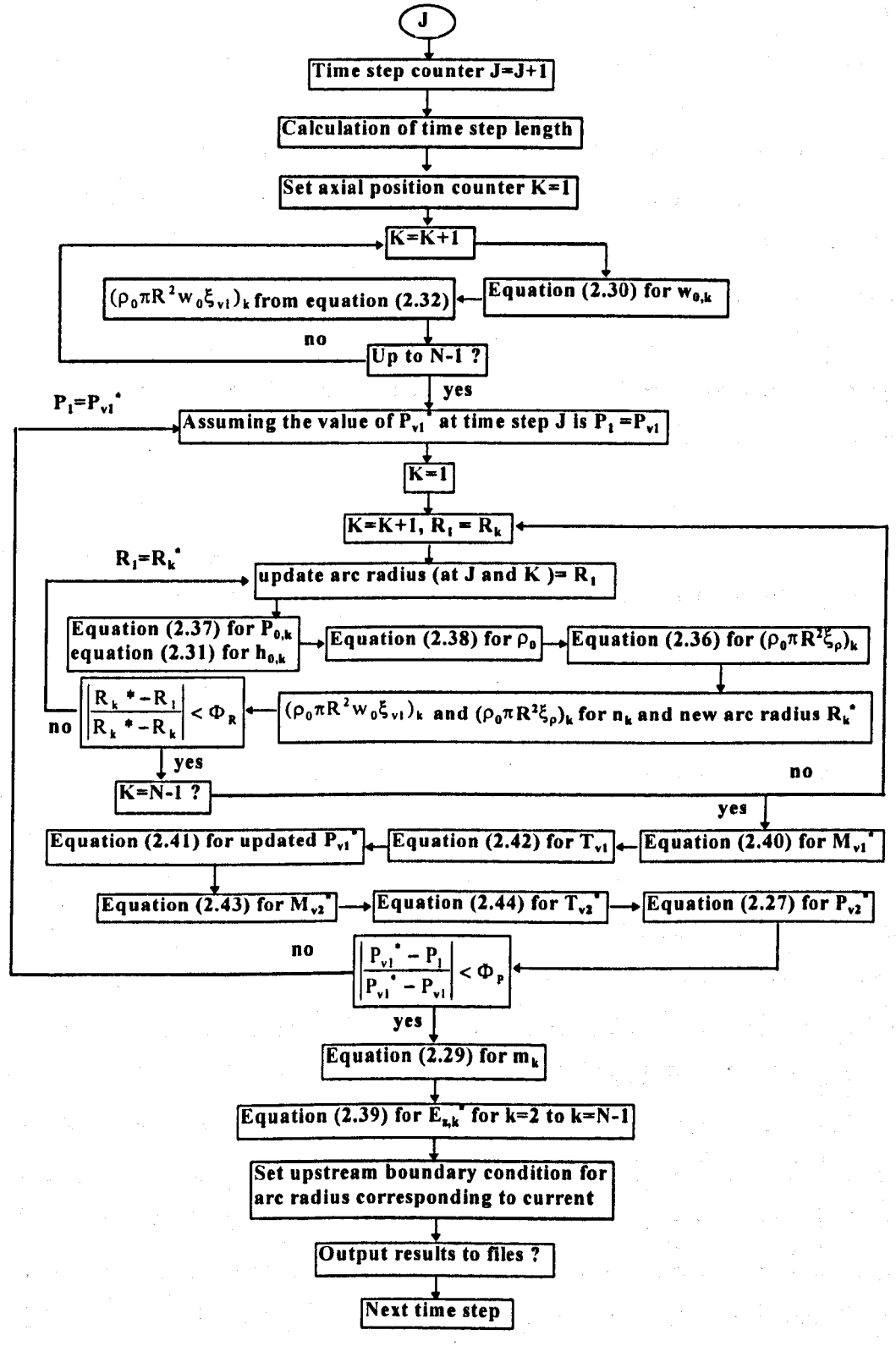

Figure 2.4 Solution procedure of the software to solve the governing equations of the simplified model for free burning arcs in a confined space.

2.2.7 Basic features of the simplified model

The simplified model which we have developed in the preceding sections is self-consistent. Given the electric current, the arc voltage will be calculated as part of the solution of the governing equations. The major simplifications are the top-hat radial temperature profile and the radial distribution of the axial velocity in the form of equation (2.10), which determine the basic features of energy balance in the arc column. The electric current and the temperature at the arc root, which we set as the upstream boundary conditions, are only approximate. It is essential to know how sensitive the solution of the governing equations will be to these two boundary conditions. We will in this section examine two steady state cases with arcing current of 500A and 5kA respectively. The gap length used in these two cases is 30mm. The pressure and temperature in Volume V_1 and Volume V_2 are maintained constant by using open boundary in order to get a steady state solution of the governing equations in the arc column.

2.2.7.1 Minimum number of slabs

Experimental investigation of Hsu et al [95] showed that the radius of free burning arcs increases rapidly from the surface of the upstream electrode. For a uniformly distributed slab system the slab thickness must be smaller than the length scale which characterises the strong acceleration of the arcing gas by the $\vec{J} \times \vec{B}$ force near the upstream electrode. The results shown in figures 2.5 to 2.10 are calculated with a current density of $10^8 A/m^2$ and a temperature of 12700K as the upstream boundary conditions for three different numbers of slabs (50, 100 and 150 uniformly distributed slabs). The results show that the thickness of the strong gas acceleration region near the upstream electrode is 2mm for the 500A case and 4mm for the 5kA case. The slab thickness is 0.6mm for the 50 slabs case, 0.3mm for the 100 slabs case and 0.2mm for the 150 slabs case. The axial velocity and the radial mass flow rate per unit length across the arc column are most affected by the number of slabs (figures 2.5, 2.6, 2.8 and 2.9). However this influence is limited to a small region near the upstream electrode. The axial electric field distribution, which determines the total electrical power input, is not sensitive to the number of slabs (figures 2.7 and 2.10). Since the length scale characterising the strong gas acceleration region near the upstream electrode increases with current, the influence of the number of slabs on higher current arcs is less significant, as can be seen from the results presented in figures 2.5 to 2.10.

Since the variation of arc properties sufficiently downstream is rather smooth, there is no need for the use of fine slabs. A slab system which stretches towards the downstream electrode will be appropriate. Assuming the slab thickness increases from the upstream electrode according to a power function, the distribution of the slab can be described by

$$z(k) = \frac{\theta^k - 1}{\theta^N - 1} d \qquad (2.45)$$

where k = 1, 2, ..., N. N is the total number of slabs, d the gap length between the two electrodes and θ is a factor controlling the distribution. The results with θ = 1.04 are shown in figure 2.11 for the 500A case. All the results in the rest of Section 2.2.7 are calculated with a slab system described by equation (2.45) and θ = 1.04.

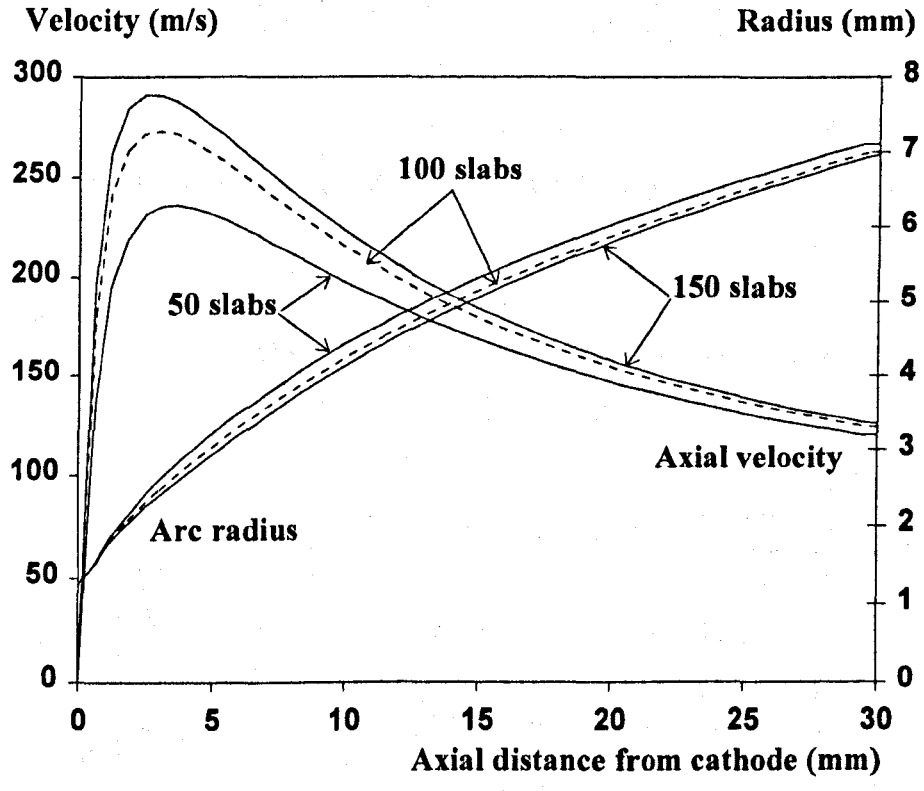

Figure 2.5 Axial velocity and arc radius of a 500A steady state SF_6 free burning arc, calculated by the simplified model with different number of slabs in the arc column. The ambient pressure is 5bar at room temperature.

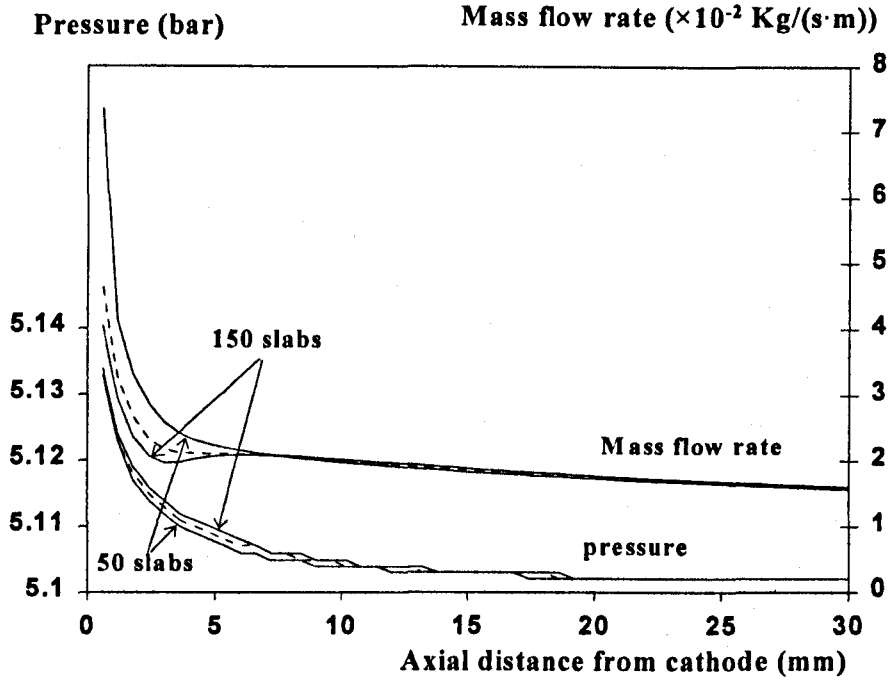

Figure 2.6 Axis pressure and radial mass flow rate per unit length across the radial boundary of a 500A steady state SF_6 free burning arc, calculated by the simplified model with different number of slabs in the arc column. The ambient pressure is 5bar at room temperature. Broken lines: 100 slabs

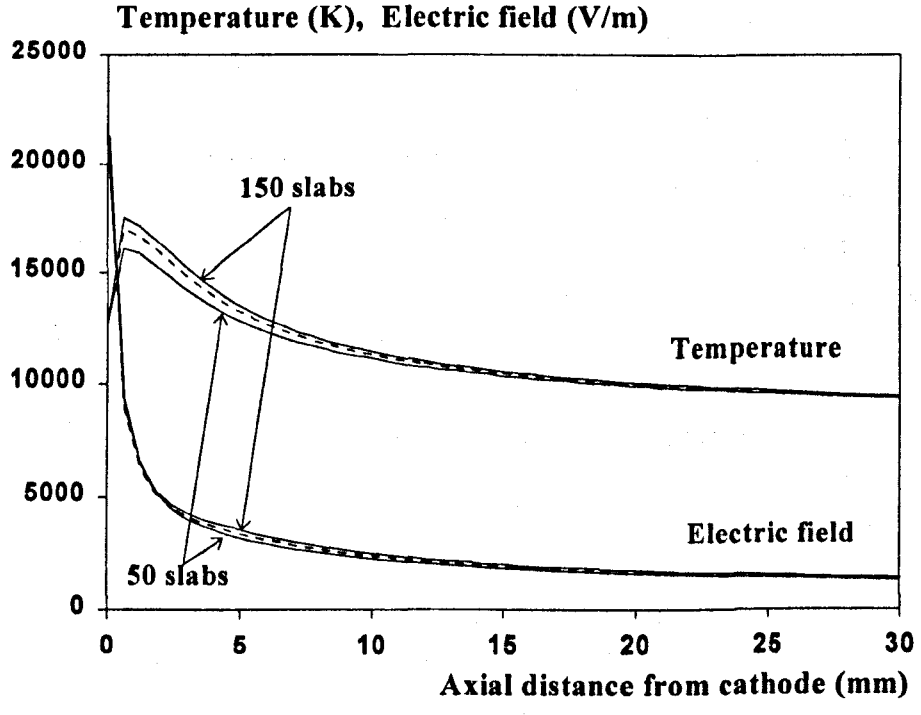

Figure 2.7 Electric field and axis temperature of a 500A steady state SF_6 free burning arc, calculated by the simplified model with different number of slabs in the arc column. The ambient pressure is 5bar at room temperature. Broken lines: 100 slabs

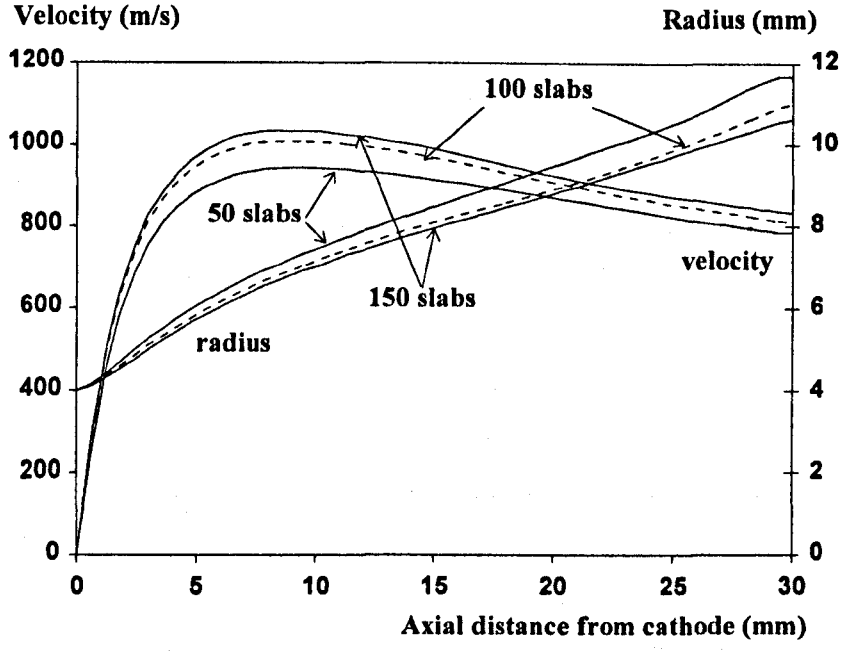

Figure 2.8 Axial velocity and arc radius of a 5000A steady state SF_6 free burning arc, calculated by the simplified model with different number of slabs in the arc column. The ambient pressure is 5bar at room temperature.

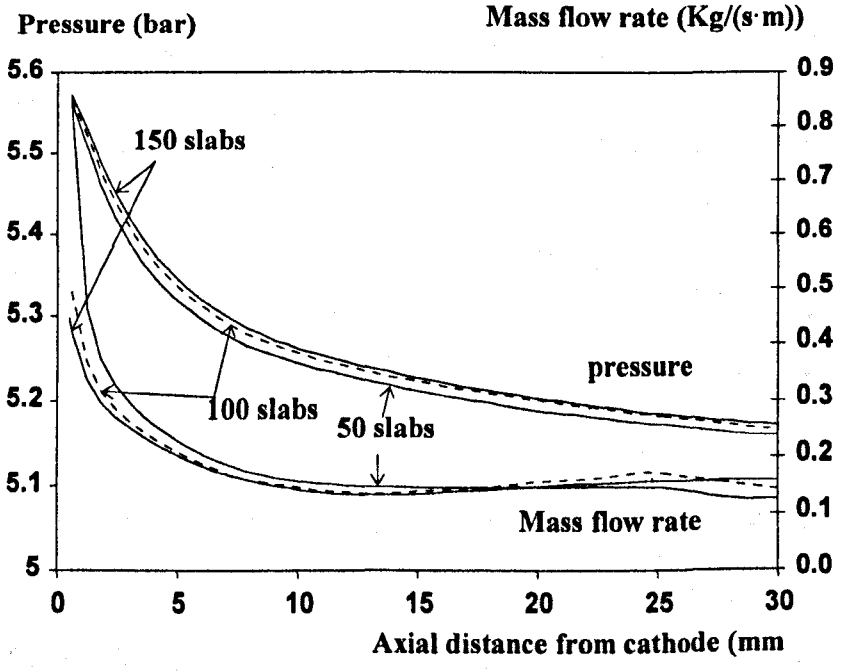

Figure 2.9 Axis pressure and radial mass flow rate per unit length across the radial boundary of a 5000A steady state SF_6 free burning arc, calculated by the simplified model with different number of slabs in the arc column. The ambient pressure is 5bar at room temperature.

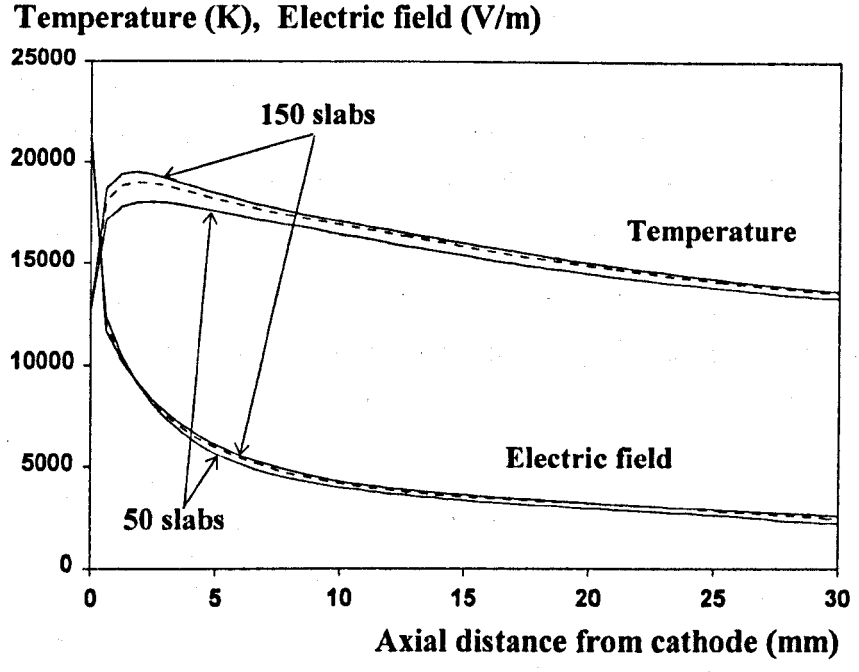

Figure 2.10 Electric field and axis temperature of a 5000A steady state SF_6 free burning arc, calculated by the simplified model with different number of slabs in the arc column. The ambient pressure is 5bar at room temperature. Broken lines: 100 slabs

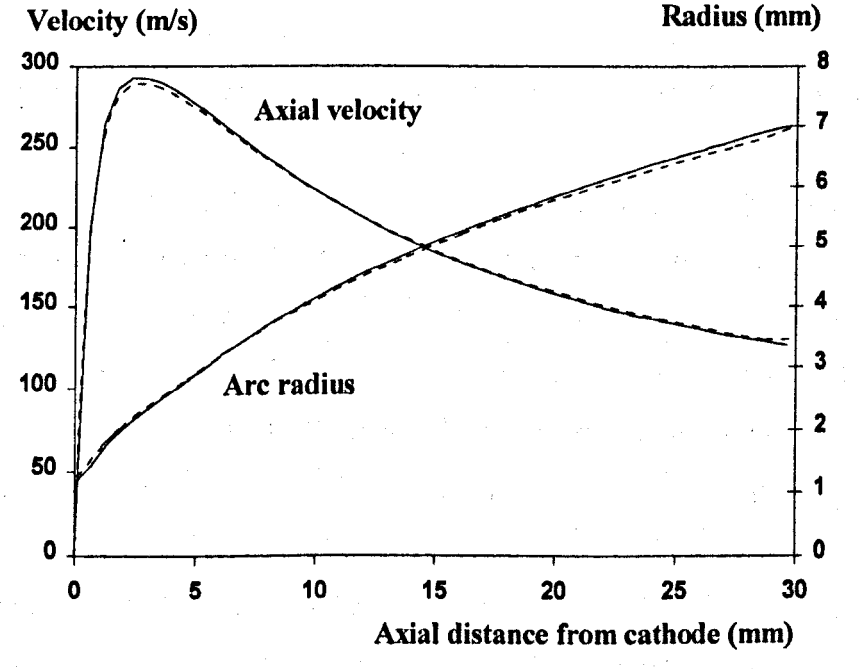

Figure 2.11 Axial velocity and arc radius of a 500A steady state SF_6 free burning arc, calculated by the simplified model with different slab distribution in the arc column. The ambient pressure is 5bar at room temperature. solid lines: 150 slabs uniformly distributed in the electrode gap. Dotted lines: 50 grids expanding towards the downstream electrode according to equation (2.45).

2.2.7.2 Influence of the upstream boundary conditions

It is well known that the flow field in free burning arcs is established by the very high current density at the upstream electrode [94,95,96,97]. Since the current density cannot be theoretically determined without consideration of the sheath-cathode interaction which is yet poorly understood, we specify the current distribution based on the experimental observation of [95]. The size of the arc root in our simplified model is calculated in terms of an average current density, J_c, at the upstream electrode

$$R_c = \sqrt{\frac{I}{\pi J_c}} \tag{2.46}$$

where I is the instantaneous arcing current. For a steady state free burning arc, equation (2.12) can be rearranged as

$$\frac{\partial}{\partial z}(\rho_0 \pi R^2 w_0^2 \xi_{v2} - \frac{\mu I^2}{4\pi} \ln R) = 0 \tag{2.47}$$

or

$$\rho_0 \pi R^2 w_0^2 \xi_{v2} - \frac{\mu I^2}{4\pi} \ln R = -\frac{\mu I^2}{4\pi} \ln R_c \tag{2.48}$$

Equation (2.48) shows that for a given current the size of the arc root fixes the integral constant of the axial momentum equation. The current density at the arc root is in the range of 5×10^7 to $2\times10^8 A/m^2$ [95,96,97,98]. The results in figures 2.12 to 2.17, which are obtained with a slab distribution defined by equation (2.45), show that the value of the current density at the arc root has significant influence on the size of the arc column and on the flow field in free burning arcs. Increasing J_c from 5×10^7 to $2\times10^8 A/m^2$ (figure 2.12) results in an increase of the maximum axial velocity from 200 to 430m/s and in an average reduction of 20% in arc radius of the 500A case. The arc voltage, which determines the electrical power input, is also increased from 70 to 93V (33%). For the 5,000A arc, increasing of the current density from 10^8 to $2\times10^8 A/m^2$ results in 20% increase in the arc voltage.

The temperature at the arc root, which is one of the three upstream boundary conditions set for the arc column, has little influence on the behaviour of the arc. The difference between the results for arc root temperatures set at 12,700K and 15,000K is less than 5%, as shown in figures 2.18 and 2.19.

The influence of the upstream boundary conditions on the results of the free burning arc has been studied. It is shown that the uncertainty in the current density at the arc root can significantly influence the axial velocity and radial mass flow rate (per unit length across the radial boundary of the arc column) in a region near the upstream electrode. However, since radiation transfer plays an important role in the energy transport of the free burning arc, the arc voltage is not so sensitive as that of the axial velocity to the change of current density at the arc root. Taking the current density at the arc root to be within the range from 5×10^7 to $2\times10^8 A/m^2$, our choice of $1\times10^8 A/m^2$ will introduce an uncertainty of 20% in the arc voltage in the steady state cases. For the transient cases which we will investigate, the pressure in the surrounding region of the arc is above 5bar. The influence of varying the current density at the arc root will be less significant because of the higher density in the arc column (See equation (2.48)). It is thus expected that the uncertainty introduced by the current density at the arc root will be less than 20% in the predicted pressure and the arc voltage in the transient cases.

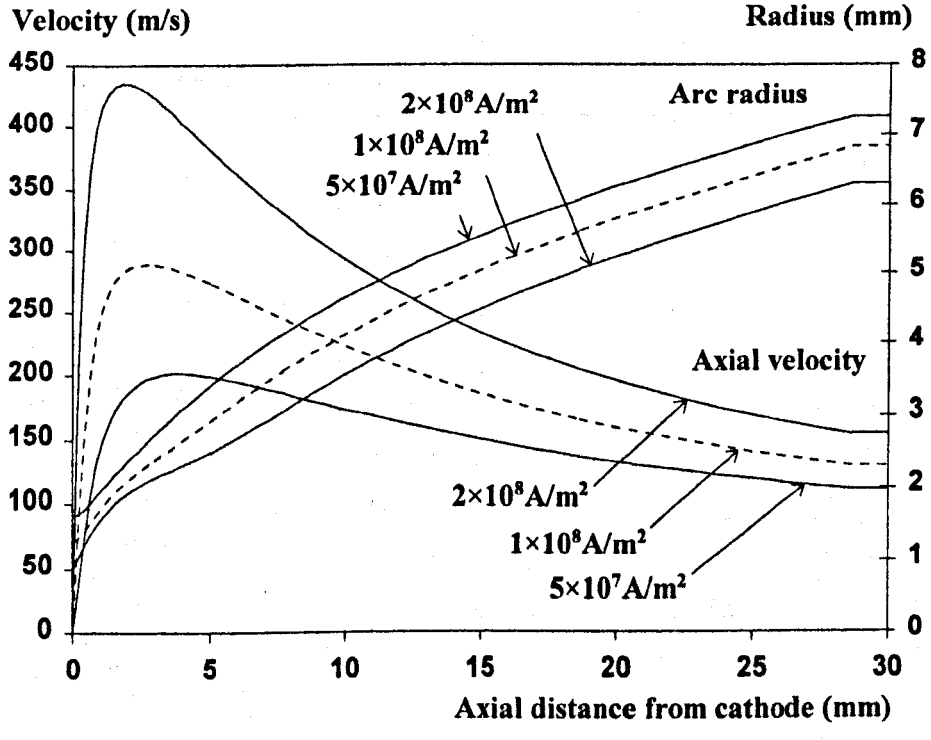

Figure 2.12 Influence of the electric current density at the arc root on the radius and axial velocity of a 500A steady state SF_6 free burning arc. The ambient pressure is 5bar at room temperature.

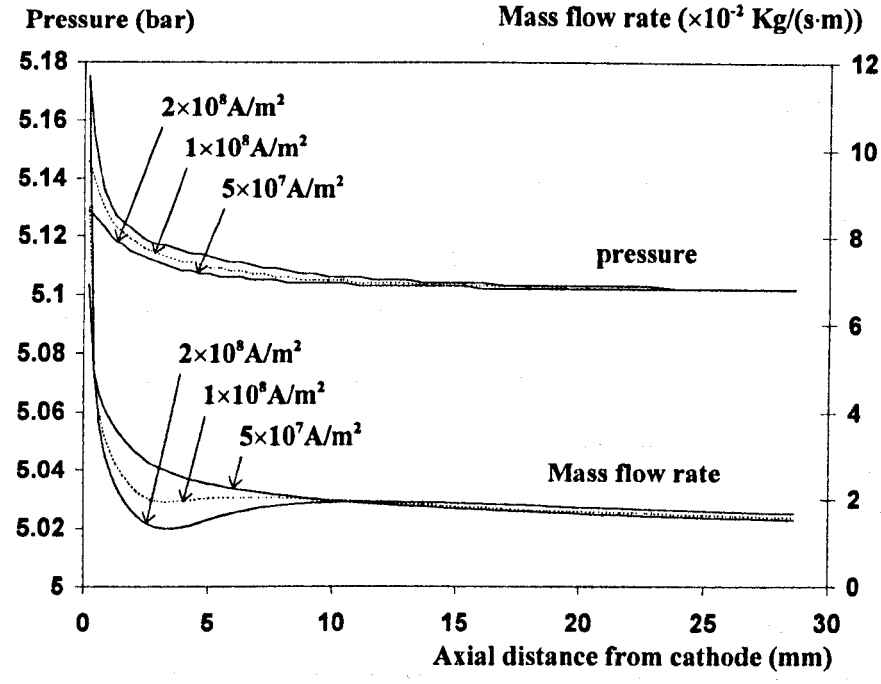

Figure 2.13 Influence of the electric current density at the arc root on the axis pressure and radial mass flow rate per unit length across the radial boundary of a 500A steady state SF_6 free burning arc. The ambient pressure is 5bar at room temperature.

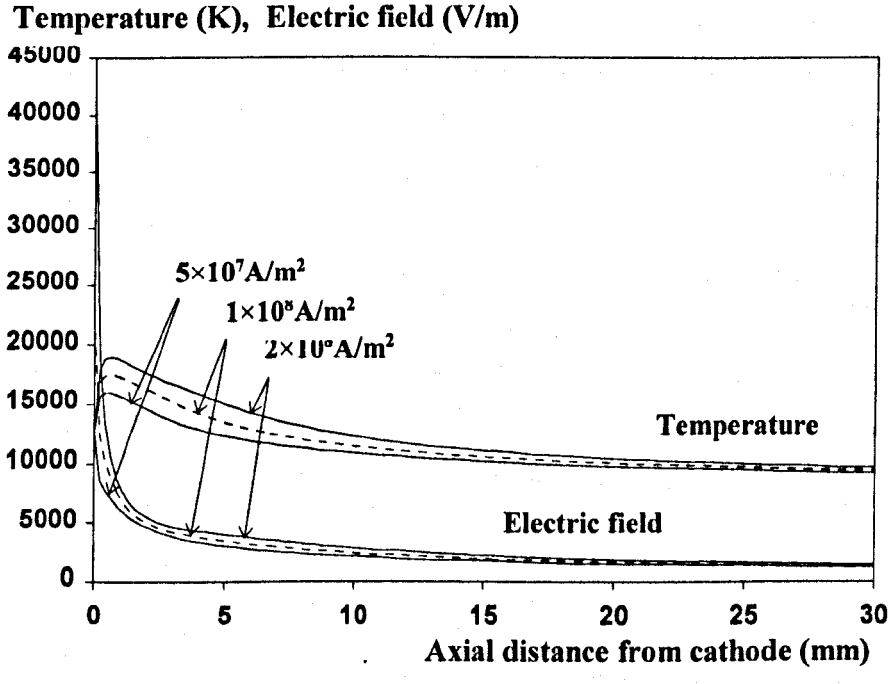

Figure 2.14 Influence of the electric current density at the arc root on the axis temperature and axial electric field strength of a 500A steady state SF_6 free burning arc. The ambient pressure is 5bar at room temperature.

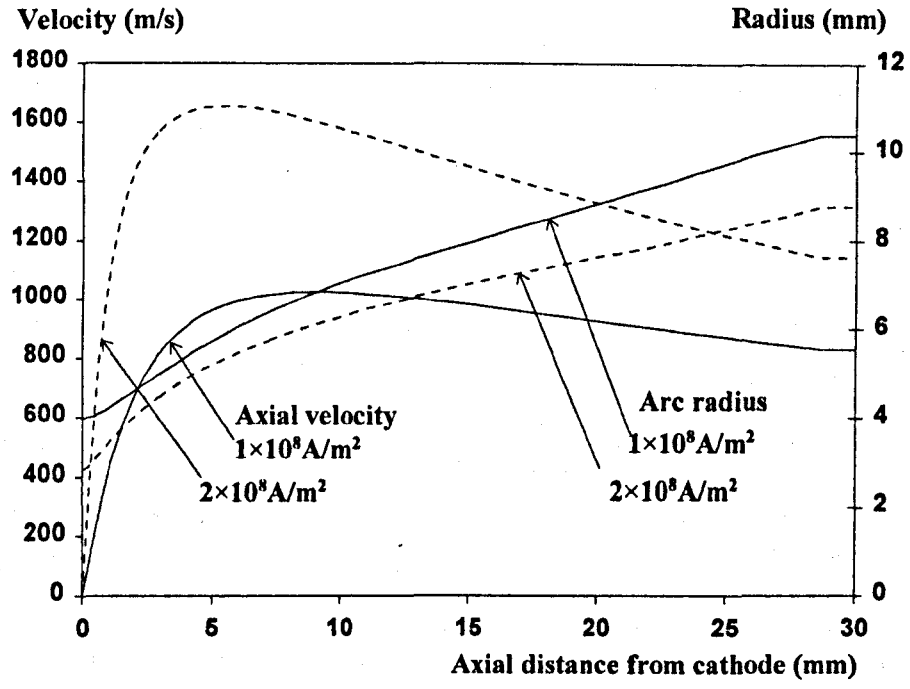

Figure 2.15 Influence of the electric current density at the arc root on the radius and axial velocity of a 5000A steady state SF_6 free burning arc. The ambient pressure is 5bar at room temperature.

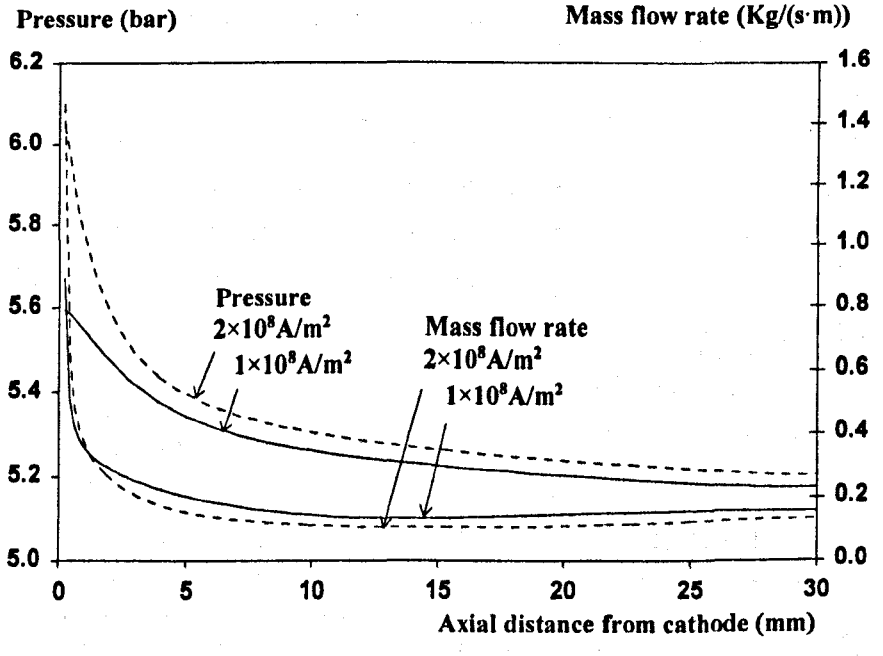

Figure 2.16 Influence of the electric current density at the arc root on the axis pressure and the radial mass flow rate per unit length across the radial boundary of a 5000A steady state SF_6 free burning arc. The ambient pressure is 5bar at room temperature.

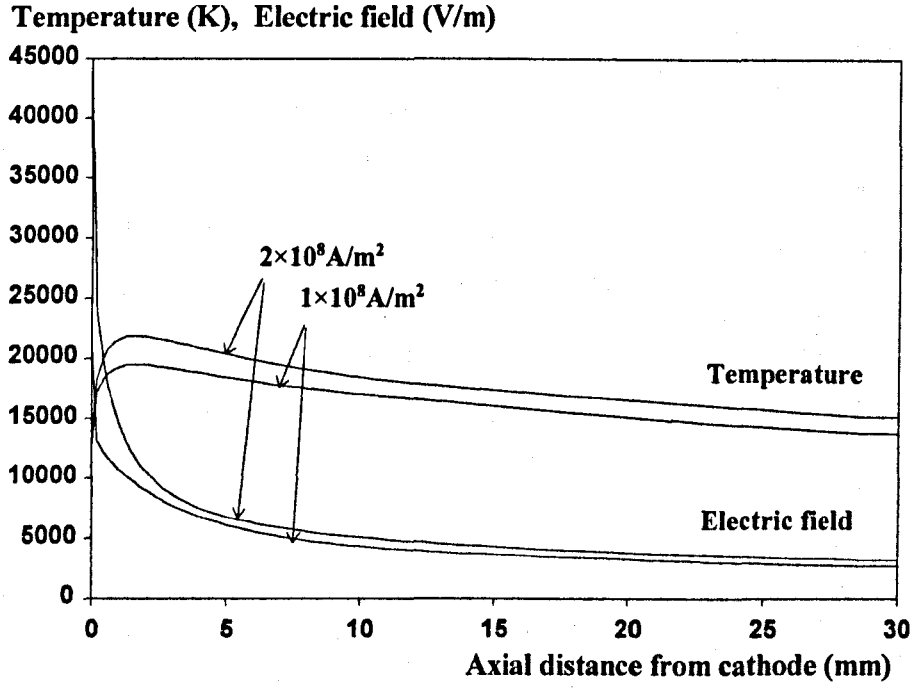

Figure 2.17 Influence of the electric current density at the arc root on the axis temperature and the axial electric field strength of a 500A steady state SF_6 free burning arc. The ambient pressure is 5bar at room temperature.

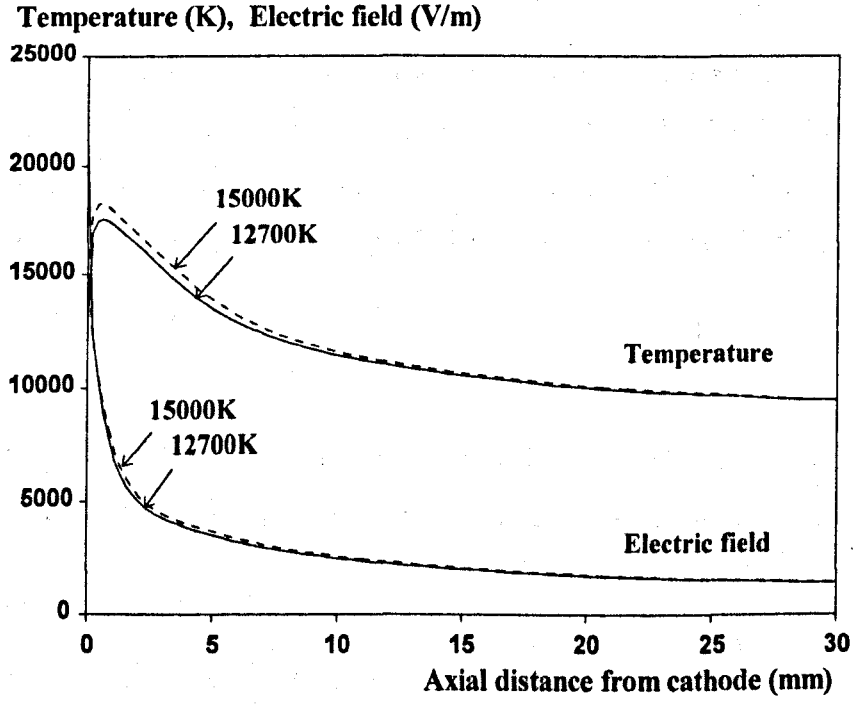

Figure 2.18 Influence of temperature at the arc root on the axis temperature and axial electric field strength of a 500A steady state SF_6 free burning arc. The ambient pressure is 5bar at room temperature.

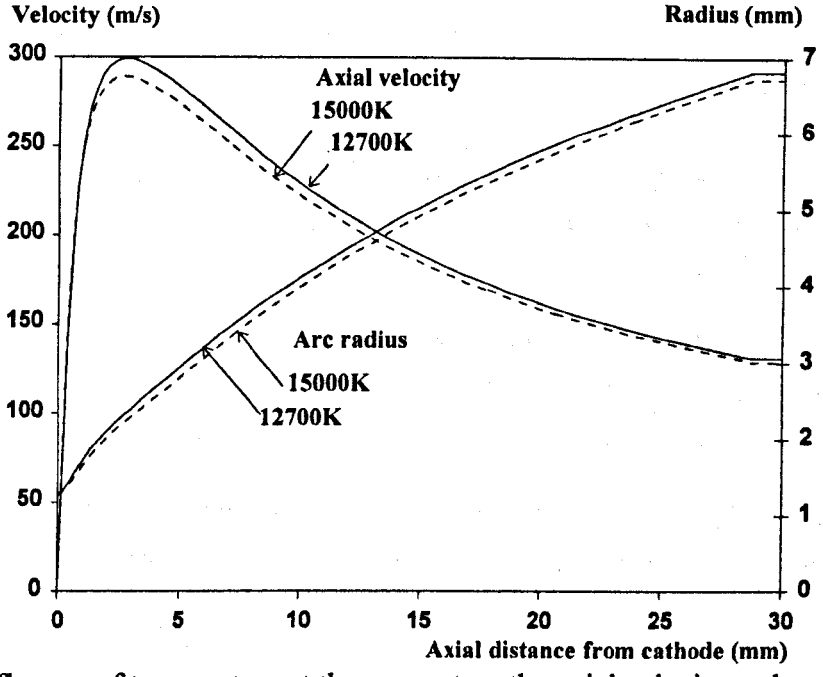

Figure 2.19 Influence of temperature at the arc root on the axial velocity and arc radius of a 500A SF_6 free burning arc with an ambient pressure of 5bar.

2.2.7.3 Explanation of the energy balance in the simplified model for steady state free burning arcs

The assumption in our model of a top-hat radial temperature profile means there is no radial thermal conduction included. Since the axial thermal conduction is also neglected, the local electrical power input on the axis must be balanced by radiation and axial convection. For steady state arcs when the kinetic energy of the arcing gas is negligible, equation (2.16) becomes

$$\rho_0 w_0 \frac{\partial h_0}{\partial z} = \sigma E_z^{\,2} - u \qquad (2.49)$$

which means the net radiation emission on the axis will become stronger than the local Ohmic heating when the axial temperature gradient is negative. Equation (2.13) can be similarly reduced to

$$\frac{\partial}{\partial z}[\rho_0 \pi R^2 w_0 \xi_{vl}(h_0 - h_{vl})] = E_z I - c_t u \pi R^2 \qquad (2.50)$$

which, with the substitution of equation (2.11), can be rewritten in the following form

$$m(h_0 - h_{vl}) + \rho_0 \pi R^2 w_0 \xi_{vl} \frac{\partial h_0}{\partial z} = E_z I - c_t u \pi R^2 \qquad (2.51)$$

Equations (2.49) and (2.51) determine the energy balance in the arc column. It is clear that the radiation leaving the radially isothermal arc column ($c_t u\pi R^2$ in equation (2.51)) could take most of the Ohmic heating if the second term on the LHS of equation (2.51) is negative and its magnitude is close to that of the first term. The results in figures (2.20) and (2.21) confirm that this situation does occur in the arc column. The results are calculated with a current density of $10^8 A/m^2$ and a temperature of 15000K at the upstream boundary. The gap length between the electrodes is 30mm and the ambient pressure is 5bar at room temperature. At 3mm from the upstream electrode in the 500A case and 13mm in the 5kA case the energy which is required to heat the radially incoming cold gas is approximately equal to that brought in by the axial convection. As a result, the Ohmic heating over the whole cross section of the arc has to be taken away by radiation (The second dotted vertical line from left in the figures).

When the axial gradient of temperature is zero, the net radiation emission on the axis will solely balance the local Ohmic heating. The radiation which leaves the arc column is $c_t EI$ and the rest of the Ohmic heating is used to heat the radially incoming cold gas. This situation occurs at 1mm from the upstream electrode in the 500A case and 2mm in the 5kA case (The first dotted vertical line from left in the figures). The energy balance for the whole arc length is listed in Table 2.2. Although the radiation which leaves the whole arc column can be as high as 70% of the electrical power input, the amount of radiation which reaches the wall of the confining space is 52.5% of the electrical power input since we have assumed that 25% of the radiation leaving the arc column is re-absorbed by the surrounding cold gas.

Table 2.2 Energy balance for the whole arc column

arcing current (A)	energy loss by radiation (W)	energy loss by convection (W)
500	65%	35%
5,000	70%	30%

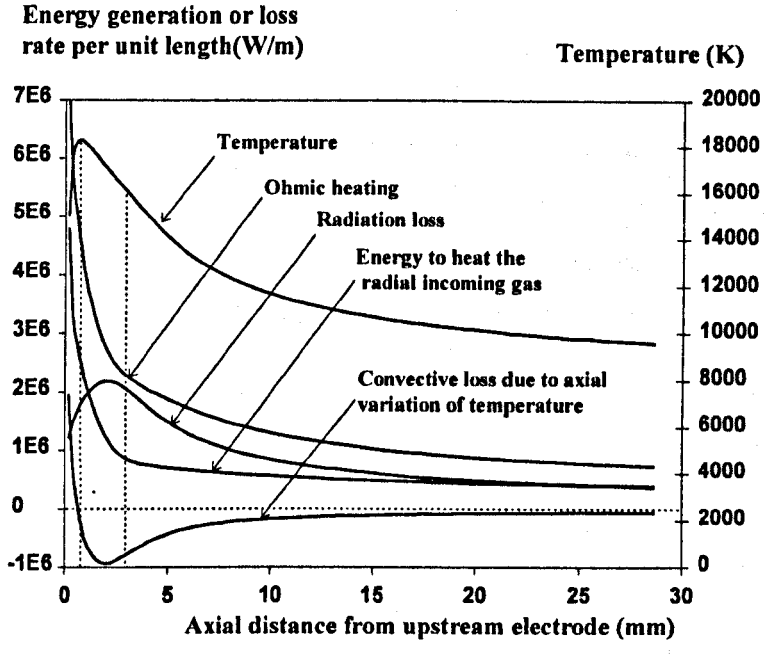

Figure 2.20 Energy balance predicted by the simplified model for the whole arc cross section as a function of the axial distance from the upstream electrode. Arcing current is 500A and the ambient pressure is 5bar. Upstream boundary conditions are: current density = $10^8 A/m^2$ and temperature = 15000K.

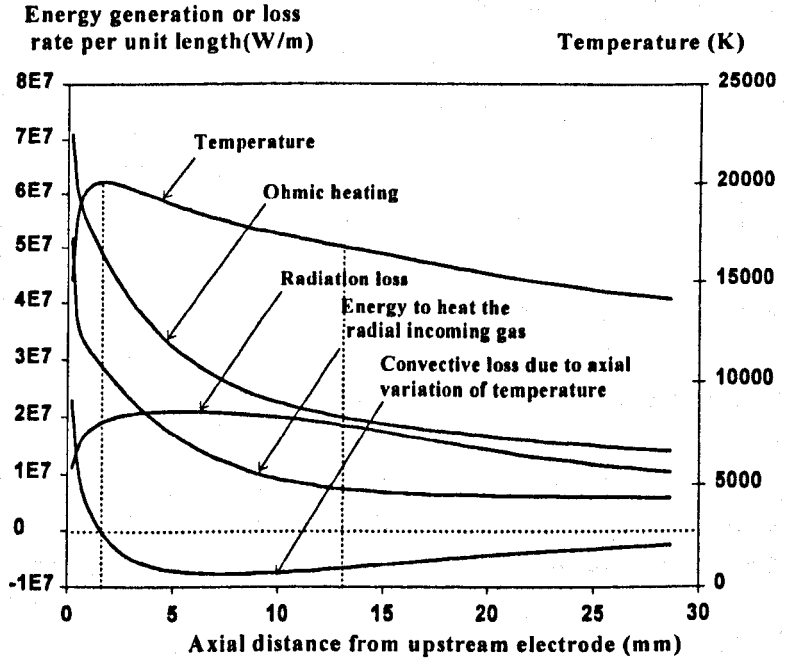

Figure 2.21 Energy balance predicted by the simplified model for the whole arc cross section as a function of the axial distance from the upstream electrode. Arcing current is 5000A and the ambient pressure is 5bar. Upstream boundary conditions are: current density = $10^8 A/m^2$ and temperature = 15000K

2.2.7.4 Effect of turbulence

There is no thermal conduction and turbulent energy exchange in the simplified model. Turbulence only affects the axial velocity. Results in figure 2.22 show that, although the axial velocity downstream of the strong gas acceleration region is sensitive to the turbulent parameter c_1 in equation (2.28), the axis temperature, axial electric field and the arc radius are not. We thus use the value of 0.012 for c_1 , which is obtained for air [94]by fitting the measured axial velocity, in our simplified model.

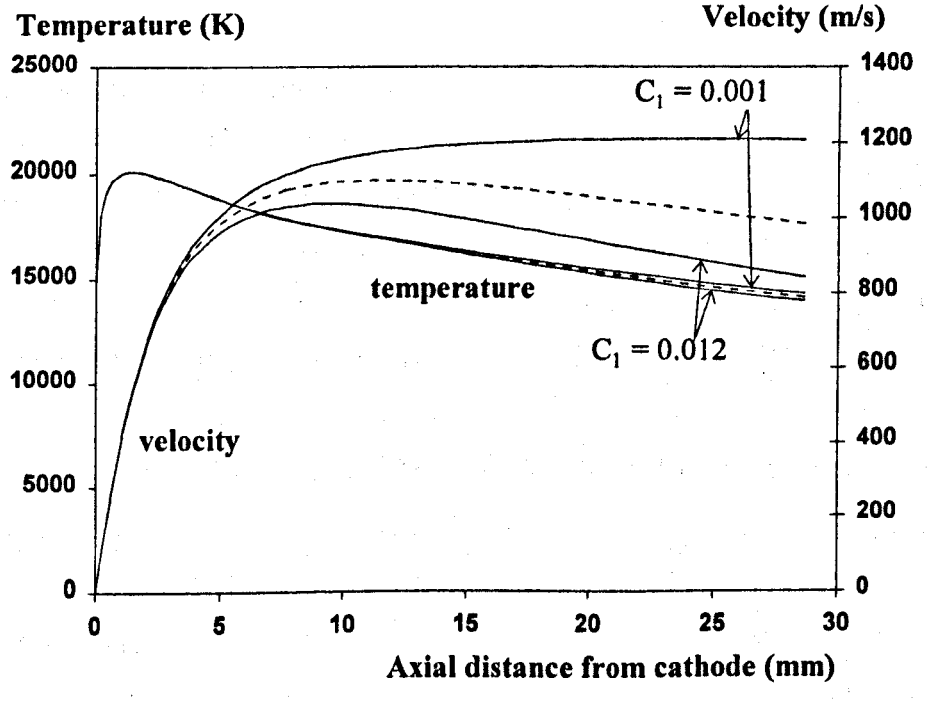

Figure 2.22 Influence of turbulence on the axis temperature and the axial velocity of a 5000A steady state SF_6 free burning arc with an ambient pressure of 5bar at room temperature. Upstream boundary conditions are: current density = $10^8 A/m^2$ and temperature = 15000K. Dotted lines: c_1 =0.006

2.3 Experimental Investigation of Free Burning Arcs in a Confined Space

The work in this section covers pressure and arc voltage measurements within an auto-expansion arcing device, which are intended to provide experimental verification of the simplified model developed in Section 2.2. The whole system consists mainly of the arcing device, the electric current source, the synchronising control and the measuring electronics. Except the shape and dimensions of the two electrodes, we have no control of the arc stability. As a result, axis-symmetry of the arc column cannot be guaranteed. We will present the results of those cases where the arc voltage is reasonably flat and smooth which is an indirect indication of the arc stability.

2.3.1 The experimental system

2.3.1.1 The auto-expansion chamber

The arcing chamber shown in figure 2.23 consists of two parts: the inner volume and the outer volume which are separated by a PTFE cylinder. The gap between the top plate of the steel spacer and the PTFE cylinder allows mass and energy exchange between the two volumes. The effective area of the gap for gas flow is 5.77×10^{-4} m^2. The internal diameter of the steel spacer is 277mm and its length is 230mm. The internal diameter of the PTFE cylinder is 80mm and its thickness in radius is 40mm. The effective volume for the inner part of the arcing chamber is 9.06×10^{-4} m^3 at 30 mm electrode separation, 9.09×10^{-4} m^3 at 40 mm and 9.12×10^{-4} mm^3 at 50 mm. The volume of the outer part of the chamber is 8.89×10^{-3} m^3. The geometry and dimensions of the electrode heads are shown in figure 2.24. The electrode material is 80% Tungsten / 20% copper.

The arc is initiated with the help of a sliding rod electrode made of steel. The rod, which has a diameter of 6mm, is normally kept in contact with the bottom electrode by the weight of the solenoid plunger. With an electric current flowing through the circuit, an arc will be initiated when the solenoid withdraws the rod electrode upwards. The solenoid is powered by a 110V DC source. The distance between the two electrodes can be adjusted in the range of 30mm to 55mm by screwing the solenoid-top-electrode assembly.

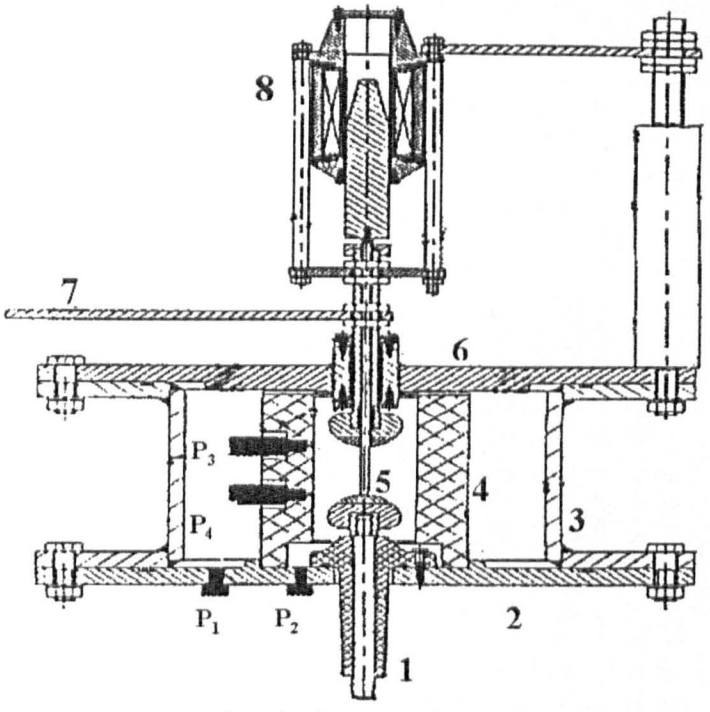

Figure 2.23 The auto-expansion arcing device used for pressure and arc voltage measurements of free burning arcs in a confined space. P_1, P_2, P_3 and P_4 are four Piezoelectric pressure transducers. The main parts of the device are: 1–live electrode; 2–bottom steel plate; 3–steel spacer; 4–PTFE cylinder; 5–steel rode for arc initiation; 6–top steel plate; 7–copper terminal for arc voltage measurement; 8—solenoid.

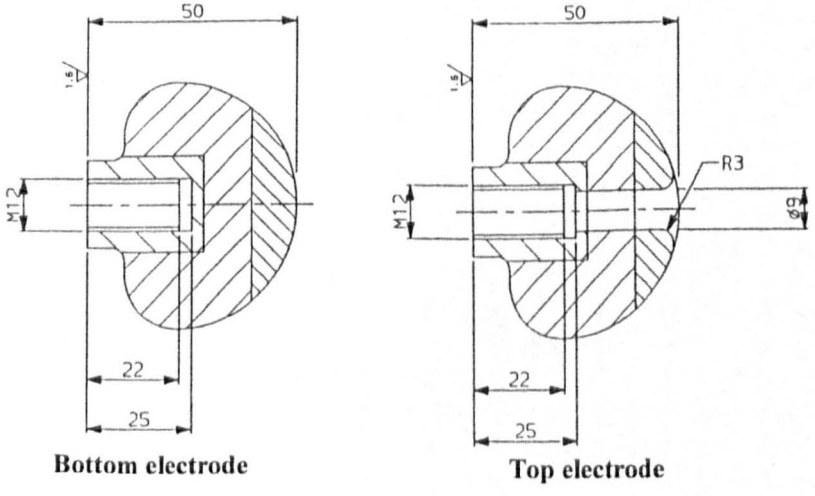

Figure 2.24 Geometry and dimensions of the electrodes in the auto-expansion arcing device. Unit is in mm.

2.3.1.2 Electric current source

The system shown in figure 2.25 was used to generate the main AC current and the low DC current for arc initiation. The frequency of the main current is 44Hz. The peak current depends on the voltage of the capacitor bank c_1 . The magnitude of the low DC current can be adjusted by changing the resistor R_1 at a given voltage on c_1. The main current is switched on by triggering the ignitron I_2. The duration of the main AC current can be controlled by setting the time of triggering the ignitron I_3 through which the remaining energy of the capacitor bank is dumped.

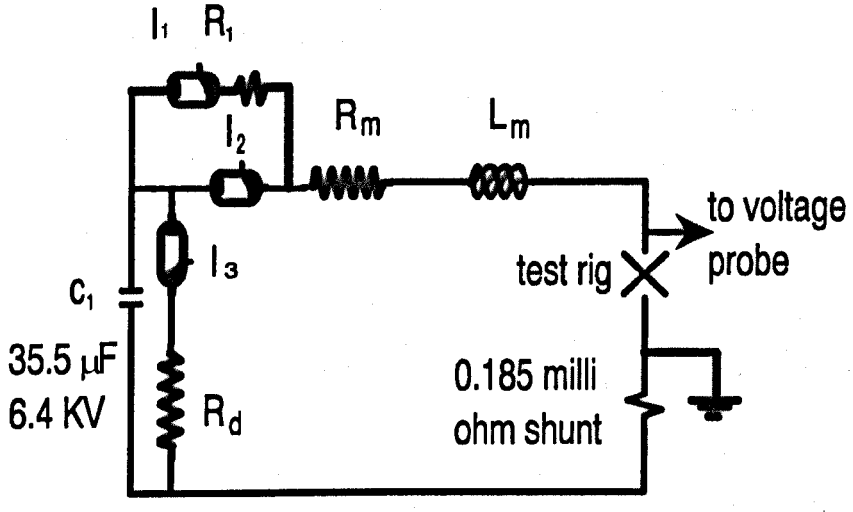

Figure 2.25 Schematic diagram of the capacitor bank system which supplies the main current and the low DC current during arc initiation.

I_1 : ignitron for firing the low DC current
R_1 : current limiting resistor (3 groups, each 6.6Ω)
I_2 : ignitron for firing the main current
C_1 : the capacitor bank
R_m : 1.6--7.5Ω
L_m : inductor, 366μF
I_3 : dump ignitron
R_d : 0.0475Ω

2.3.1.3 Synchronising control of the system

The synchronising control of the experiment system is provided by a cam timer in conjunction with a capacitor bank controller (figure 2.26). The cam timer controls the delay between the activation of the solenoid and the triggering of the capacitor bank controller. The

triggering pulses for the low DC current, the oscilloscope, the main AC current and the dump of the capacitor bank are delivered by four timers in the capacitor bank controller (figure 2.26). It has been found that the mini-switches which are connected to the cam timer for the 110V DC source and the capacitor bank controller should be positioned well away from the start point of the switching finger so that the cam will have sufficient time to develop a stable speed and ensure an accurate time gap between the two triggering signals.

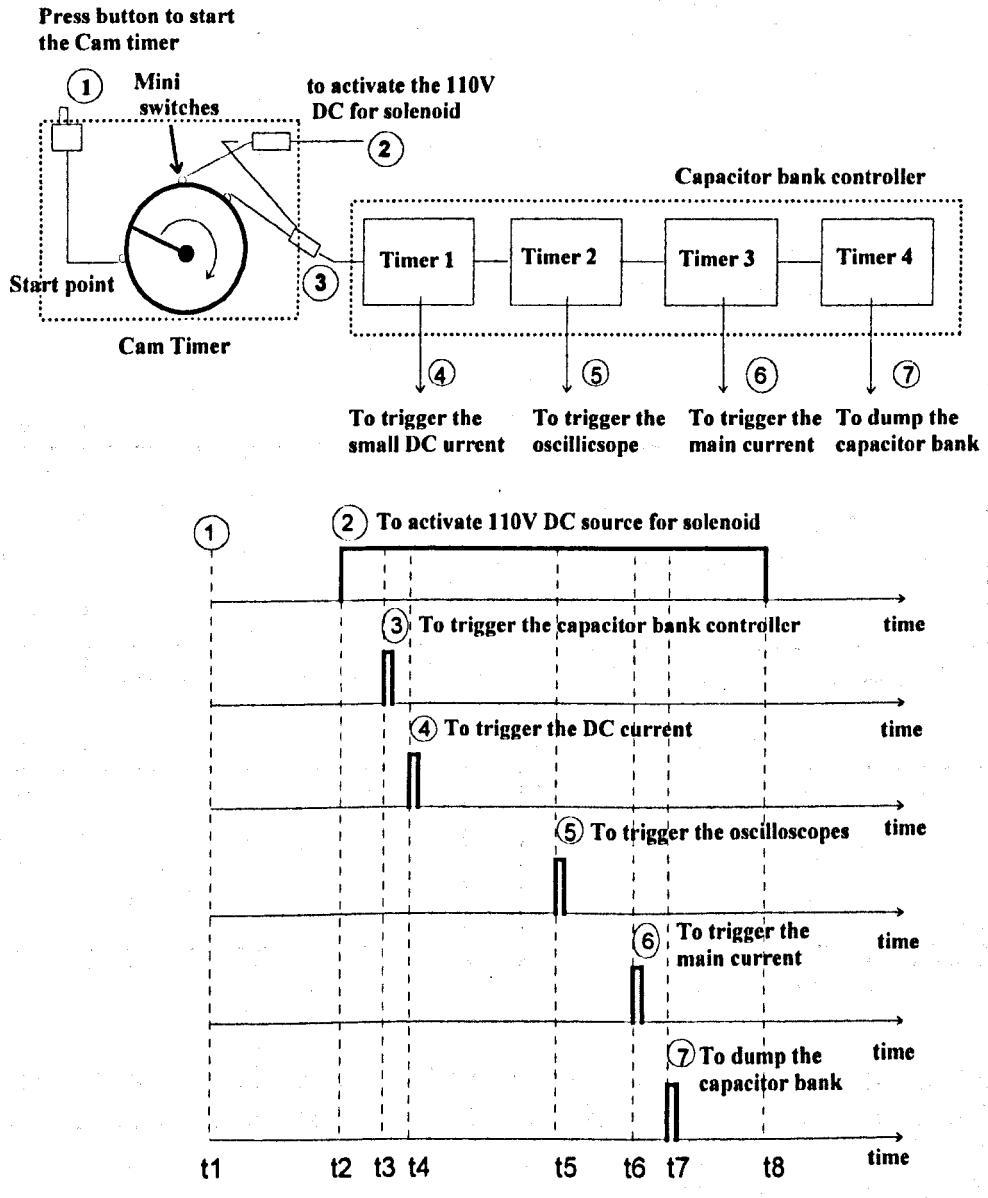

Figure 2.26 The synchronising control system for pressure and arc voltage measurement in the auto-expansion arcing device.

2.3.1.4 Instrumentation

Four Kistler piezoelectric pressure transducers (type 601A) were used to measure the pressure transients inside the chamber. Two pressure transducers (P_3 and P_4 in figure 2.23) are screwed in the PTFE cylinder. In front of the diaphragm of each pressure transducer there is a hole of 1.5mm in diameter and 7mm in length. The other two are mounted flush with the surface of the bottom plate. P_1 is 110mm away from the centre of the plate and measures the pressure in the outer volume. P_2 is 50mm away from the centre and measures the pressure in the inner volume. The pressure transducers and charge amplifiers (type 5007) are calibrated under quasi-steady conditions using a pressure controller. Figure 2.27 shows that the output from the charge amplifiers is linearly proportional to the pressure. To avoid electromagnetic interference in the measuring system, seven isolation transformers and three Tektronix oscilloscopes (two TDS 420 and one 2221) have been used. The whole system is shown in figure 2.28.

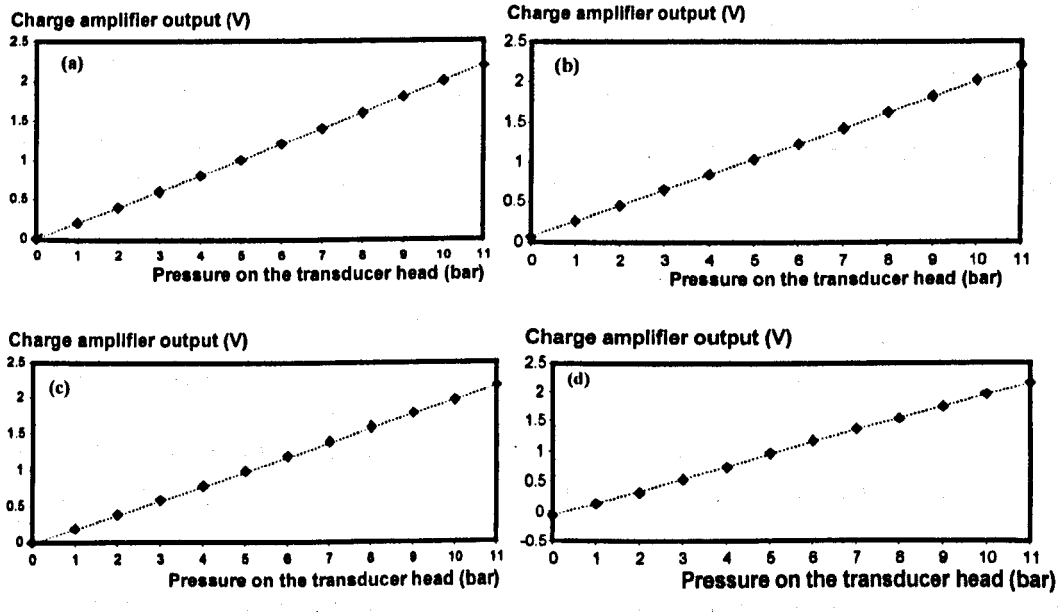

Figure 2.27 Linearity calibration of the pressure transducer and charge amplifier pairs. Pressure source: Steady state pressure controller. (a)—results for P_1 ; (b)— for P_2 ; (c)— for P_3 ; (d)— for P_4

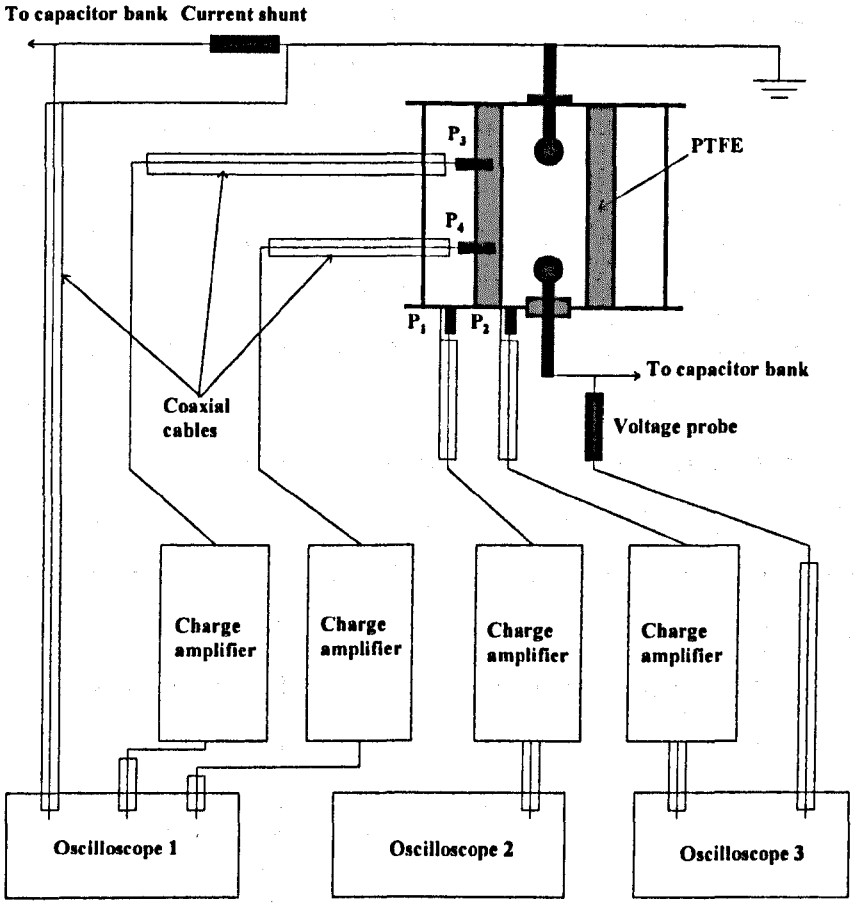

Figure 2.28 Electronic circuit to measure pressure, arc voltage and electric current. All charge amplifiers and oscilloscopes are powered by their own insulation transformers in order to eliminate electric current loops in the measuring circuit.

2.3.2 Experimental results

2.3.2.1 Experimental error

Piezoelectric pressure transducers are suitable for measurement of mechanical vibrations and shocks. They have also been used to measure the pressure transients in high voltage circuit breakers [120,121,122]. Piezoelectric pressure transducers produce electronic charges when exposed to a dynamic pressure. The electronic charges are then converted by a charge amplifier into a voltage output which is linearly proportional to the amount of charge. There is a built-in discharge circuit in each charge amplifier which is required to adjust the dynamic response of the pressure transducer—charge amplifier pair to the pressure variation being measured. The time constant of this discharge process is set to "medium" which is satisfactory for the experimental conditions. The linearity of the pressure transducer is better

than 1%. The total error introduced by the charge amplifier is less than 3.5%. The maximum error is therefore less than 4.5%. P_1 and P_2 are mounted flush with the inner surface of the bottom plate. They directly measure the local pressure. The acoustic delay of P_3 and P_4 caused by the hole in front of them is estimated by assuming a sound speed at room temperature. It is less than 0.1ms. The accuracy of arc voltage and current measurement is better than 5%.

To evaluate the possible influence of high voltage pulses on the pressure transducer output, a test has been carried out where the arc extinguishes before the ignitron for the main current is triggered. The results are shown in figure 2.29. There are two high voltage pulses at 40ms and 115ms respectively. The first voltage pulse at 40ms is generated when the low DC arc extinguishes and the second is the triggering signal for ignitron I_2 (figure 2.25). It is clear that the pressure oscillation of P_2, P_3 and P_4 takes place at a time when the arc voltage becomes unstable, which implies the onset of arc instability. The output of P_2, P_3 and P_4 shows pressure waves of 55 to 75 Hz superimposed by a 500Hz oscillation which tend to decay after the DC arc extinguishes. The uncertainty in pressure measurement due to these oscillations is 0.1bar for P_2, P_3 and P_4 and less than 0.02bar for P_1. The voltage pulses have no visible influence on the pressure transducers.

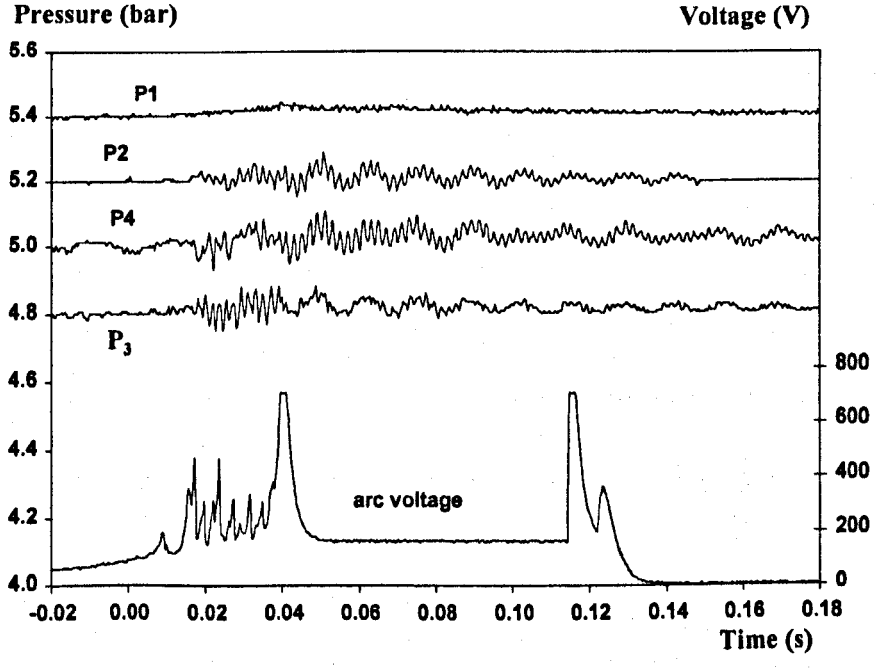

Figure 2.29 Influence of high voltage pulses on the output of pressure transducers. The electrode separation for this case is 30mm and the filling pressure of SF_6 is 5bar absolute. The pressure coordinate for P_1, P_2 and P_3 is shifted respectively by 0.4bar, 0.2bar and -0.2bar. (Case SF6024)

2.3.2.2. Arcing history of a typical case

The actual peak value of the 44Hz main arcing current cannot be predetermined since the DC current consumes considerable amount of the energy stored in the capacitor bank and the remaining energy supplies the main AC current. The peak of the main current can only be adjusted according to experience. Measurements have been taken for electrode separation of 30mm, 40mm and 50mm. It has been difficult to sustain the DC arc in cases with longer electrode separation and lower main arcing current because of the high voltage required on the capacitor bank. There are no measurements for the 50mm electrode separation at 20kA peak because of severe erosion of the sliding rod electrode.

The speed of the solenoid is slowed down by the friction between the sliding rod and a rubber ring which seals the hole accommodating the sliding rod. The speed is also affected by the filling pressure inside the chamber. A higher filling pressure means greater force acting on the head of the sliding rod. Care must be taken to ensure that the main current is switched on only when the sliding rod fully clears the electrode gap. A typical case is shown in figure 2.30.

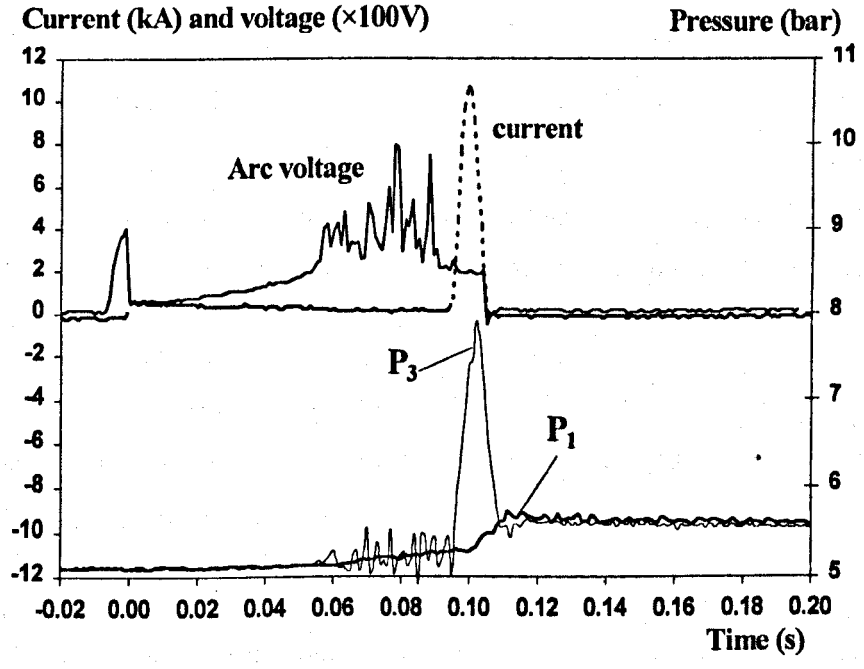

Figure 2.30 History of arc initiation, application of the main AC current, arc voltage and the output from two pressure transducers for a typical case of free burning arcs in a confined space. The electrode separation is 40mm and the filling pressure of SF_6 is 5.1 bar absolute. (Case SF6744)

The time zero corresponds to the moment when the oscilloscopes in figure 2.28 are triggered. The sliding rod detaches the tip of the bottom electrode shortly after the triggering of the DC current and thus initiates the arc. The voltage of the DC arc increases when the rod electrode moves away from the bottom electrode. The arcing current decreases linearly with time. The electrode gap has been fully cleared at 80ms. The main half-cycle AC current is fired at an instant of 92ms.

The two semi-spherical electrodes shown in figure 2.24 are intended to stabilise the main AC arc. The arc voltage measurement in figure 2.30 implies that the DC arc is initially in a stable state when the sliding rod withdraws upwards. There follows a clear onset of random moving of the arc column. The arc voltage quickly settles down at a lower value when the main AC current is fired. The results given in this chapter are those with minimum fluctuations in the arc voltage of the main AC current.

2.3.2.3 30mm electrode separation

With 30mm electrode separation, the DC arc can be easily sustained and the main AC arc is stable. Measurements have been carried out for three peak currents which are 7kA, 10.6kA and 19kA. For the 7kA case, the arcing current, arc voltage and the results from all four pressure transducers are given in figures 2.31 to 2.34. Since the magnitudes of P_2, P_3 and P_4 are very close, we will only present one of them for the other cases. The results for the 10.6 kA case are shown in figure 2.35, and the results for the 19kA case in figures 2.36 and 2.37. The average arc voltage over ten shots for the 30mm electrode separation case is 160V.

2.3.2.4 40mm electrode separation

It is found that the DC arc extinguishes before the application of the main current at 5kA. Results for two currents, 10.7kA and 20.9kA are presented in figures 2.38 and 2.39. The average arc voltage over ten shots is 195V.

2.3.2.5 50mm electrode separation

Measurement for the 50mm electrode separation case has been made only at current level of 12kA. The DC arc cannot be sustained at lower peak current and the measurement at higher peak current is not possible due to severe erosion of the rod electrode. The results for the 12kA case are shown in figure 2.40. The arc voltage in this particular case behaves differently from cases with shorter electrode separation. The arc voltage decreases continuously over the main arcing period.

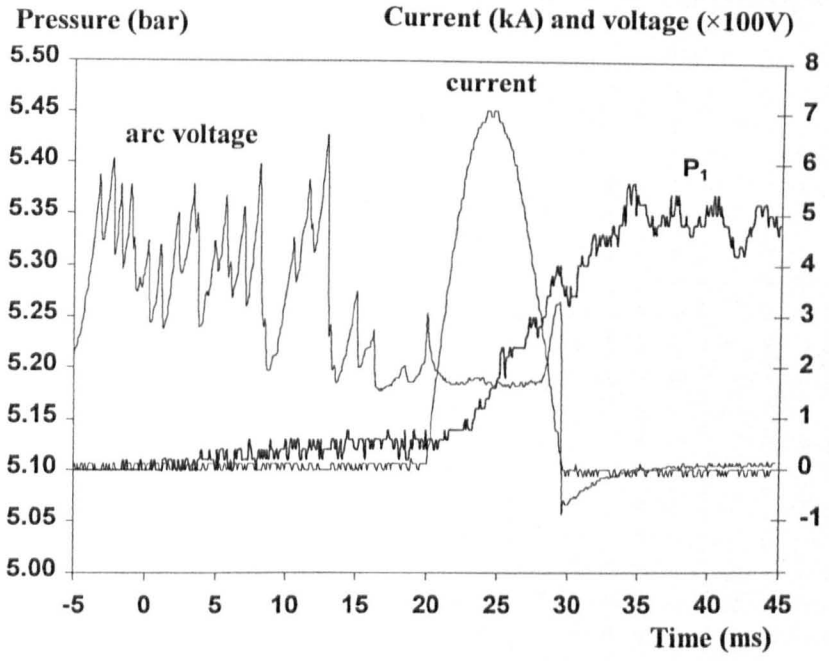

Figure 2.31 Arcing current, arc voltage and pressure transient in the outer volume (P_1) for a 30mm electrode separation. Peak current is 7kA and the filling pressure of SF_6 is 5.1bar absolute. (Case SF6214)

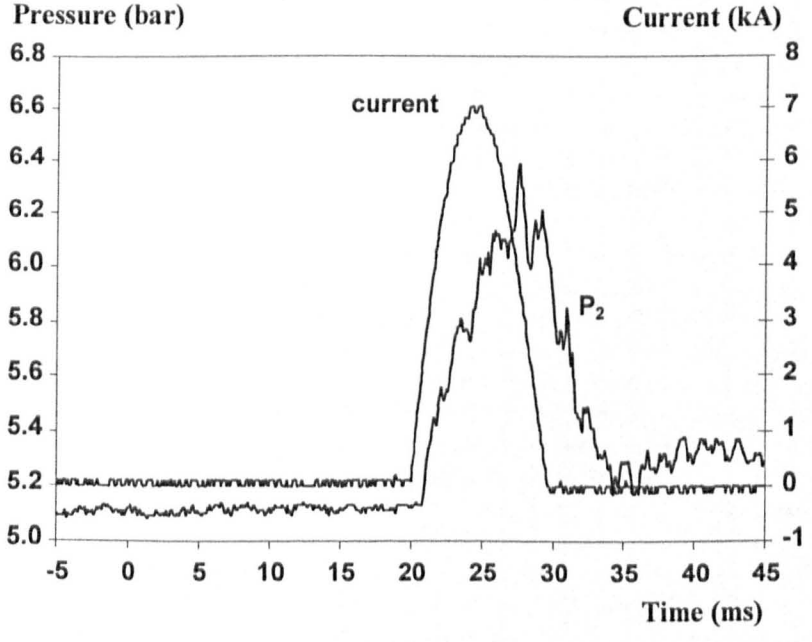

Figure 2.32 Pressure transient inside the PTFE cylinder (P_2) for a 30mm electrode separation. Peak current is 7kA and the filling pressure of SF_6 is 5.1bar absolute.

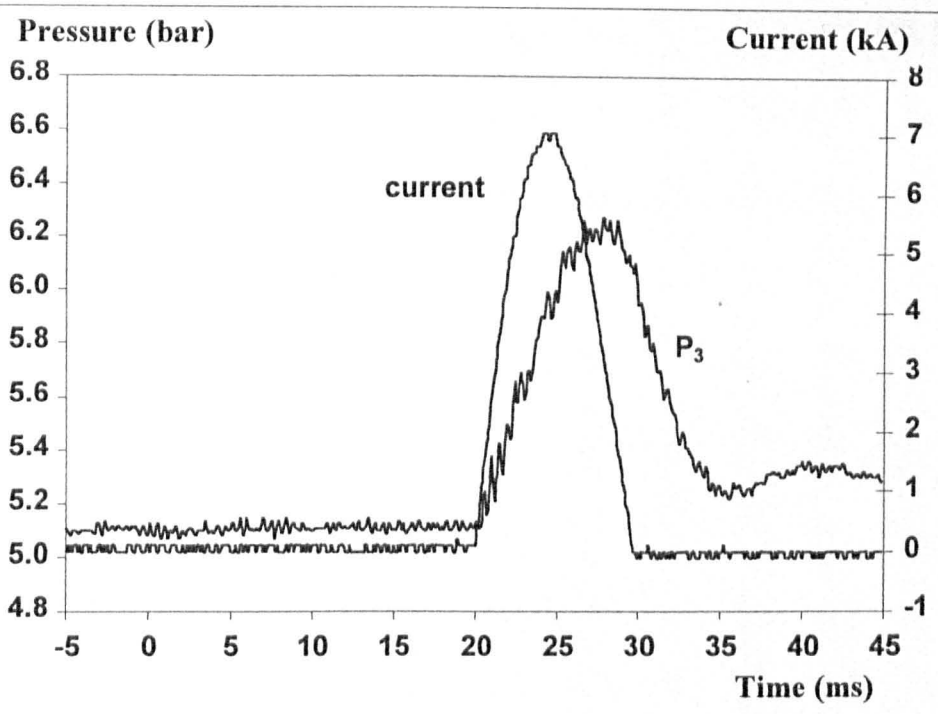

Figure 2.33 Pressure transient inside the PTFE cylinder (P_3) for a 30mm electrode separation. Peak current is 7kA and the filling pressure of SF_6 is 5.1bar absolute.

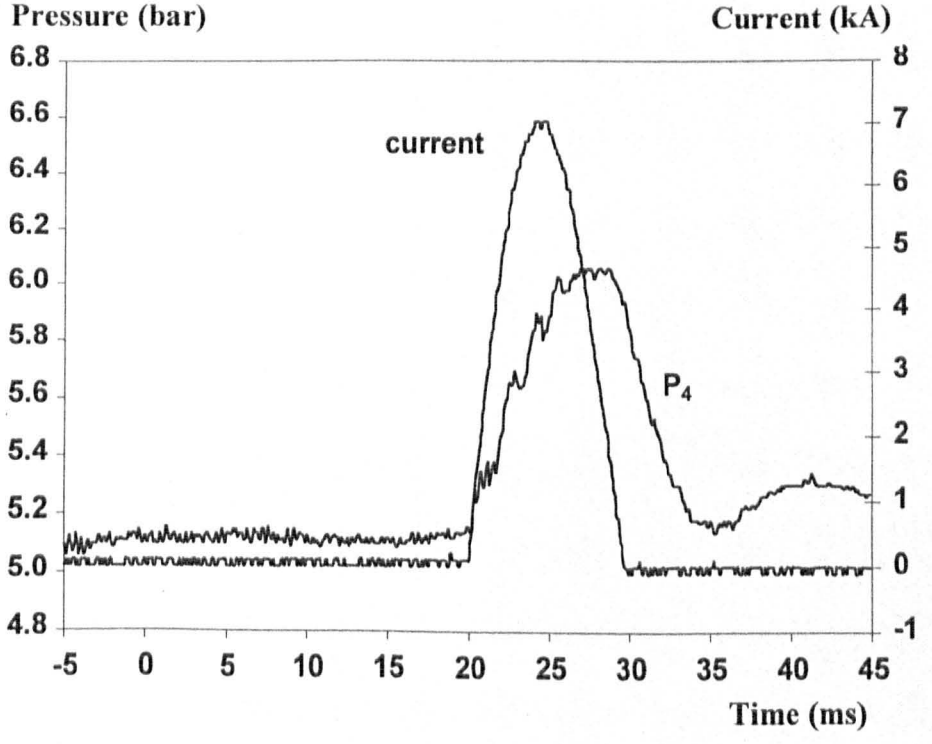

Figure 2.34 Pressure transient inside the PTFE cylinder (P_4) for a 30mm electrode separation. Peak current is 7kA and the filling pressure of SF_6 is 5.1bar absolute.

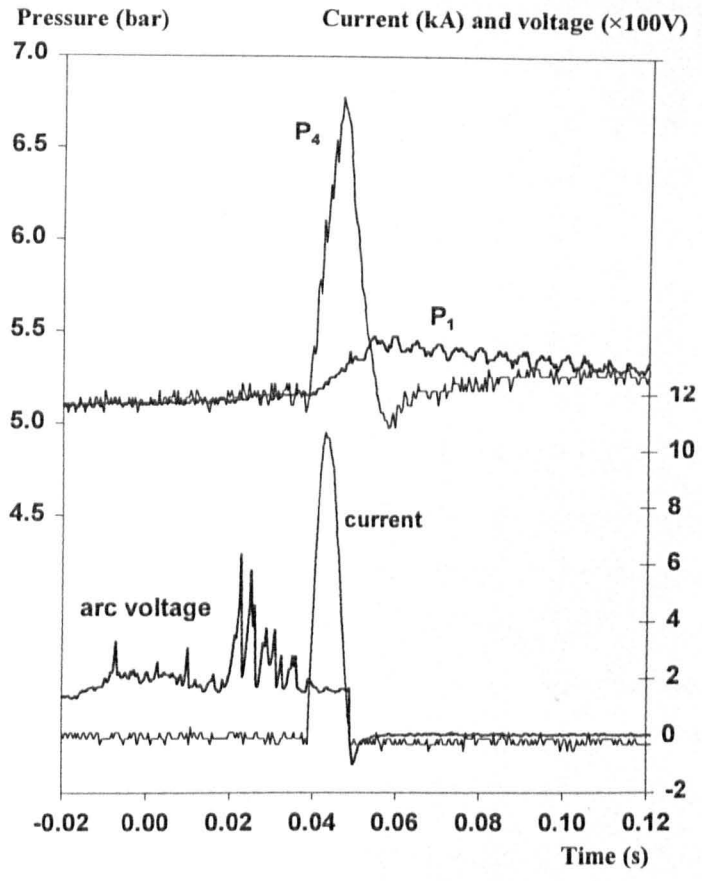

Figure 2.35 Arcing current, arc voltage and pressure transients in the arcing chamber for a 30mm electrode separation. Peak current is 10.6kA and the filling pressure of SF_6 is 5.1bar absolute. (Case SF6384)

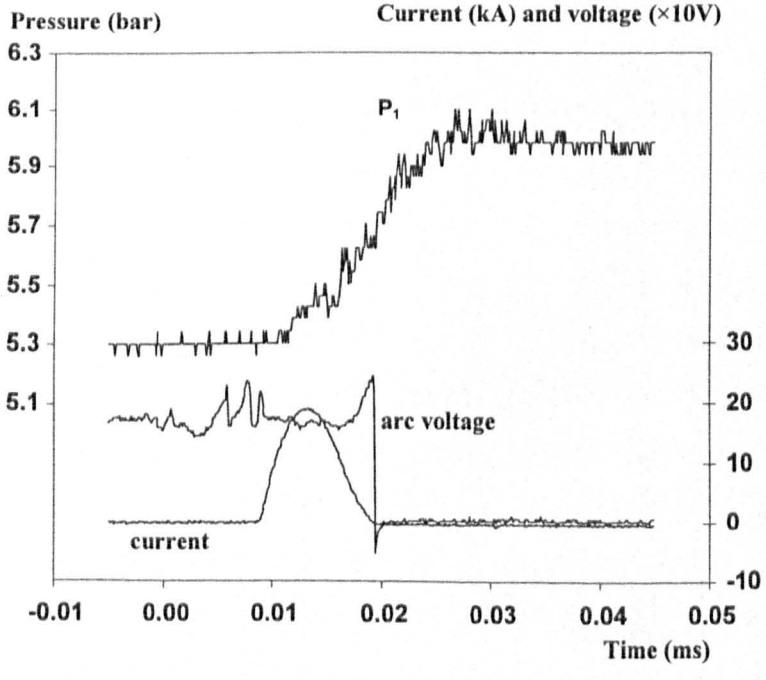

Figure 2.36 Pressure transient in the outer volume (P_1) for a 30mm electrode separation. Peak current is 19kA and the filling pressure of SF_6 is 5.3bar absolute. (Case SF6444)

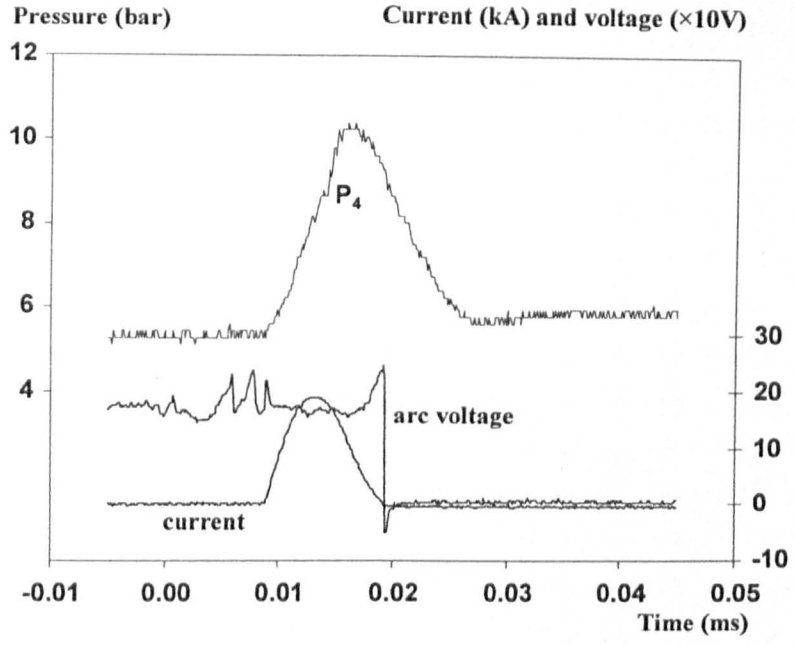

Figure 2.37 Arcing current, arc voltage and pressure transients inside the PTFE cylinder for a 30mm electrode separation. Peak current is 19kA and the filling pressure of SF_6 is 5.3bar absolute.

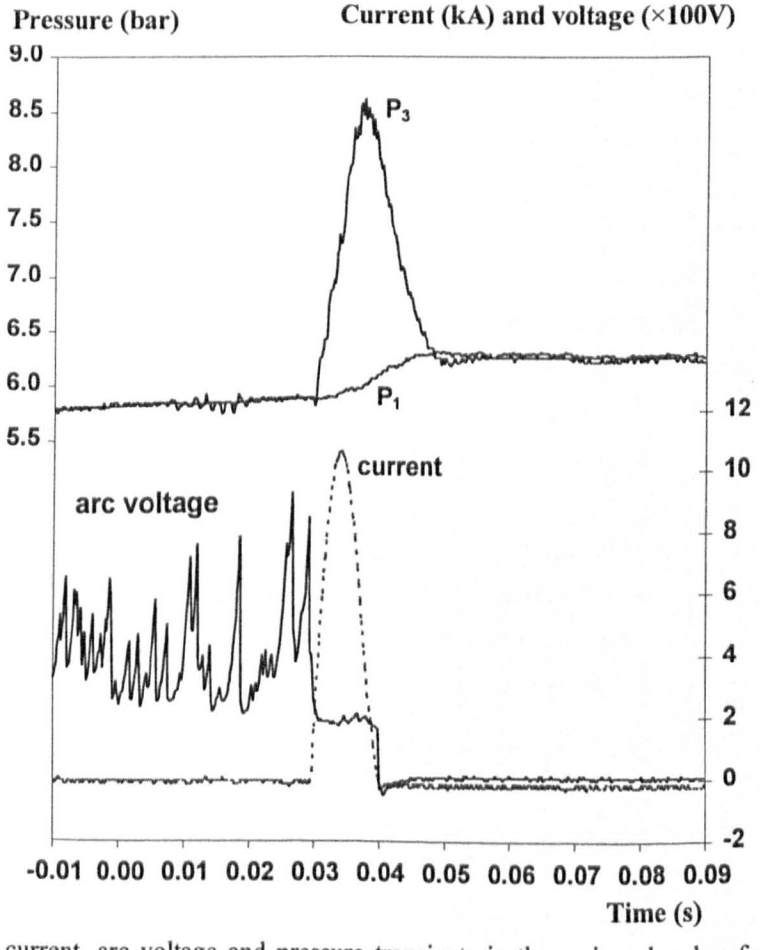

Figure 2.38 Arcing current, arc voltage and pressure transients in the arcing chamber for a 40mm electrode separation. Peak current is 10.7kA and the filling pressure of SF_6 is 5.8bar absolute. (Case SF6964)

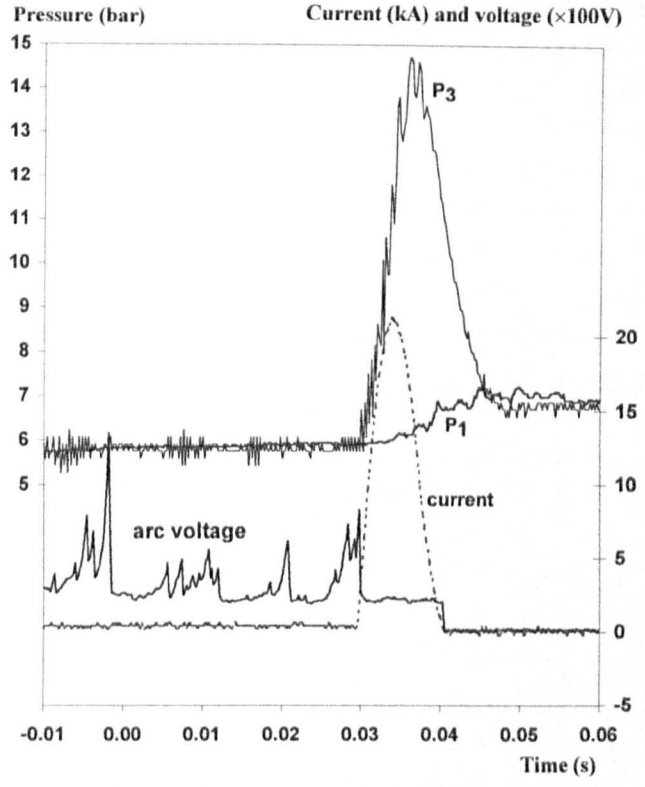

Figure 2.39 Arcing current, arc voltage and pressure transients in the arcing chamber for a 40mm electrode separation. Peak current is 20.9kA and the filling pressure of SF_6 is 5.75bar absolute. (Case SF6914)

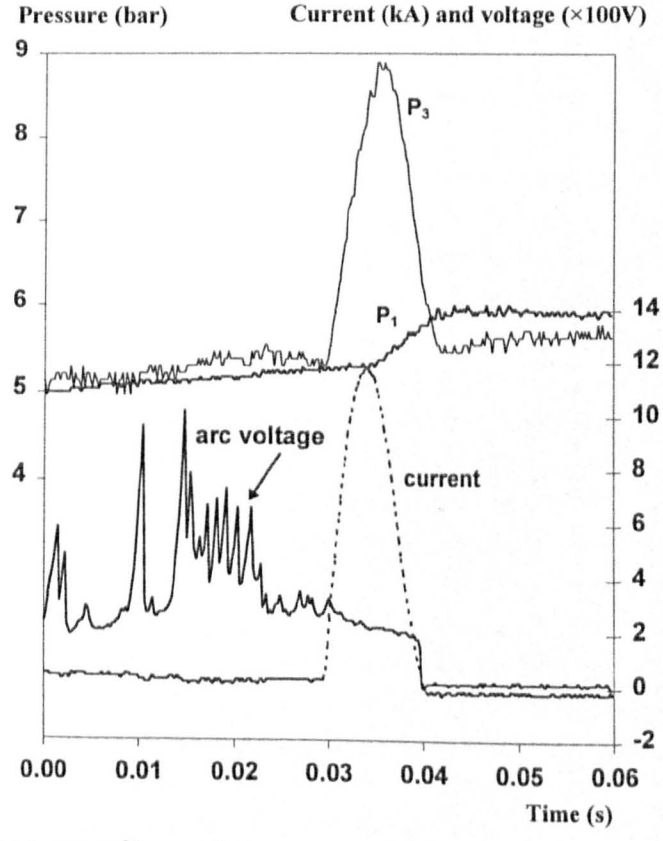

Figure 2.40 Arcing current, arc voltage and pressure transients in the arcing chamber for a 50mm electrode separation. Peak current is 12kA and the filling pressure of SF_6 is 5.0bar absolute. (Case SF6594)

2.3.2.6 Pressure rise in the arcing chamber

The arcs under investigation burns in a cylindrical volume which exchanges mass and energy with the outer volume. The transient pressure inside the PTFE cylinder (P_2, P_3 and P_4) in all the cases follows the current waveform with a phase delay of 2.5ms. The pressure variation is the result of two effects; the heating of the arc and the variation of the size of the arc column which is more or less in step with the current. The pressure rises to its peak after the current passes its peak but well before the current zero. The relation between the peak current and the peak pressure of P_4 is indicted in figure 2.41.

The pressure in the outer volume changes more smoothly than in the PTFE cylinder and it continues to rise after current zero because of the pressure difference in the two volumes. The pressure rise in the outer volume is related to the electrical energy input as shown in figure 2.42.

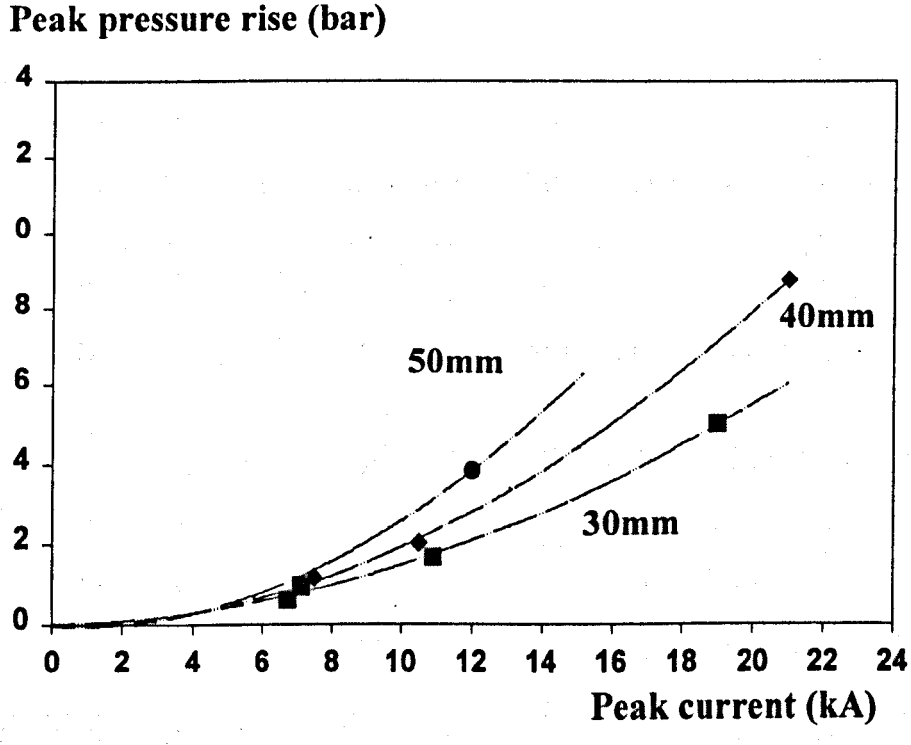

Figure 2.41 Maximum pressure rise (maximum instantaneous pressure-filling pressure) at location P4 as a function of peak current. Squares: 30mm electrode separation; diamonds: 40mm; circles: 50mm.

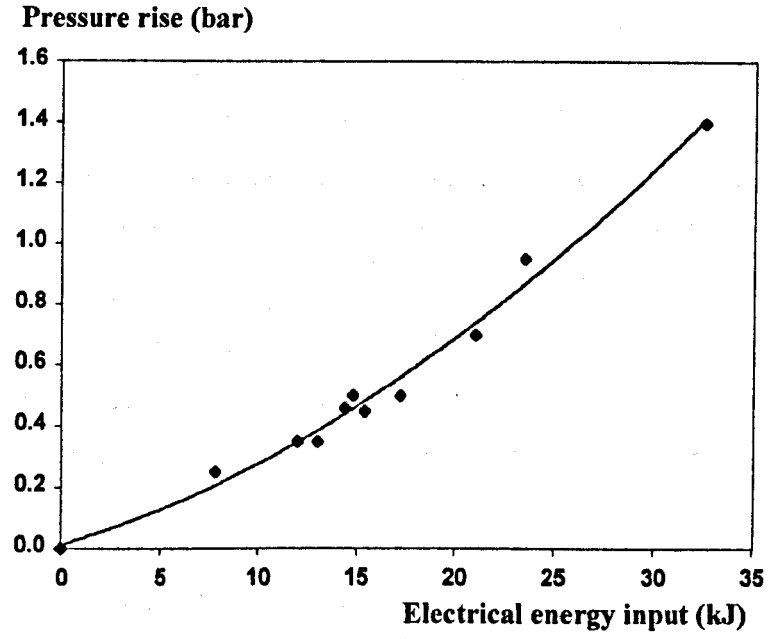

Figure 2.42 Pressure rise in the outer volume of the arcing chamber as a function of the electrical energy input regardless of the electrode separation.

2.3.2.7 Effects of ablation

Ablation of the PTFE cylinder has been measured by a digital scale with an accuracy of 0.1g. The weight of the PTFE was measured after experiments with a fixed electrode separation at all current levels. The total energy input is calculated from the arc voltage and current. The energy required to ablate the PTFE material is 1.19×10^7 J/Kg [102] (corresponding to a PTFE temperature of 3,400K). The results are given in Table 2.3.

Ablation of the PTFE cylinder may contribute to the pressure variation in the arcing chamber. For all three electrode separations, the maximum ablated PTFE vapour in a single shot is 1g (40mm electrode separation at 20.9kA), which is only 3.7% of the weight of SF_6 inside the PTFE cylinder or 0.3% of the gas in the arcing chamber. We will thus neglect the effect of wall ablation in the calculation of pressure variation in the arcing chamber.

Table 2.3

electrode separation	3cm	4cm	5cm
energy input (J)	367,881	484,534	192,787
PTFE ablated (g)	10.2	14.9	3.5
percentage of energy input used for ablation	33%	34%	20%

2.4 Comparison of Experimental and Computational Results

Experimental results on free burning arcs in a confined space are rare. Huang et al [122,123] reported some pressure measurement in a steel pot where a free burning SF_6 arc was maintained. However arc voltage was given for only one case. We will compare the predicted and measured pressure and arc voltage for the steel pot and for the auto-expansion arcing device separately. The arcing medium is SF_6 .

The parameters used in the simplified model are: $c_e = 0.35$, $c_t = 0.4$, $c_a = 0.25$ and $c_l = 0.012$. The average current density at the arc root is $10^8 A/m^2$ and the temperature at the upstream boundary is 15,000K.

2.4.1. Free burning arcs in a pot

The pot was made of steel with a volume of $3.9\times10^{-3}m^3$. The SF_6 gas was initially at room temperature. The arc burns between two semi-spherically-headed electrodes separated at 41mm. The pressure was measured by a Kistler piezoelectric transducer (Model 601A) in conjunction with a charge amplifier (Model 5001). The pressure transducer is connected to the pot through a thin tube which provides both electrical insulation and thermal protection to the pressure transducer. The pressure results presented in [123,124] have been corrected for the acoustic delay caused by the thin tube.

Computer simulation has been done for three cases with following peak current and absolute filling pressure: 20kA at 1.5bar, 16kA at 1.73bar, and 21kA at 3.1bar. The arc voltage measurement is available for the 20kA case. The results in figures 2.43 to 2.45 show that the predicted pressure variation (the difference between the instantaneous pressure and the filling pressure) agrees with the measurement within an uncertainty of 20%. The difference between the predicted and measured arc voltage for the 21kA case is 40V on average, or 20% of the measured value. Considering the sheath potential drop of 17.5V [125] for free burning SF_6 arcs, the prediction agrees well with experimental results.

When the current of free burning arcs is approaching zero, the measured arc voltage increases due to growing arc resistance in the experiments. That our model produces the opposite trend for low current (below 1.5kA in figure 2.43) implies that the top hat temperature profile is only valid for high current free burning arcs.

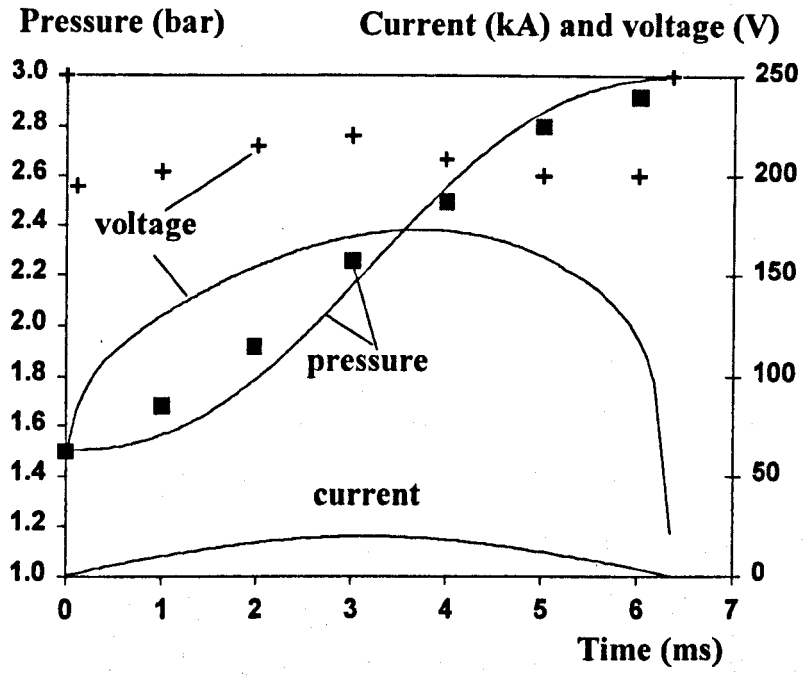

Figure 2.43 Arc voltage of a free burning arc and pressure variation in a metallic pot filled with SF_6 gas initially at 300K and 1.5bar. The peak of the 78Hz sinusoidal current is 20kA. + and ■: experiments; Solid lines: prediction

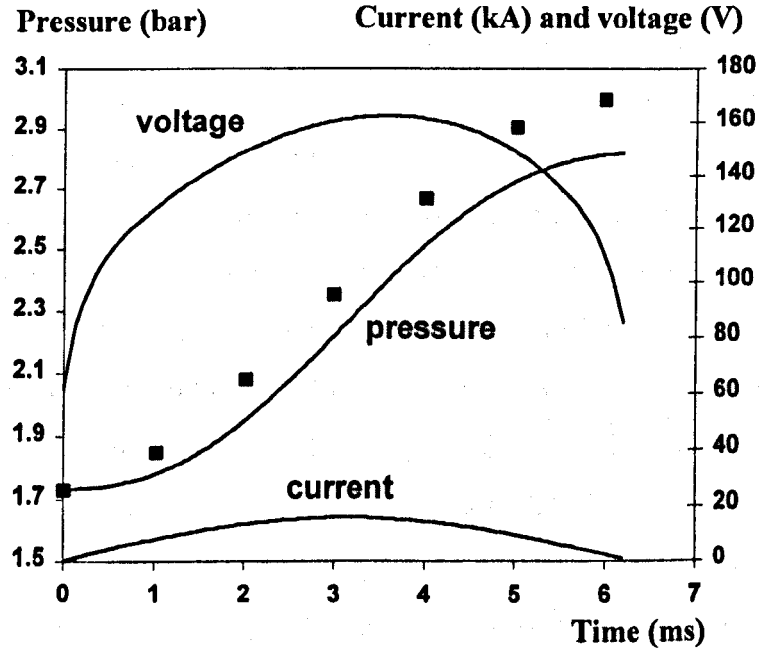

Figure 2.44 Arc voltage of a free burning arc and pressure variation in a metallic pot filled with SF_6 gas initially at 300K and 1.73bar. The peak of the 78Hz sinusoidal current is 16kA. No arc voltage measurement is available. Squares: experiments; Solid lines: prediction

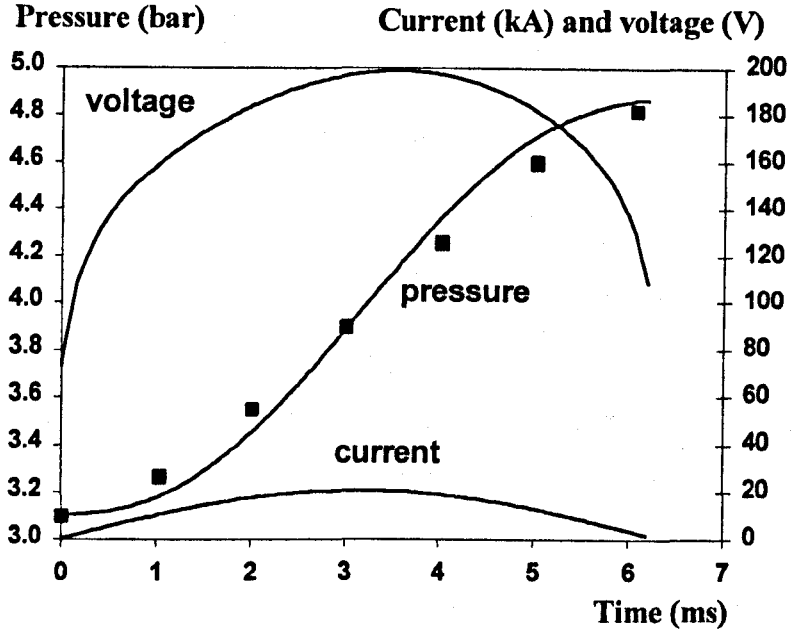

Figure 2.45 Arc voltage of a free burning arc and pressure variation in a metallic pot filled with SF_6 gas initially at 300K and 3.1bar. The peak of the 78Hz sinusoidal current is 21kA. No arc voltage measurement is available. Squares: experiments; Solid lines: prediction

2.4.2 Free burning arcs in the auto-expansion arcing device

The effective volume for the inner part of the arcing chamber is 9.06×10^{-4} m^3 at 30 mm electrode separation, 9.09×10^{-4} m^3 at 40 mm and 9.12×10^{-4} mm^3 at 50 mm. The volume of the outer part of the chamber is 8.89×10^{-3} m^3. The area for gas exchange between the two volumes is $5.77\times10^{-4}m^2$. The solution for a 500A steady state arc is used as the initial conditions for the transient simulation. The cases simulated are: 7kA with filling pressure of 5.1bar for 30mm electrode separation (figure2 2.31 to 2.34), 10.7kA with filling pressure of 5.8bar for 40mm (figure 2.38) and 12kA with filling pressure of 5.0bar for 50mm (figure 2.40).

Since the contribution of ablation to the pressure variation in the arcing chamber is small (The mass of ablated PTFE is 3.7% of the weight of SF_6 in the PTFE cylinder), we neglect ablation in our model. The results in figures 2.46 and 2.47 show that the simplified model can reasonably predict the pressure variation in both volumes for the period before the pressure peak. There is large discrepancy for case 3. The predicted pressure variation in Volume V_1 is higher than the measurement by 30% (figure 2.46). The predicted arc voltages agree with measurements around the peak current within 10% if we take account of the cathode and anode falls of 17.5V for SF_6 free burning arcs [125]. Similar to the cases in the steel pot, large discrepancies in arc voltage occur at the low current ends. There are two possible reasons:

firstly it is due to the top-hat assumption for the radial temperature profile which is only valid for high current arcs. Secondly, the arc column may become unstable and have an irregular shape at low current. The arc voltage is thus unpredictable.

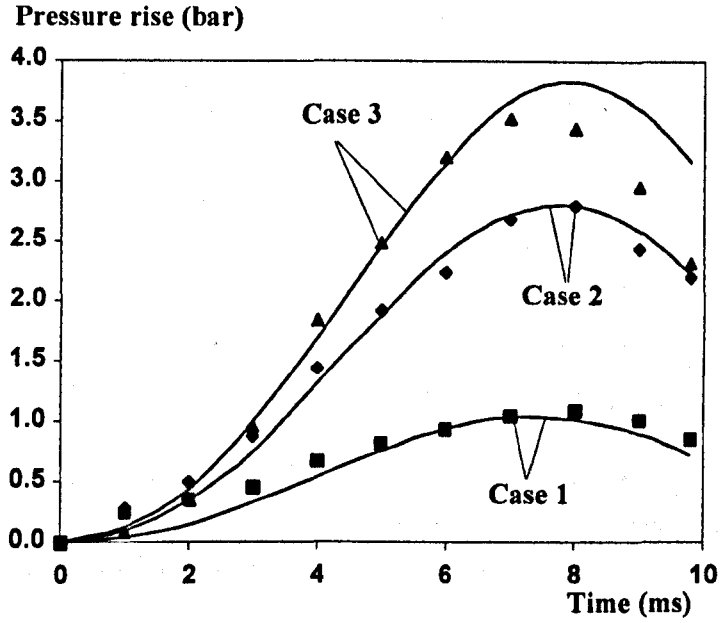

Figure 2.46 Pressure variation (difference between instantaneous pressure and filling pressure) inside the PTFE cylinder for three cases. Case 1: 7kA with filling pressure of 5.1bar for 30mm electrode separation, Case 2: 10.7kA with filling pressure of 5.8bar for 40mm electrode separation and Case 3: 12kA with filling pressure of 5.0bar for 50mm electrode separation. Lines: prediction by simplified model and symbols are experimental results.

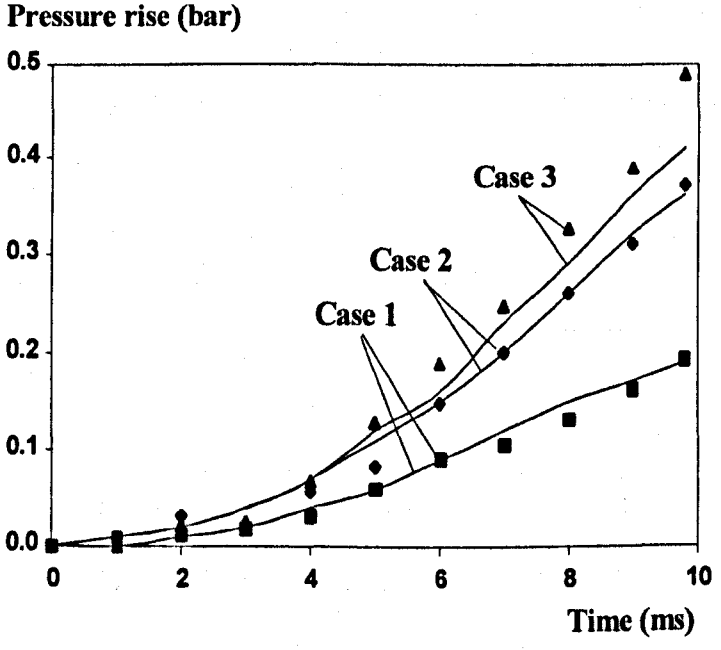

Figure 2.47 Pressure rise (difference between instantaneous pressure and filling pressure) in the outer volume for three cases. See figure 2.46 for experimental conditions.

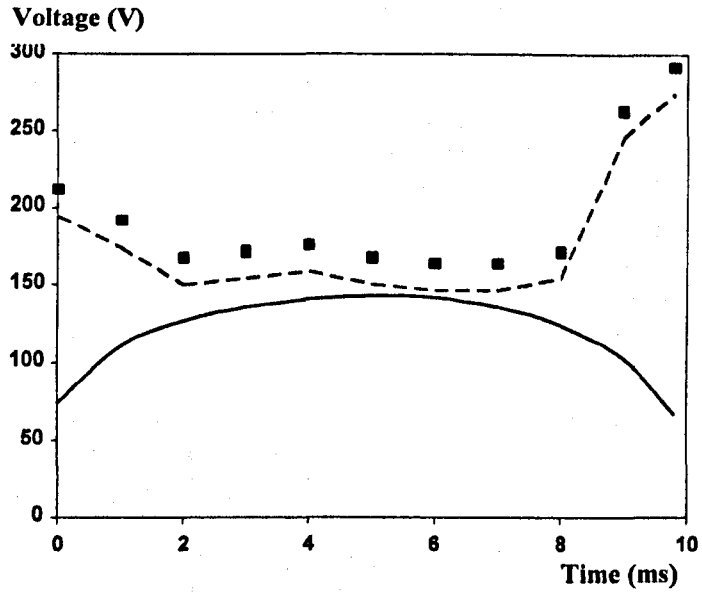

Figure 2.48 Arc voltage for Case 1: 7kA with filling pressure of 5.1bar for 30mm electrode separation. Solid line: prediction by simplified model, Symbols: measurements, Dashed line: measurements deducted by 17.5V of electrode sheath voltage drop[125].

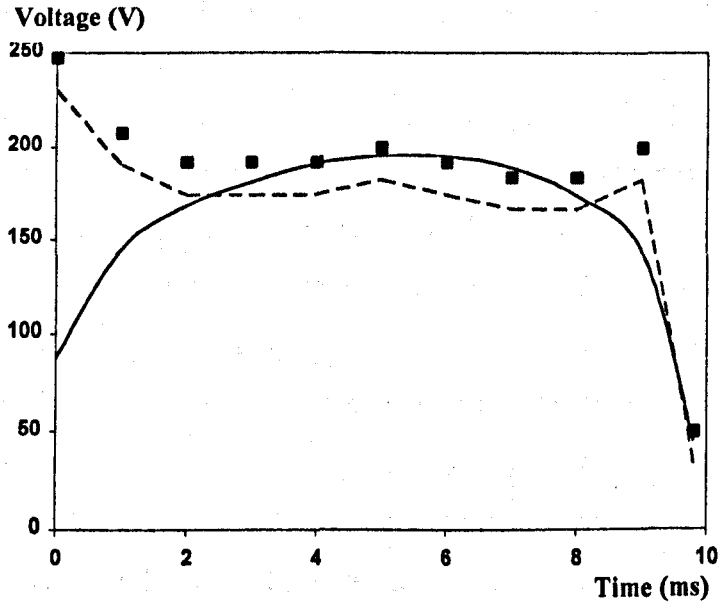

Figure 2.49 Arc voltage for Case 2: 10.7kA with filling pressure of 5.8bar for 40mm electrode separation. Solid line: prediction by simplified model, Symbols: measurements, Dashed line: measurements deducted by 17.5V of electrode sheath voltage drop[125].

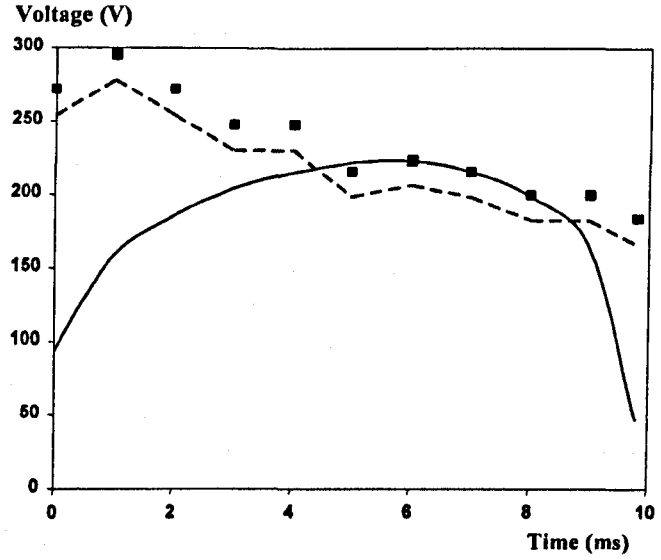

Figure 2.50 Arc voltage for Case 3: 12kA with filling pressure of 5.0bar for 50mm electrode separation. Solid line: prediction by simplified model, Symbols: measurements, Dashed line: measurements deducted by 17.5V of electrode sheath voltage drop[125].

2.5 Conclusions

A simplified model for free burning arcs in a confined space has been developed in this chapter. This model assumes a top-hat type radial temperature profile for the arc and uses a known radial distribution of the axial velocity in the arc column. The confining space is divided into two regions, namely the arc column and the surrounding cold region. The thermal properties in the surrounding region are assumed to be uniform. The governing equations are integrated radially from the axis to the arc radius and the problem is thus reduced to one dimensional. The average current density and arc temperature at the arc root are required as the upstream boundary conditions. Arc voltage and pressure measurements have been carried out in an auto-expansion arcing device at different electrode separation and filling pressures. The predicted arc voltage and pressure variation in the confining space agree reasonably well with the measurements under the experimental conditions. Large discrepancies in arc voltage occur at the low current ends (below 1.5kA), which are mainly attributed to the assumption of the top-hat radial temperature profile for the arc, which is not valid for low currents. The simplified model should therefore be used in applications where the arcing current is above 1.5kA for most of the arcing time. The advantage of such a simplified model is the low computing cost. It can also easily be used for preliminary optimisation studies of the gas discharge parameters, such as the dimensions of the various parts of the arcing chamber.

CHAPTER THREE DIFFERENTIAL MODEL FOR ARCS IN AXISYMMETRIC FLOW

3.1 Introduction

The work on a differential model for electric arcs in axisymmetric flow, which was initiated in January 1997, has been encouraged by the success of Kwan [46] in application of a commercial CFD package, PHOENICS [111], to computer simulation of arcs in puffer circuit breakers. The results obtained by implementing a two dimensional differential model into PHOENICS have been verified for both cold flow and arc-flow interaction. In addition to the model of Kwan [46], ablation of wall material, the electromagnetic force generated by the arcing current and its magnetic field, and modelling of a moving contact have been included in the present model. With a commercial CFD package users have little access to the source program. When the acing gas is highly compressible and is subjected to strong heat sources, specification of boundary conditions for the governing equations and the control of numerical stability are no less challenging than the development of the differential arc model itself.

Simulation of a moving contact alone is a very complicated issue, which will be addressed later.

Following the development of the differential model, we will in this Chapter investigate three individual cases which can be characterised by one of the following fundamental processes which are of vital importance in circuit breaker arcs: the effect of self-generated electromagnetic force on high current arcs, arc-shock interaction, and the modelling of turbulence for arcs in supersonic nozzle. Computer simulation of the whole arcing process in an auto-expansion circuit breaker will be separately presented in Chapter Four in view of the substantial volume of work which needs to be reported.

3.2 Basic Equations in Cylindrical Polar Coordinate System

It is shown in Section 1.2.3 that, neglecting the density fluctuation the turbulent effects can be represented by the Reynolds stress $(-\rho\overline{u_i'u_j'})$ in the momentum equation and the term $-\rho\overline{u_i'e'}$ in the energy equation, which, by the definition of turbulent eddy viscosity, are treated in analogue with the laminar viscous terms. In a cylindrical polar coordinate system, the turbulent conservation equations can be written in the following conservative form

$$\frac{\partial \rho\phi}{\partial t}+\frac{1}{r}\frac{\partial}{\partial r}[r\rho v\phi - r\Gamma\frac{\partial \phi}{\partial r}]+\frac{\partial}{\partial z}[\rho w\phi - \Gamma\frac{\partial \phi}{\partial z}]=S_\phi \qquad (3.1)$$

where ϕ, Γ and S_ϕ are respectively the dependent variable, the diffusion coefficient and the source term, which are listed in Table 3.1 for the mass, momentum and energy equations. Gas flow in circuit breakers are usually axially dominant. Neglecting the gravitational force which acts on the arcing gas, the source terms in Table 3.1 can be represented by

$$S_w=-\frac{\partial P}{\partial z}+(\vec{J}\times\vec{B})_z \qquad (3.2)$$

$$S_v=-\frac{\partial P}{\partial r}+\frac{1}{r}\frac{\partial}{\partial r}[r(\mu+\mu_t)\frac{\partial v}{\partial r}]+\frac{\partial}{\partial z}[(\mu+\mu_t)\frac{\partial w}{\partial r}]-\frac{2\mu v}{r^2}+(\vec{J}\times\vec{B})_r \qquad (3.3)$$

$$S_h=\frac{dP}{dt}+\sigma E^2-q+\Phi \qquad (3.4)$$

where Φ is the energy dissipation due to laminar and turbulent viscous effect

$$\Phi=\frac{1}{r}\frac{\partial}{\partial r}[r(\mu+\mu_t)w\frac{\partial w}{\partial r}] \qquad (3.5)$$

Calculation of the electric and magnetic fields in the conducting region, which is based on Maxwell's equations in a simplified form, is presented in Section 3.6.

Table 3.1

Equation	ϕ	Γ	S_ϕ
continuity	1	0	0
z-momentum	w	$\mu + \mu_t$	S_w
r-momentum	v	$\mu + \mu_t$	S_v
enthalpy	h	$(k + k_t)/c_p$	S_h

3.3 Boundary Conditions for the Flow Equations

For arcs in axisymmetric flow field, the derivative of all dependent variables with respect to the radial coordinate, r, is set at zero on the axis where r = 0. Other boundary conditions will be described below.

3.3.1 Inlet

When there is gas flowing into the arcing chamber, the mass flow rate per unit area, which is a surface source, is specified. If the incoming gas originates from a stagnant region at pressure P_0 and temperature T_0 , the mass flow rate can be calculated by the isentropic equation (2.20) with A_m = 1.0 and P_{v1} being taken as P_0, P_{v2} as the local pressure at the inlet and T_{v1} as T_0 . The total energy flux at the inlet, which include the enthalpy flux and the kinetic energy flux, is equal to the mass flow rate multiplied by the stagnation enthalpy which is c_pT_0 . Since we are solving the energy equation in terms of enthalpy, its flux at the inlet can be calculated by deducting the kinetic energy flux from the total energy flux. The kinetic energy flux is the mass flow rate multiplied by ($w^2/2$) where w is the local velocity at the inlet

$$w = \sqrt{\frac{2\gamma}{\gamma - 1} R_g T_0 [1 - (\frac{P}{P_0})^{\frac{\gamma - 1}{\gamma}}]} \qquad (3.6)$$

where P is the local pressure at the inlet. The momentum flux at the inlet is equal to the mass flow rate multiplied by the velocity w. When the inlet plane is perpendicular to the axis of symmetry, the momentum flux is mainly a source for the axial momentum equation, the source for the radial momentum is usually negligible. During the computation, the inlet

pressure P is updated and the mass, momentum and energy influxes are subsequently adjusted. When a converged solution is approached, the local pressure should satisfy both the isentropic equations (2.20) and (3.6) and the governing equations in the form of equation (3.1). The momentum and energy diffusion at the inlet are neglected.

3.3.2 Exit

In circuit breaker applications, the exit of the arcing chamber is usually connected to a low pressure vessel and gas leaves the arcing chamber at a high Peclet number. Under such conditions, the momentum and energy diffusion can be neglected in comparison with their corresponding convective terms. Thus, downstream boundary conditions other than the pressure at the exit will not be necessary.

3.3.3 Solid wall without ablation

The velocity component perpendicular to the wall is zero. Along the wall surface, there is a laminar boundary layer between the wall and the turbulent flow. Because of the large number of cells which would be required to resolve the laminar boundary layer, it is not possible to model the complete structure of a turbulent boundary layer which is between the main stream and the laminar sub-layer. The centre of the cells adjacent to the wall is usually in the fully developed turbulent flow. Wall functions are usually employed to provide boundary conditions for the momentum equation along the wall surface. The universal velocity distribution near a wall is [126]

$$\frac{w}{w_*} = \frac{1}{K}\ln[D(\frac{w_* y}{\nu})] \tag{3.7}$$

where K = 0.435 and D = 9.0 are two constants. ν is the laminar kinematic viscosity and y is the distance from the cell centre to the wall. w_* is the shear velocity defined by

$$\tau_w = \rho w_*^2 \tag{3.8}$$

where τ_w is the shear stress imposed on the cell by the wall and ρ is the density. By defining a skin friction coefficient c_f as

$$c_f = (\frac{w_*}{w_c})^2 = \frac{\tau_w}{\rho w_c^2} \tag{3.9}$$

where w_c is the velocity at the cell centre, equation (3.7) can be re-arranged as

$$c_f = [\frac{K}{\ln(DR_e\sqrt{c_f})}]^2 \quad (3.10)$$

where c_f can only be solved iteratively and R_e is the Reynolds number at the cell centre

$$R_e = \frac{w_c y_c}{\nu} \quad (3.11)$$

The effect of the wall friction is represented by a source term in the momentum equation directed along the wall surface. During the solution procedure, the Reynolds number can be calculated by equation (3.11) based on the intermediate value of w_c , and the skin friction coefficient can then be determined by equation (3.10). The source for the momentum equation, which is the shear stress of the wall, is calculated by equation (3.9).

Energy loss by heat conduction relies heavily on the wall material. For modern high voltage auto-expansion circuit breakers, the nozzle is made of PTFE, which has a small thermal conductivity. Compared with the huge amount of electrical energy input in a period of typically 20ms, the energy loss to metallic contacts and PTFE walls is small. For a 245kV auto-expansion circuit breaker, assuming a peak current of 25kA at 50Hz, the average arc voltage is 800V. The power input is 1.25×10^7 W. The surface area of the arcing chamber is less than $0.15m^2$. To loss 10% of the power input by thermal conduction at the wall, it will require a temperature gradient of 1.6×10^8 K/m in PTFE, or 16,000K difference over a 0.1mm thickness. Practically the temperature of PTFE surface is lower than 4,000K, and this temperature gradient can never be maintained over the time of interest. Adiabatic condition is therefore assumed for the enthalpy equation at all solid walls without ablation.

3.3.4 Solid wall with ablation

When ablation occurs at the nozzle surface, evaporated wall material will be injected into the flow. As pointed out in Chapter one, radiation is the main source of energy for ablation in circuit breakers [101,102]. The physical process of ablation of PTFE is yet poorly understood. As a first approximation, we will treat the ablation of PTFE as a quasi-steady process, which means that the amount of evaporated wall material is proportional to the amount of radiation available for ablation. The mass flow rate per unit area as a surface source is independent of the local gas state. However, the velocity at which the vapour is injected depends on its density which is in turn determined by the vapour temperature and the local

pressure. The temperature of the vapour is around 3400K [102] and the energy which is required to break the chain of PTFE molecules (depolymerisation) and to raise the PTFE from room temperature to 3400K is 1.19×10^7 J/kg. We thus specify surface source for the mass, enthalpy and the momentum normal to the wall surface. There is no source for the momentum along the wall surface. Since we are dealing with single phase flow of SF_6, the properties of the vapour have to be approximated by those of SF_6. The uncertainty in the results which is introduced by this approximation is small [84].

3.3.5 Electrode (Contact) surface

The boundary conditions at the surface of the fixed electrode are the same as those for solid walls without ablation. Wall friction is neglected at the surface of the moving electrode. At the circumferential surface of the moving electrode, radial velocity is zero and adiabatic condition for the energy equation is assumed. The boundary conditions at the moving interface between the moving electrode and the arcing gas will be discussed in Section 3.5

3.4 Subsidiary Models

3.4.1 Radiation model

The approximate model of radiation transfer, which was proposed by Zhang et al [49], has achieved considerable success in predicting arc behaviour in circuit breakers. This model is one dimensional and assumes a monotonic radial profile of temperature. However, in the solution process of the governing equations, the monotonic feature of the radial temperature profile may be temporarily violated. To ensure a converging solution of the arc equations, appropriate numerical procedures for the radiation model must be developed which can suppress any hot spot away from the symmetric axis in the radial temperature profile. In situations as shown in figure 3.1, radiation transfer in terms of volumetric energy source is calculated as follows

1) Search the maximum temperature T_m. There will be no radiation if T_m is lower than 8000K;

2) Search in the negative r-direction (towards the symmetric axis) of the first cell whose temperature is just above and nearest to 4,000K, its radial position is designated by R_{4k} ;

3) Search in the negative r-direction the first cell whose temperature is nearest to $0.83T_0$ (temperature on axis), its radial position is R_{83} ;

4) The arc's radiation radius is defined as $0.5(R_{4k} + R_{83})$;

5) q_e , the radiation from those cells whose radius is less than R_{83} , is calculated in terms of the net emission coefficient for an isothermal arc. The total amount of radiation emitted from the arc core, Q_e , is then calculated by integrating q_e over all emitting volumes ($r < R_{83}$) per unit length ;

6) The radiation absorption coefficient for those cells between R_{83} and R_{4K} (inclusive) assumes a profile of

$$\frac{q_a(r)}{q_0} = 1.1 - \left(\frac{R_{4K} + R_{83} - 2r}{R_{4K} - R_{83}}\right)^2 \qquad (3.12)$$

where q_0 is the maximum absorption coefficient which is located at $0.5(R_{4k} + R_{83})$;

7) Calculate the total radiation absorption Q_a by integrating $q_a(r)$ over all absorbing volumes ($R_{4K} \geq r \geq R_{83}$) per unit length. If there is only one absorbing cell, Q_a will be q_0 multiplied by the cell volume ;

8) Assuming that 80% (for arcs in supersonic nozzle) of the radiation emission from r = 0 to the cell whose radius is just less than R_{83} is re-absorbed at the arc edge, q_0 in equation (3.12) can then be determined ;

9) calculate $q_a(r)$ according to equation (3.12) ;

10). Set q_e to be positive and q_a to be negative .

It must be made clear that the percentage of radiation from the arc centre which is re-absorbed at the arc edge has no universal value. For arcs burning in supersonic nozzle with normal flow, about 80% of the radiation from the arc centre is re-absorbed at the arc edge [49]. However for arcs in auto-expansion circuit breakers where ablation of nozzle material is active, this value has been found to be 50% [105]. Thus, we will use a value of 80% in this chapter for investigation of arcs in supersonic nozzles and use a value of 50% in Chapter Four for computer simulation of arcs in an auto-expansion circuit breaker.

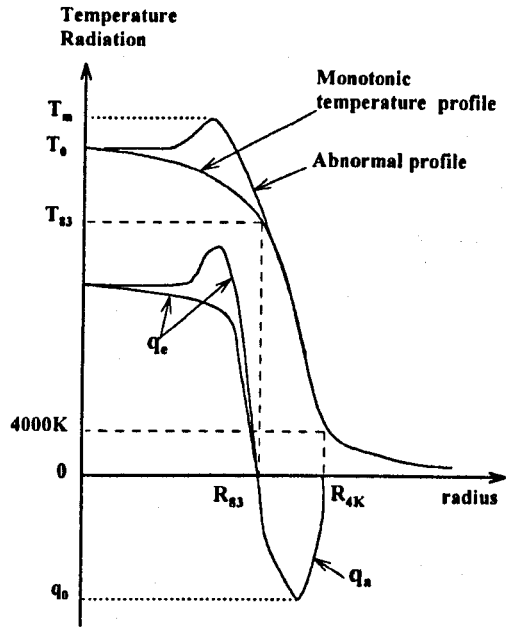

Figure 3.1 Schematic diagram of the approximate radiation model which is used in the differential arc model

3.4.2 Turbulence model

The concept of turbulence has been given in Section 1.2.3. Most of the existing turbulent models use the concept of eddy viscosity which is defined in a Cartesian coordinate system as

$$-\rho\overline{u_i'u_j'} = \mu_t\left(\frac{\partial u_i}{\partial x_j}+\frac{\partial u_j}{\partial x_i}\right)-\frac{2}{3}\rho k\delta_{ij} \qquad (3.13)$$

where δ_{ij} is the Kronecker delta and k is the turbulence kinetic energy which is a measure of the normal turbulence stresses. k is normally absorbed in the time averaged pressure. μ_t is not a fluid property. It depends on the state of turbulence and can only be obtained by a turbulence model. The turbulent energy exchange coefficient, k_t which represents the term $-\rho\overline{u_i'e'}$ in the energy equation, is related to the turbulent eddy viscosity by equation (1.17). The turbulence Prandtl number is assumed to be unity.

For dimensional reasons, μ_t is proportional to a turbulence velocity scale V_s and a turbulence length scale L_s :

$$\mu_t = C\rho V_s L_s \qquad (3.14)$$

where C is an empirical parameter. Turbulence models differ in the calculation of the velocity scale and the length scale.

3.4.2.1 Prandtl mixing length model

Prandtl mixing length model is also known as zero equation model [127] since the length and velocity scales are directly related to the mean flow. For arcs burning in axis-symmetric flow fields with dominating axial flow, the length scale is proportional to the local thermal radius which characterises the boundary of the high velocity core. The velocity scale is constructed from the local velocity gradient and the length scale. The eddy viscosity can then be calculated by

$$\delta = \sqrt{\int_0^{R_{2K}} (1 - \frac{\rho}{\rho_{2K}}) 2r dr} \tag{3.15a}$$

$$\mu_t = \rho (c_1 \delta)^2 \left| \frac{\partial w}{\partial r} + \frac{\partial v}{\partial z} \right| \tag{3.15b}$$

where δ is the thermal radius and c_1 is a turbulence parameter the value of which is to be adjusted according to experimental results. The radial integration in Equation (3.15a) is performed from r = 0 to r = R_{2k} which is the first point at 2000K from the axis because the pressure outside the arc column may vary significantly in the radial direction and render the integral in Equation (3.15a) negative.

3.4.2.2 K-epsilon model

More sophisticated turbulence models are based on additional equations which calculate the velocity and length scales for the turbulence. For the K-epsilon model, they are related to the time averaged turbulent kinetic energy and its dissipation rate [127] which are determined from

$$\frac{\partial(\rho k)}{\partial t} + \nabla \bullet (\rho \vec{V} k - \frac{\rho \nu_t}{\sigma_k} \nabla k) = \rho (P_k - \varepsilon) \tag{3.16}$$

$$\frac{\partial(\rho \varepsilon)}{\partial t} + \nabla \bullet (\rho \vec{V} \varepsilon - \frac{\rho \nu_t}{\sigma_\varepsilon} \nabla \varepsilon) = \rho \frac{\varepsilon}{k} (c_{1e} P_k - c_{2e} \varepsilon) \tag{3.17}$$

$$P_k = \upsilon_t \left[2(\frac{\partial w}{\partial z})^2 + 2(\frac{\partial v}{\partial r})^2 + 2(\frac{v}{r})^2 + (\frac{\partial w}{\partial r} + \frac{\partial v}{\partial z})^2 \right] \tag{3.18}$$

where the kinematic viscosity ν_t is related to k and ε by

$$\upsilon_t = C_\mu k^2 / \varepsilon \tag{3.19}$$

and the turbulent Prandtl number for thermal conduction is assumed unity. The constants in equations (3.16) to (3.19) are usually set at

c_μ=0.09, $c_{1\varepsilon}$=1.44, $c_{2\varepsilon}$=1.92, σ_k=1.0, σ_ε=1.3

which appear to have a wide range of applicability when applied to shear flow [127].

The turbulent kinetic energy and its dissipation rate at the inlet of an arcing chamber are rarely known. Empirically, we set k at 0.9% of the local kinetic energy and ε is derived from k by assuming a length scale of 9% of the width of the inlet

$$k_{in} = 0.009\frac{w_{in}^{\ 2}}{2} \tag{3.20}$$

$$\varepsilon_{in} = 0.1643\frac{k_{in}^{\ 2}}{0.09d_{in}} \tag{3.21}$$

where d_{in} is the radial width of the inlet. Axisymmetric conditions are also imposed on k and ε on the axis. In the region adjacent to the solid wall, following equations are used to fix the value of k and ε

$$k = \frac{c_f w_c^{\ 2}}{0.3} \tag{3.22}$$

$$\varepsilon = \frac{0.1643k^{\frac{3}{2}}}{y_c K} \tag{3.23}$$

where the symbols on the RHSs are defined in Section 3.3.3.

3.4.3 Ablation model

PTFE is almost exclusively used as the nozzle material in modern high voltage auto-expansion circuit breakers for its high mechanical strength and good insulation property. As mentioned in Section 1.3.4, radiation is the main source of energy for ablation of the nozzle material. If we assume that 50% (for arcs in auto-expansion circuit breakers) of the radiation from the arc core is re-absorbed at the arc edge, the other 50% will reach the nozzle wall. Since the physical process of the ablation of PTFE by radiation is poorly understood, we assume a constant vapour temperature of 3400K [102]. The total energy which is required to break the chain of the PTFE molecules (depolymerisation energy) and to raise the temperature of the PTFE vapour from room temperature to 3400K is 1.19×10^7 J/kg. Denoting the radiative flux at the nozzle wall by I_n, the mass flux at the nozzle wall will be

$$F_m = \frac{I_n}{H_v} \tag{3.24}$$

where $H_v = 1.19\times10^7$ J/kg. Since we are dealing with single phase flow of SF_6 , uncertainties will be introduced in the results due to the difference in the thermal properties between SF_6 and PTFE vapour. It is shown in figure 3.2 that the two most important quantities which will affect the fluid dynamics solution, namely the density and the product of density and enthalpy, are very close to each other. The product of density and enthalpy for PTFE vapour [128]differ from that of SF_6 [114] within 10% and the density within an average of 25%. The electrical conductivity of these two species are also very close [84]. Since the volume fraction of PTFE vapour in the storage volume where a high pressure source will be built up in the high current phase of an auto-expansion circuit breaker is less than 30% [105], it is thus expected that the uncertainty in the results introduced by the ablation model will be around 10%.

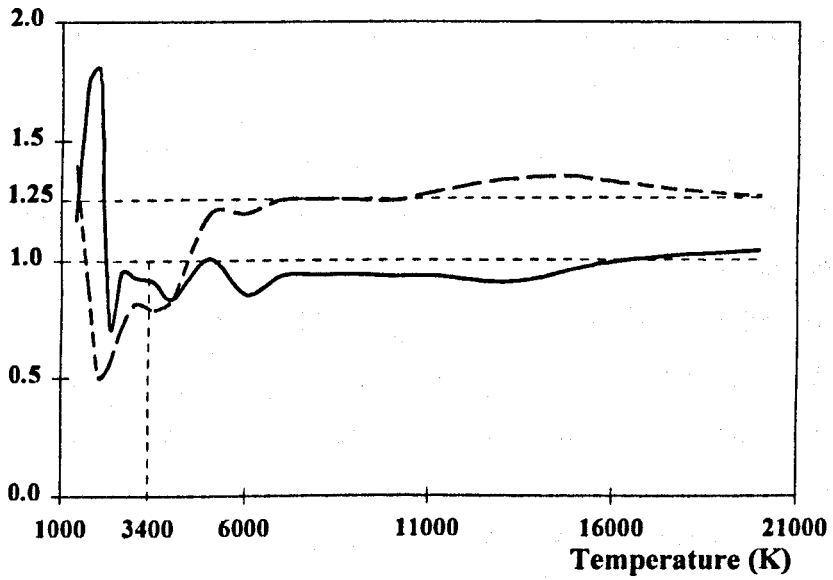

Figure 3.2 Comparison of the thermal properties of SF_6 and PTFE vapour. Solid curve: product of density and enthalpy of SF_6 to PTFE vapour. Broken line: density of SF_6 to PTFE vapour. Source of data: PTFE [128]; SF_6 [114].

The velocity at which the PTFE vapour is injected into the SF_6 flow is determined by the mass flow rate and the density of the vapour which in our approximate model is set to that of SF_6 at 3400K. Assuming the density of SF_6 at 1bar and 3400K is ρ_1 , the momentum flux (as radial surface source) will be

$$F_v = \frac{F_m^{\,2}}{\rho_l P} \tag{3.25}$$

where P is the local pressure at the nozzle surface in bar. The enthalpy flux is

$$F_h = F_m H_v \tag{3.26}$$

3.5 Modelling of Moving Contact

One of the basic features of a high voltage circuit breaker is the moving contact. In an auto-expansion circuit breaker, the moving part is usually the nozzle and hollow contact assembly, as shown in figure 3.3. Since the speed of the moving contact and nozzle is usually several meters per second, the gas flow generated by their movement can be neglected. We assume in our model that the nozzle and the hollow contact are at rest and the solid contact is moving.

When a fixed grid system is used in the computation, conservation of mass, momentum and energy requires that the effect of a moving contact be represented by source terms in two layers of cells which are separated by the moving surface of the contact. When a contact is moving, the space evacuated by it will be quickly filled up by the gas around it. The gas will have a velocity equal to that of the moving contact. For the cells immediately upstream of the moving contact (assuming the contact is moving downstream), the effects of the moving contact can be represented by a mass, momentum and an energy source per unit area (outwards), which are surface sources. In PHOENICS, the CFD package which we will use to implement out differential model, when a volume source of mass (sink) is specified, the momentum and energy associated with the outgoing mass will be automatically taken away. We thus convert the surface sources for mass, momentum and energy for the cells upstream of the moving contact into a volume mass source. Mathematically, the volume source of mass is

$$S_m = \frac{w_e \rho}{\Delta z} \tag{3.27}$$

where w_e is the speed of the contact, ρ and Δz are respectively the density of gas and the axial width of the cell immediately upstream of the moving contact. Numerically, when a cell is un-blocked in a time interval of Δt, its density, velocity and enthalpy are copied from the cell

upstream of it. The total mass, momentum and energy, which are required to fill the newly unblocked cell, are just equal to those which leave the upstream cell in the time interval of Δt. Thus, the mass, momentum and energy are conserved in the simulation of moving contact. The skin friction at the contact surface is small and is neglected.

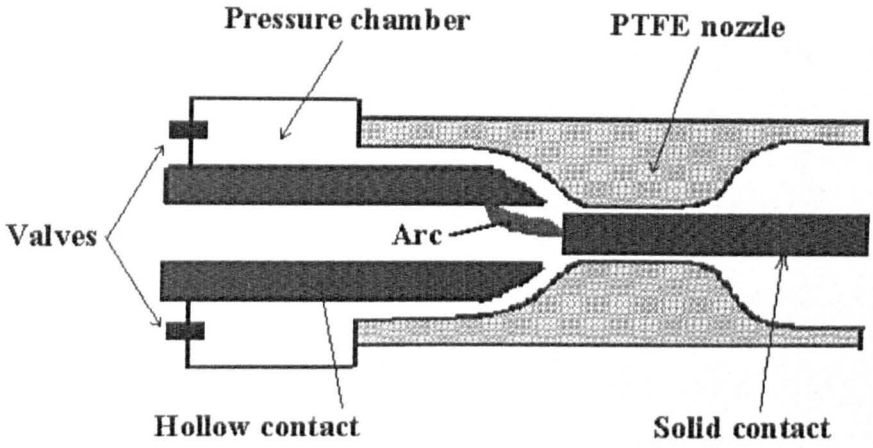

Figure 3.3 Schematic diagram of the arcing chamber in a modern high voltage auto-expansion circuit breaker

3.6 Calculation of the Electric and Magnetic Fields

3.6.1 Theory

The electromagnetic quantities which are required in our differential model are the electrical conductivity, the current density and the magnetic flux density. Circuit breaker arcs are a kind of low frequency plasma. The displacement current and the force exerting on space charges can be neglected in comparison with the convective current and Lorentz force. The induced electric field due to arc motion in its own magnetic field is much lower than the electric field imposed by the external circuit. Hall current and the current due to ion slip are also negligible since circuit breaker arcs are collision dominated. Under above conditions, equation (1.10) is reduced to

$$\vec{J} = \sigma \vec{E} \tag{3.28}$$

When the diameter of an arc is much smaller than its length (slender), the equo-potential lines inside the arc column are parallel and the electric field can be calculated by a

generalised Ohm's law in the form of equation (2.5). On the other hand, if the arc column is fat in comparison with its length or the diameter of the arc root is greater than that of the electrode, the equal-potential lines inside the arc column, especially near the electrodes, are bent so that the use of equation (2.5) will give unacceptable results for the calculation of Lorentz force and Ohmic heating. Under quasi-steady conditions, equation (1.11) can be reduced to the following form by taking divergence on both sides and representing electric field by the gradient of electrostatic potential

$$\nabla\cdot(\sigma\nabla\phi)=0 \tag{3.29}$$

which must be used to obtain the current density and electric field inside the arc column.

The gas or nozzle material away from the arc is insulating. Equation (1.13) must be used to obtain the electric field

$$\nabla\cdot(\varepsilon\nabla\phi)=0 \tag{3.30}$$

The solutions of equations (3.29) and (3.30) are linked by the boundary conditions at an interface which joins the domains for these two equations. We place this interface at the arc edge where the electrical conductivity is sufficiently small (say 10^{-3} $(\Omega\bullet m)^{-1}$) in comparison with that at the arc centre. The boundary conditions at the interface can thus be approximated by continuity of the electrostatic potential. By taking the value of σ at the interface to be $\sigma = c_2\ \varepsilon$, the solution of equation (3.29) will automatically satisfy Equation (3.30). The proportionality, c_2 which has a dimension of (1/s), can be determined by matching $c_2\ \varepsilon$ to the electrical conductivity at the interface, say 10^{-3} $(\Omega\bullet m)^{-1}$.

The magnetic field induced by the arc current has only an azimuthal component because of the axisymmetric feature of the arc column. Assuming the permeability of the arcing medium, μ, to be homogenous, the magnetic field can be calculated by

$$B=\frac{\mu_0\int_0^r J_z 2\pi\xi d\xi}{2\pi r} \tag{3.31}$$

where J_z is the axial component of the current density.

The electrostatic potential is of long range and the solution of equation (3.29) is sensitive to its boundary conditions as well as the locations of these boundaries . For a CFD domain as shown in figure 3.4 which represents a typical geometry of nozzle arc, the true boundary conditions on curve g-h for equation (3.29) are unknown. The computation domain for equation (3.29) is therefore extended in the radial direction to line e-d. There are two

reasons for this extension. The first is that the solution of equation (3.29) inside the CFD domain becomes less sensitive to the location of the boundary conditions provided that e-d is sufficiently far away from the axis. The second reason is that with an orthogonal grid system for the potential domain the boundary conditions for equation (3.29) can be conveniently cast into the numerical scheme which will be presented in next section.

Axisymmetric conditions are imposed for ϕ on the axis a-b and $\partial\phi/\partial n = 0$ at all boundaries other than the electrodes (contacts). n is the normal direction of boundary surface. When there are two electrodes present in the domain, one of which (for example on line b-c) will be set at $\phi = 0$. The potential at the other electrode (line a-f) will be adjusted until the specified current is satisfied. With known electrical conductivity in the domain, the solution of equation (3.29) can be more efficiently obtained by using following procedures:

1) Solve equation (3.29) with a fixed value of ϕ on line a-f, say 5V
2) calculate the electric field and the total current I_{5V}
3) The potential and the electric field under the specified current can be obtained by multiplying those of 5V on line a-f with the parameter I_s / I_{5V} where I_s is the specified current.

It should be noted that the above procedures are valid only for the boundary condition $\partial\phi/\partial n = 0$ at the non-conducting boundaries. The current density distribution on the cathode surface is modelled by defining a circular conducting spot whose radius is determined by equation (2.46). The electrical conductivity on the electrode surface outside this spot is set at a small value.

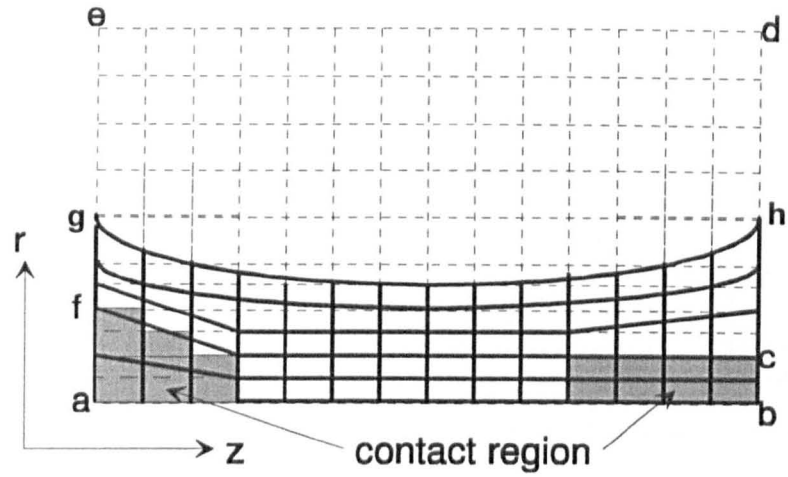

Figure 3.4 The CFD domain (solid lines) and the orthogonal grid system (broken lines) used for the solution of equation (3.29).

3.6.2 Numerical scheme in cylindrical polar coordinate system

Equation (3.29) takes the following form in a cylindrical polar coordinate system

$$\frac{\partial}{\partial z}(\sigma\frac{\partial \phi}{\partial z})+\frac{1}{r}\frac{\partial}{\partial r}(r\sigma\frac{\partial \phi}{\partial r})=0 \qquad (3.32)$$

To cast equation (3.32) into a finite volume form in the orthogonal grid system shown in figure 3.5, we integrate it over a cell by assuming a uniform electrical conductivity.

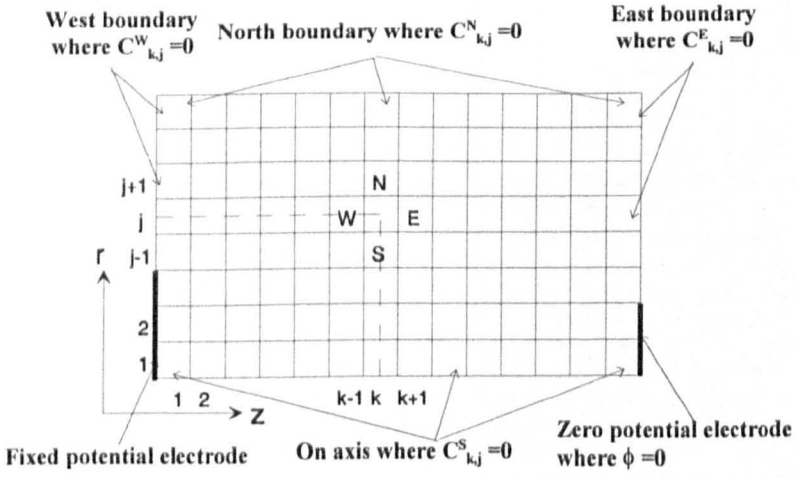

Figure 3.5 Finite volume in a cylindrical polar coordinate system for the calculation of electrostatic potential.

The electric current from cell (k+1, j) into cell (k, j) is

$$F^E = \frac{4\pi r_j \delta r_j}{\frac{\delta z_k}{\sigma_{k,j}} + \frac{\delta z_{k+1}}{\sigma_{k+1,j}}}(\phi_{k+1,j} - \phi_{k,j}) = C^E{}_{k,j}(\phi_{k+1,j} - \phi_{k,j}) \tag{3.33}$$

where δz is the axial width of an cell and δr the radial width. C^E is the conductance between centres of the two cells. The electric current through the other three faces are

$$F^W = \frac{4\pi r_j \delta r_j}{\frac{\delta z_k}{\sigma_{k,j}} + \frac{\delta z_{k-1}}{\sigma_{k-1,j}}}(\phi_{k-1,j} - \phi_{k,j}) = C^W{}_{k,j}(\phi_{k-1,j} - \phi_{k,j}) \tag{3.34}$$

$$F^N = \frac{4\pi \delta z_k}{\frac{\delta r_j}{r_j \sigma_{k,j}} + \frac{\delta r_{j+1}}{r_{j+1}\sigma_{k,j+1}}}(\phi_{k,j+1} - \phi_{k,j}) = C^N{}_{k,j}(\phi_{k,j+1} - \phi_{k,j}) \tag{3.35}$$

$$F^S = \frac{4\pi \delta z_k}{\frac{\delta r_j}{r_j \sigma_{k,j}} + \frac{\delta r_{j-1}}{r_{j-1}\sigma_{k,j-1}}}(\phi_{k,j-1} - \phi_{k,j}) = C^S{}_{k,j}(\phi_{k,j-1} - \phi_{k,j}) \tag{3.36}$$

The solution of Equation (3.32) requires

$$F^E + F^W + F^S + F^N = 0 \tag{3.37}$$

which gives the discretized form of equation (3.32)

$$\begin{aligned}&(C^E{}_{k,j} + C^W{}_{k,j} + C^S{}_{k,j} + C^N{}_{k,j})\phi_{k,j} \\ &- C^E{}_{k,j}\phi_{k+1,j} - C^W{}_{k,j}\phi_{k-1,j} - C^S{}_{k,j}\phi_{k,j-1} - C^N{}_{k,j}\phi_{k,j+1} = 0\end{aligned} \tag{3.38}$$

The boundary conditions for equation (3.38) are set in terms of the coefficients Cs. At the north boundary (as indicated in figure 3.5) $C^N{}_{k,j}$ is set at zero so $\phi_{k,j+1}$ will not be required. At the axis $C^S{}_{k,1}$ is at zero since the solution of equation (3.38) should be axisymmetric. At the east and west boundaries other than the electrode surface, $C^E{}_{k,j}$ and $C^W{}_{k,j}$ are respectively set at zero. At the boundary of the zero-potential electrode, $\phi_{k+1,j}$ =0 and $C^E{}_{k,j}$ for the boundary cell is

$$C^E{}_{k,j} = \frac{4\pi r_j \sigma_{k,j} \delta r_j}{\delta z_k} \tag{3.39}$$

and $C^{W}_{k,j}$ for the boundary cell at the fixed potential electrode (5V) is

$$C^{W}_{k,j} = \frac{4\pi r_j \sigma_{k,j} \delta r_j}{\delta z_k} \tag{3.40}$$

The electrical field strength is calculated by

$$E_z = \frac{F^W - F^E}{4\pi r_j \delta r_j \sigma_{k,j}} \tag{3.41}$$

$$E_y = \frac{F^S - F^N}{4\pi r_j \delta z_k \sigma_{k,j}} \tag{3.42}$$

3.7 PHOENICS

PHOENICS [111] has been extensively used at the University of Liverpool to model circuit breaker arcs since 1992. The results from PHOENICS have been verified under various conditions [44]. The differential model for auto-expansion circuit breakers developed in this chapter will be implemented into PHOENICS version 2.0 which is capable of catching shocks in the flow field. All boundary conditions which are discussed in Section 3.3 are treated as sources terms.

3.8 Some Fundamental Processes Associated with Circuit Breaker Arcs

3.8.1 The effects of self-induced magnetic field on a high current SF_6 arc in a supersonic nozzle

It is well known that the Lorentz force due to interaction of the arcing current and its own magnetic field is the cause for strong gas acceleration in a free burning arc [1]. However the effects of the self-generated Lorentz force on a nozzle arc are less clear as the arc also burns in a pressure gradient generated by other means, say a high pressure reservoir. The objective of the present investigation is to carry out a comparative study on the importance of the Lorentz force for a 30kA SF_6 arc in an enlarged nozzle of Benenson et. al [129]. An upstream electrode is placed at the nozzle inlet. The dimensions of the enlarged nozzle are: Throat diameter=47.5mm, axial distance of throat to nozzle inlet=59.4mm, nozzle length =

95mm, inlet diameter=95mm, exit diameter=59.85 mm, electrode diameter=19.5mm, axial distance of electrode tip to nozzle inlet = 9.5 mm.

The transport properties of the arcing medium (SF_6) may be affected by the magnetic field induced by the arc. The gas pressure in the nozzle is between 2.5bar to 9bar. The temperature is around 20,000K in the arc centre. For a 30kA nozzle arc, the maximum self-induced magnetic flux density is 0.6 Tesla at the edge of the arc root. Whether or not the magnetic field will affect the transport properties of an SF_6 plasma depends on the ratio of two frequencies: the Larmor (cyclotron) frequency due to the self-induced magnetic field and the collision frequency of an electron with other particles in the plasma. The average drift velocity of electrons in an electric field is determined by the frequency at which an average electron makes a collision with other particles in the plasma. As a first approximation, the electrical conductivity can be related to collision frequency of an electron with other particles by the following relationship

$$\sigma = \frac{e^2 n_e}{2 m_e \nu_m} \tag{3.43}$$

where e is the electronic charge, n_e the number density of electrons, m_e the mass of an electron and ν_m is the momentum transfer collision frequency of an electron with other particles in the plasma. The Larmor frequency of an electron under the effect of a magnetic flux density B is

$$\nu_L = \frac{eB}{2\pi m_e} \tag{3.44}$$

The number density of electrons [130] and the electrical conductivity [114] at three temperatures are listed in Table 3.2. The electron number density is approximately proportional to pressure, while the electrical conductivity is not sensitive to the pressure. The exit pressure and the maximum magnetic flux density are therefore used in the calculation. The results in Table 3.2 show that an electron will experience at least 30 collisions with other particles in the course of a Larmor circle under the effect of the self-induced magnetic field. Collisions between electrons and other particles remain the dominant process which is responsible for momentum and energy transfer in the plasma. The influence of the self-induced magnetic field on the transport properties can thus be neglected.

Prandtl mixing length theory is used to model the turbulent arc. For the nozzle under investigation, it has been found that c_l in equation (3.15) = 0.04 is satisfactory. Body fitted

co-ordinates are used in the grid system. A total number of 70×70 cells are used in the flow domain.

Table 3.2

Temperature (K)	Pressure (bar)	number density of electrons (m^{-3})	electrical conductivity ($\Omega^{-1}m^{-1}$)	collision frequency of an electron with other particles (s^{-1})	Larmor frequency (s^{-1})
8,000	2.5	2×10^{22}	1,300	9.5×10^{11}	1.7×10^{10}
14,000	2.5	1.7×10^{23}	5,500	5×10^{11}	1.7×10^{10}
20,000	2.5	5×10^{23}	10,000	7×10^{11}	1.7×10^{10}

The temperature field and the equal-potential lines for the 30kA arc is illustrated in Figure 3.6. The most evident effect of the self-generated magnetic force is the modification to the pressure field which is shown in figures 3.7 and 3.8. The pressure difference on the axis with and without the magnetic forces reaches 2 bar (figure 3.9). The gas near the cathode region is strongly accelerated by the magnetic driving force (figure 3.10). A careful examination of the results shows that the velocity and enthalpy at the nozzle exit are not sensitive to the magnetic field. However, the increase in gas density due to pressurisation at the arc centre enhances the axial energy convection and it results in an arc voltage of 472V which is 8% higher than that without magnetic field (447V). The enthalpy and kinetic energy fluxes at the exit are shown in figure 3.11.

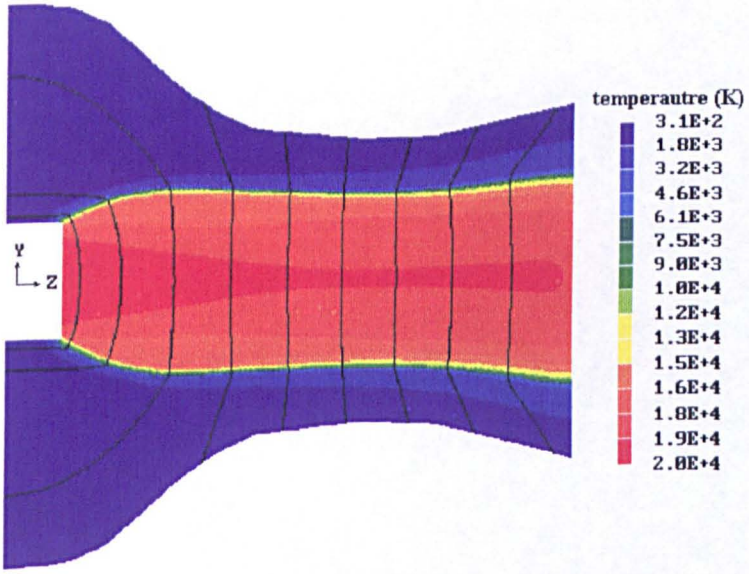

Figure 3.6 Temperature field and equal-potential lines of a 30kA SF_6 arc in a supersonic nozzle. The upstream stagnation pressure is 9 bar and the stagnation temperature is 313K. The exit pressure is 2.5bar.

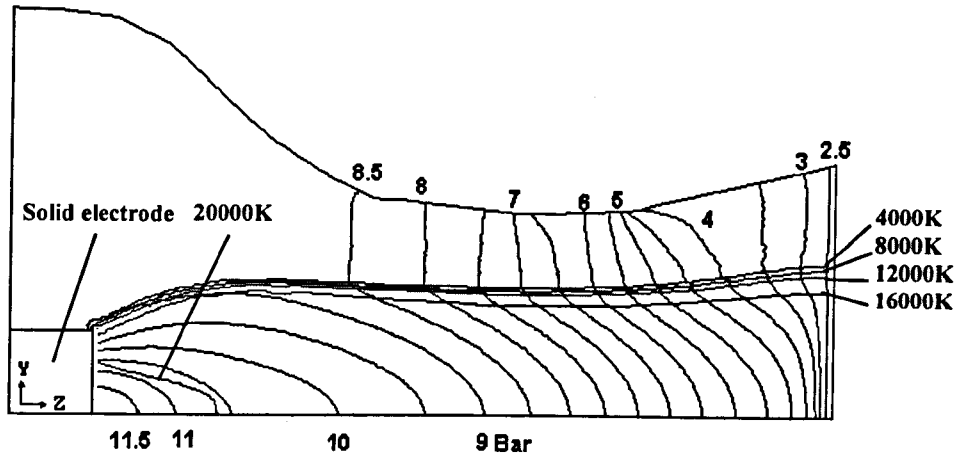

Figure 3.7 Pressure and temperature contours in the enlarged EPRI nozzle with self-generated Lorentz force. See figure 3.6 for arcing conditions.

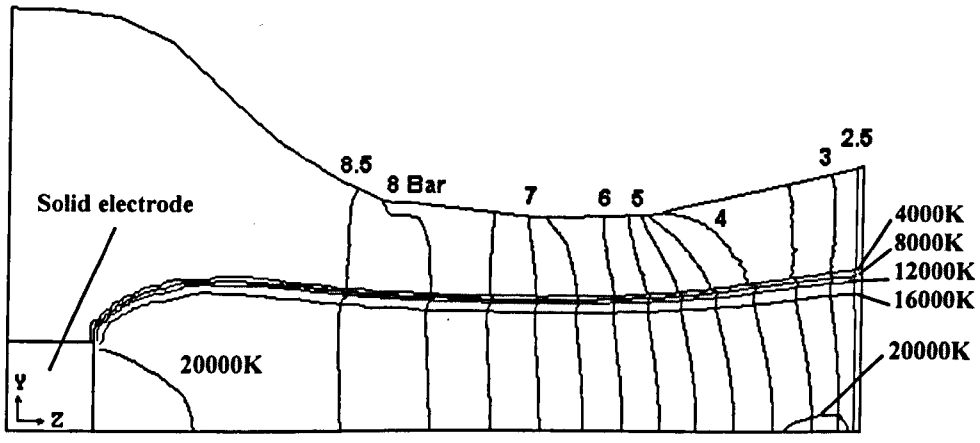

Figure 3.8 Pressure and temperature contours in the enlarged EPRI nozzle without self-generated Lorentz force. See figure 3.6 for arcing conditions.

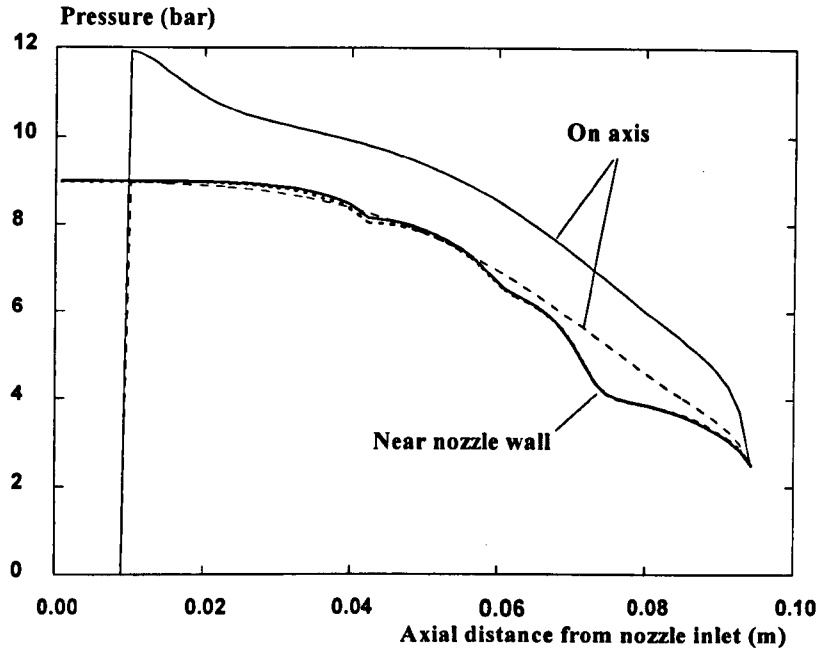

Figure 3.9 Pressure on nozzle axis and near the nozzle wall. Solid lines: with magnetic force; Broken lines: without magnetic force. Pressure distributions near the wall are nearly identical. See figure 3.6 for arcing conditions

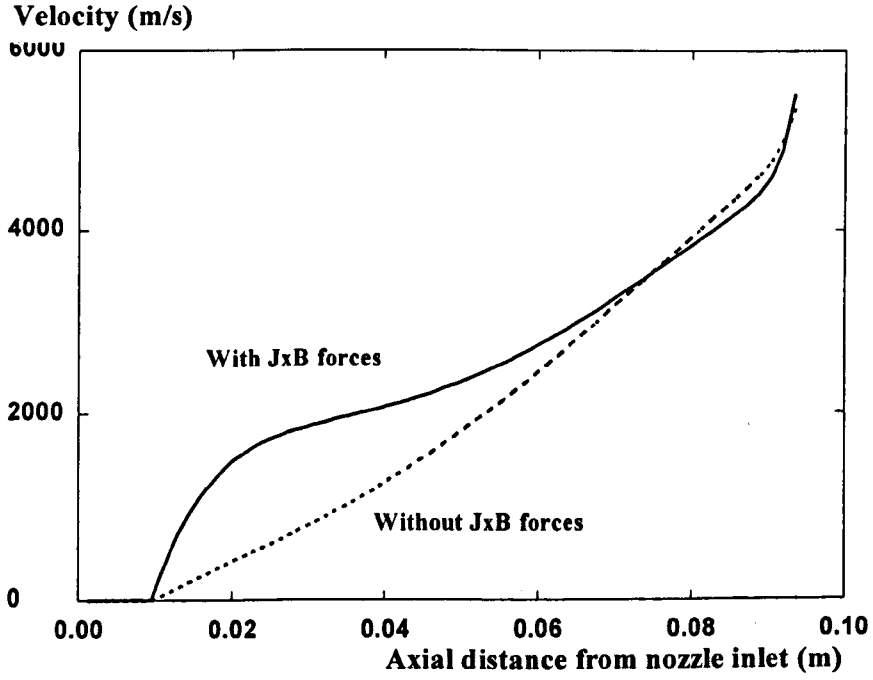

Figure 3.10 Velocity on axis for the 30kA SF_6 arc. See figure 3.6 for arcing conditions

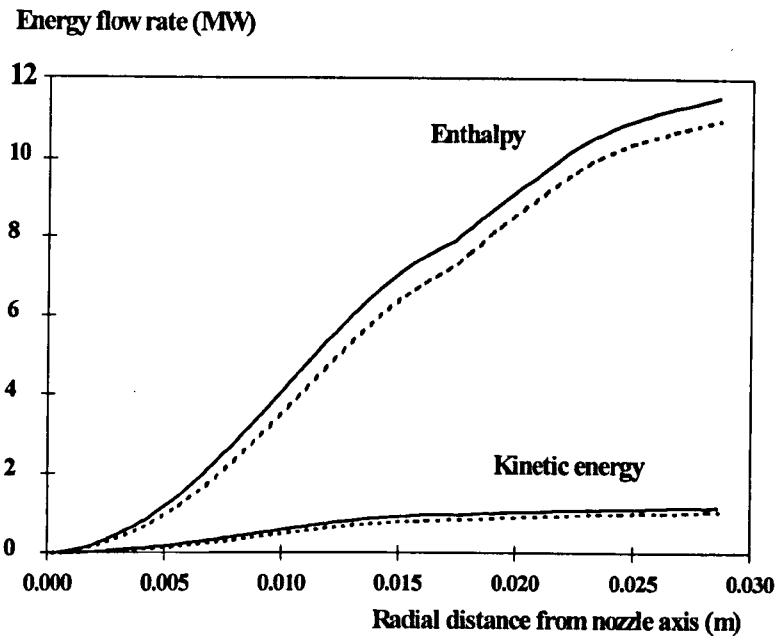

Figure 3.11 Radially integrated energy flow rate at the nozzle exit. Solid lines: with J×B force; Broken lines: without J×B force.

3.8.2 Electrical and aerodynamic behaviour of arcs under shock conditions

Supersonic nozzles are commonly used in modern gas blast circuit-breakers as well as in other arc devices. Shock inside the nozzle cannot be avoided during the operation of a puffer circuit breaker [131]. It has been recognised that, in the absence of an arc, shock can occur in the diverging section of the nozzle if the ratio of exit pressure to that at the inlet is higher than the critical value which is determined by the nozzle geometry and the gas properties. The presence of an arc substantially alters the flow in the nozzle since the density within the thermal influence region of the arc is very low in comparison with the cold surrounding flow. In addition, an SF_6 arc in an accelerating flow is unstable and is usually in a turbulent state. It is therefore expected that the presence of an arc will have profound effects on the shock which in turn affects the arc. The close coupling between the arc and the surrounding flow determines the aerodynamic and electrical behaviour of a nozzle arc.

There is very little systematic investigation on arc-shock interaction. Experimental observation was limited to the arc section outside the nozzle or to that downstream of an orifice plate [129,132]. High speed photography shows that arc is broadened after the shock. Campbell et al [133] have observed a deterioration of thermal interruption capability of a

supersonic nozzle under shock conditions. It is therefore important, especially for current interruption, to understand the arc-shock interaction inside a supersonic nozzle.

Some preliminary computer simulated results of arc-shock interaction have recently been reported [92]. Their investigation is restricted to two currents and one pressure ratio. The present investigation has greatly extended the range of discharge conditions within which strong arc-shock interaction is expected. Special attention is paid to the aerodynamic and electrical behaviour of SF_6 arcs under shock conditions.

Numerical results have been obtained for the nozzle shown in figure 3.12 for which the nozzle inlet radius is 12.5×10^{-3} m and that of the exit 19.2×10^{-3}m. The throat radius is 6.25×10^{-3} m. The throat is 15.6×10^{-3} m away from the inlet plane and the nozzle length is 68.7×10^{-3} m. Body fitted grid system is adopted in the computation to accommodate the curved boundary of the nozzle. Fine radial grids are used in the arc region and axially refined grids are employed in the arc-shock interaction region. Altogether 80×80 cells are used to obtain the results.

All the results presented in this thesis are calculated with Prandtl mixing length model (c_1 in equation (3.15) = 0.04). The upstream stagnation pressure is 9bar. In the absence of the arc the position of the shock for a back pressure of 3bar is shown in figure 3.13. In the presence of the arc, the flow and pressure fields have been substantially altered. The pressure and temperature contours are given in figures 3.13 to 3.15 for currents 200A, 500A and 1500A, respectively. The new shock centre is moved upstream and it no longer has the features of a plane shock. The centre of the shock is not very sensitive to the current. There is a region where arc and shock interact strongly. In this interaction region flow separates because of the adverse pressure gradient which causes arc deformation (broadening) as shown in figure 3.16. Flow separation further modifies the pressure distribution as the shock cannot penetrate a sub-sonic flow.

Under the present boundary conditions at the exit, gas may be drawn in from outside the nozzle as shown in figure 3.17. For the 200A case reverse flow occurs in the arc core and the surrounding thermal layer. This reverse flow region will become smaller and move away from the axis when the current is increased. A shock cannot be easily identified in the region near the axis by conventional definition. The flow in the 500A and 1500A cases after the rapid pressure rise is still supersonic (figure 3.18). For the 200A case, the reduction in the flow Mach number in Figure 3.18 cannot be correlated to the steep pressure rise on the axis (figure

3.19) since it continues to drop rapidly even after the pressure rise. The axis pressure rise is broadened and the magnitude of the pressure rise on the axis is also reduced when current is increased (figure 3.19). Similar pressure variation along the nozzle wall is also observed although the pressure rise is stronger and is within a shorter distance (figure 3.20). The flow decelerates to sonic or subsonic after the pressure rise (figure 3.21). Because of the strong Ohmic heating in the arc core region, the axis temperature is not sensitive to the pressure rise (figure 3.22). The arc and its surrounding flow before the interaction zone is hardly affected and the pressure distribution is a weak function of current.

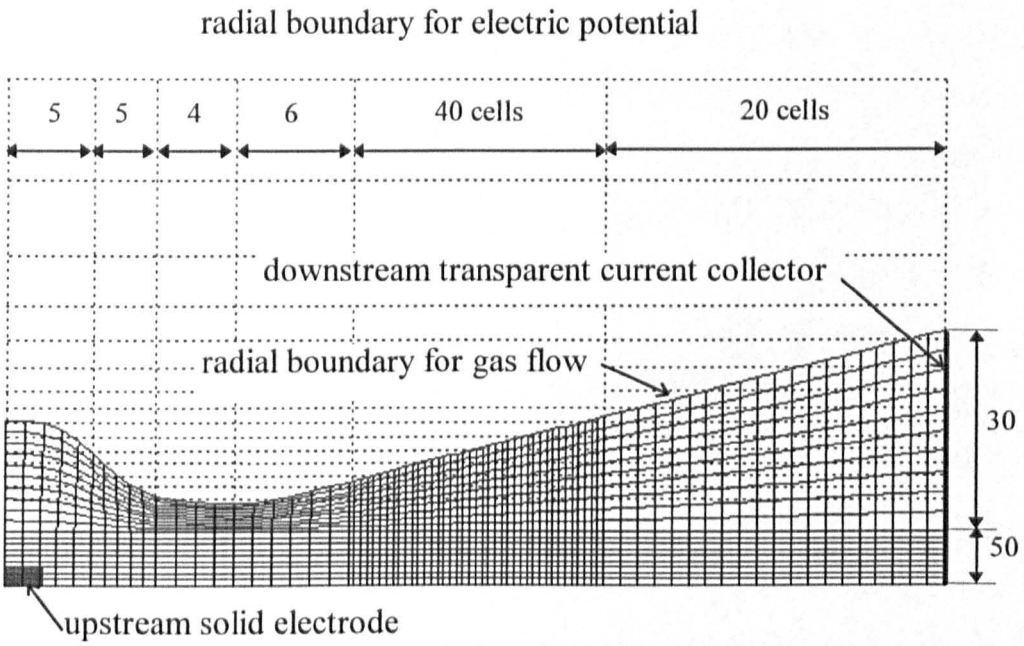

Figure 3.12 Grid system used for arc-shock investigation. Body fitted grids are used for the gas flow (solid lines) while orthogonal grids are used for the calculation of electric potential (dotted lines). The number captioning the arrowed lines indicates the cell number in the region.

It has been noticed that the region of the pressure rise both near the axis and the nozzle wall moves slightly downstream when current increases. This seems to be in conflict with the expectation that the location of this region should approach the shock position of the cold flow case without arc when current reduces to zero. The axial pressure profile upstream of the pressure rise (figures 3.19 and 3.21) approaches the cold flow case when current reduces, which agrees with what is expected. However, the new shock centre near the wall depends on

the arc shape in the interaction zone. Because of the enlargement of the arc region and the low flow entrainment, the oncoming supersonic external flow encounters an equivalent compression corner which gives rise to compression waves. The bunching of these compression waves forms the new shock centre close to the nozzle wall. The axial variation of arc enlargement is more gentle for higher currents. This explains the qualitative trend of the location of the shock with the currents.

Because of flow separation there is a large region in the divergent section of the nozzle where flow is extremely stagnant. Thermal recovery in this region is expected to be very slow, thus reducing the interruption capability.

A typical electrostatic potential distribution is shown in figure 3.23. Since the nozzle is made of insulating materials the equi-potential lines intersect with the nozzle wall. Radial potential gradient within the arc is much smaller than the axial gradient even in the arc-shock interaction region. Thus the calculation of electric field using slender arc model should be a good approximation as shown in figure 3.24.

The V-I characteristic of the nozzle arc is given in figure 3.25. The change in arc voltage in the presence of a shock can be attributed to the increase in arc size and in pressure in the divergent section due to arc-shock interaction. The former tends to lower the arc voltage. The increase in pressure results in a larger radiation loss. Thus, it tends to increase the arc voltage. These two competing factors are responsible for the voltage minimum and a slight positive slope of the V-I characteristic after the current being above approximately 650A. On the whole, the voltage of an arc with shock is lower than that of the shock free case. Increase of the exit pressure results in the shock centre moving further upstream and in a further reduction of arc voltage for a given current (figure 3.26).

The effects of Lorentz force caused by the interaction of the arc current with its own magnetic field has also been investigated. The effects are negligible for the current range investigated. It is not possible at present to compare with experiments. As mentioned previously experimental observation is so far limited to the case where arc is outside the nozzle, a situation which is very different from the one investigated here. However, some qualitative features are similar, such as the broadening of the arc cross section and a slight lowering in arc voltage [129].

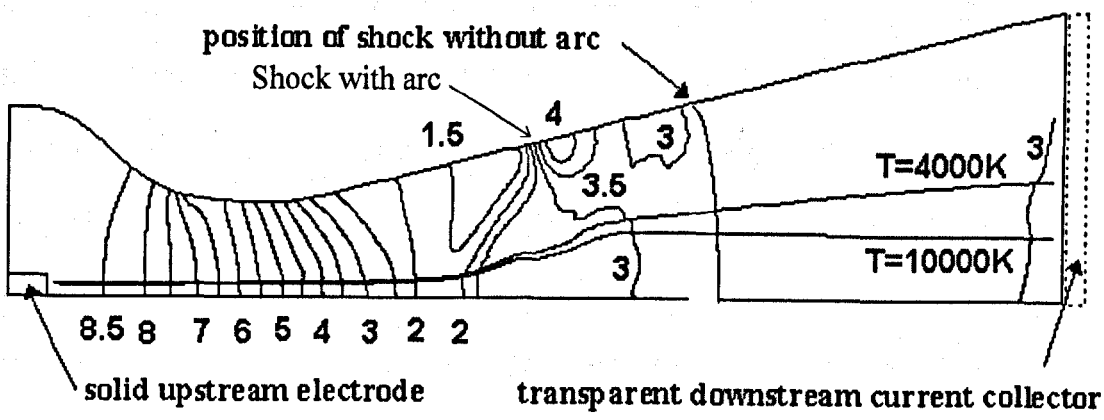

Figure 3.13 Pressure and temperature contours for a 200A non-slender arc. The exit pressure is 3bar. The electrode arrangement is the same as in figure 3.12

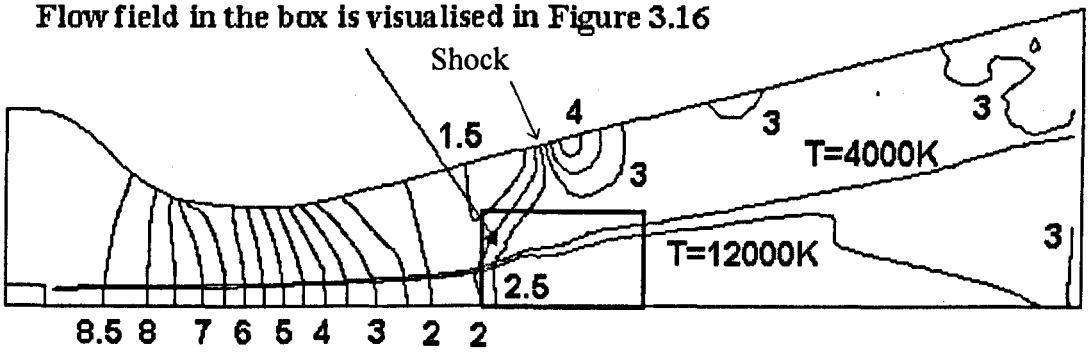

Figure 3.14 Pressure and temperature contours for a 500A non-slender arc. The exit pressure is 3×10^5 Pa. The electrode arrangement is the same as in figure 3.12.

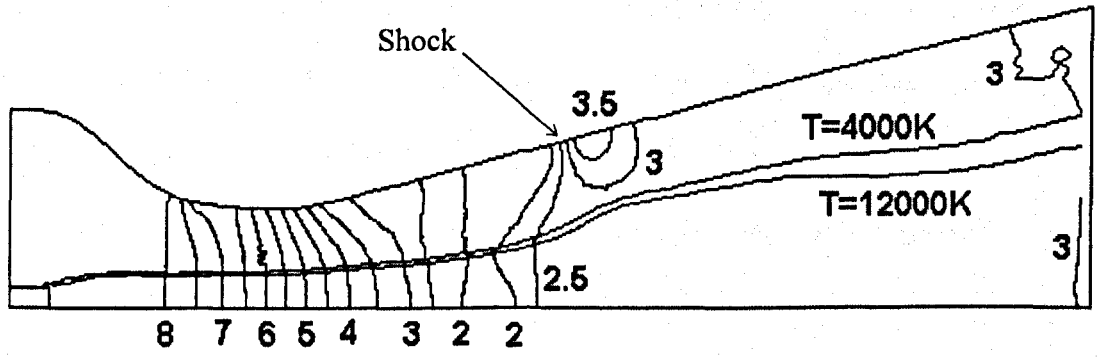

Figure 3.15 Pressure and temperature contours for a 1500A non-slender arc. The exit pressure is 3bar. The electrode arrangement is the same as in figure 3.12.

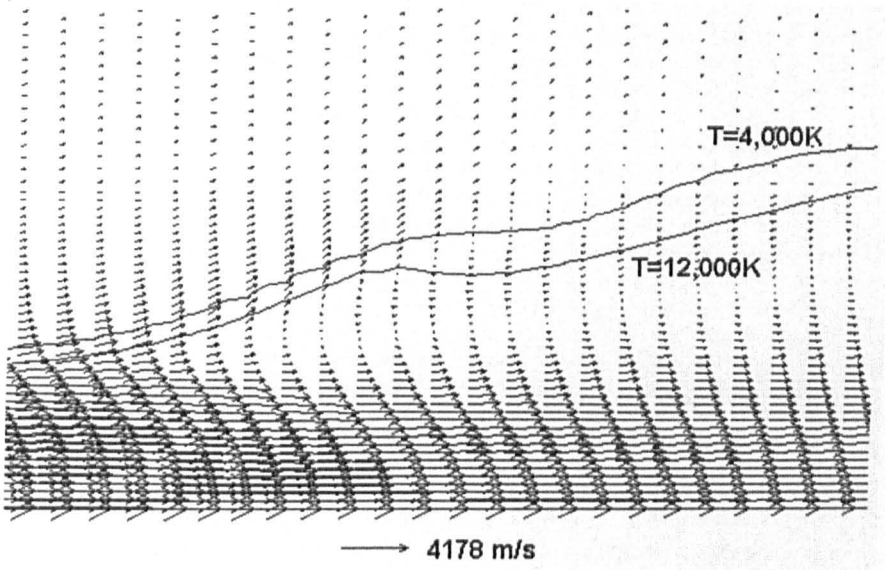

Figure 3.16 Broadening of the arc column by flow separation in the arc-shock interaction region for a 500A arc. Conditions are the same as in Figure 3.14. The position of this figure is shown in figure 3.14.

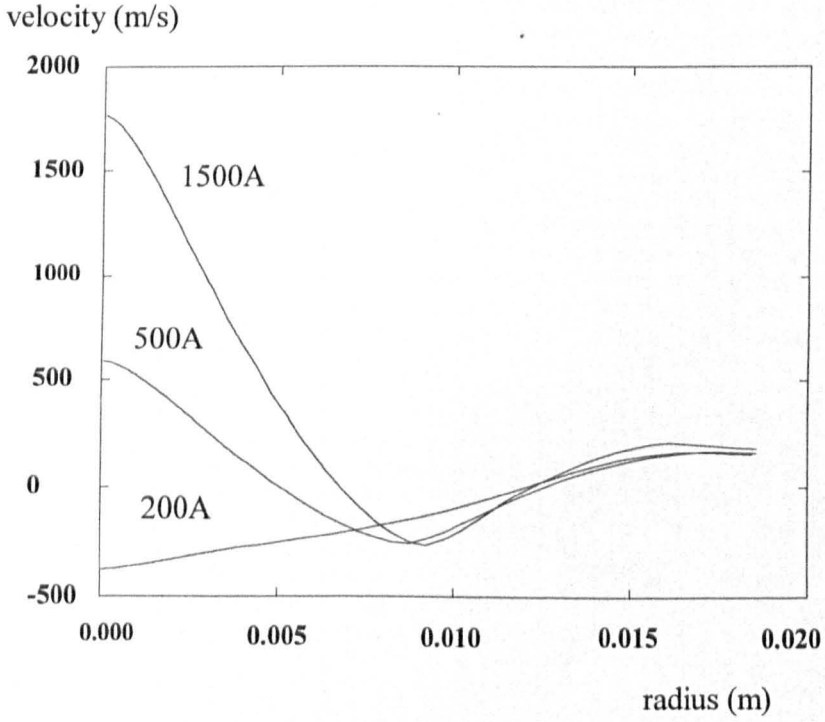

Figure 3.17 Radial profile of the axial velocity component at the nozzle exit for arc current 200A, 500A and 1500A. The exit pressure is 3bar.

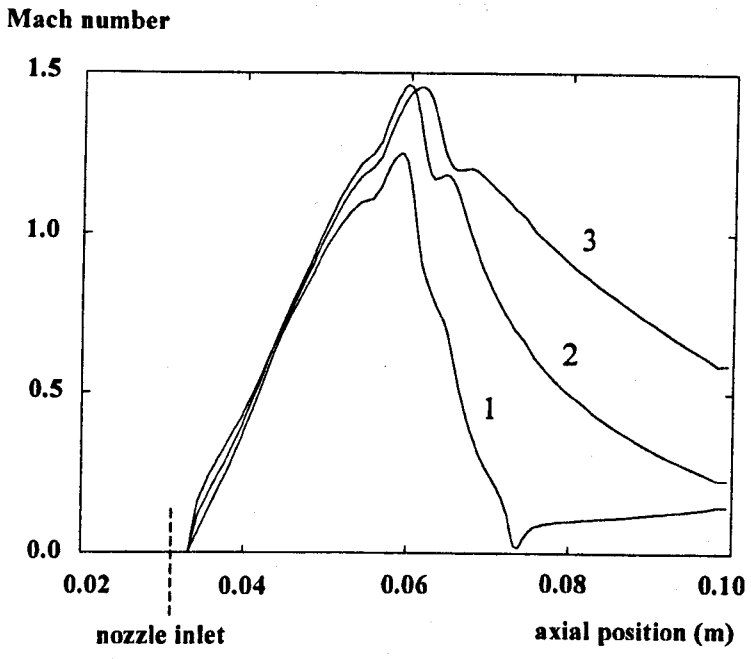

Figure 3.18 Mach number on axis of the nozzle for current 200A, 500A and 1500A. The exit pressure is 3bar. Curve 1: 200A; Curve 2: 500A; Curve 3: 1500A.

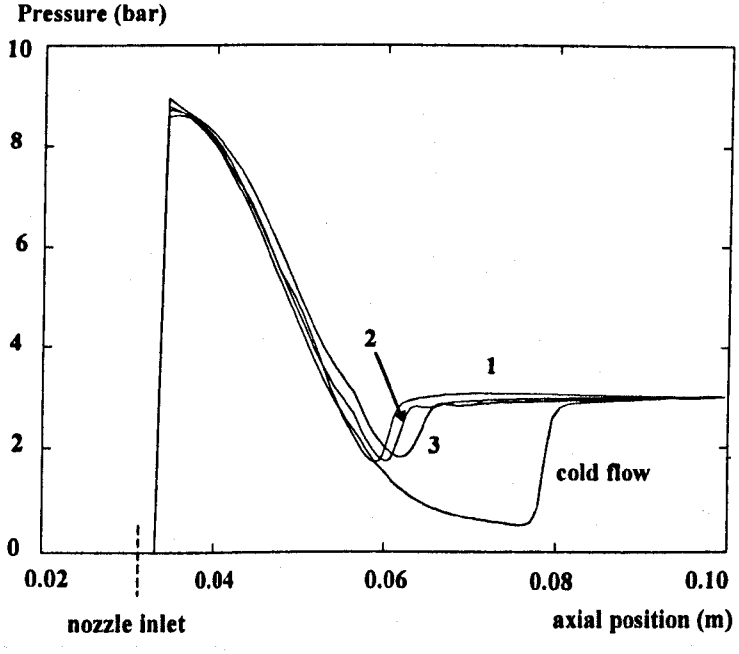

Figure 3.19 Pressure on axis of the nozzle for current 200A, 500A ,1500A and for the cold flow case. The exit pressure is 3bar. Curve 1: 200A; Curve 2: 500A; Curve 3: 1500A.

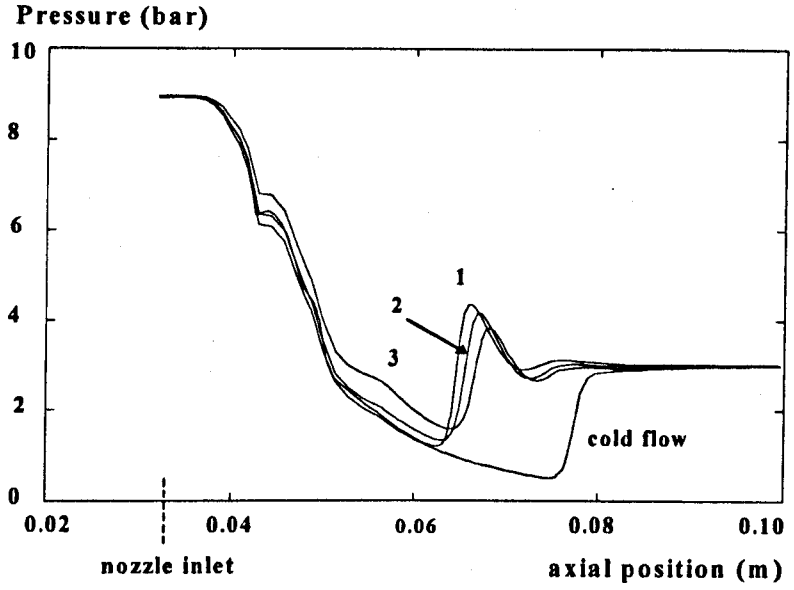

Figure 3.20 Pressure along the wall of the nozzle for current 200A, 500A, 1500A and for the cold flow case. The exit pressure is 3bar. Curve 1: 200A; Curve 2: 500A; Curve 3: 1500A.

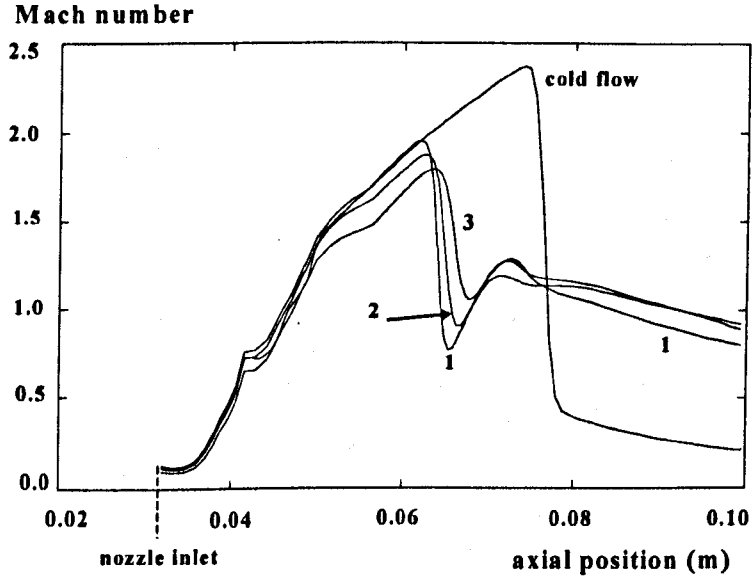

Figure 3.21 Mach number along the wall of the nozzle for current 200A, 500A, 1500A and for the cold flow case. The exit pressure is 3bar. Curve 1: 200A; Curve 2: 500A; Curve 3: 1500A.

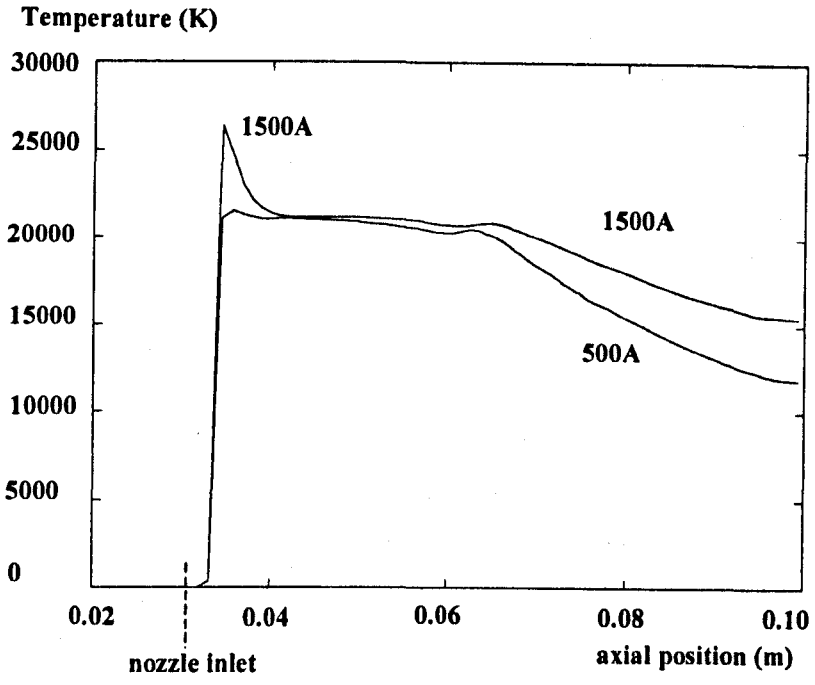

Figure 3.22 Axis temperature for arc current 500A and 1500A. The exit pressure is 3bar.

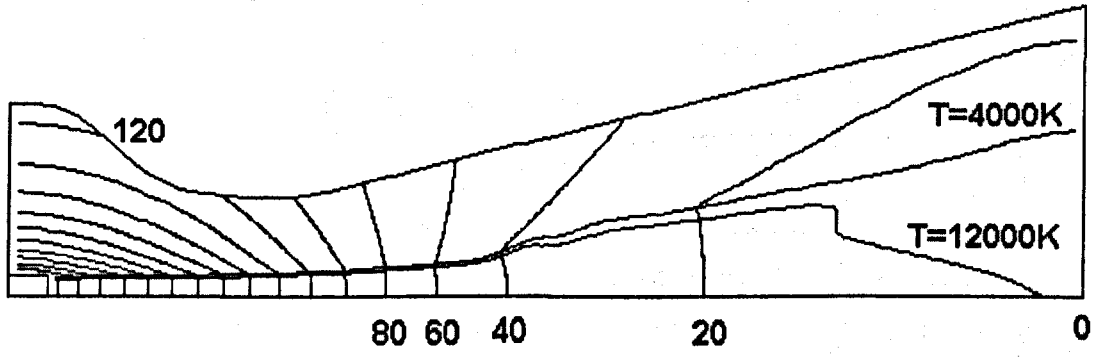

Figure 3.23 Electrostatic potential contours inside the nozzle for a 500A arc. The results are calculated by the non-slender model. The exit pressure is 3bar. The arc voltage is 320V. The gap between two adjacent lines is 20V. The electrode arrangement in figure 3.12 is used in the calculation.

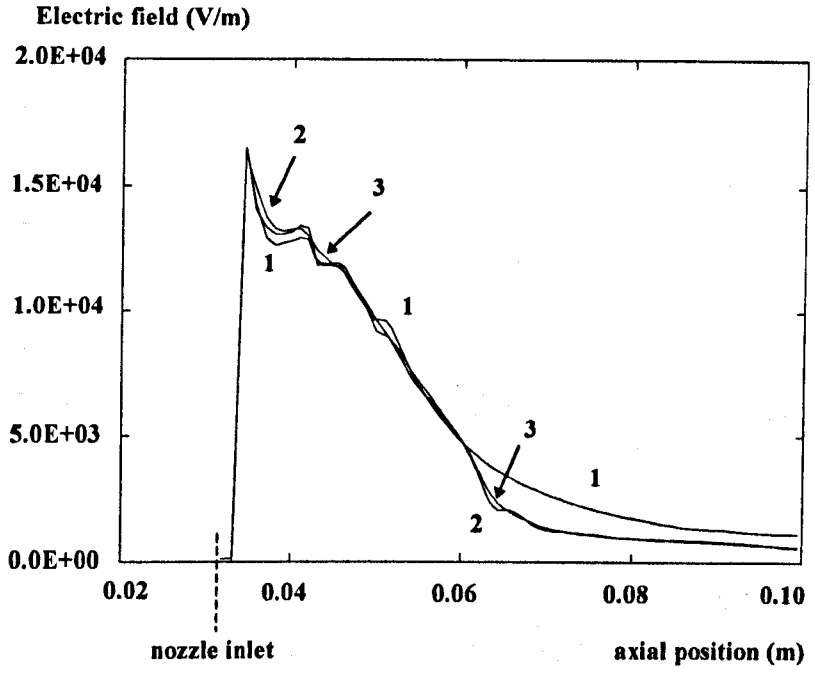

Figure 3.24 Axial electric field component on axis of the nozzle for a 500A arc. Curve 1: slender model with exit pressure of 0.2bar (no shock); Curve 2: slender model with exit pressure of 3bar ; Curve 3: non-slender model with exit pressure of 3bar .

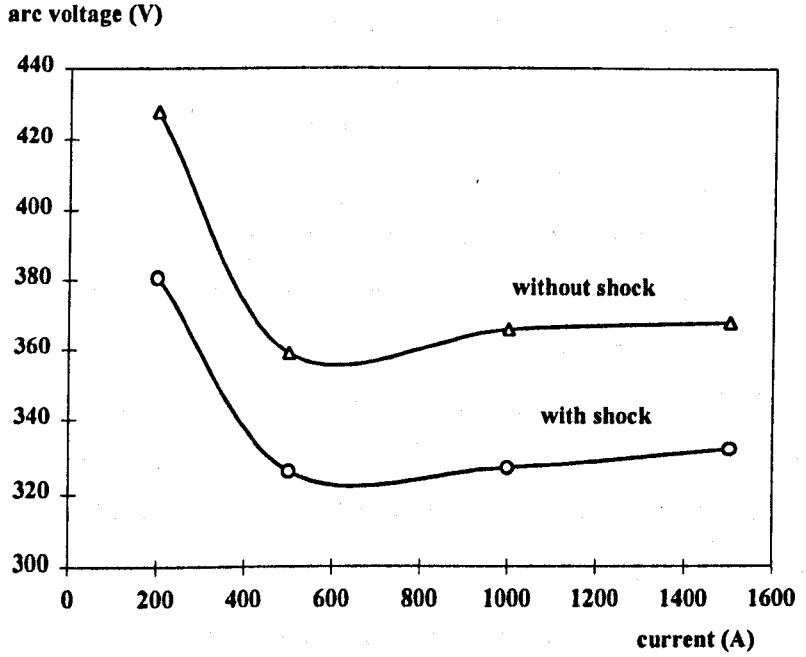

Figure 3.25 Voltage-current characteristics for the nozzle arrangement under investigation. The results are calculated by the slender arc model. The exit pressure is 3bar for the shock cases and 0.2bar for the shock free cases.

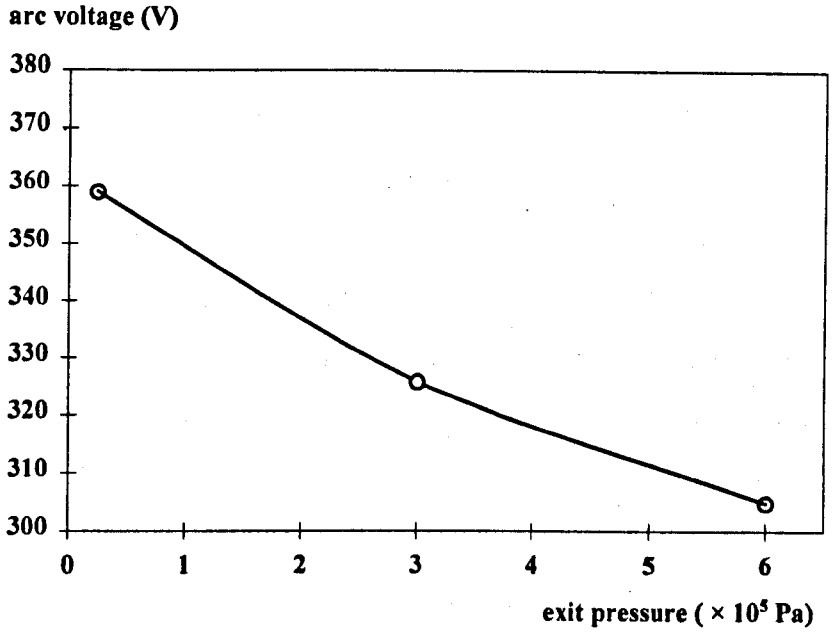

Figure 3.26 Arc voltage as a function of exit pressure of the supersonic nozzle for a 500A case. The results are calculated using the slender arc model.

3.8.3 A Comparative study of turbulence models for SF_6 arcs in a supersonic nozzle

High pressure arcs burning in a supersonic nozzle are often used for material processing, waste disposal, and for current interruption in circuit-breakers. In these devices, the arc is strongly accelerated by the pressure gradient and is often in a turbulent state [31]. For high voltage circuit-breakers, SF_6 is exclusively used for its high insulation strength and high interruption capability of fault currents. The present investigation is solely concerned with the modelling of SF_6 arcs in gas-blast circuit-breakers under turbulent conditions.

Arcs in a supersonic nozzle usually attain an axis temperature higher than 15,000K. The radial temperature profile has very high gradients, especially at the core edge, due to radiation absorption there [134]. Because of the low gas density within the high temperature core the gas velocity can reach a few thousands meters per second [134,91,42,135]. This high velocity shear layer (e.g. in a jet) is usually attributed as the cause of arc instability [31,135]. The modelling of turbulent arcs, therefore, follows the same line as that of a turbulent jet. However, an arc differs from an ordinary fluid jet in that the gas is highly compressible and there is a strong source of heat (Ohmic input). The momentum and energetic aspects of the arc are closely coupled. Recent investigation of the on-set of arc instability shows that the main

driving mechanism for arc instability is the density fluctuation in the region where temperature gradient is very high[136].

Up to now, modelling of turbulent arc is almost exclusively based on the turbulence models for shear layer flows. Although density fluctuation in some turbulence models has been taken care of by taking the density weighted averages[137] the extra computation cost and the uncertainty in the values of turbulence parameters make the adoption of this approach at present not fruitful. There is also another added difficulty: that is to relate the density averaged quantity to those measured in laboratory, which are usually time averaged. However, the application of the Prandtl mixing length turbulence model to arcs in supersonic flow has had considerable success in predicting the thermal interruption capability of a gas-blast circuit-breaker[138] although the turbulence parameters need to be adjusted for a given geometry of the nozzle.

For shear layer flows, the K-epsilon turbulence model has long been popular since the five turbulence parameters are not very sensitive to flow conditions and the default values (see Section 3.4.2.2) can usually make reasonable prediction. Compared with the Prandtl mixing length model the wide range of applicability of the turbulence parameters is the main advantage of the K-epsilon model although the computational cost of the K-epsilon model is considerably higher. It is for this reason that we undertake to apply this turbulence model to SF_6 turbulent nozzle arcs. If the default values of the K-epsilon's turbulence parameters can be equally applied to turbulent SF_6 arcs under a range of gas discharge conditions, scaling of thermal plasma engineering systems will become a reality.

The objective of this investigation is to carry out a comparative study of two turbulent models, the Prandtl mixing length model and the K-epsilon model, when applied to turbulent SF_6 arcs burning a supersonic nozzle. The spectroscopic temperature measurements by Lesberg and Pietsch[45,139] are used to judge the relative merits of these two turbulence models. The SF_6 arcs in the experiments were burning under turbulent conditions. The temperature results are the average value over several shots, the exact number of which is not given. An experimental error of 14% was given in [139]. The exposure time of the spectroscopic system is 30μs. Since the diameter of the turbulent DC arc varies with time, the radial uncertainty in the results can be estimated based on the change in arc diameter with respect to time, which can be derived from the photographs of the arc column taken by high speed camera [139], which is 0.15mm for the 1800A case.

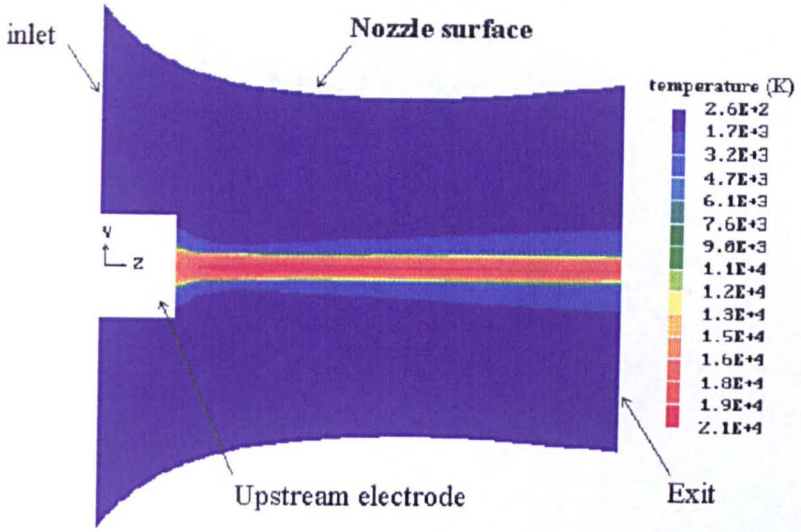

Figure 3.27 Geometry of the Aachen nozzle which is used for the comparison of the behaviour of turbulence models. The arcing current in this figure is 600A and the turbulent parameter C_1 for the Prandtl mixing length model is set at 0.20. Upstream stagnant pressure is 9bar and exit pressure is 2.5bar.

Computation has been carried out for the supersonic nozzle used by Lesberg and Pietsch [45,139] (figure 3.27) for which the upstream stagnation pressure of SF_6 is 9 bar at room temperature. The length of the nozzle is 55mm and the throat diameter of the nozzle is 36.7mm. The diameter of the solid upstream electrode is 10.86mm and its length is 7.86mm. A total number of 95(radial)×45(axial) cells are used for the 600A and 1800A DC cases and 125(radial)×45 (axial) are used for 100A DC case. Body fitted coordinate system is used to model the curved nozzle shape. The grids are refined in the arc region.

Large discrepancies exist between the radial temperature profile predicted by the K-epsilon model with its five default values and the measurements of Lesberg and Pietsch [45,139]. Results shown in figures 3.28 to 3.30 indicate that turbulent energy exchange is slightly over-represented for the 100A case but seriously under-represented for the 600A and 1800A cases (curves labelled $C_{1\varepsilon}$ =1.44) by the default values in the K-epsilon model. The disagreement for the 1800A case is well beyond the estimated experimental uncertainty which is shown in figure 3.30. Lowering $C_{1\varepsilon}$ in equation (3.17) of the K-epsilon model has the effect of reducing the turbulent dissipation rate and thus increases the turbulent kinetic energy which in turn enhances the turbulent exchange. The value of $C_{1\varepsilon}$ to best fit the temperature measurements is 1.6 for the 100A case, 1.1 to 1.2 for the 600A case and 0.96 for the 1800A

case. The results shown in figures 3.28, 3.29 and 3.30 indicate that the default value of 1.44 of $C_{1\varepsilon}$ seriously under-represents the turbulent energy exchange for the 1800A case. By contrast, a value of 0.20 for C_l in equation (3.15) of the Prandtl mixing length model gives acceptable agreement between the predicted and measured radial temperature profile at the nozzle throat (figures 3.31, 3.32 and 3.33). The K-epsilon turbulence model with $C_{1\varepsilon} = 1.2$ and the Prandtl mixing length model with $C_l = 0.20$, both of which produce radial temperature distributions very close to the measurement at the nozzle throat for the 600A case, are used to compare the behaviour of these two models. Prandtl mixing length model predicts slightly higher axis temperature than the K-epsilon model in most of the arc column (figure 3.34) since Prandtl mixing length model gives little turbulent energy exchange near the axis (figure 3.35) according to equation (3.15) and equation (1.17). The results near the upstream electrode will not be compared since the K-epsilon model used here is for high Reynolds number flow only. The results further downstream are not sensitive to this near electrode region.

Prandtl mixing length model predicts lower turbulent kinematic viscosity at the arc centre but higher at the edge of the arc column than the K-epsilon model (figure 3.36). This explains the radial temperature distributions in figure 3.37 at the nozzle throat which results in a higher axial electric field for the Prandtl mixing length case (figure 3.34) despite the higher axis temperature (figure 3.34). Nevertheless, the difference between the predicted arc voltages is less than 10V for this particular case (figure 3.38, 569V by Prandtl mixing length model and 560V by K-epsilon model). The difference in other variables is small as can be seen in figures 3.39 to 3.42.

The behaviour of two most popular turbulent models, the Prandtl mixing length model and the K-epsilon model are investigated in this section. It is found that both models tend to under-represent the turbulent energy exchange in the arc column when arcing current increases. At least one of the five parameters in the K-epsilon model needs to be adjusted in order to achieve agreement between the predicted and measured radial temperature profiles at the throat of a supersonic nozzle in the current range 100A to 1800A, while a value of 0.20 of C_l in equation (3.15) is applicable for all three currents investigated. By matching the radial temperature profiles at the nozzle throat for the 600A case, these two turbulence models behave rather similarly in the region free of influence of the upstream electrode. For turbulent SF_6 arcs, consideration of the range of applicability of the turbulence parameters and the cost of computation has made the Prandtl mixing length model preferable to the K-epsilon model.

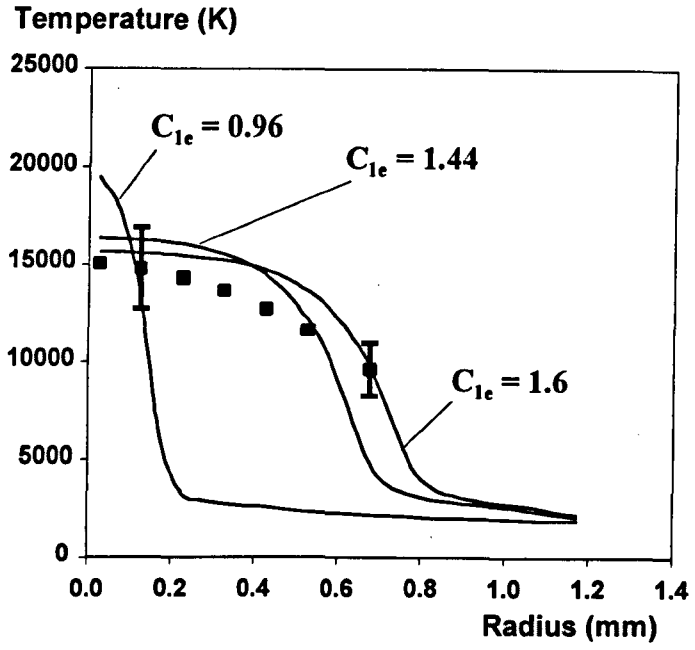

Figure 3.28 Radial temperature distributions of the 100A SF_6 arc (DC) at the nozzle throat with different C_{1e} in the K-epsilon model. The upstream stagnation pressure is 9bar and exit pressure is 2.5bar. Squares: measurements.

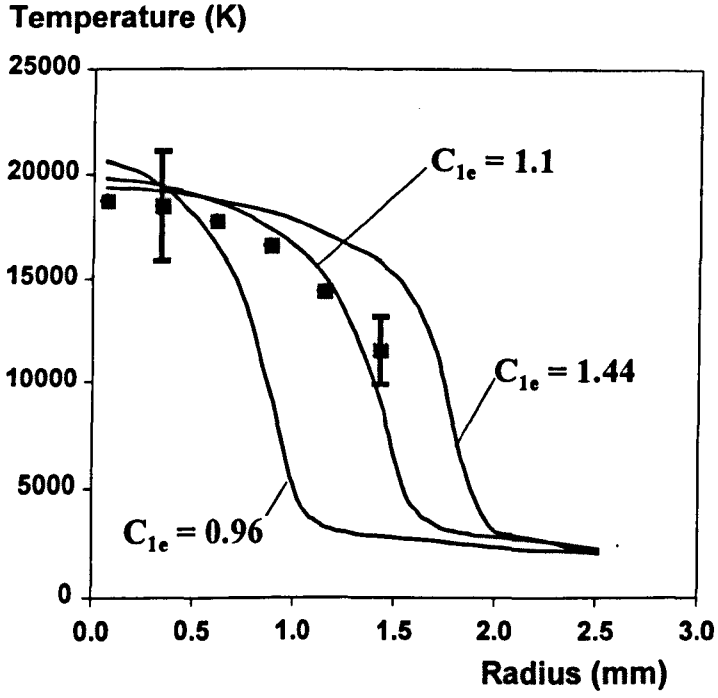

Figure 3.29 Radial temperature distributions of the 600A SF_6 (DC) arc at the nozzle throat with different C_{1e} in the K-epsilon model. The upstream stagnation pressure is 9bar and exit pressure is 2.5bar. Squares: measurements.

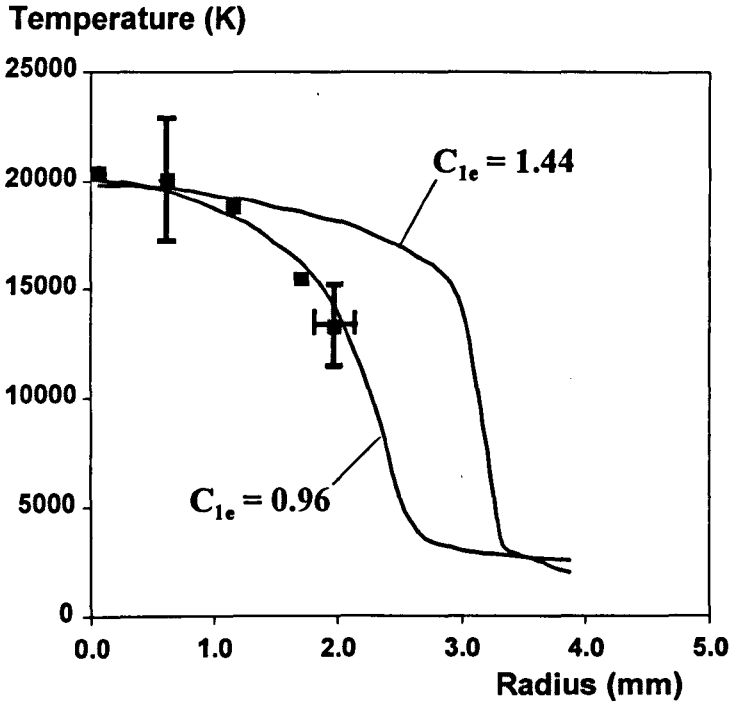

Figure 3.30 Radial temperature distributions of the 1800A (DC) SF_6 arc at the nozzle throat with different C_{1e} in the K-epsilon model. The upstream stagnation pressure is 9bar and exit pressure is 2.5bar. Squares: measurements.

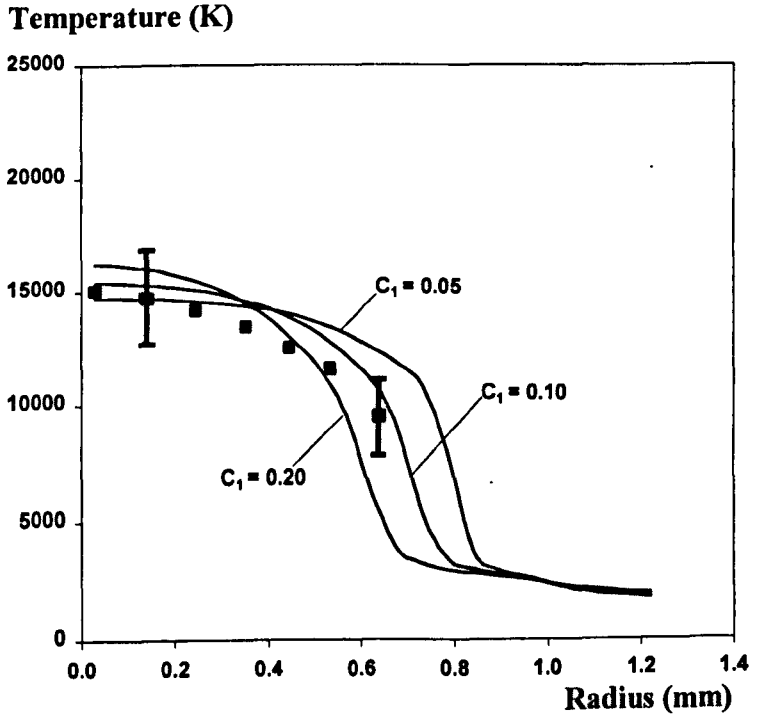

Figure 3.31 Radial temperature distributions of the 100A SF_6 arc (DC) at the nozzle throat with different C_1 in the Prandtl mixing length model. The upstream stagnation pressure is 9bar and exit pressure is 2.5bar. Squares: measurements.

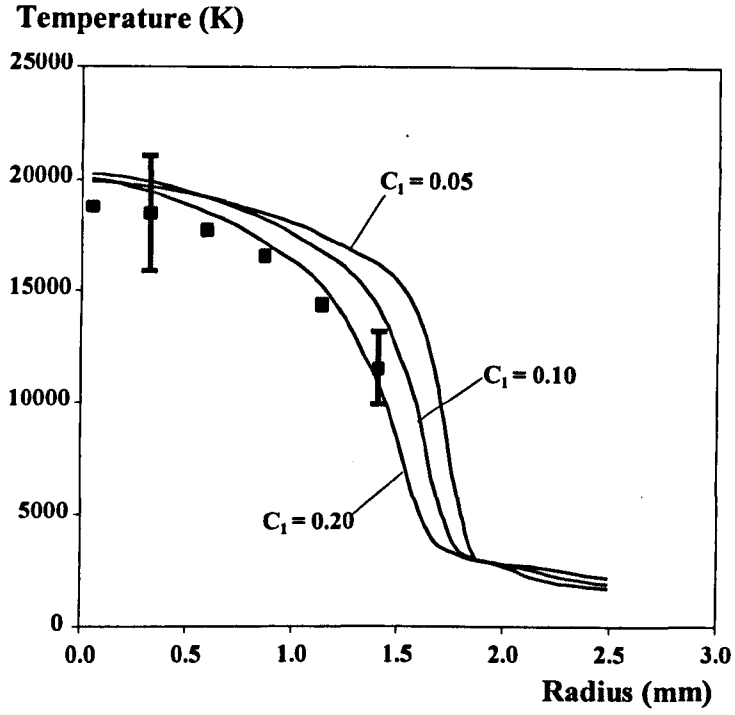

Figure 3.32 Radial temperature distributions of the 600A SF_6 arc (DC) at the nozzle throat with different C_1 in the Prandtl mixing length model. The upstream stagnation pressure is 9bar and exit pressure is 2.5bar. Squares: measurements.

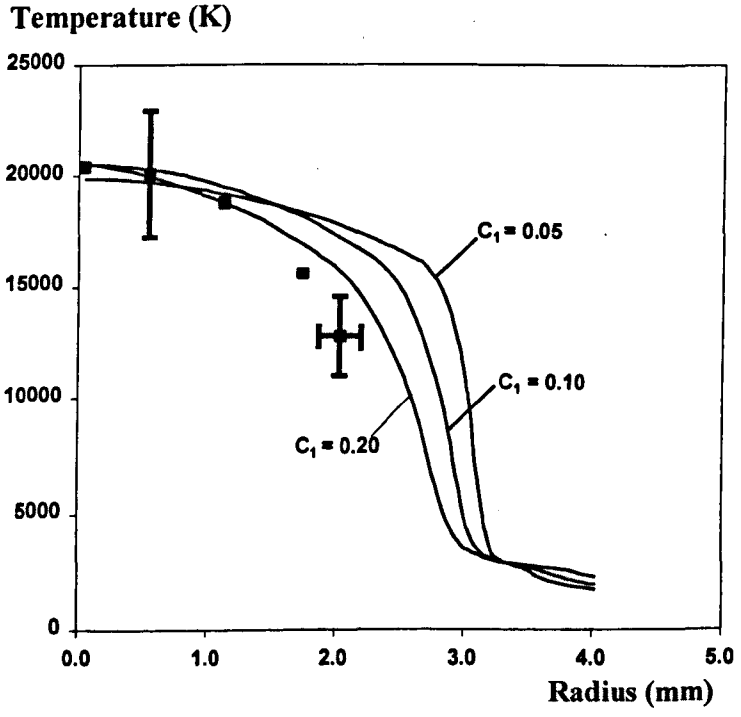

Figure 3.33 Radial temperature distributions of the 600A SF_6 arc (DC) at the nozzle throat with different C_1 in the Prandtl mixing length model. The upstream stagnation pressure is 9bar and exit pressure is 2.5bar. Squares: measurements.

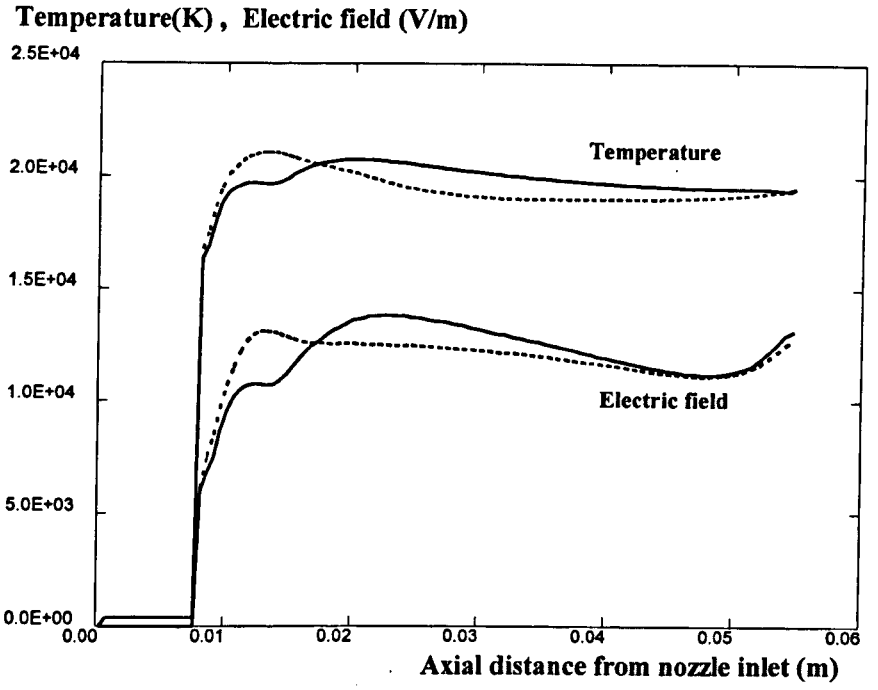

Figure 3.34 Axis temperature and axial electric field of the 600A SF_6 arc. The upstream stagnation pressure is 9bar and exit pressure is 2.5bar. Solid lines: Prandtl mixing length model with $C_l = 0.20$; Broken lines: K-epsilon model with $C_{le} = 1.2$

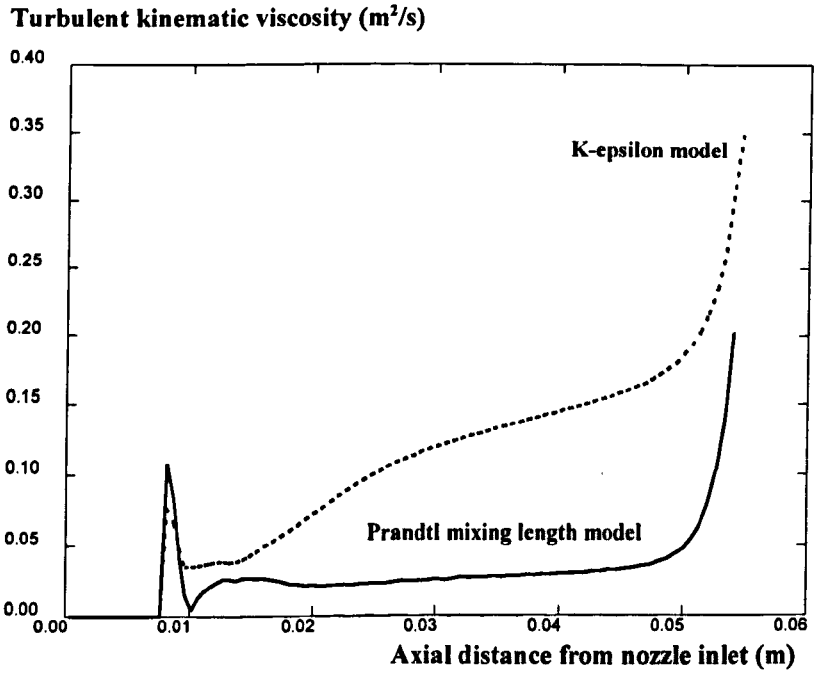

Figure 3.35 Turbulent kinematic viscosity near axis of the 600A SF_6 arc. The upstream stagnation pressure is 9bar and exit pressure is 2.5bar. Solid line: Prandtl mixing length model with $C_l = 0.20$; Broken line: K-epsilon model with $C_{le} = 1.2$

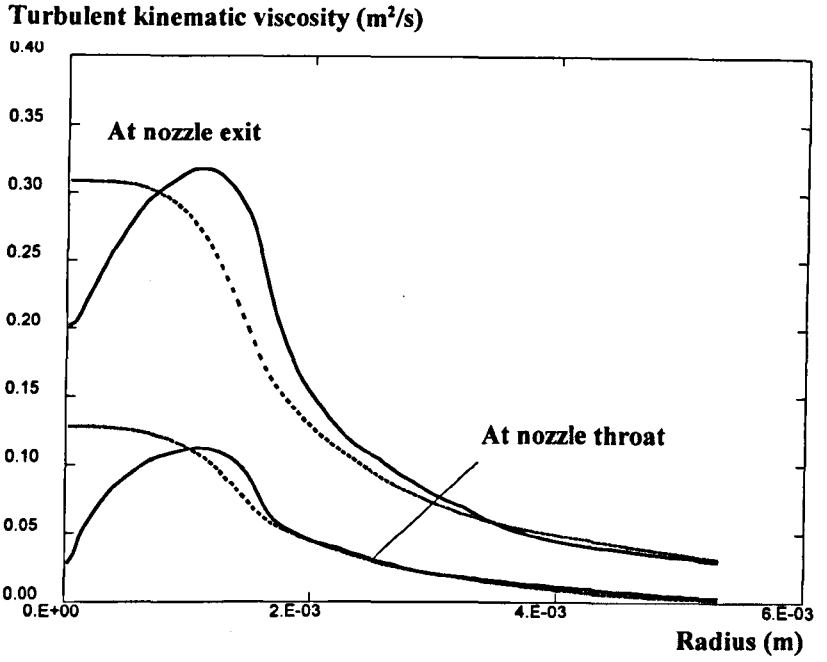

Figure 3.36 Radial distribution of turbulent kinematic viscosity of the 600A SF_6 arc. The upstream stagnation pressure is 9bar and exit pressure is 2.5bar. Solid lines: Prandtl mixing length model with $C_l = 0.20$; Broken lines: K-epsilon model with $C_{le} = 1.2$

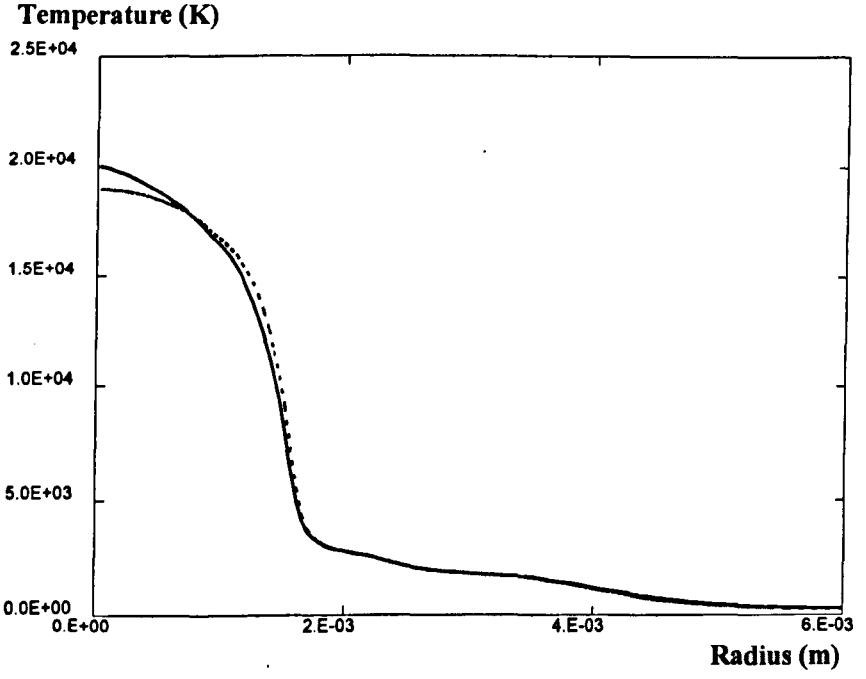

Figure 3.37 Radial temperature distribution of the 600A SF_6 arc at the nozzle throat. The upstream stagnation pressure is 9bar and exit pressure is 2.5bar. Solid line: Prandtl mixing length model with $C_l = 0.20$; Broken line: K-epsilon model with $C_{le} = 1.2$

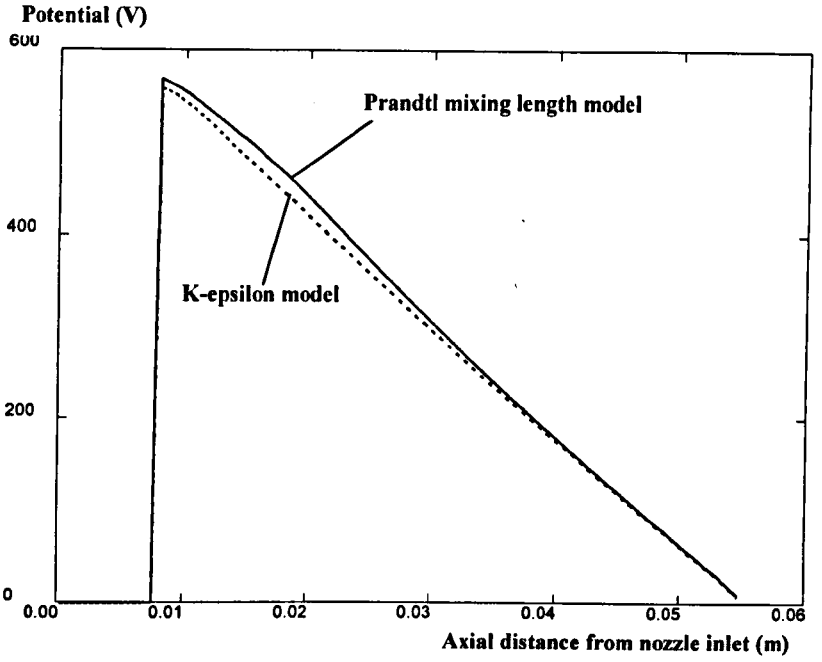

Figure 3.38 Predicted arc voltage of the 600A SF_6 arc. The upstream stagnation pressure is 9bar and exit pressure is 2.5bar. Solid line: Prandtl mixing length model with C_l = 0.20; Broken line: K-epsilon model with C_{le} = 1.2

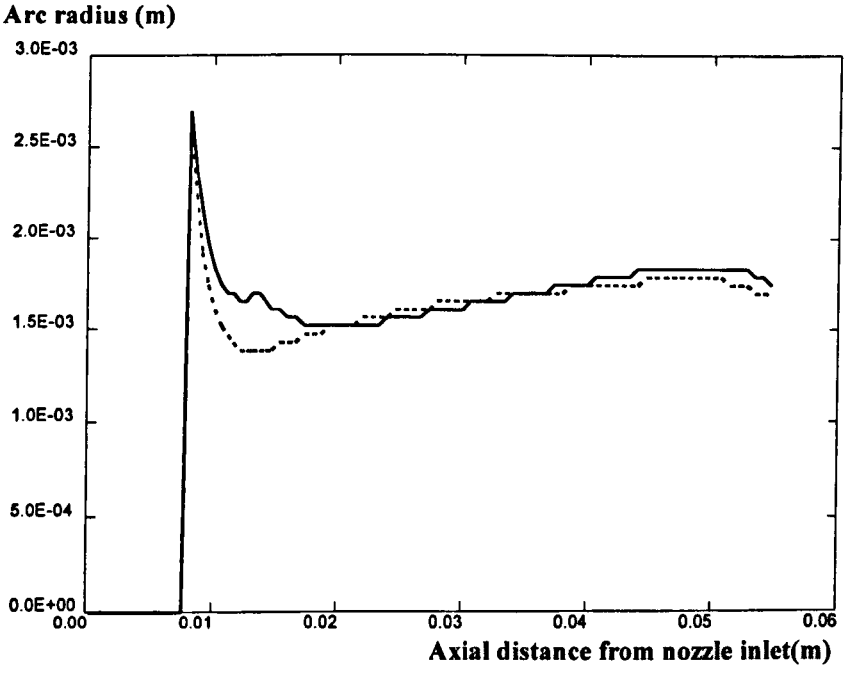

Figure 3.39 Radius of the 600A SF_6 arc. The upstream stagnation pressure is 9bar and exit pressure is 2.5bar. Solid line: Prandtl mixing length model with C_l = 0.20; Broken line: K-epsilon model with C_{le} = 1.2

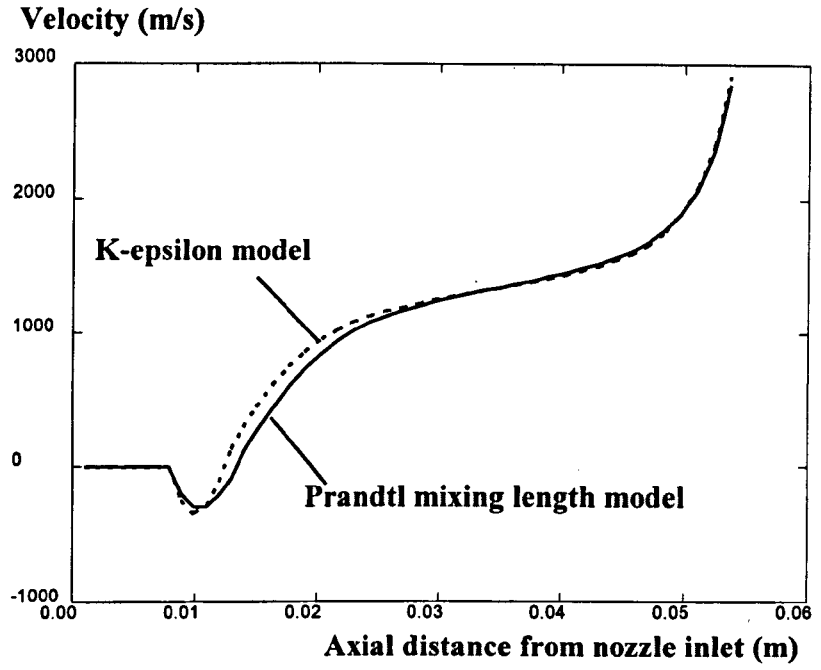

Figure 3.40 Axial velocity on axis of the 600A SF_6 arc. The upstream stagnation pressure is 9bar and exit pressure is 2.5bar. Solid line: Prandtl mixing length model with C_l = 0.20; Broken line: K-epsilon model with C_{le} = 1.2

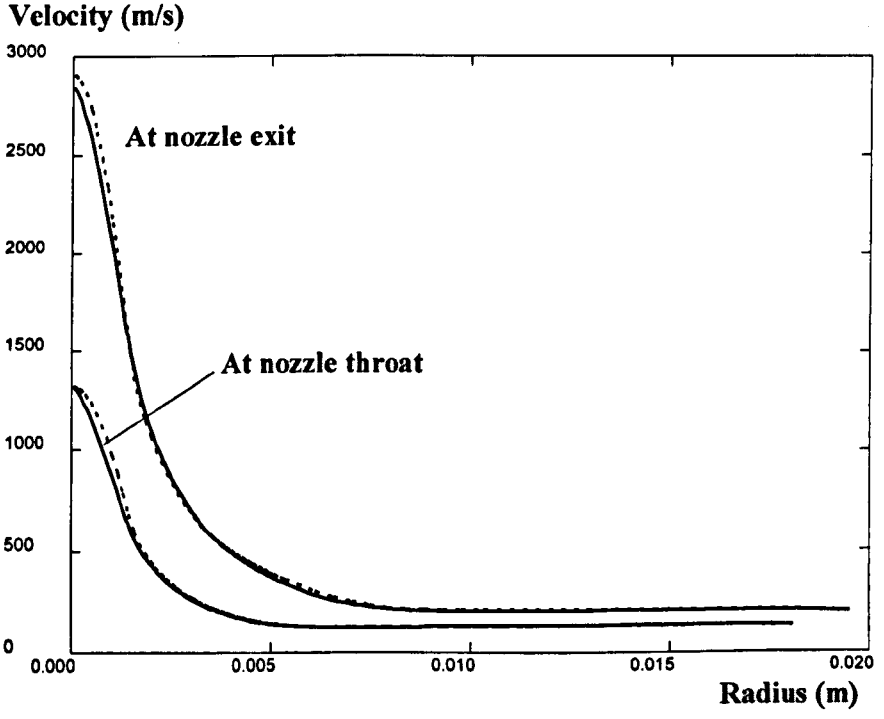

Figure 3.41 Radial distribution of the axial velocity for the 600A SF_6 arc. The upstream stagnation pressure is 9bar and exit pressure is 2.5bar. Solid lines: Prandtl mixing length model with C_l = 0.20; Broken lines: K-epsilon model with C_{le} = 1.2

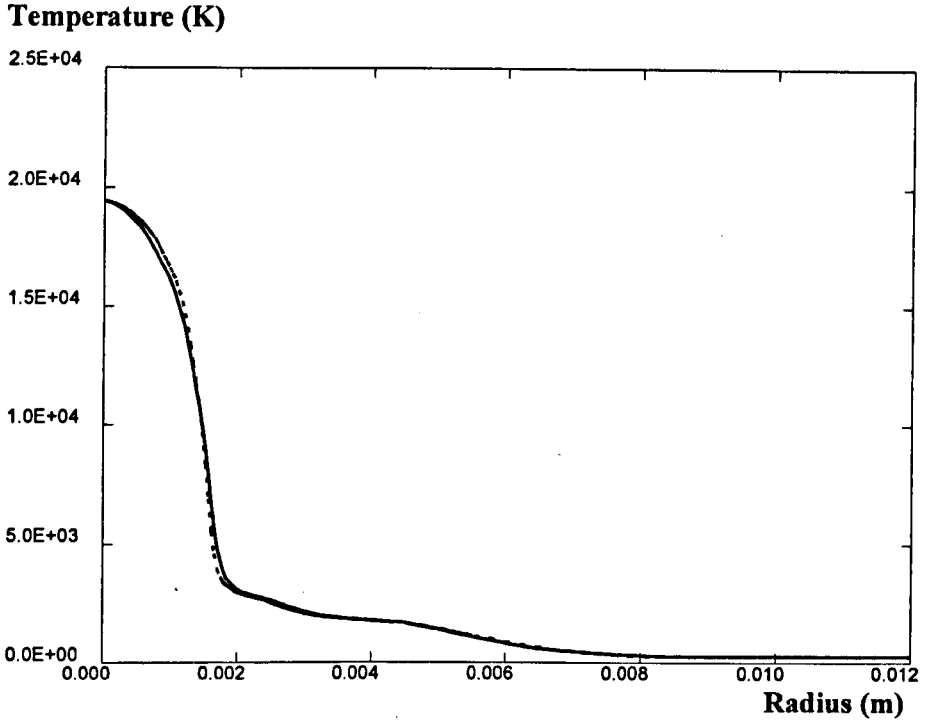

Figure 3.42 Radial temperature distribution of the 600A SF_6 arc at the nozzle exit. The upstream stagnation pressure is 9bar and exit pressure is 2.5bar. Solid line: Prandtl mixing length model with $C_l = 0.20$; Broken line: K-epsilon model with $C_{1\varepsilon} = 1.2$

3.9 Conclusions

A two dimensional differential model for arcs burning in self-generated flow is developed. The governing equations for the turbulent flow are written in their conservative form. Boundary conditions with nozzle ablation of the arcing chamber are specified in terms of source terms. Full closure of the governing equations requires a knowledge of the electric and magnetic fields in the flow domain, the calculation of which is discussed in Section 3.6. The effects of a moving contact is represented by volumetric mass sources in the cells adjacent to the moving surface of the contact. The model is implemented in PHOENICS version 2.0 and is applied to three specific cases in this chapter.

We studied the effect of the electromagnetic force on high current arcs burning in a supersonic nozzle. Results show that the pressure on the nozzle axis is most influenced by the $\vec{J} \times \vec{B}$ force which is induced by the arcing current. The predicted pressure difference on the axis with and without the $\vec{J} \times \vec{B}$ force included could reach 2bar for a 30kA arc in SF_6. Gas is

strongly accelerated at the upstream electrode. The arc voltage is not sensitive to the $\vec{J} \times \vec{B}$ force.

Shocks cannot be avoided during the operation of a circuit breaker. Results based on the differential model show that the presence of shock in the diverging section of a supersonic nozzle causes flow separation, and hence, broadens the arc column. The shock has a very complicated structure and the centre is moved slightly upstream towards the nozzle wall in the current range investigated (200A—1500A). The shock strength reduces when arcing current is increased. Compared with the shock free case, the arc voltage is reduced and the V-I characteristic has a minimum. Flow separation creates a very stagnant region which is expected to recover very slowly during the current zero period. It is therefore expected that the presence of shock will have adverse effects on the thermal as well as dielectric recovery capability.

Turbulence in flow is a very complicated phenomenon and so far there is no universal model. Most of the existing models are based on the concept of turbulent eddy viscosity and assume negligible density fluctuation. A comparative study carried out in Section 3.8.3 shows that both the Prandtl mixing length model and the two equation K-epsilon model tend to under-represent the turbulent energy exchange in a supersonic nozzle when the arcing current increases. One of the five parameters ($C_{1\varepsilon}$) in the K-epsilon model has to be adjusted in order to produce results comparable with the radial temperature measurement. The adjusted value of $C_{1\varepsilon}$ depends on current. However, for Prandtl mixing length model C_l is not current sensitive. For turbulent SF_6 arcs, consideration of the range of applicability of the turbulence parameters and the cost of computation have made the Prandtl mixing length model preferable to the K-epsilon model.

CHAPTER FOUR COMPUTER SIMULATION OF THE ARCING PROCESS IN AN AUTO-EXPANSION CIRCUIT BREAKER

4.1 Introduction

Auto-expansion circuit breakers are a new generation of high voltage switching device. An auto-expansion circuit breaker differs from a puffer circuit breaker in that the gas flow which is required to quench the arc at a natural current zero is generated by the presence of the arc itself in the arcing chamber. The flow at the initial stage of the arcing process is built up by the strong electromagnetic force near the contacts. Ablation is active in the high current phase which contributes to the pressure build-up in the storage volume. Thus, the effects of $\vec{J} \times \vec{B}$ force and the ablation of wall material by arc radiation must be accounted for.

The behaviour of an auto-expansion circuit breaker at current zero depends on the full history of the arcing process. It has been shown in Chapter Two that a simplified model for free burning arcs in a confined space can be used with reasonable accuracy to predict the pressure variation in an arcing chamber, if the volume of the arcing chamber is much larger than that of the arc column. However in a modern high voltage auto-expansion circuit breaker, the arc can be initiated in the auxiliary nozzle whose size is comparable with that of the arc column. Under such circumstances application of a simplified model will be rather limited and a two dimensional model in its full differential form is essential.

The arcing chamber in an auto-expansion circuit breaker usually has an axisymmetric structure and the flow inside it could be turbulent. The work in this chapter, which is based on the differential model developed in Chapter Three, simulates the whole arcing process in a 245kV auto-expansion circuit breaker under conditions corresponding to a short circuit test case. We first introduce the geometry and dimensions of the arcing chamber in Section 4.2 and the test conditions in Section 4.3. The grid system is given in Section 4.4 and the parameters in the differential model are set in Section 4.5. The results are presented in four successive sections which respectively describe the initiation of the auto-expansion arc (Section 4.6), the high current phase (Section 4.7), the pre-current zero period (Section 4.8), and the thermal recovery process (Section 4.9). Conclusions are given in Section 4.10.

4.2 Geometry of the Arcing Chamber

The work in this chapter only involves the arcing chamber of the auto-expansion circuit breaker. As mentioned in Chapter Three, the moving part in an auto-expansion circuit breaker is the hollow contact and nozzle assembly and it is very difficult computationally to model such a complex moving body. In our model we keep the hollow contact and nozzle assembly at rest and assume that the other contact (solid contact) is moving in an opposite direction at the same speed as the hollow contact. This approximation leads to an uncertainty in the flow field which is of the order of the speed of the moving contact. In addition, the time scale for the gas to fill in the space evacuated by the moving body is determined by the average speed of the thermal motion of the molecules of the arcing gas. The average speed of SF_6 molecules at room temperature is around 150m/s which is close to its sound speed. The speed of the moving contact is 6.5m/s, which is only 4% of the speed of the SF_6 molecules. The gas can quickly fill up the space left behind by the moving contact, and the transient nature of the arcing process will not be much affected by the above approximation on the relative movement between the two contacts. A schematic diagram of the arcing chamber is shown in Figure 4.1. The hollow contact and the nozzle are both connected to an exhaust volume which has a constant pressure. The exits of the hollow contact and the nozzle are indicated by the dual arrows in figure 4.1.

The nozzle and the flow guide are both made of PTFE. The material of the contact tips is 80% Tungsten and 20% copper. The effects of contact melting are not important in the case

investigated since the flow blows the metal vapour outside of the arcing chamber. The auxiliary PTFE nozzle has a same inner diameter as that of the hollow contact (figure 4.1).

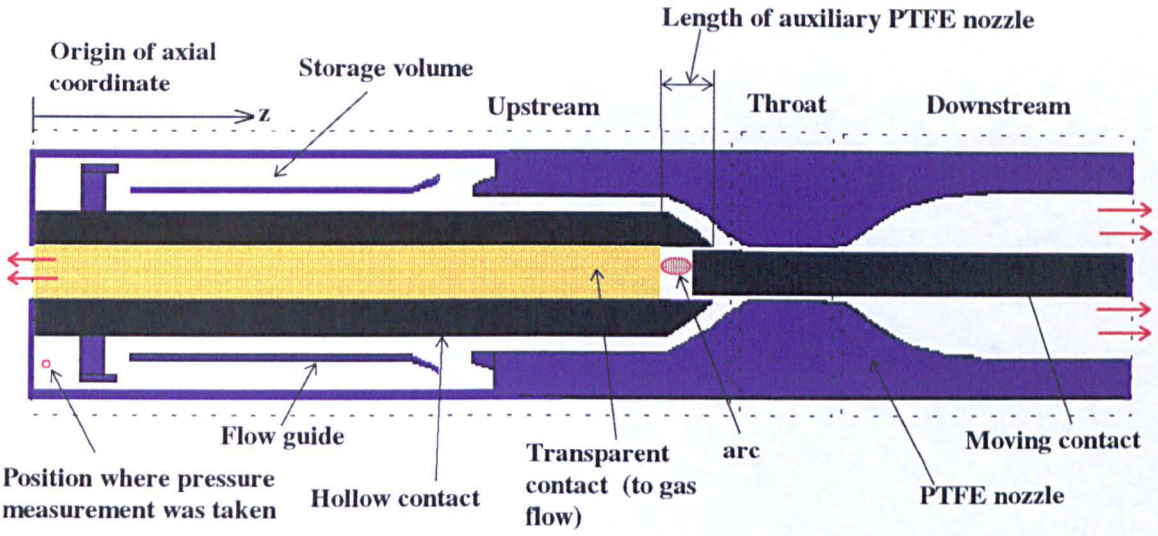

Figure 4.1 Geometry of the arcing chamber in a 245kV auto-expansion circuit breaker.

4.3 Test Conditions and Available Results

Results in this section were obtained by Reyrolle during short circuit tests. The filling pressure of SF_6 in the auto-expansion circuit breaker is 6.9bar absolute at room temperature. For the particular test case which is to be simulated, the peak current is 29.5kA in the first loop, 26.3kA in the second loop and 24.93kA in the final loop. The total arcing time is 23.40ms. The speed of the moving contact is 6.5m/s. The rate of change of the electric current immediately before the final current zero is -8.9A/μs. The pressure variation in the storage volume was measured at a position shown in figure 4.1 and the results are presented in figure 4.2. Thermal failure is recorded under a recovery voltage of 2kV/μs (in magnitude) for this particular case. The instantaneous current at contact separation is 27kA which is the value at time zero in figure 4.2. Meaningful test results are extremely difficult to obtain at The Reyrolle Short Circuit Test Station. The results given here are the only available results for the comparison with theory.

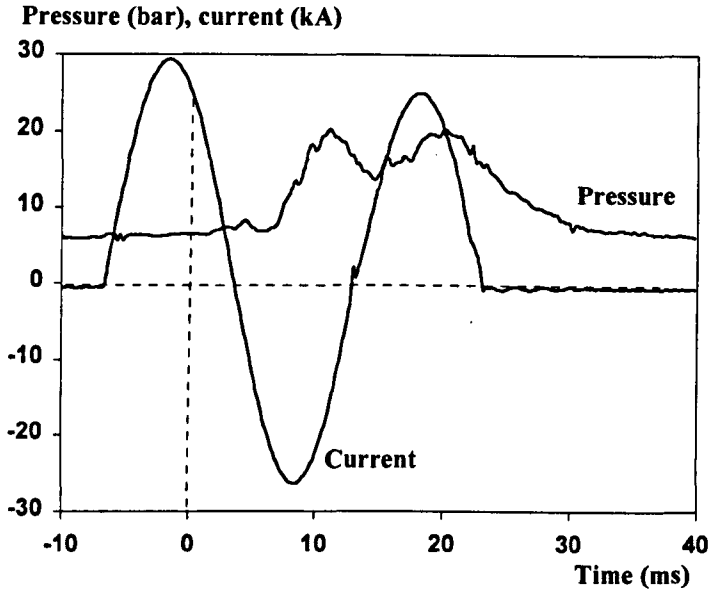

Figure 4.2 Short circuit current flowing from the hollow contact to the solid contact and the pressure measurement at a position indicated in figure 4.1. Results are obtained by Reyrolle during short circuit test. The time zero in this figure corresponds to the instant of contact separation in the short circuit test.

4.4 Grid System

Body fitted coordinate (BFC) grid system is used in order to model the complex geometry of the arcing chamber. Because of the large size of the CFD domain, a compromise has to be made between the total number of cells and computing cost. The general rule is that in the radial direction the grids are densely populated in the arc region and in the axial direction dense grids are used in regions where flow field undergoes rapid change. A typical BFC grid system for the arcing chamber is shown in figure 4.3. There are 120 cells in the axial direction and 70 cells in the radial direction in the high current phase. Orthogonal grids are employed in the solid contact region where there are 45 cells in the radial direction. Shortly before current zero when the current decreases to about 3.5kA, the total number of cells is increased to 149 in the axial direction and 145 in the radial direction. The number of cells in the first 2mm in the radial direction from the axis is increased from 30 in the high current phase to 75 at the current zero period.

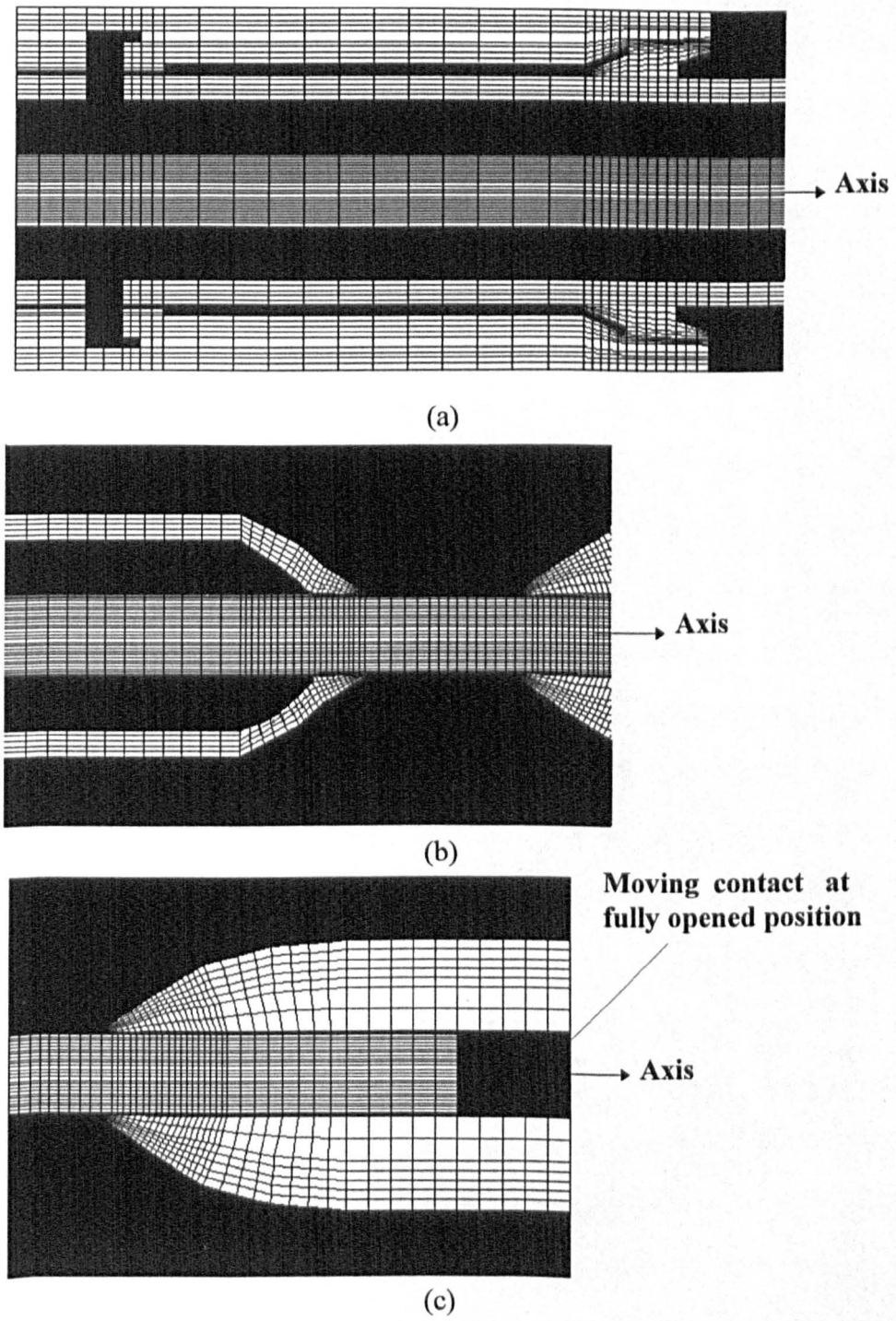

Figure 4.3 A typical BFC grid system for the arcing chamber in an auto-expansion circuit breaker. (a)—hollow contact and storage volume; (b)—nozzle throat ; (c)—downstream part of the nozzle.

4.5 Parameters in the Model

Adjustable parameters have to be introduced in the model despite the fact that we solve the flow equations in their full differential form. Radiation transfer inside the nozzle supplies the energy to ablate the PTFE material. Claessens et al [105] have shown that good agreement between predicted and measured pressure variation in the storage volume of a high voltage auto-expansion circuit breaker can be obtained by assuming that 50% of the electrical power input in the arc column is lost to the wall in radiation and is used to ablate the nozzle surface. For arcs in the high current phase Ohmic heating on the axis is approximately equal to the radiative energy loss. We assume that 50% of the net radiation emission from the arc centre is re-absorbed at the arc edge and the other 50% reaches the nozzle wall. Considering that a small amount of radiation may be lost to the surroundings, we further assume that 90% of the radiation which reaches the wall is capable of ablating PTFE to a vapour temperature of 3400K [102]. The total energy which is required to break the chain of PTFE molecules (depolymerisation energy) and to raise the PTFE vapour from room temperature to 3400K is 1.19×10^7 J/kg.

Prandtl mixing length model is used for the reason given in Section 3.8.3. Since there are no test results on the auto-expansion circuit breaker which can be used to calibrate the turbulence model, we set the parameter C_l in equation (3.15) to 0.2, which is obtained by fitting the measured radial temperature profile in a supersonic nozzle [45,138]. It must however be made clear that thermal recovery of a residual plasma after current zero in a circuit breaker heavily depends on turbulent cooling. At least one test result of the critical RRRV is required to calibrate the turbulence model for a particular nozzle geometry.

The electric field in the arcing chamber is calculated by solving equation (3.32) in a rectangular domain which is radially extended from the CFD domain. The potential on the solid contact is set at zero in our model although it is the live part in the short circuit test. To avoid confusion, the sign of the electric current given in this chapter is defined at the solid contact. A positive value means the arcing current is directed from the transparent contact to the solid contact. A circular spot is defined on the tip of the low-potential contact to simulate the cathode spot and its radius is calculated based on an average current density of $10^8 A/m^2$ [95]. The surface of the contact tip outside of this spot carries negligible current by assuming a local electrical conductivity of 10^{-3} $(\Omega\bullet m)^{-1}$. Figure 4.4 shows the case when the moving

solid contact is the low potential contact with R_c being the radius of the cathode spot based on a uniform current density of $10^8 A/m^2$.

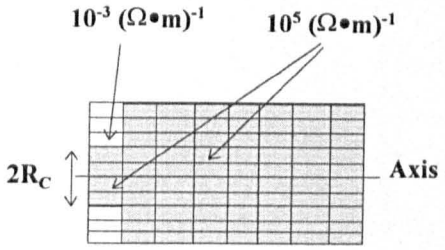

Figure 4.4 Simulation of the effect of cathode spot on electric current restriction on the contact surface. R_c is the radius of the cathode spot based on a uniform current density of $10^8 A/m^2$.

4.6 Arc Initiation

Arc initiation by contact separation is a very complicated non-equilibrium process. The mechanisms involved are beyond the scope of the present work. We have to start the arc in an artificial manner. Further more, the instantaneous current at contact separation could be very high (e.g. 27kA in the case under simulation). It is not possible to simulate the gas breakdown and the subsequent development to arc. We assume that the initial state is that of a low current free burning arc in a small gap between the two contacts. The current is then ramped up to the required value in a very short time. The low current initial arc has very little influence on the subsequent development of the arc and the flow in the circuit breaker.

The arc column is assumed to be axisymmetric. Since the arc is initiated in the hollow contact, a transparent contact (to gas flow) must be placed in the hollow contact so that the arcing current can be collected from the arc column (figure 4.1). There is no Ohmic heating in the transparent contact region. Radiation transfer at the arc root is complicated by the presence of the moving solid contact. We assume that there is no radiation re-absorption at the arc edge in the two slabs parallel to the radial direction which are adjacent to the moving surface of the solid contact.

For the case under investigation, we start the free burning arc at 2kA and ramp it up to 26.32kA in 0.2ms (figure 4.5). The contact separation at time zero is simply given a value of

8mm which is much smaller than the contact separation of 150mm when the circuit breaker is at its fully opened position.

Since we use a constant speed of 6.5m/s for the solid contact, its stroke is linearly proportional to time. The contact separation at time zero is 8mm. The positions of the tip of the solid contact at seven instants is shown in figure 4.6. Results at the seven instants will be given in the following sections. The initial radial temperature distribution in the arc column is

$$T(r) = T_0 - \frac{T_0 - 300}{R_0} r \qquad (4.1)$$

where T_0 is the axis temperature and R_0 is the radius of the hot column at time zero. For an initial current of 2kA, T_0 is assumed to be 20000K and R_0 to be 5mm. The solid contact acts as the cathode for the initial free burning arc. There is no axial variation in the initial temperature field. The relative position of the initial hot column in the arcing chamber is shown in figure 4.7.

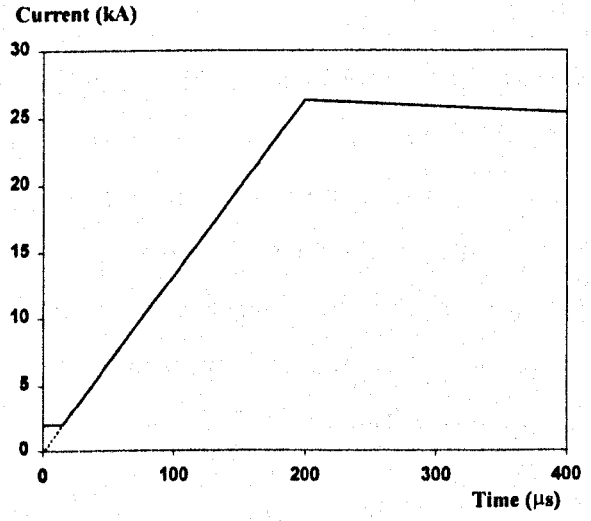

Figure 4.5 The electric current waveform used for arc initiation in the arcing chamber. The current remains constant at 2kA for the first 15μs and is then ramped up to 26.32kA in 175μs.

Once the transient process is initiated, Ohmic heat and radiation transfer inside the arc column lead to the rapid build-up of a strong heat source. The flow field then experiences violent disturbance due to the high compressibility of the arcing gas (SF_6). The temperature and flow field at 7.1μs and 2kA is shown in figure 4.8. Flow at the arc centre is built up by the electromagnetic force of the arcing current. On the other hand, flow at the arc edge is dominated by gas expansion which is caused by radiation re-absorption in this layer. When

the arcing current is ramped up to 12.78kA in 97μs, the hot column has been extended towards the exit of the hollow contact by 5mm (figure 4.9). Ablation of the auxiliary PTFE nozzle in the hollow contact has created a high pressure region near its inner surface (figure 4.10) where the temperature of the gas is elevated to over 3000K (figure 4.11). Interaction between the mobile arc column and the stagnant cold gas results in a circulation region as shown in figure 4.8. This circulation region dies out when the hot column continues to extend towards the exit of the hollow contact(figures 4.12 and 4.13). Referring to the axial distribution of pressure, axial velocity and Mach number on the axis as shown in figures 4.14, 4.15, and 4.16, it appears that shock waves have been formed in front of the hot column and propagate into the low pressure region. The average speed at which the shock travels is 190m/s at 200μs and 375m/s at 280μs. It is greater than the sound speed of SF_6 at 300K. Figure 4.17 shows the temperature field at 280μs which is 80μs after the arcing current has reached its maximum. The hot patch due to ablation of PTFE has extended into the inlet of the storage volume (figure 4.17) .

It can be seen from figures 4.13 and 4.17 that the temperature at the arc root is very high and reaches 33000k. There are two reasons: the first is that we neglected the radiation re-absorption at the arc edge in a region very close to the tip of the solid contact, which results in a smaller arc radius. The temperature of the arc root has thus to be increased to maintain the necessary electrical conductance. The second reason is that the flow in the cold gas which surrounds the arc root is directed towards the arc column as a result of nozzle ablation (figure 4.18). This radially inwards flow cools and constrains the arc root.

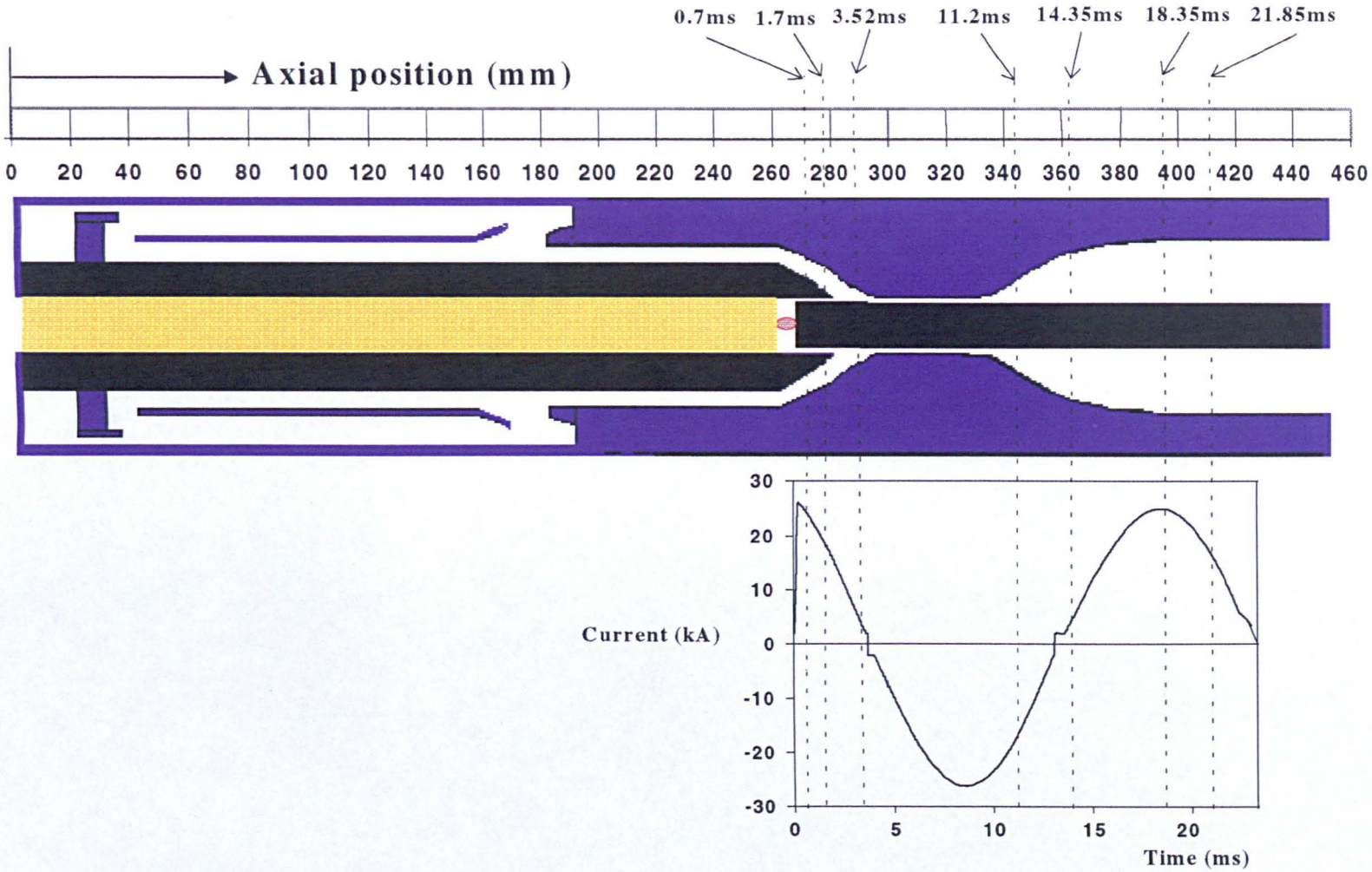

Figure 4.6 The arcing current and the position of the tip of the moving solid contact as a function of time. The vertical dotted lines indicate the position of the tip of the moving contact at various instants. Total arcing time is 23ms.

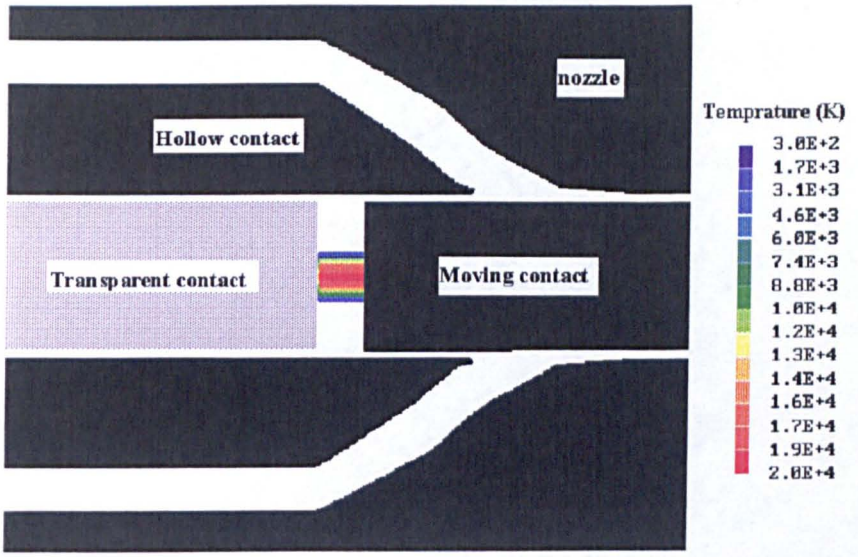

Figure 4.7 The axially isothermal hot column for arc initiation at 2kA in the arcing chamber.

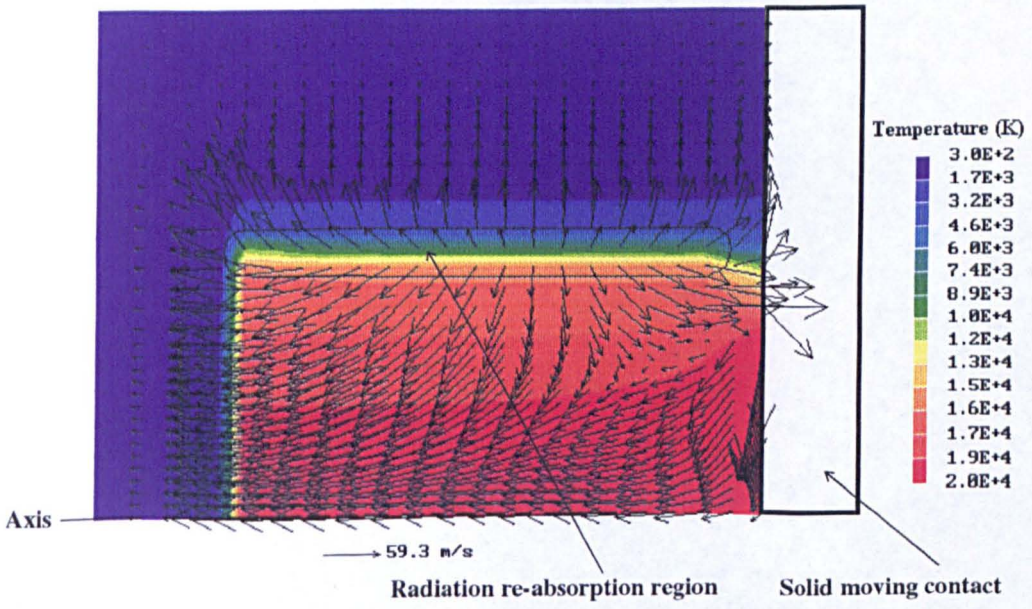

Figure 4.8 Temperature field and velocity vector at an instant of 7.1μs. Arcing current is 2kA. The oval circle indicates the radiation re-absorption region at the arc edge. See figure 4.6 for the position of the solid contact and current waveform.

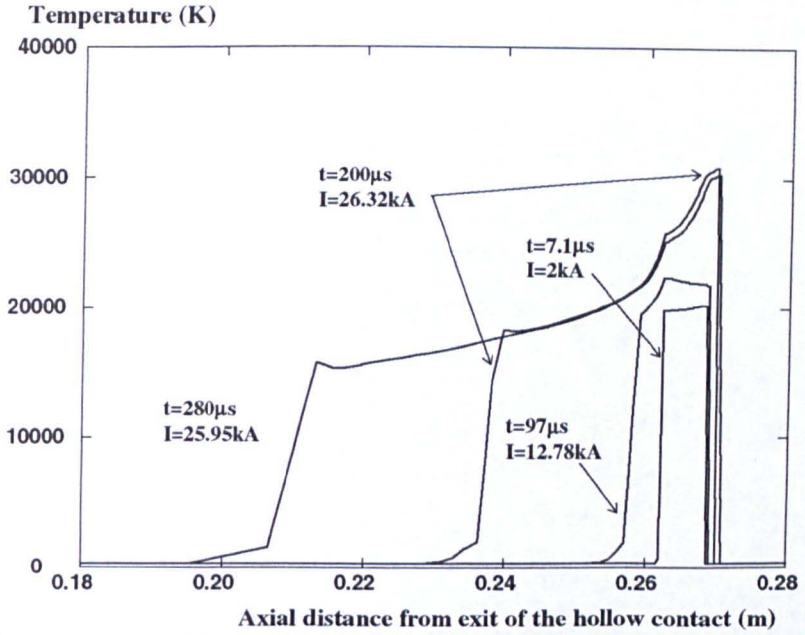

Figure 4.9 Axis temperature distribution at four instants when the arcing current is ramped up in the initial stage of the arcing process. See figure 4.6 for the position of the solid contact and current waveform.

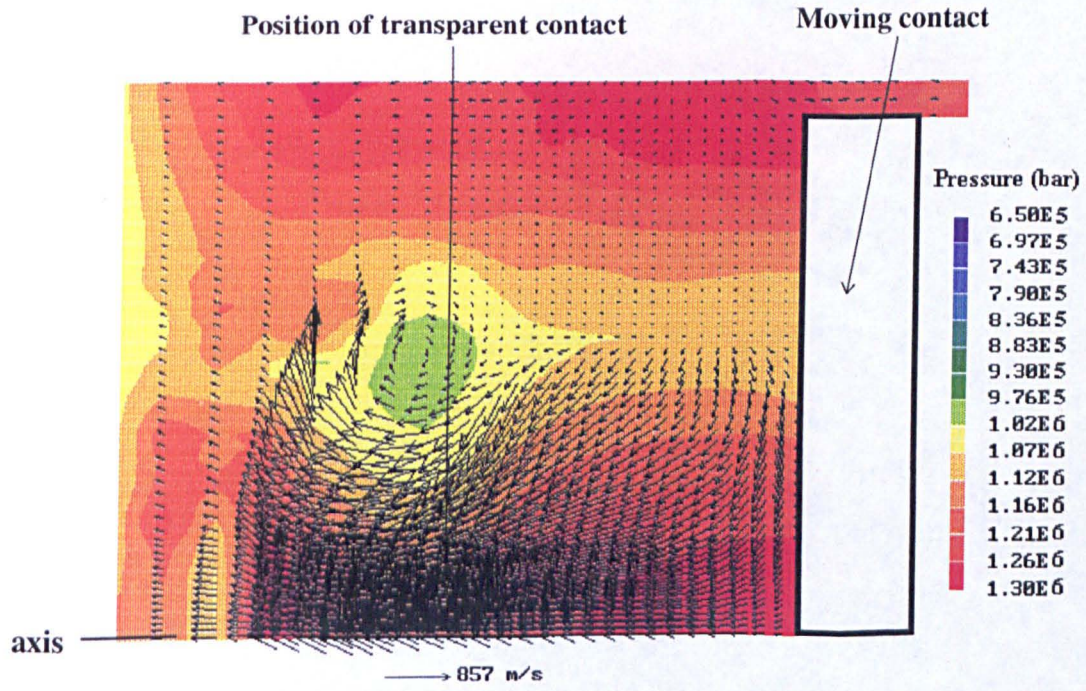

Figure 4.10 Pressure and velocity field at 97μs with arcing current of 12.78kA. See figure 4.6 for the position of the solid contact and current waveform.

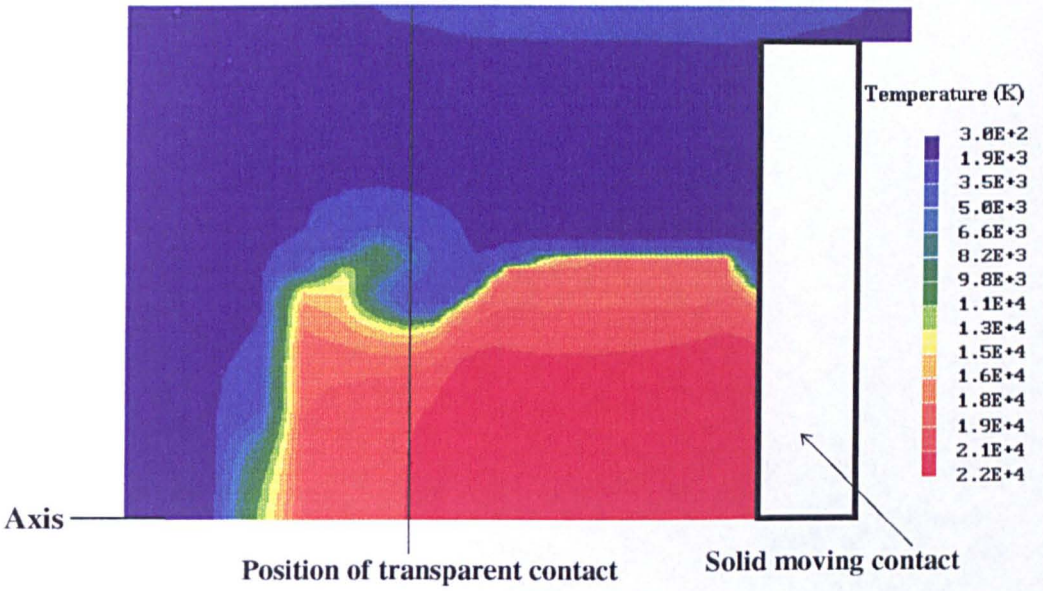

Figure 4.11 Temperature field of the free burning arc at 97μs with arcing current of 12.78kA. See figure 4.6 for the position of the solid contact and current waveform.

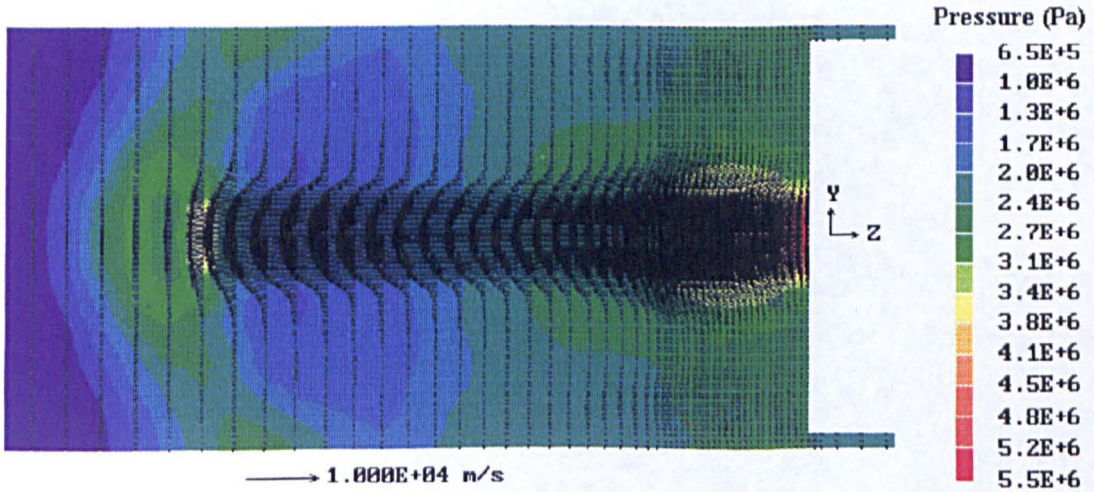

Figure 4.12 Pressure and velocity field at 200μs with arcing current of 26.32kA. See figure 4.6 for the position of the solid contact and current waveform.

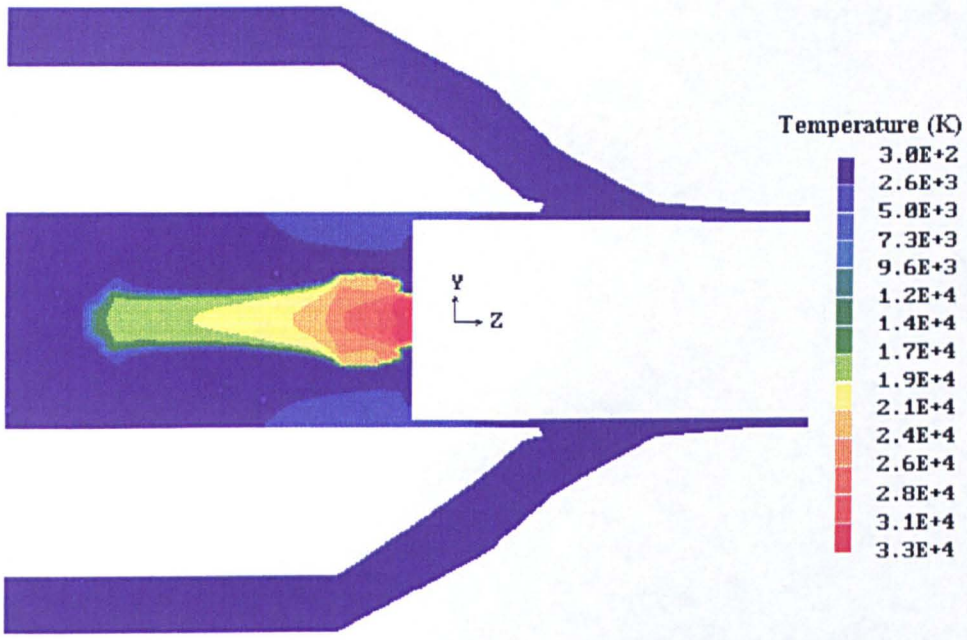

Figure 4.13 Temperature field at 200μs with arcing current of 26.32kA. See figure 4.6 for the position of the solid contact and current waveform.

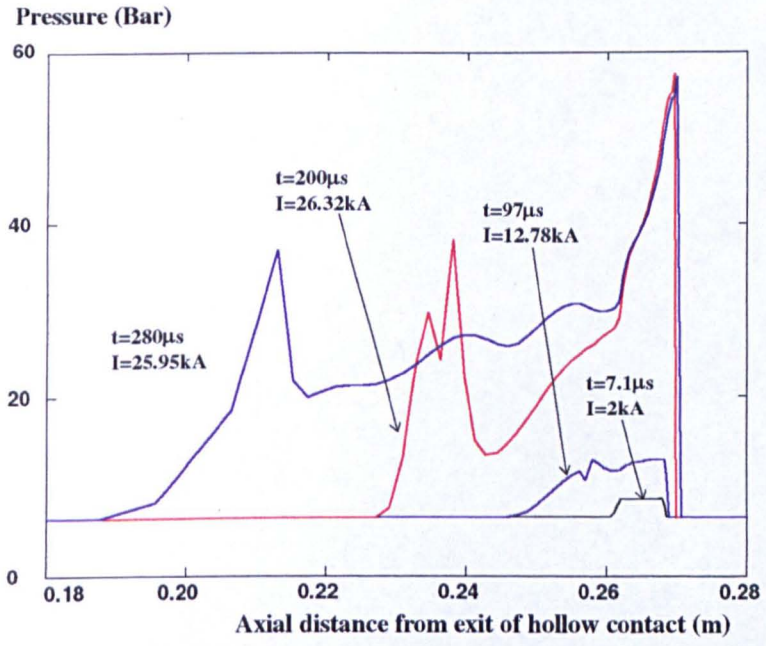

Figure 4.14 Axis pressure distribution at four instants when the arcing current is ramped up in the initial stage of the arcing process. See figure 4.6 for the position of the solid contact and current waveform.

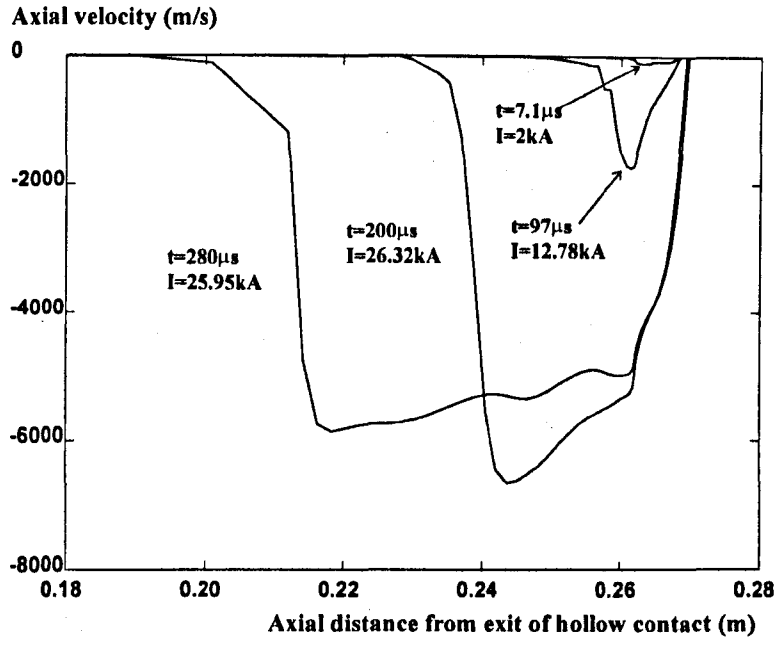

Figure 4.15 Axial velocity on axis at four instants when the arcing current is ramped up in the initial stage of the arcing process. See figure 4.6 for the position of the solid contact and current waveform.

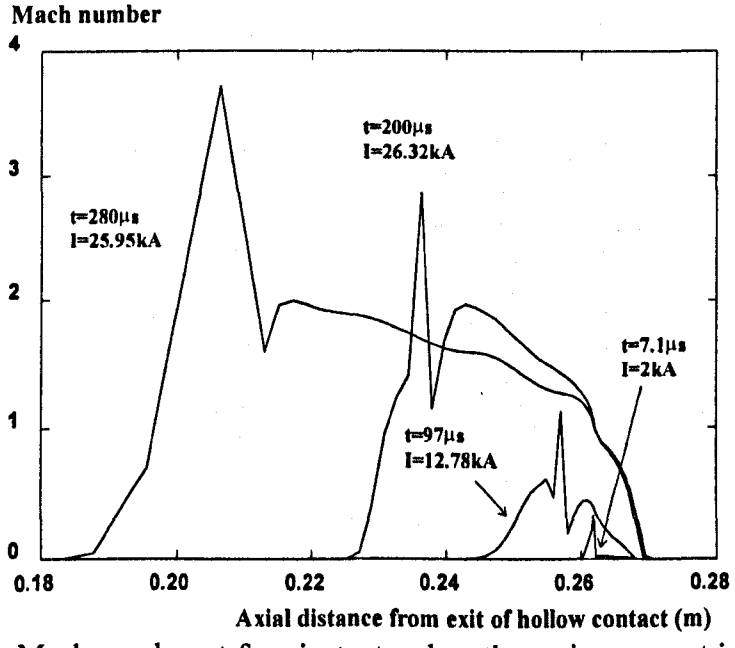

Figure 4.16 Axis Mach number at four instants when the arcing current is ramped up in the initial stage of the arcing process. The Mach number of SF_6 at pressure above 16bar is obtained by linear extrapolation of those at 8bar and 16bar at the same temperature. See figure 4.6 for the position of the solid contact and current waveform.

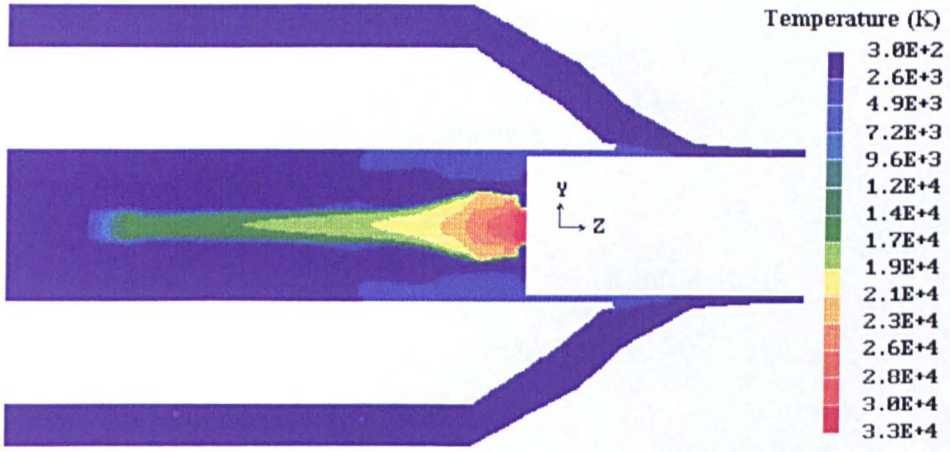

Figure 4.17 Temperature field at 280μs with arcing current of 25.95kA. See figure 4.6 for the position of the solid contact and current waveform.

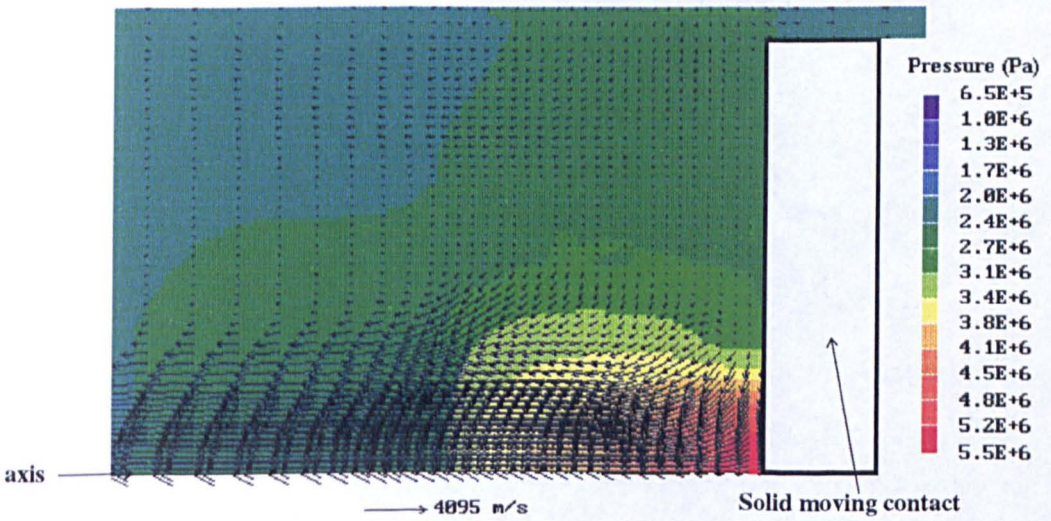

Figure 4.18 Pressure and velocity field at 200μs with arcing current of 26.32kA. See figure 4.6 for the position of the solid contact and current waveform.

4.7 The High Current Phase

The high current phase in this particular case starts at 0.2ms when the arcing current has been ramped up from 2kA to 26.32kA (figure 4.19). It ends at 23ms when the arcing current falls to 3.439kA. During this period, arc heating and ablation of the nozzle material force hot gas to flow into the storage volume where the cold gas is compressed by, and mixed with the incoming hot gas and a high pressure reservoir is gradually set up. There are two intermediate current zeros in the high current phase. The magnitude of the arcing current around these current zeros is held at 2kA in order to prevent the arc from extinction in the axial flow. This is to simulate the experimental situation, where arc extinction usually occurs at the third current zero and to reduce the computational time. For the case we are investigating, it would be convenient to clarify the high current phase in terms of two sub-periods which are characterised by the position of the solid contact. The first sub-period is between 0.2ms to 4ms (labelled SP_1 in figure 4.19). The arc is burning outside of the nozzle and the arcing current decreases from 26.32kA to -2kA (figure 4.19). The second sub-period refers to the rest of the high current phase.

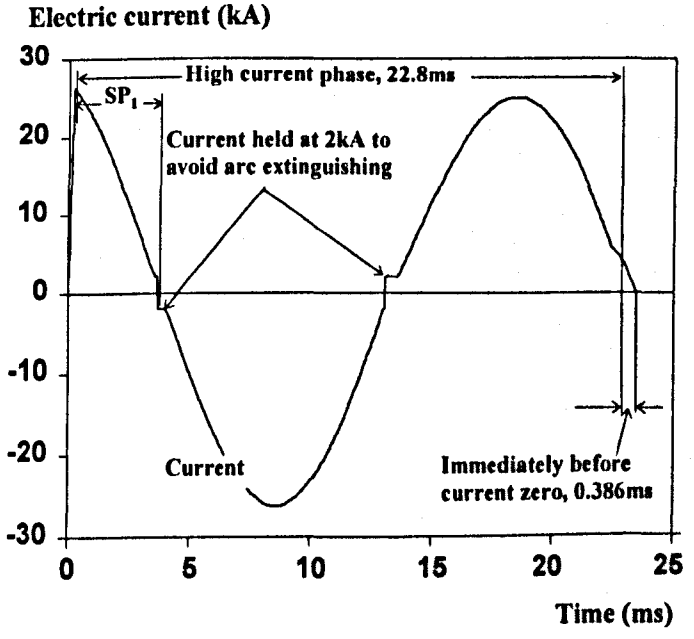

Figure 4.19 Current waveform for the high current phase. It starts from 0.2ms with arcing current of 26.32kA and ends at 23ms when the arcing current falls to 3.439kA. The period immediately before current zero is also shown.

4.7.1 Arc burning outside of the nozzle throat

The hot gas column reaches the exit of the hollow contact in less than 0.7ms from the initiation of the arc (figure 4.20). At this stage there are no longer shock waves in the hollow contact and the axis pressure has become smooth (figure 4.21). The extreme high pressure at the arc root is due to the electromagnetic pinch effect of the arcing current. When the solid contact withdraws further towards the nozzle throat, increasing gas leakage through the gap between the solid and hollow contacts reverses the flow in front of the solid contact (figure 4.22) and the arc root spreads over the whole surface of the tip of the solid contact due to convective effect (figure 4.23). The temperature at the arc root is reduced from 32000K at 0.7ms to 19000K at 1.7ms and the pressure at the arc root is also reduced from 65bar to 22bar (figure 4.21).

The arcing current is rapidly decreasing when the solid contact moves out of the hollow contact. Contraction of the hot column in the hollow contact and the outgoing flow contribute to the rapid drop of pressure in the hollow contact. The arcing current at 3.52ms is 2.65kA. The axis pressure in the hollow contact has decreased to the exit pressure or become even lower at 3.52ms, as shown in figure 4.21. Flow from the storage volume which is at a relatively higher pressure brings cold gas into the hollow contact (figure 4.24) and forms a low temperature layer between the arc column and the inner surface of the hollow contact (figure 4.25).

Flow field has experienced rapid change in this sub-period due to the evacuation of the hollow contact by the solid contact. Pressure rise in the storage volume is small in this sub-period since the bore of the hollow contact has been blocked by the solid contact for arcing current above 15kA (See figure 4.6 for current waveform).

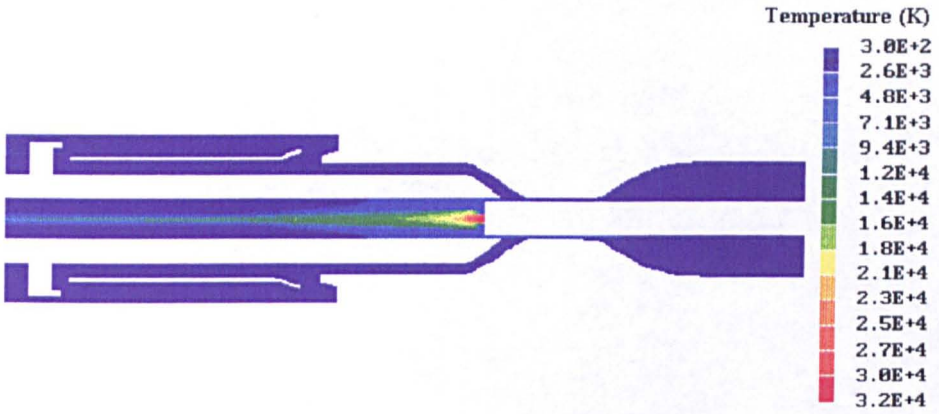

Figure 4.20 Temperature field at 0.7ms with arcing current of 24kA. The solid contact is cathode. See figure 4.6 for the position of the solid contact and current waveform.

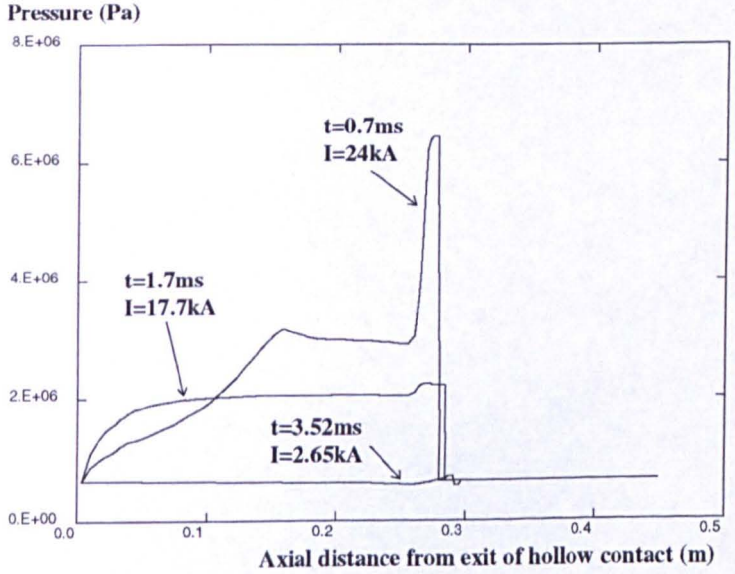

Figure 4.21 Axis pressure at three instants when the solid contact withdraws out of the hollow contact. See figure 4.6 for the position of the solid contact and current waveform.

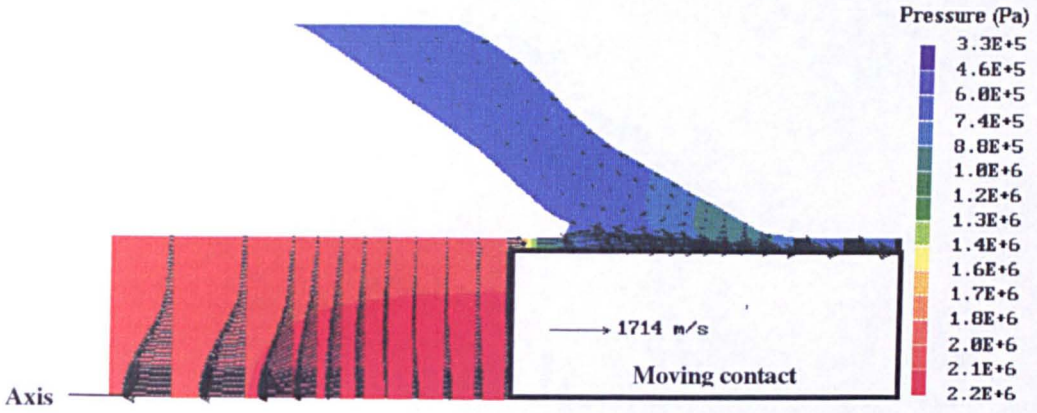

Figure 4.22 Flow field at 1.7ms with arcing current of 17.7kA. See figure 4.6 for the position of the solid contact and current waveform.

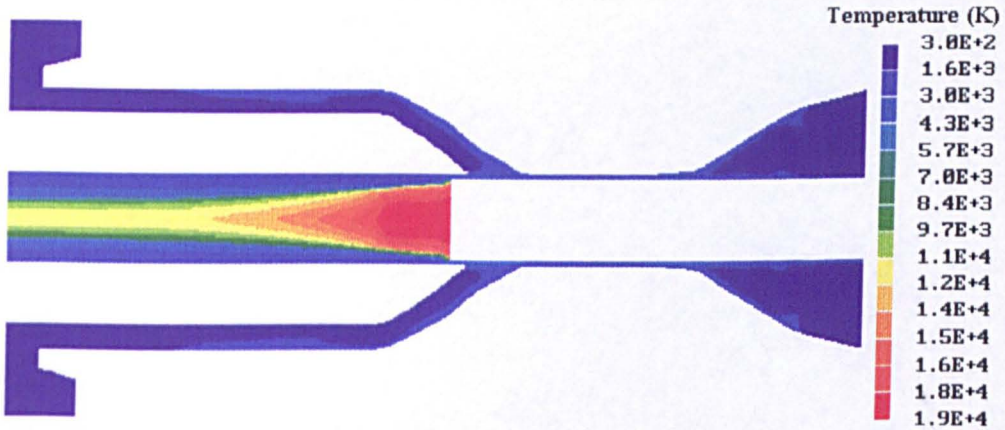

Figure 4.23 Temperature field at 1.7ms with arcing current of 17.7kA. The arc root has spread over the whole surface of the solid contact due to gas expansion towards the nozzle throat. The solid contact is cathode. See figure 4.6 for the position of the solid contact and current waveform.

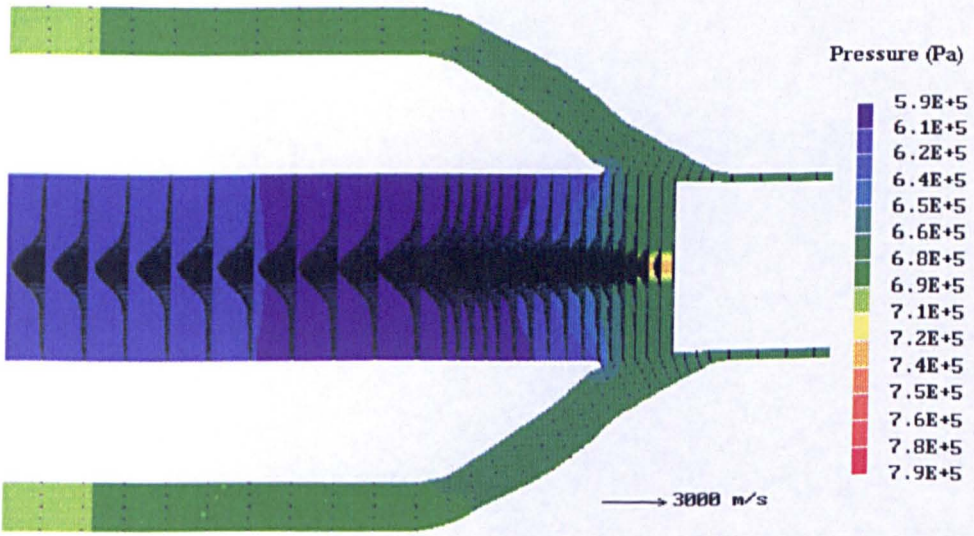

Figure 4.24 Pressure and vector field at 3.52ms with arcing current of 2.65kA. See figure 4.6 for the position of the solid contact and current waveform.

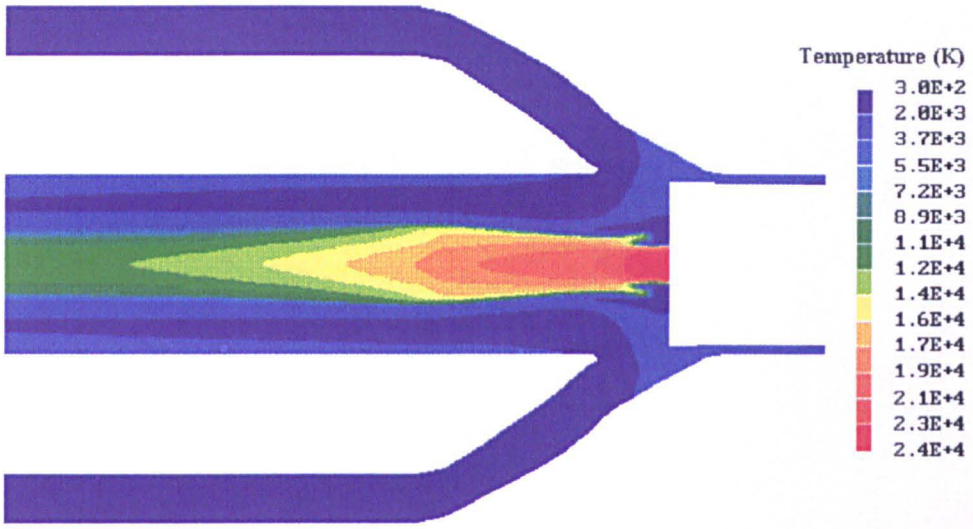

Figure 4.25 Temperature field at 3.52ms with arcing current of 2.65kA. The cold layer between the arc column and the inner surface of the hollow contact is formed by the gas flow from the storage volume which is at a higher pressure but lower temperature. The solid contact is cathode. See figure 4.6 for the position of the solid contact and current waveform.

4.7.2 Arc burning in the nozzle throat

When the solid contact withdraws into the nozzle throat (figure 4.26), ablation of PTFE by radiation from the arc causes the hot gas to flow towards the storage volume and the hollow contact (figure 4.27). Arc in the nozzle throat is burning in pure PTFE vapour. The axis temperature and pressure are respectively shown in figure 4.28 and figure 4.29 for three instants when the solid contact withdraws into the nozzle throat. The three instants correspond respectively to the position of the tip of the solid contact at the upstream end of the nozzle throat (3.72ms), at the middle of the nozzle throat (7ms) and close to the downstream end of the nozzle throat (9.5ms). The relative position of the solid contact and the current waveform can be found in figure 4.6. The difference in temperature in front of the tip of the solid contact is caused by the arcing current and the flow field in front of the contact. When the arc is burning outside of the nozzle throat (3.72ms), the current is low (-2kA) and the flow in front of the solid contact is not strong, which result in an axis temperature of 20000k. The solid contact has become anode at these instants. When the tip of the solid contact is at the middle of the nozzle throat (7ms), strong radially inwards flow of PTFE vapour cools the high current arc (-22.67kA) and produces a temperature of 25000K in the arc root. However, when the tip of the solid contact moves near the downstream end of the nozzle throat, more PTFE vapour leaves the nozzle throat through the gap between the contact and the nozzle. Arc cooling in

front of the solid contact by radially inflow of PTFE vapour becomes less efficient and the arc column extends towards the nozzle surface. This results in a decreasing temperature in the arc root, which is 19000K at 9.5ms. The high pressure in the nozzle throat (figure 4.29) drives hot gas to flow towards the storage volume. The hot gas with a temperature of about 3500K has reached the flow guide with a speed of 500V/s (figures 4.30 and 4.31) at 7ms. The incoming hot gas rapidly raises the pressure inside the storage volume (figure 4.32).

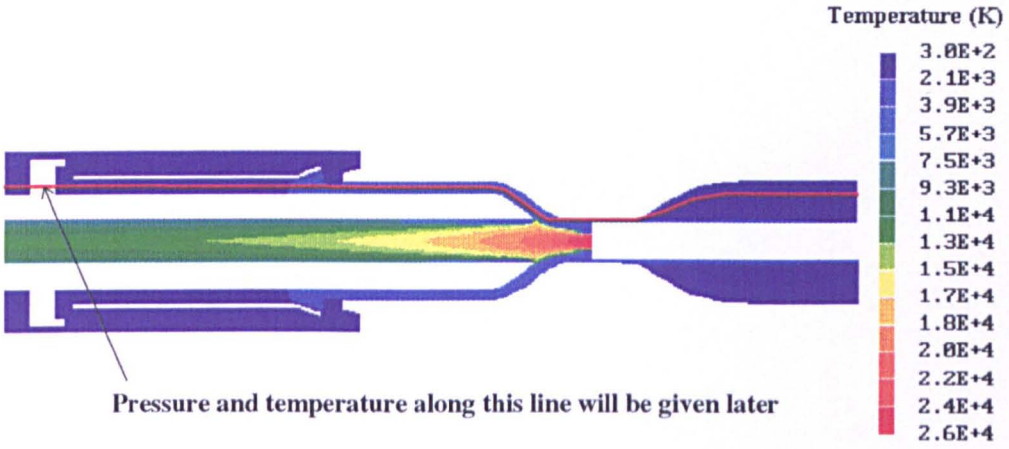

Figure 4.26 Temperature field at 7ms with arcing current of -22.67kA.

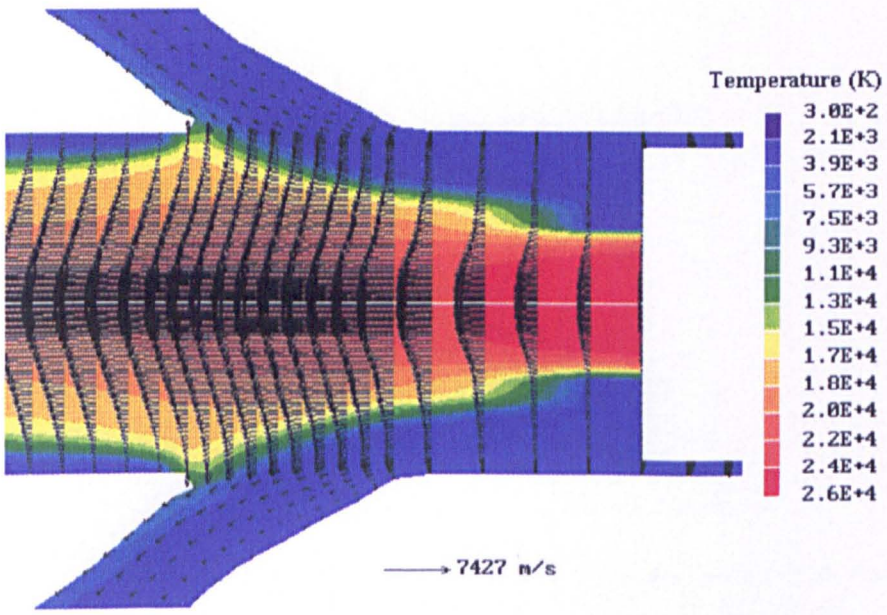

Figure 4.27 Temperature and velocity vector field at 7ms with arcing current of -22.67kA.

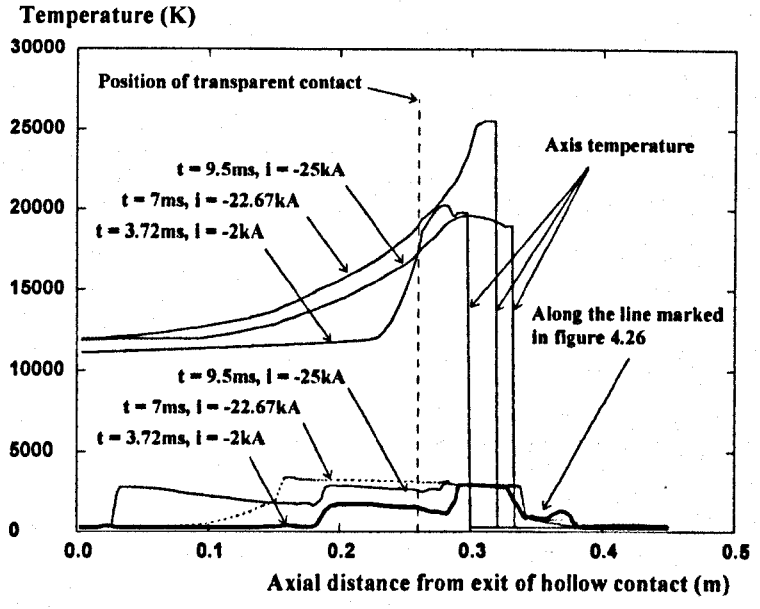

Figure 4.28 Temperature on the axis and along the red line marked in figure 4.26 at three instants when the solid contact withdraws into the nozzle throat. See figure 4.6 for the position of the solid contact and current waveform.

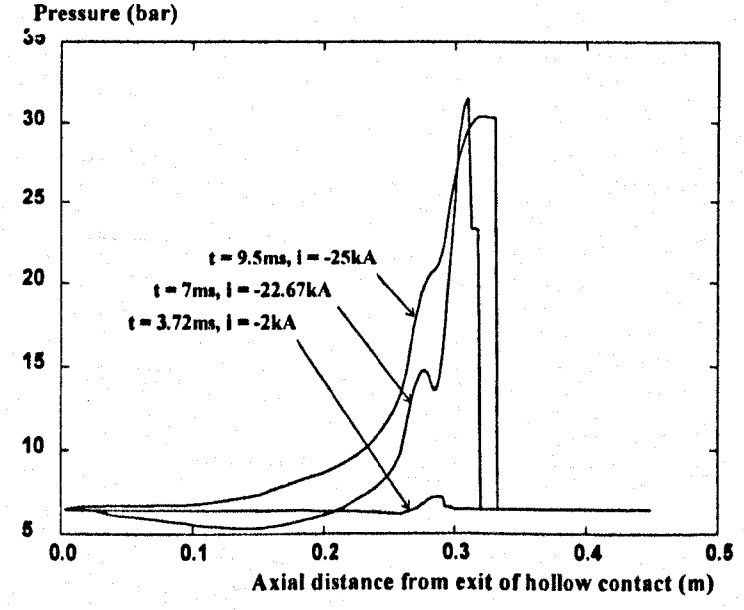

Figure 4.29 Axis pressure at three instants when the solid contact withdraws into the nozzle throat. See figure 4.6 for the position of the solid contact and current waveform.

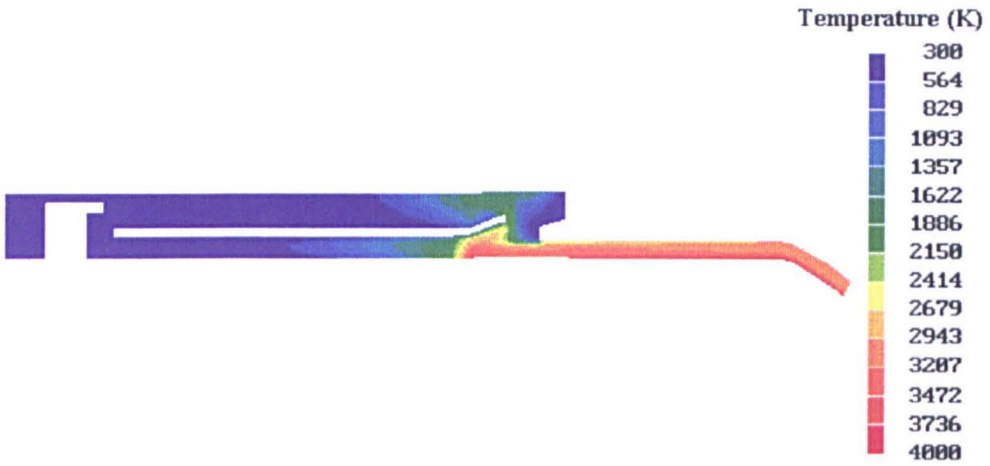

Figure 4.30 Temperature field in the storage volume at 7ms with arcing current of -22.67kA.

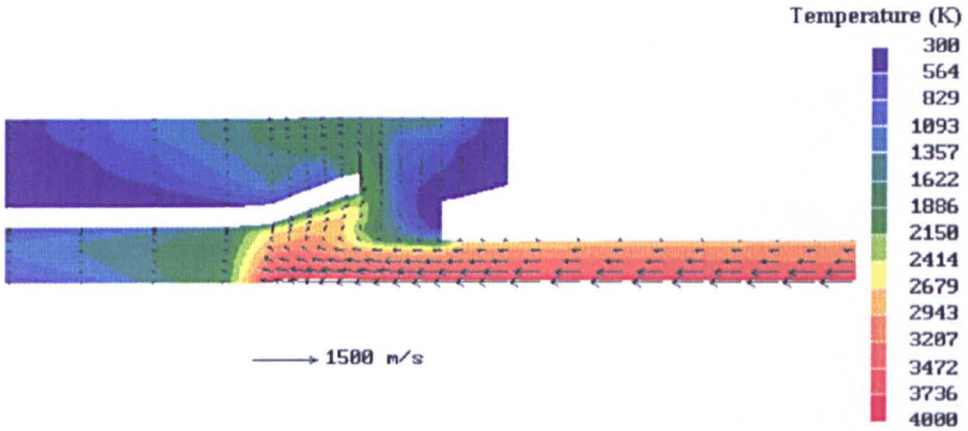

Figure 4.31 Velocity vector at 7ms when hot gas is driven into the storage volume by the high pressure in the nozzle throat.

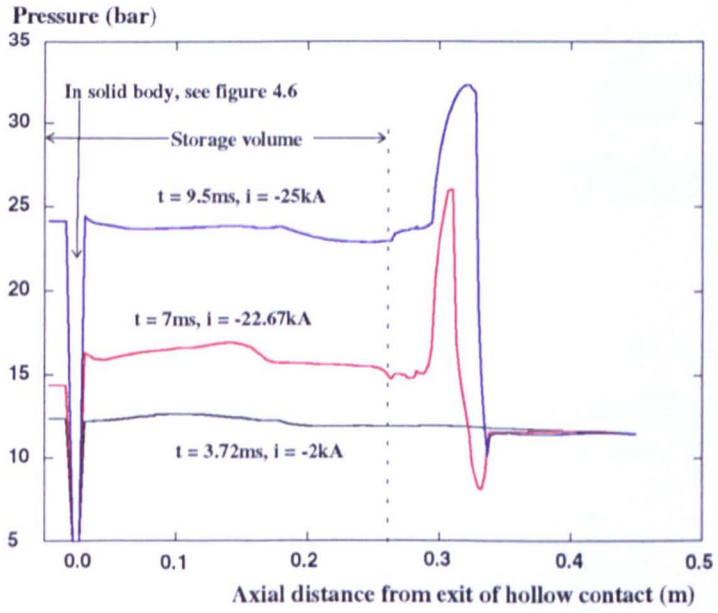

Figure 4.32 Pressure distribution along the line marked in figure 4.26. See figure 4.6 for the position of the solid contact and current waveform.

Pressure inside the storage volume is rather uniform and remains around 20bar by the time when the solid contact is clearing the nozzle throat (figure 4.33). The temperature field at 11.2ms is shown in figure 4.34 where hot gas is ejected out of the nozzle throat by the high pressure gradient at the downstream end of the nozzle throat. The arcing current is -16.75kA which is on the positive slope of the second loop in figure 4.6. The velocity vector and temperature field in figure 4.35 show that the hot gas coming from the arc column mixes with the cold gas while circulating around the flow guide. Only a cold patch is left on the outer side of the flow guide. Radial profiles of the temperature and axial velocity at three axial positions are given in figure 4.36 and figure 4.37 respectively. In the hollow contact, gas is accelerated by the axial pressure gradient (figure 4.38) and the flow on the axis attains supersonic velocity (figure 4.39). Flow in the nozzle throat is subsonic at 11.2ms since the solid contact is still partly blocking the flow at the exit of the nozzle throat (figure 4.38). The Mach number is 0.5 at z = 324mm (figure 4.39).

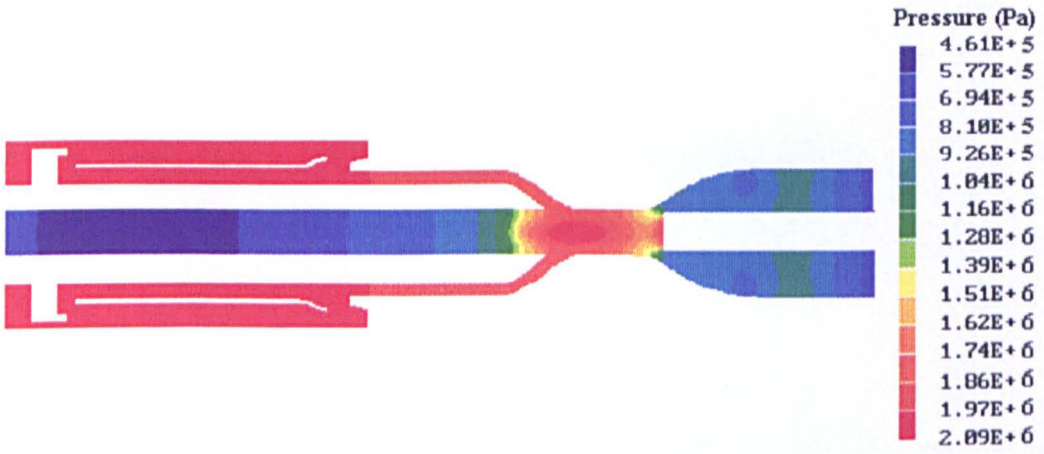

Figure 4.33 Pressure field at 11.2ms with arcing current of -16.75kA. The solid contact has just vacated the nozzle throat and hot gas are ejected from the throat. See figure 4.6 for the position of the solid contact and current waveform.

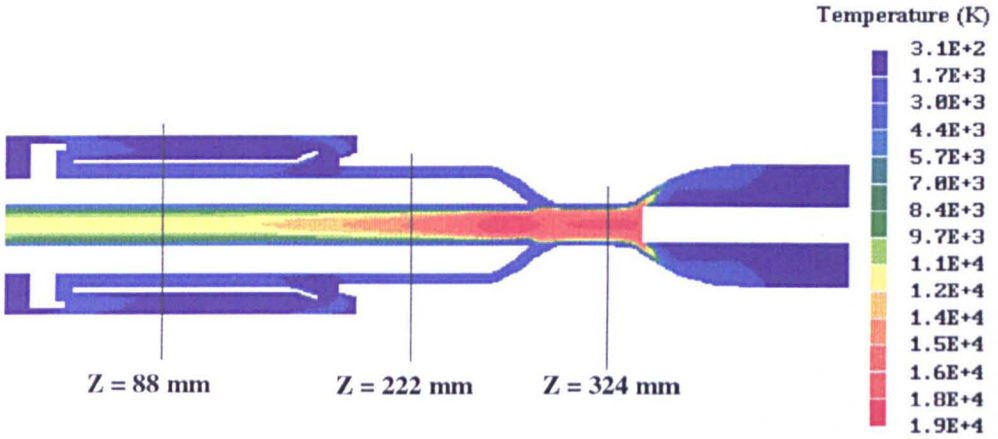

Figure 4.34 Temperature field at 11.2ms with arcing current of -16.75kA. The solid contact has just vacated the nozzle throat and hot gas are ejected from the throat. The radial temperature distributions at the three axial positions are shown in figure 4.36. See figure 4.6 for the position of the solid contact and current waveform.

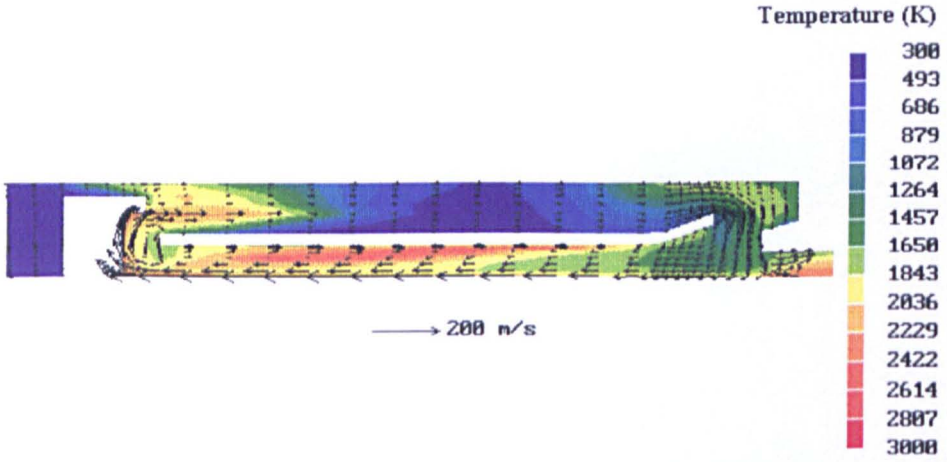

Figure 4.35 Temperature and velocity vector in the storage volume at 11.2ms with arcing current of -16.75kA. See figure 4.6 for the position of the solid contact and current waveform.

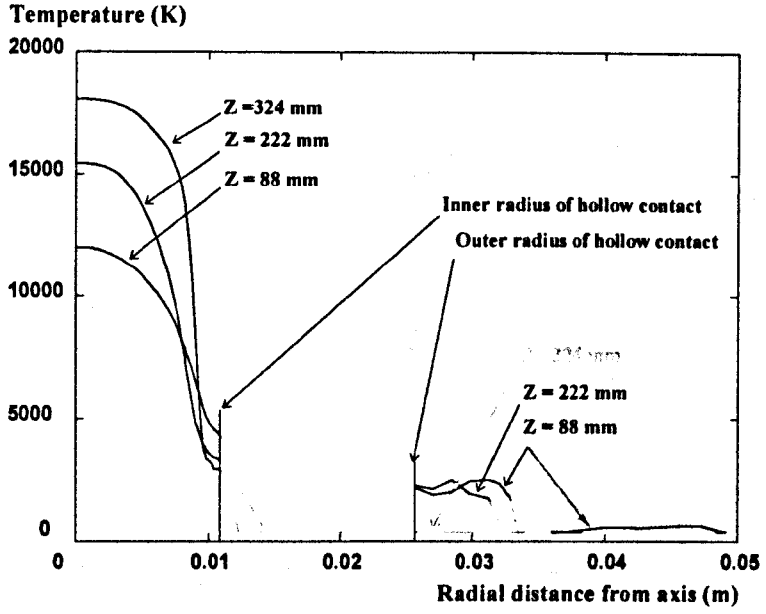

Figure 4.36 Radial temperature distribution at three axial positions which are indicated in figure 4.34 for the arc at 11.2 ms with arcing current of -16.75kA. See figure 4.6 for the position of the solid contact and current waveform.

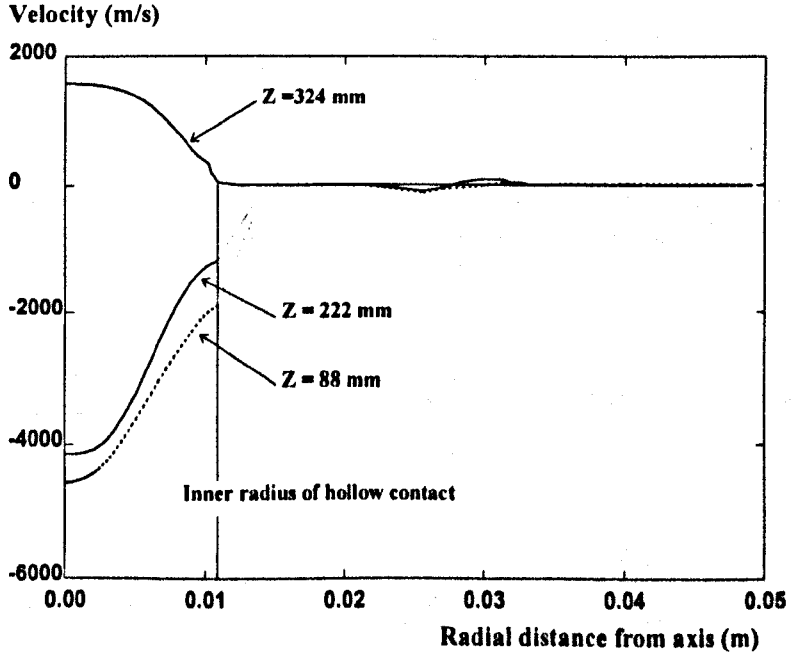

Figure 4.37 Radial distribution of the axial velocity at three axial positions for the arc at 11.2 ms with arcing current of -16.75kA. See figure 4.6 for the position of the solid contact and current waveform.

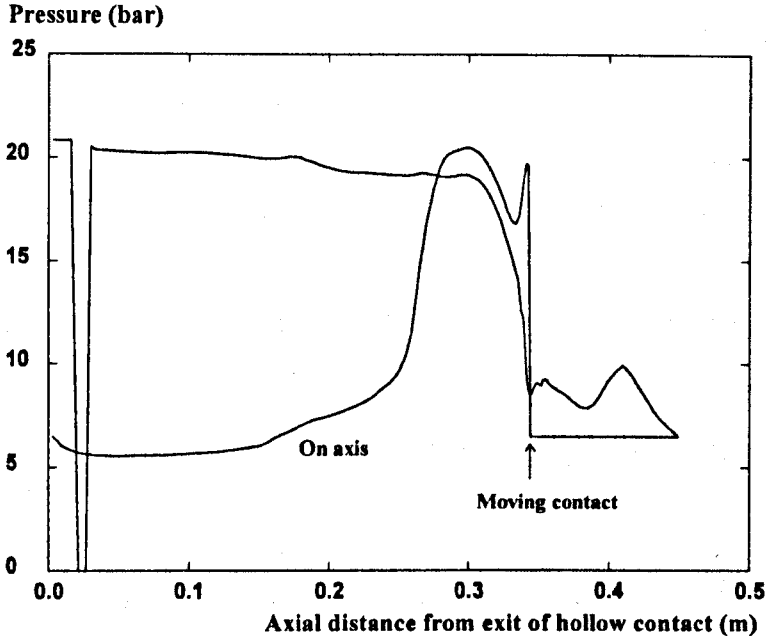

Figure 4.38 Axial pressure distribution on axis and along a line indicated in figure 4.26 for the arc at 11.2 ms with arcing current of -16.75kA. See figure 4.6 for the position of the solid contact and current waveform.

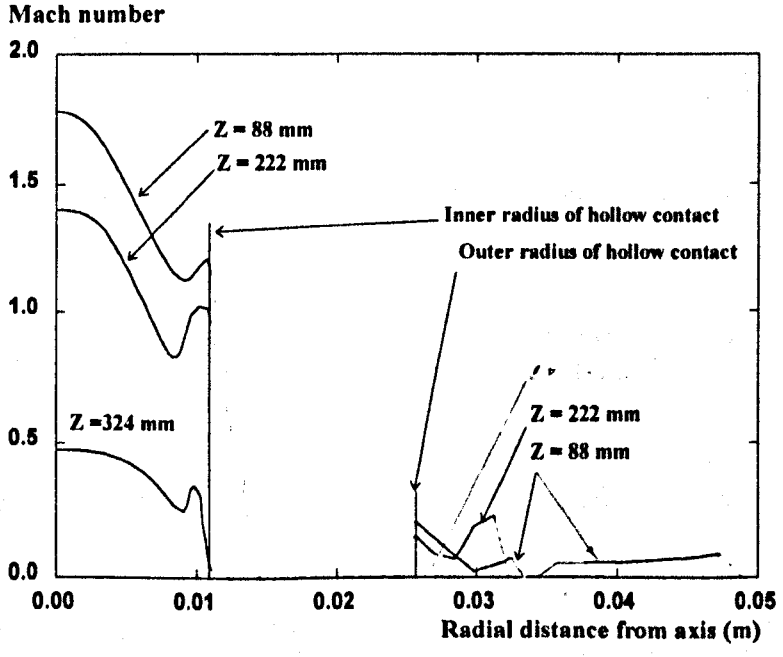

Figure 4.39 Radial distribution of Mach number at three axial positions for the arc at 11.2 ms with arcing current of -16.75kA. See figure 4.6 for the position of the solid contact and current waveform.

Ruchti and Niemyer [102] presented experimental results of electric field for steady state arcs burning in blackened PTFE tubes. The length of the tubes ranges between 44 and 88mm and the radius of the tube varies between 2 and 7mm. The arcing current in their experiment is from 1 to 7kA. In our case, the length of the cylindrical nozzle throat is 43mm and its radius is 11mm. The axial electric field at the middle of the cylindrical nozzle throat is plotted in figure 4.40 at ten instants with different arcing current. The solid contact is outside of the nozzle throat for all the currents in figure 4.40. The shadow area represents the experimental results of [102]. Figure 4.40 implies that the arc in the nozzle throat can be described as ablation dominated only when the arcing current is higher than 15kA, and the arc can be treated as quasi-steady. The arc radius and temperature are not sensitive to the current as long as it is higher than 15kA for the nozzle geometry under investigation. The axial electric field inside the arc column is thus a linear function of the instantaneous current. However, the stagnation pressure inside the nozzle throat has no simple relationship with the arcing current since the pressure at the ends of the nozzle throat cannot remain constant. The predicted axial electric field agrees with experimental results within 5%.

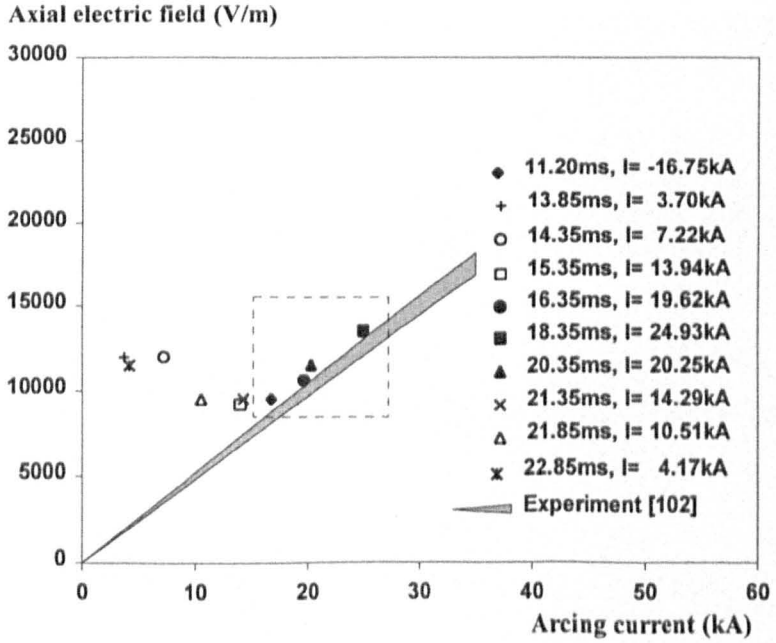

Figure 4.40 Predicted axial electric field in the arc column at the middle of the cylindrical throat of the grey PTFE nozzle in a 245kV auto-expansion circuit breaker . The shadow area is given by Ruchti and Niemyer [102] for steady state arcs burning in blackened PTFE tube. See figure 4.6 for the position of the solid contact and current waveform.

Large discrepancy in electric field exists for arcing current below 15kA. When the arcing current is sufficiently high (above 15kA in our case), ablation of the nozzle surface by arc radiation forms a stagnation point in the nozzle throat (figure 4.41). The flow field in the nozzle throat is thus controlled by ablation and the arc is burning in an ablation dominated environment (figure 4.42). When the current falls below 15kA, the stagnation point moves up to the region between the nozzle throat and the hollow contact (figure 4.41) and the flow in the nozzle throat becomes unidirectional (figure 4.43). Radial incoming vapour from the nozzle surface due to ablation only forms a thermal layer near the wall. The maximum axial electric field moves up to the stagnation point (figure 4.44) where the cross flow from the storage volume cools the arc and forms a minimum in arc radius (figure 4.43). By contrast, the arc radius has a maximum at the same location for arcing current above 15kA which results in a minimum in axial electric field as shown in figure 4.44 (curve labelled 18.35ms, 24.93kA). The axis Mach number at four instants are given in figure 4.45. Flow on the axis remains supersonic in the hollow contact during the high current phase. Ohmic heating on the axis is approximately balanced by radiative energy loss (figures 4.46 and 4.47). A typical electrostatic potential field is shown in figure 4.48 for arcing current of 24.93kA at 18.35ms.

Contact movement and nozzle ablation strongly affect the flow field around the arc column which in turn has considerable influence on arc voltage. The predicted arc voltage is plotted in figure 4.49. The jump in arc voltage at positions labelled 1,2 and 3 in figure 4.49 are all caused by abrupt change in arc radius due to flow reversal in front of the solid contact. Position 1 corresponds to flow reversal shown in figure 4.22 shortly before the solid contact moves out of the hollow contact while Position 3 corresponds to a similar situation shortly before the solid contact moves out of the cylindrical nozzle throat. Increase of arc voltage at Position 2 is caused by a sudden reduction in arc radius due to a transition in flow field in front of the solid contact shortly after the solid contact moves out of the hollow contact, which can be demonstrated by the difference in flow field between figures 4.22 and 4.24. There are two reasons for the rise of arc voltage at Position 4: the first is that axial convection is enhanced after the solid contact clears the nozzle throat, which increases energy loss from the arc column and causes the arc voltage to rise. The second reason is that the arcing current at Position 4 is falling rapidly below 15kA and the electric field in the throat will increase according to figure 4.40. Decrease in arc voltage at Position 5 represents a transition when the arc becomes ablation dominated above 15kA. When the solid contact withdraws into the

nozzle throat, vapour injection due to nozzle ablation cools and constrains the arc column which is reflected by the linear growth of arc voltage with respect to time between Position 6 and Position 3.

Results given in figure 4.50 show that the model is capable of modelling the arcing phenomena in the high current phase despite the approximations which we have made to the radiation and ablation process.

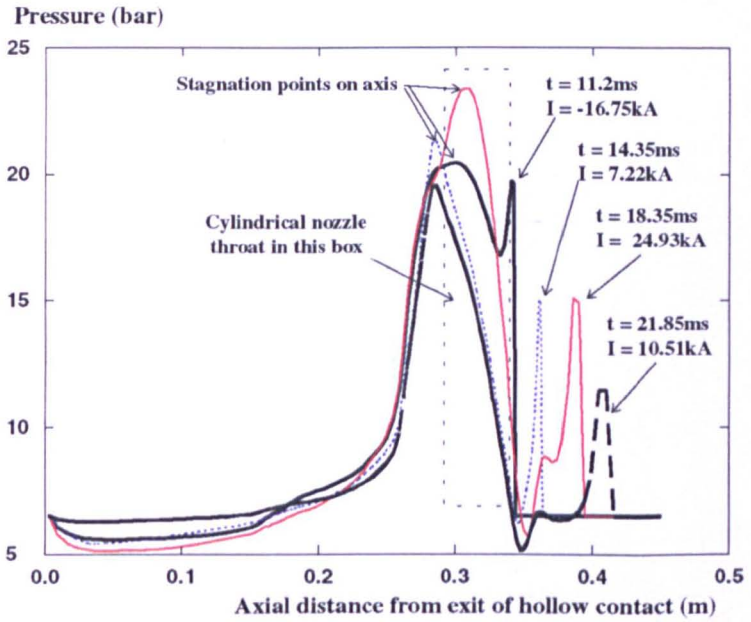

Figure 4.41 Axis pressure at four instants. The position of the tip of the solid contact is indicated by the arrowhead of the labelled lines. See figure 4.6 for the position of the solid contact and current waveform.

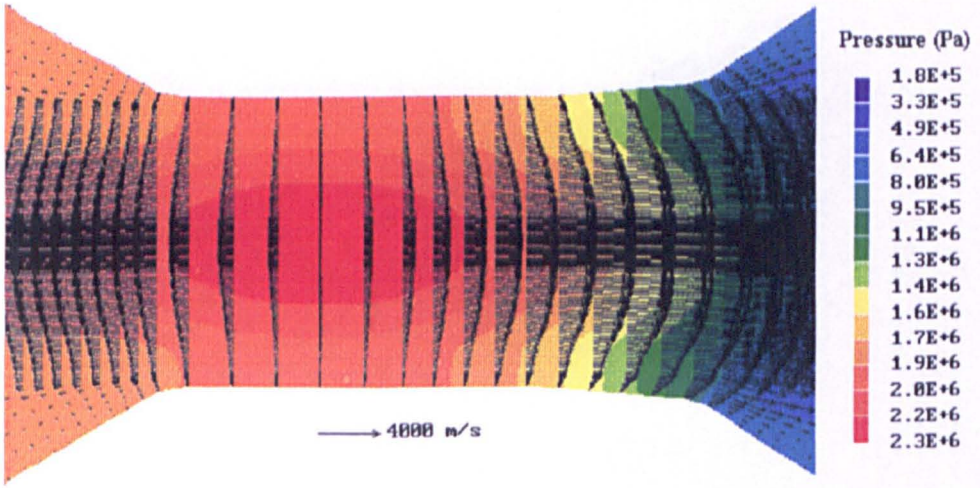

Figure 4.42 Pressure and velocity vector field at 18.35ms with arcing current of 24.93kA. See figure 4.6 for the position of the solid contact and current waveform.

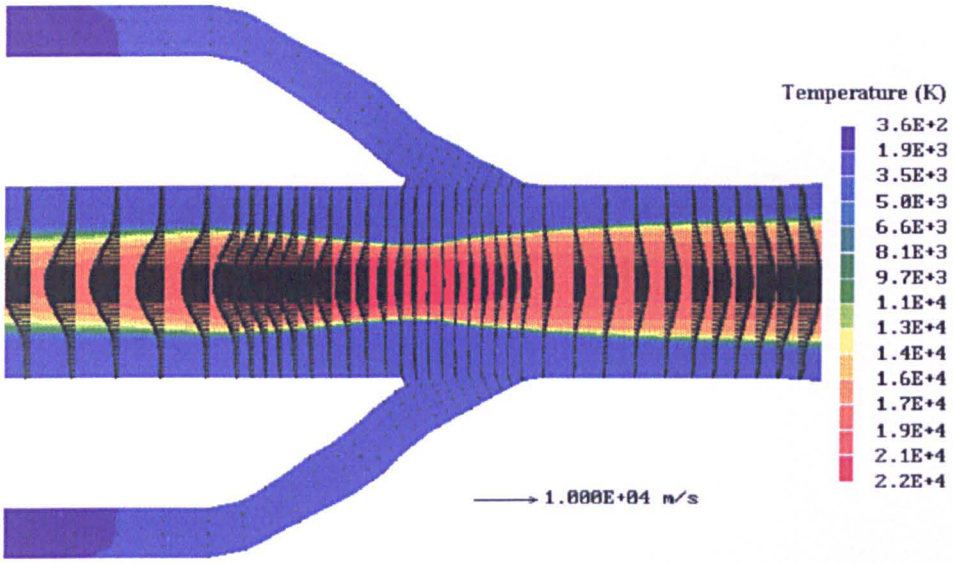

Figure 4.43 Temperature and velocity vector field at 21.85ms with arcing current of 10.51kA. See figure 4.6 for the position of the solid contact and current waveform.

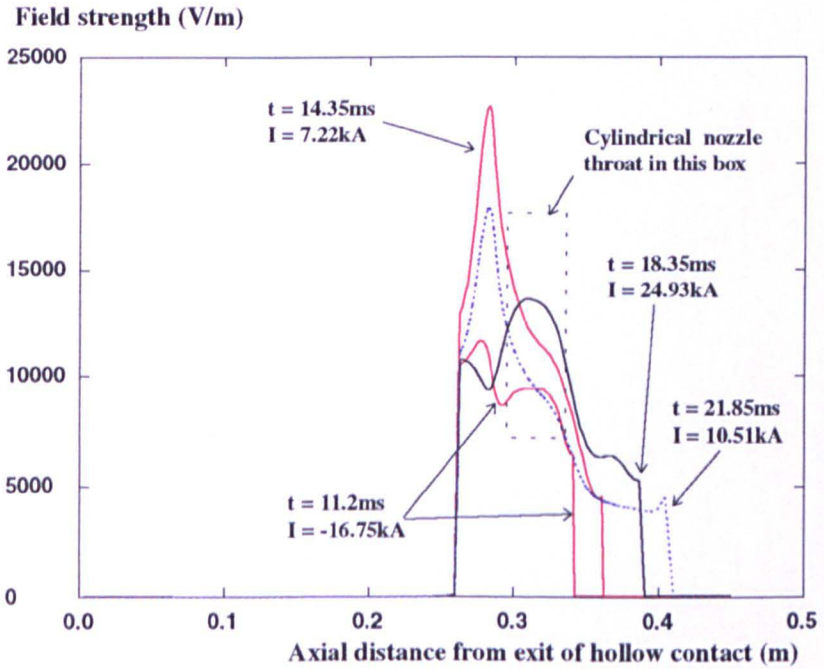

Figure 4.44 Axial electric field strength on the axis at four instants in the arcing process. See figure 4.6 for the position of the solid contact and current waveform.

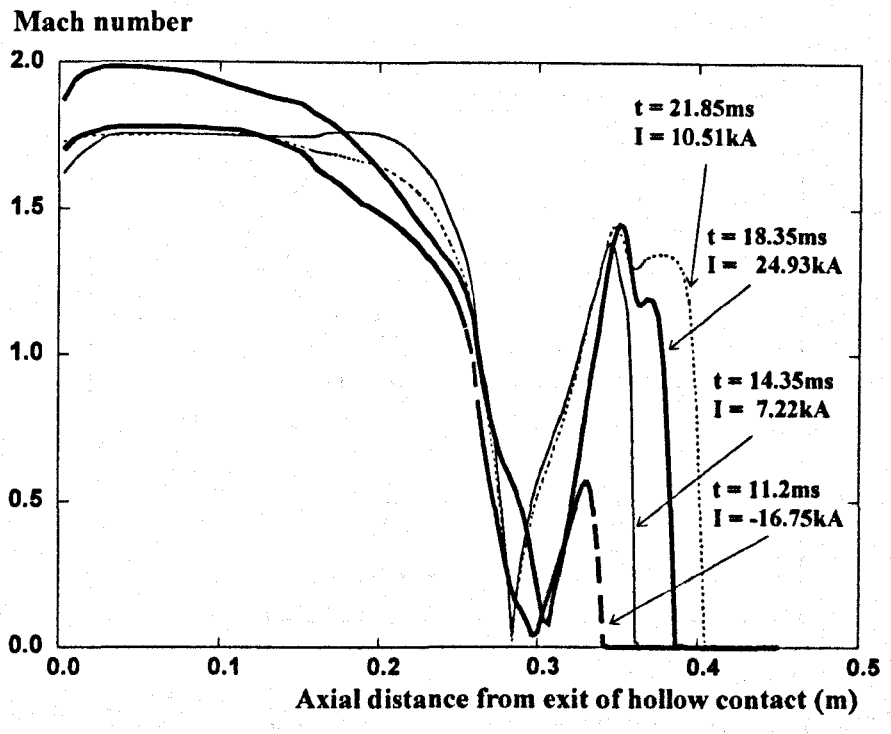

Figure 4.45 Axis Mach number at four instants in the arcing process See figure 4.6 for the position of the solid contact and current waveform. The position of the tip of the solid contact is indicated by the arrowhead of the labelled lines

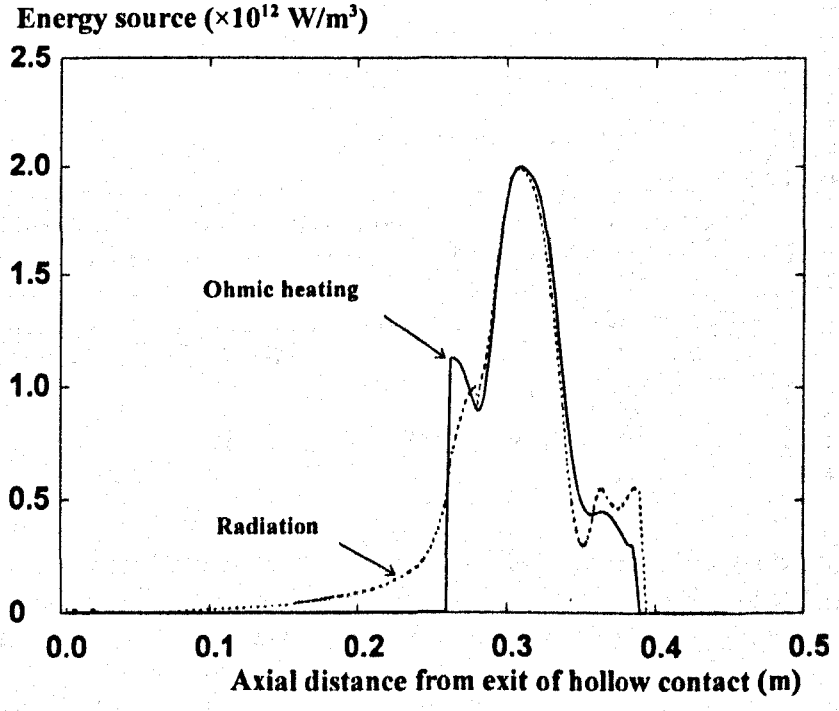

Figure 4.46 Ohmic heating and radiative energy loss on the axis at 18.35ms with arcing current of 24.93kA. See figure 4.6 for the position of the solid contact and current waveform.

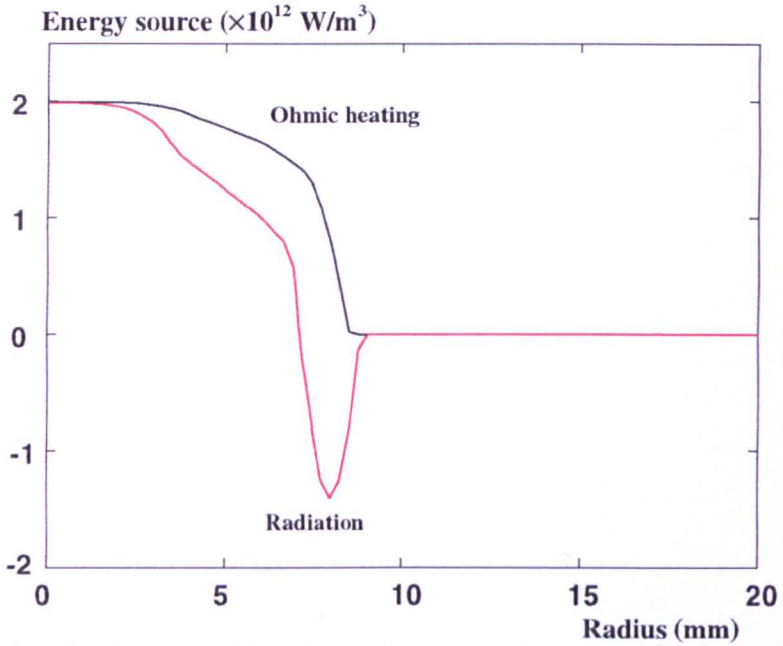

Figure 4.47 Radial distribution of Ohmic heating and radiative energy loss per unit volume at the middle of the nozzle throat (312mm from exit of hollow contact) at 18.35ms with arcing current of 24.93kA. See figure 4.6 for the position of the solid contact and current waveform.

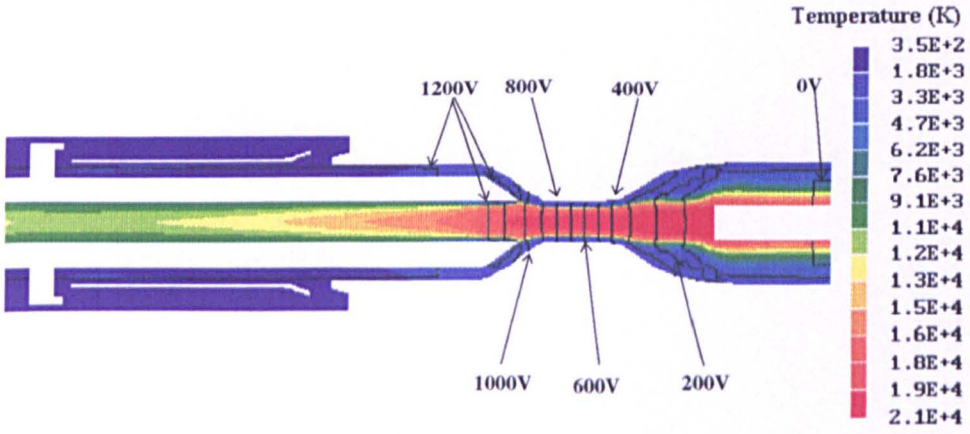

Figure 4.48 Temperature and electrostatic potential field at 18.35ms with arcing current of 24.93kA. The predicted arc voltage is 1200V. The equal-potential line of 0V is not ideally at the exit plane due to the large cell size used at the exit of the nozzle (see figure 4.3).

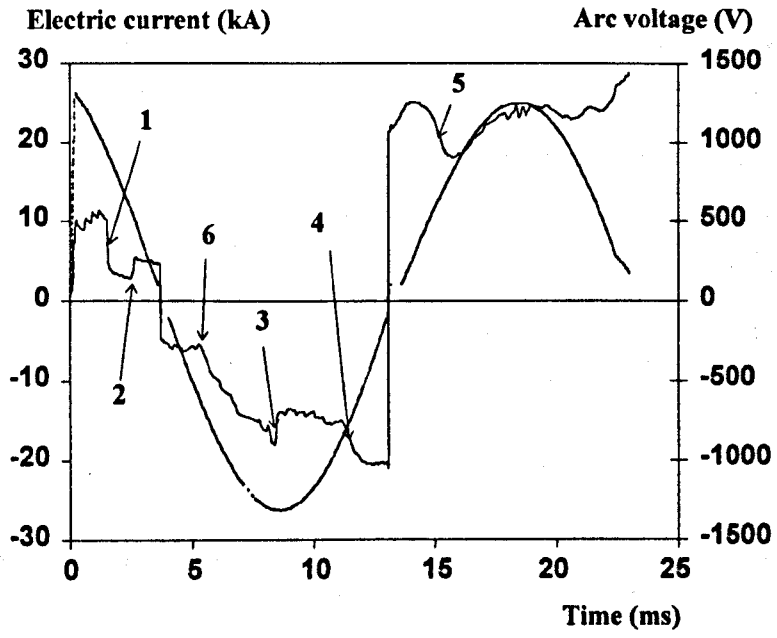

Figure 4.49 Predicted arc voltage for a 245 kV auto-expansion circuit breaker by the non-slender arc model.

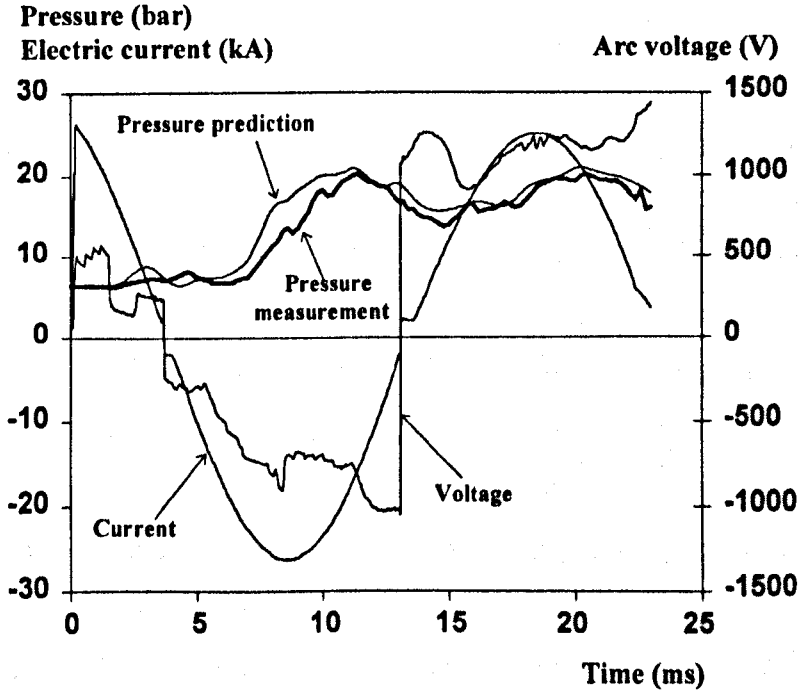

Figure 4.50 Predicted and measured pressure variation at a position indicated in figure 4.1 inside the storage volume of the 245kV auto-expansion circuit breaker under simulation.

4.8 The Role of the Storage Volume and the Pre-current Zero Period

To guarantee successful interruption of a fault current by an auto-expansion circuit breaker, the switching arc between the contacts must be cooled down and converted into a good insulator in the vicinity of current zero. The gas between the two contacts should withstand the recovery voltage from the power system. The gas flow which is required to cool the arc is maintained by the pressure in the storage volume, which depends on the high current phase. We will first review the flow in the storage volume in Section 4.8.1 and then present the results immediately before current zero in Section 4.8.2.

4.8.1 Flow in the storage volume

The geometry and dimensions of the storage volume are decisive factors in circuit breaker design. They together control the temperature and speed at which gas from the storage volume flows through the main nozzle and the hollow contact around current zero. The temperature and velocity vector in the storage volume are shown in figure 4.51 for five instants in the high current phase. The position of the solid contact and the current waveform can be found in figure 4.6. Pressure rise in the storage volume starts to rise rapidly (figure 4.50) when the solid contact withdraws into the nozzle throat.

At 7ms the arcing current is close to its peak in the second loop. A hot patch at a temperature of 3600K has reached the flow guide ((a) in figure 4.51). The incoming flow is diverted by the flow guide on its both sides. However flow on the inner side of the flow guide travels faster than that on the outer side. Pressure difference in the storage volume is small over the arcing process (figures 4.32, 4.33 and 4.38). The hot gas flowing on the inner side of the flow guide is turned around by the reflector and moves on the other side. The cold gas originally in the storage volume mixes with the incoming hot gas and is subjected to compression due to pressure rise in the storage volume. At 11.4ms, the current is decreasing and the solid contact has vacated the nozzle throat (figure 4.6). Gas is flowing out from the storage volume since the pressure in the nozzle has become lower than that in the storage volume (compare pressure distributions in figure 4.38 with that in figure 4.32). The cold patch on the outer side of the flow guide thus moves towards the exit of the storage volume (13.4ms and 2kA).

When the current enters into its third loop, pressure in the nozzle throat increases in step with the current, and flow in the passage to the storage is reversed again (19.85ms and 22.4kA). The speed of the incoming hot gas is much lower than that in the second loop due to the high pressure which has been built up in the storage volume ((a) and (d) in figure 4.51 are at the same current level). The cold patch moves into the flow passage when the current approaches its final zero. The flow guide has played an extremely important role in shaping the cold gas flow from the storage volume immediately before current zero.

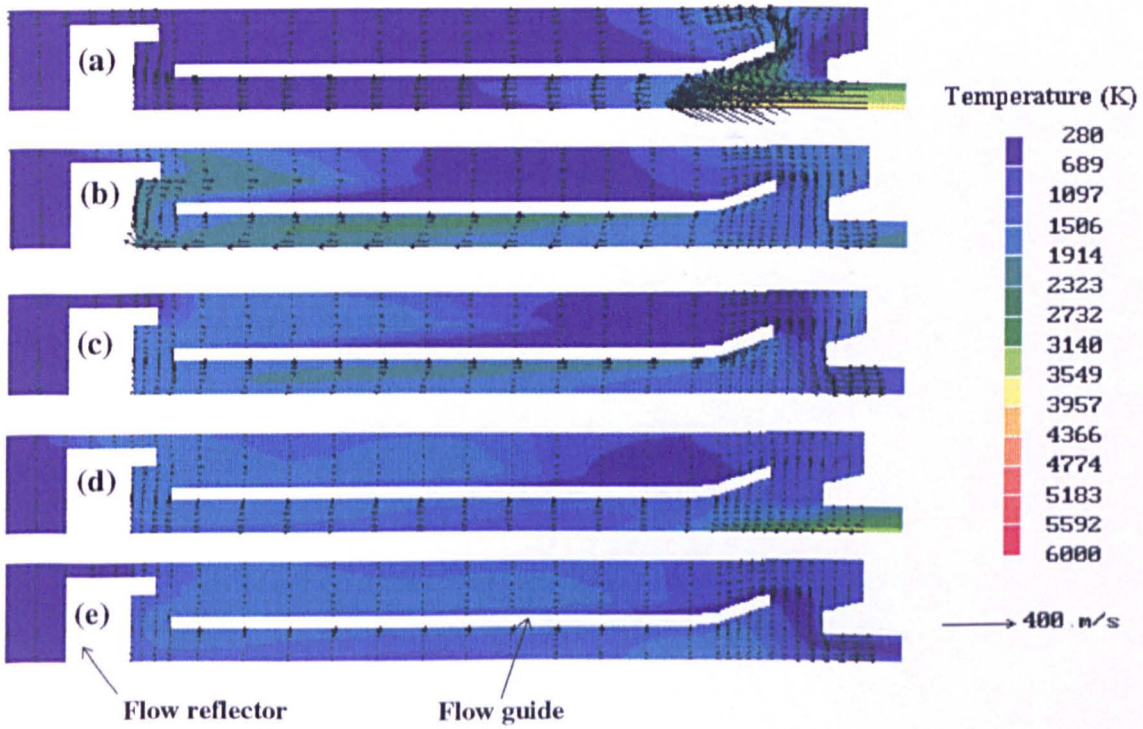

Figure 4.51 Temperature and velocity vector at five instants in the high current phase. See figure 4.6 for the position of the solid contact and current waveform.
(a) – at 7ms and -22.67kA ; (b) – at 11.4ms and -15.38kA ; (c) – at 13.4ms and 2kA;
(d) – at 19.85ms and 22.4 kA ; (e) – at 23ms and 3.44kA

4.8.2 Pre-current zero period

Since the arc radius is rapidly decreasing when the current approaches zero, the grid near the axis must be refined to ensure sufficient number of cells in the arc column at low currents. For the present simulation, the number of cells in the first 2mm from the axis is increased from 30 to 75 and that in the axial direction is increased from 120 to 145 at 3.44kA before current zero.

The axial electric field in the arc column is calculated by equation (2.5) when the current is lower than 3.44kA since the diameter of the arc column is much smaller than the arc length. Electromagnetic force has been neglected since the current is low. The solid contact is no longer moving in the period of 386.4μs before the final current.

The rate of change of current before current zero is -8.9A/μs. It takes 386.4μs for the current to reach zero. We use 150 uniform time steps for the first 300μs (2μs per time step), 50 uniform time steps for the next 50μs (1μs per time step), and 182 uniform time steps for the remaining 36.4μs (0.2μs per time step).

The arc has its maximum temperature in the region between the hollow contact and the nozzle throat when the current is below 15kA due to cooling of the cross flow from the storage volume (figure 4.43). The arc temperature is 25000K at 186μs before current zero with an arcing current of 1659A (figure 4.52). However, temperature decay in this region becomes the fastest when the current falls below 1kA. By contrast, arc temperature between the nozzle throat and the solid contact has a very slow decay rate owing to the flow field shown in figure 4.53. The axis Mach number is less than 0.5 (figure 4.54). The flow on the axis has become subsonic shortly before current zero while the flow in the cold gas remains still supersonic (figure 4.55).

Flow inside the arc column in front of the solid contact is reversed when the current falls below 1kA. The electromagnetic force is not included in the calculation immediately before current zero. A careful examination of the evolution of the pressure field in front of the solid contact shows that when the current decreases rapidly, the arc column becomes thinner. Once the diameter of the arc root becomes smaller than half of that of the solid contact, a stagnation point is formed at the surface of the solid contact (figure 4.56) and gas flows from this stagnation point into the arc root. The flow from the contact surface collides with the oncoming flow from the upstream and form another stagnation point. However, since the low gas density and flow speed of the two jets, the stagnation point is not visible from figure 4.56.

At low current, gas is drawn into the nozzle from outside the downstream exit of the arcing chamber under the fixed pressure boundary condition at the exit. In PHOENICS, the axial gradient of all dependent variables at the exit is assumed to be zero. Thus, when reverse flow exists at the exit, gas will come into the nozzle with an enthalpy and velocity that are equal to those at the exit. This corresponds to a situation where there is a rather stagnant hot

patch around the exit of the arcing chamber at current zero. The effect of axial thermal conduction can still be neglected.

Arc-flow interaction in the diverging section of the nozzle results in flow reversal inside the arc column which significantly slows down the decay of the arc column before current zero. This circulation region is formed when the arcing current is falling from 1kA to 500A (figure 4.57). It persists at current zero and leaves a region with temperature higher than 12000K (figures 4.58 and 4.59). A detailed examination of the evolution of pressure field in the flow reversal region shows that the adverse pressure gradient between the arc and the cold flow is responsible for the formation of reverse flow. Flow at the exit of the cylindrical nozzle throat is subsonic in the arc column but supersonic in the ambient gas. However pressure in the ambient region further downstream cannot support supersonic flow with the nozzle geometry in the downstream region and a shock is formed at a location close to the downstream end of the nozzle throat. The Mach number after the shock could be greater than one since one dimensional theory is no longer valid here. The steep pressure rise in the cold flow (figure 4.61) raises the pressure in the arc column since the arc column is actually a thermal boundary layer. As a result, the subsonic flow in the arc will decelerate under the axially positive pressure gradient. At current higher than 1kA the pressure rise in the cold flow is less than 1.5bar (curve 0 in figure 4.61) and flow in the arc column has sufficient momentum to overcome the pressure gradient. However, when the arcing current reduces, the pressure rise associated with the shock in cold flow becomes stronger and flow in the arc column can no longer resist the axially positive pressure gradient. Once the reverse flow region is formed energy in the arc column cannot be efficiently moved and a hot column will be left at current zero. With the arc radius before current zero (figure 4.62), the axial electric field has its minimum in the reverse flow region (figure 4.63). Flow reversal has certainly adverse effect on the thermal recovery process of the auto-expansion circuit breaker. The radial temperature distribution at three axial positions are shown in figures 4.64, 4.65 and 4.66. The arc column upstream of the nozzle throat at current zero is shown in figure 4.67 and the pressure and Mach number field downstream of the nozzle throat are given in figures 4.68 and 4.69. The axis pressure and pressure in the storage volume at current zero is given in figure 4.70.

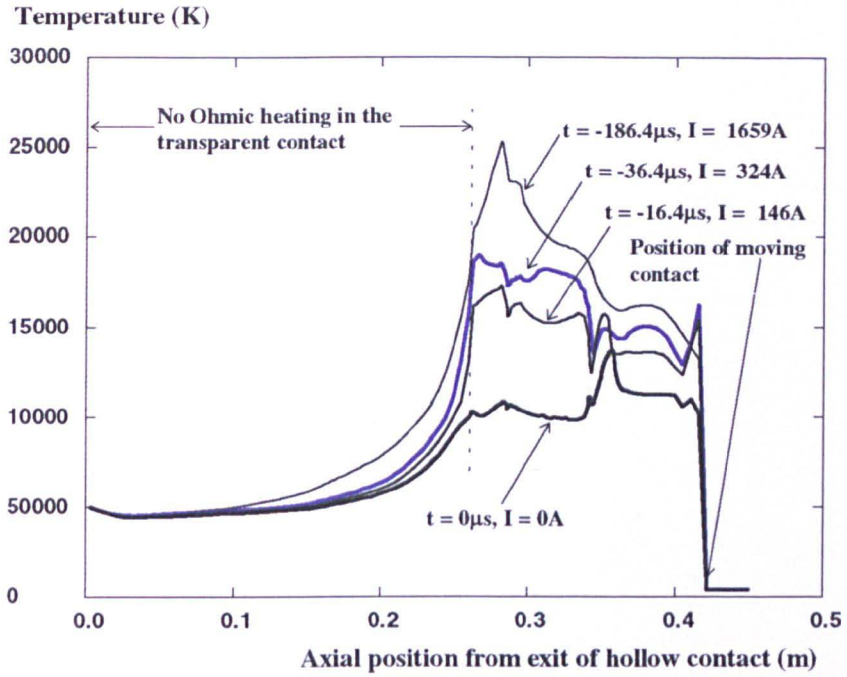

Figure 4.52 Axis temperature before the final current zero. Time shown in this figure is relative to the instant of current zero. See figure 4.6 for the position of the solid contact and current waveform.

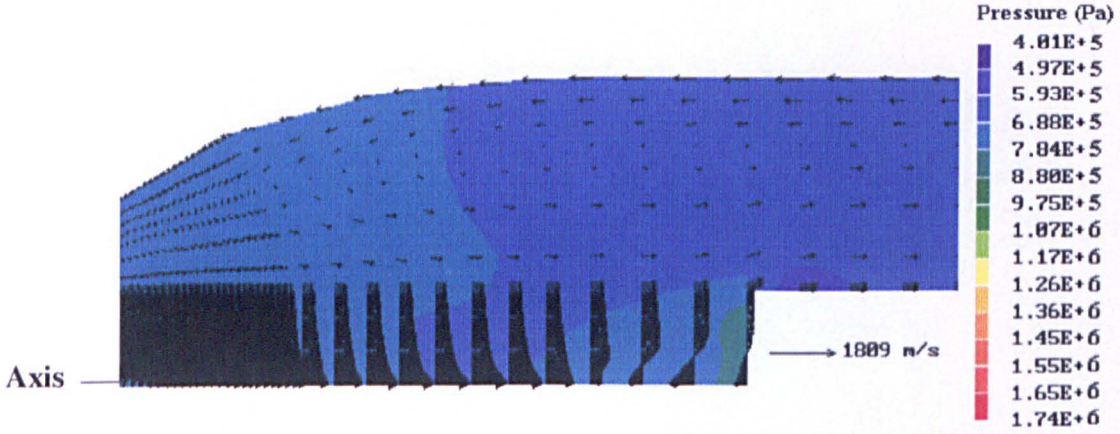

Figure 4.53 Pressure and velocity vector in the downstream section of the nozzle at current zero. Large vortex occurs in the ambient flow.

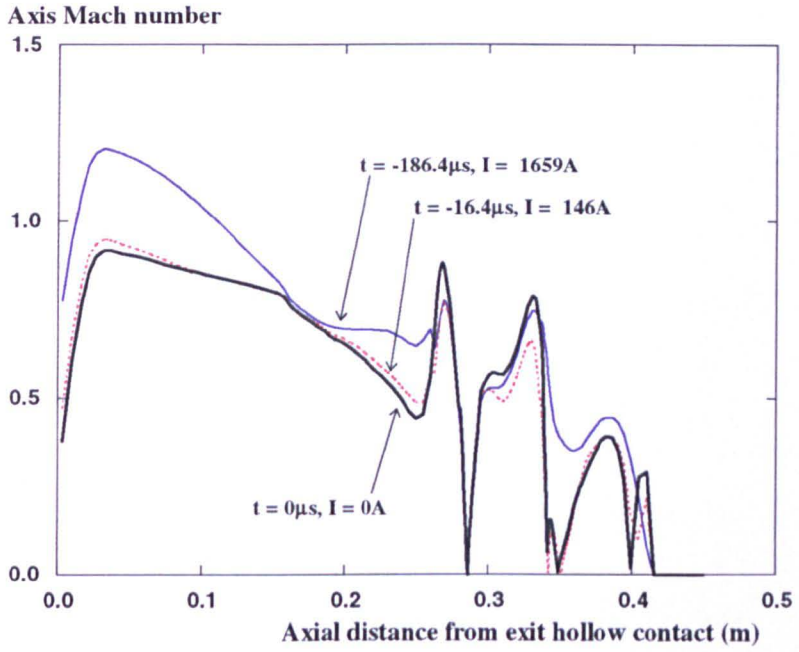

Figure 4.54 Axis Mach number before the final current zero. Time shown in this figure is relative to the instant of current zero. See figure 4.6 for the position of the solid contact and current waveform.

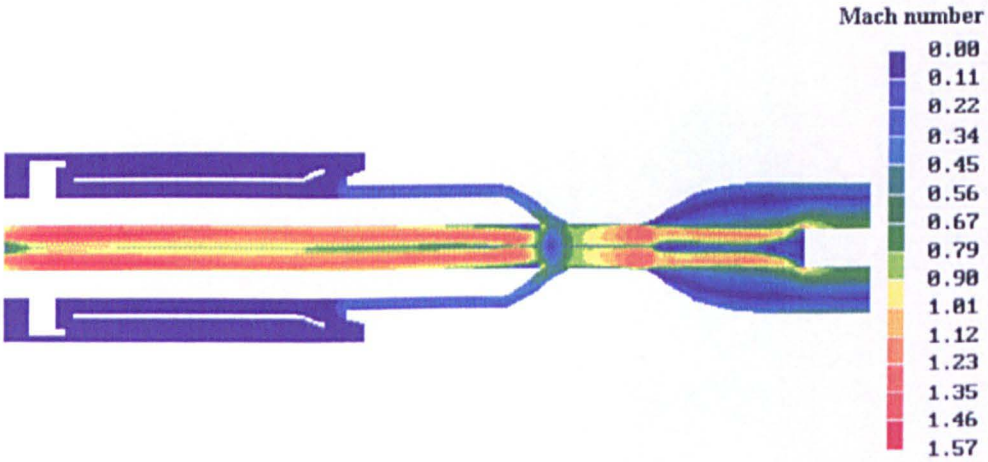

Figure 4.55 Mach number at current zero.

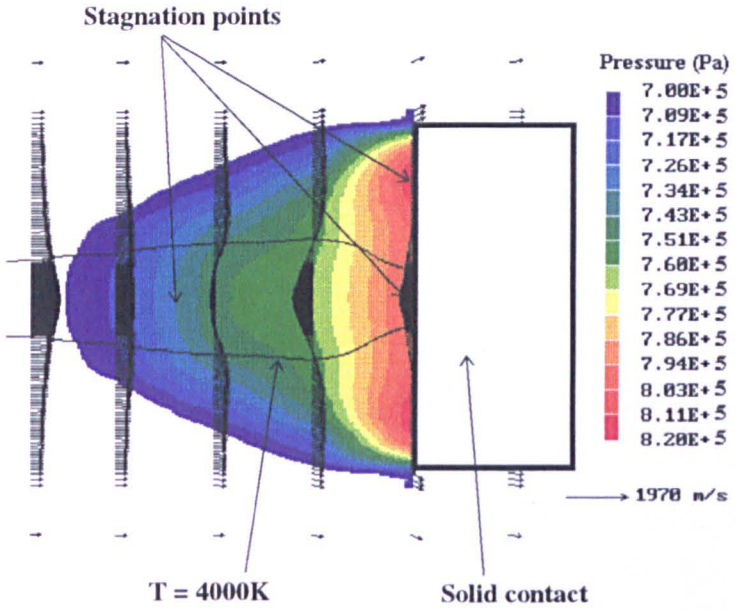

Figure 4.56 Pressure field in front of the downstream contact. The solid contact is no longer moving at this instant.

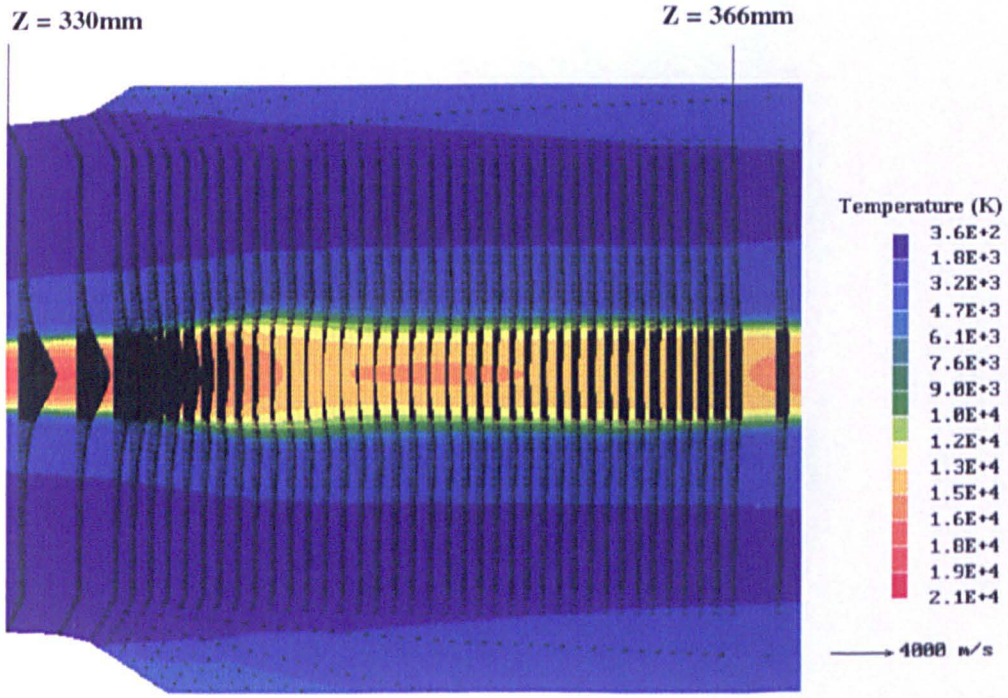

Figure 4.57 Temperature and velocity vector at 56.4μs before current zero. Arcing current is 502A.

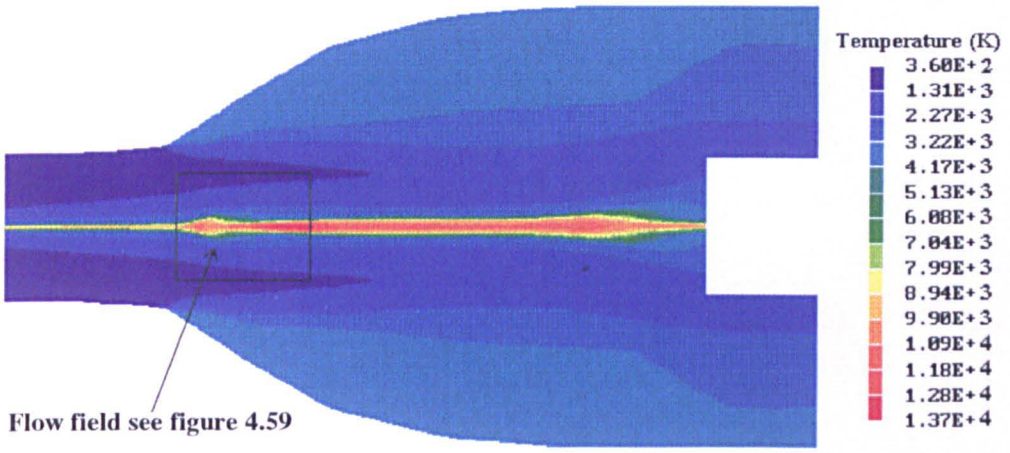

Figure 4.58 Residual hot column at current zero in the downstream section of the nozzle.

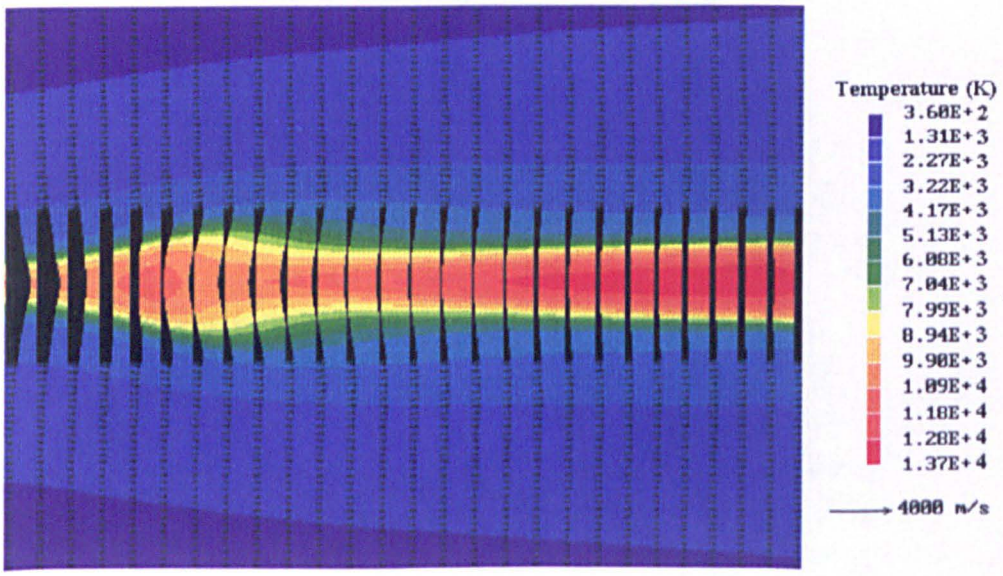

Figure 4.59 Flow reversal in the residual plasma at column zero.

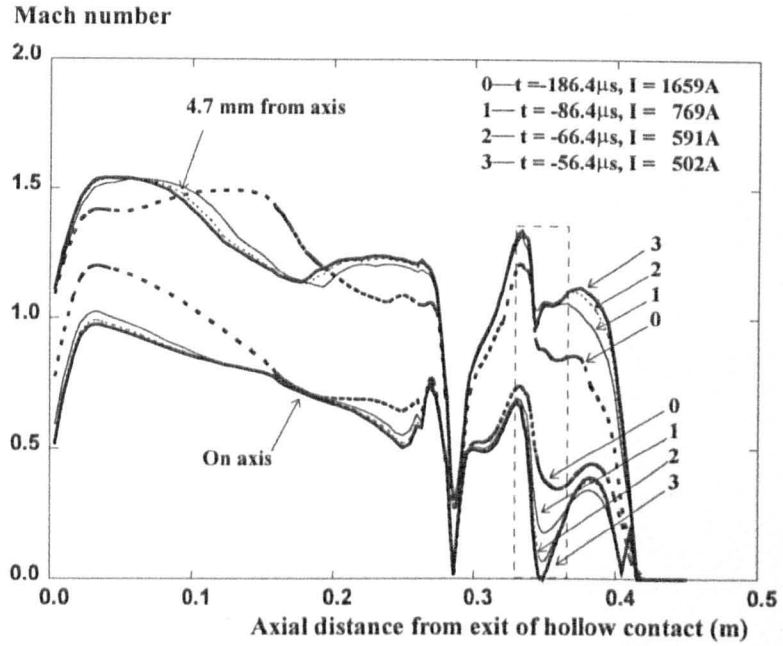

Figure 4.60 Mach number before current zero. Time shown in this figure is relative to the instant of current zero. See figure 4.6 for the position of the solid contact and current waveform.

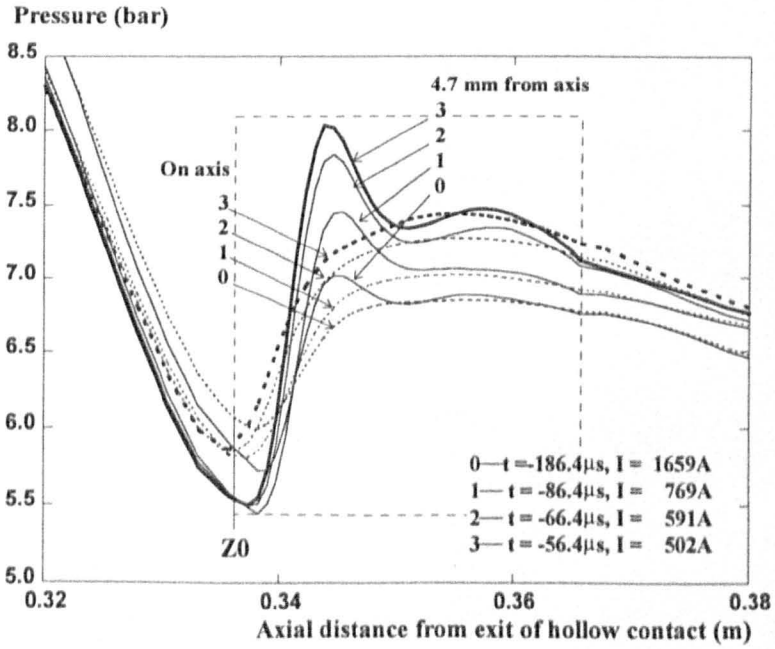

Figure 4.61 Axial pressure distribution in the arc column and in the cold flow at three instants over which flow reversal is formed in the arc column at the downstream exit of the cylindrical nozzle throat. Time shown in this figure is relative to the instant of current zero. See figure 4.6 for the position of the solid contact and current waveform.

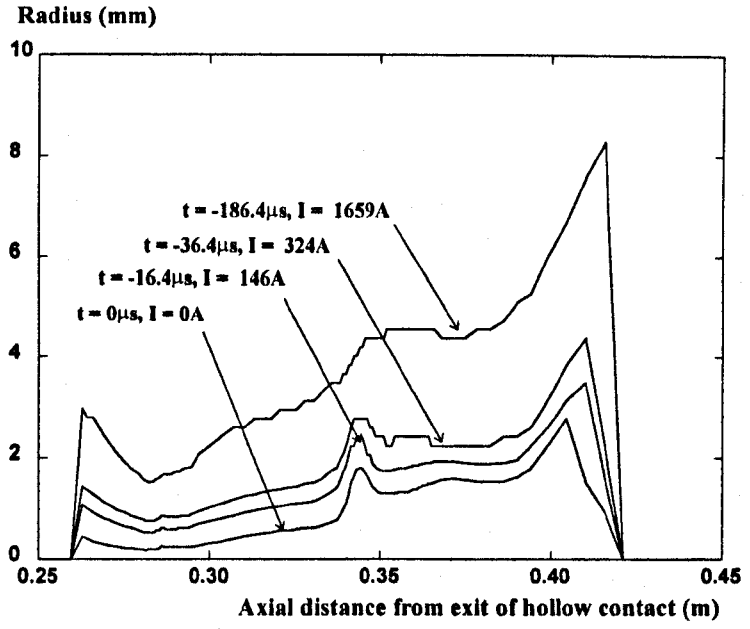

Figure 4.62 Arc radius before the final current zero. Time shown in this figure is relative to the instant of current zero. See figure 4.6 for the position of the solid contact and current waveform.

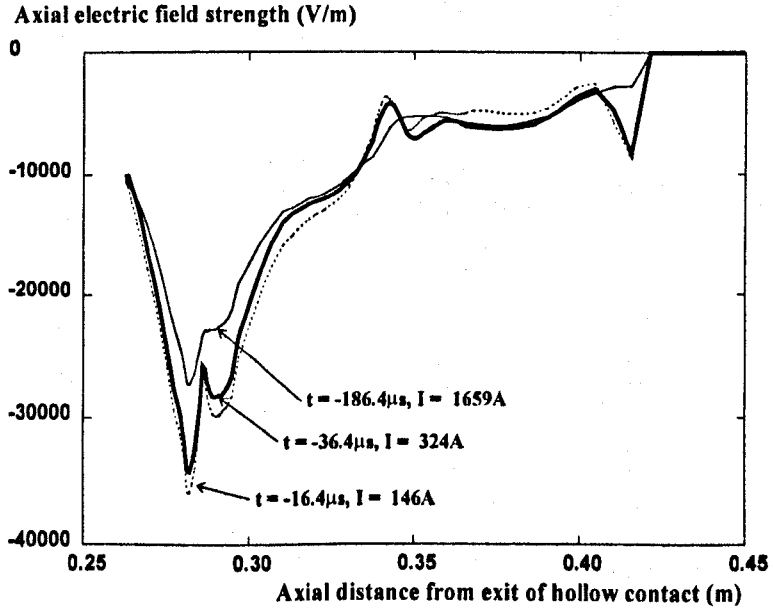

Figure 4.63 Axial electric field before current zero. Time shown in this figure is relative to the instant of current zero. See figure 4.6 for the position of the solid contact and current waveform.

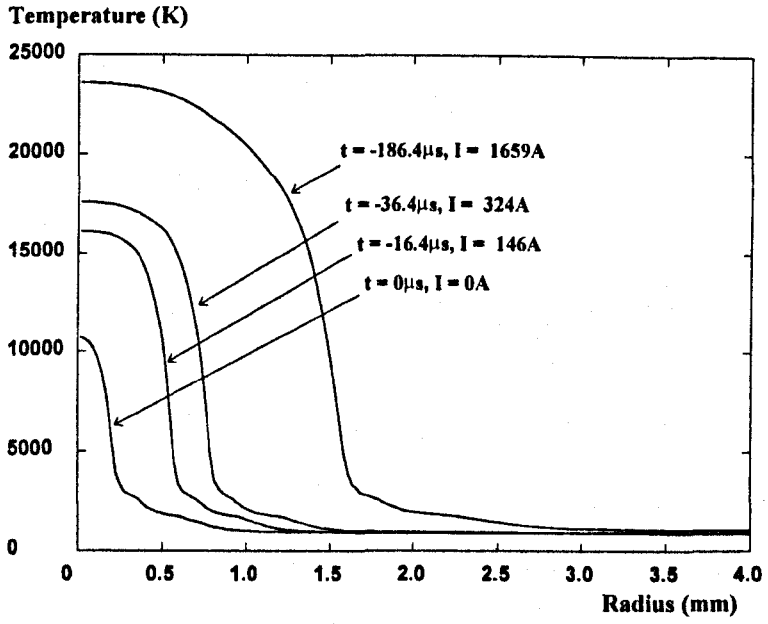

Figure 4.64 Radial temperature distribution at current zero at 284 mm from exit of the hollow contact. See figure 4.6 for the position of the solid contact and current waveform. Time shown in this figure is relative to the instant of current zero.

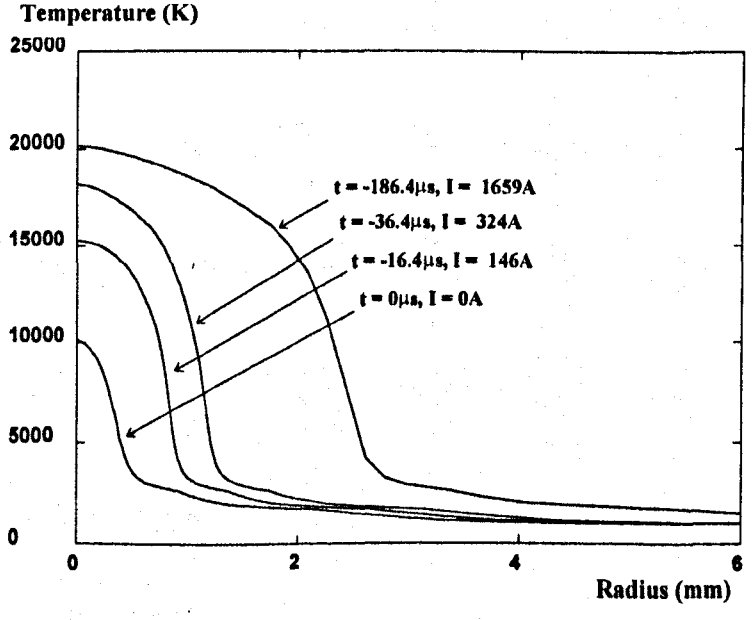

Figure 4.65 Radial temperature distribution at current zero at 312 mm from exit of the hollow contact (at the middle of the nozzle throat) . See figure 4.6 for the position of the solid contact and current waveform. Time shown in this figure is relative to the instant of current zero.

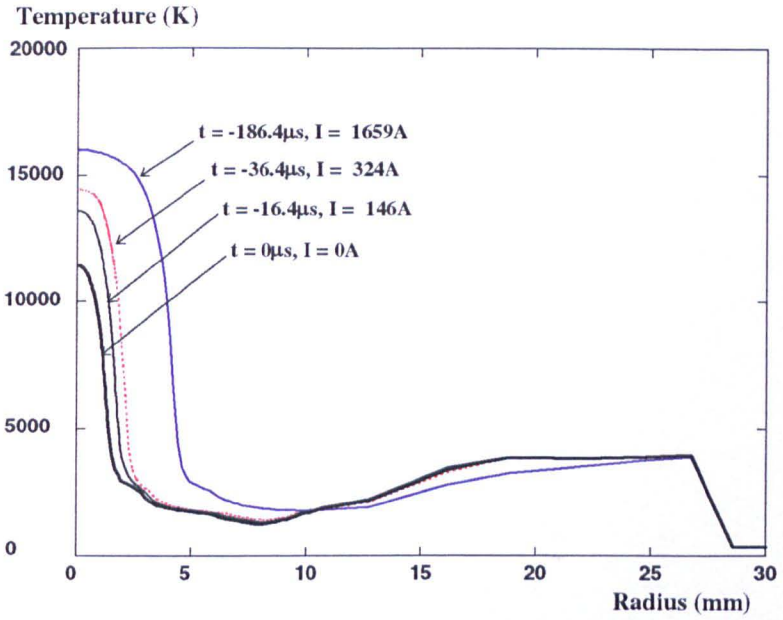

Figure 4.66 Radial temperature distribution at current zero at 366 mm from exit of the hollow contact. See figure 4.6 for the position of the solid contact and current waveform.

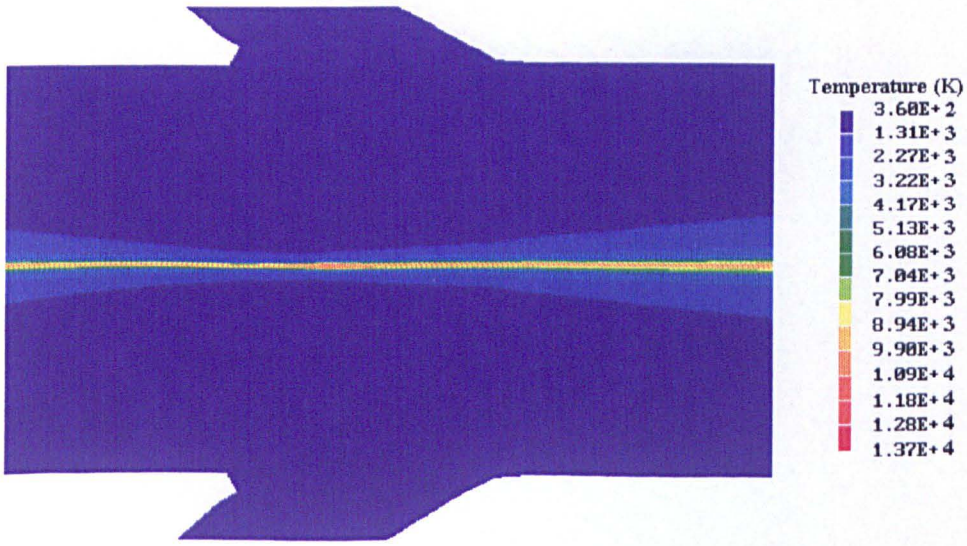

Figure 4.67 Temperature field between the hollow contact and the cylindrical nozzle throat at current zero.

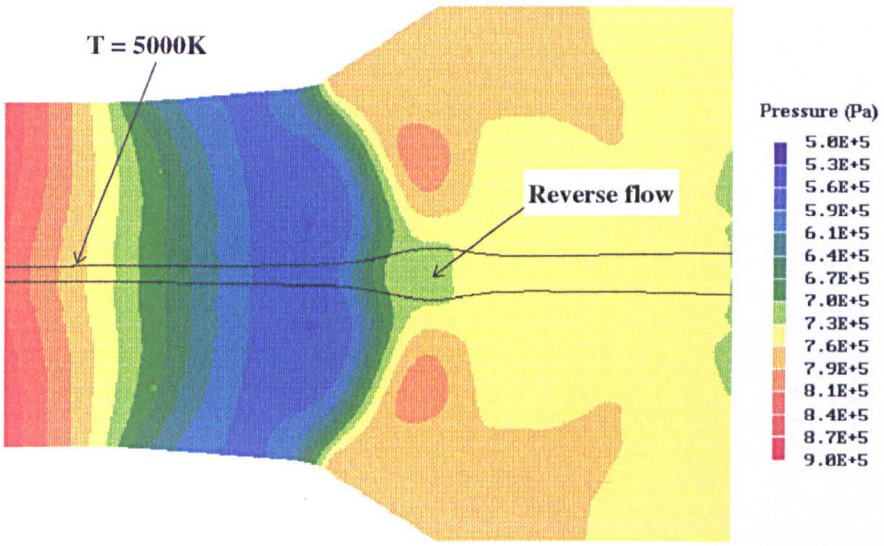

Figure 4.68 Pressure field at the downstream end of the cylindrical nozzle throat at current zero.

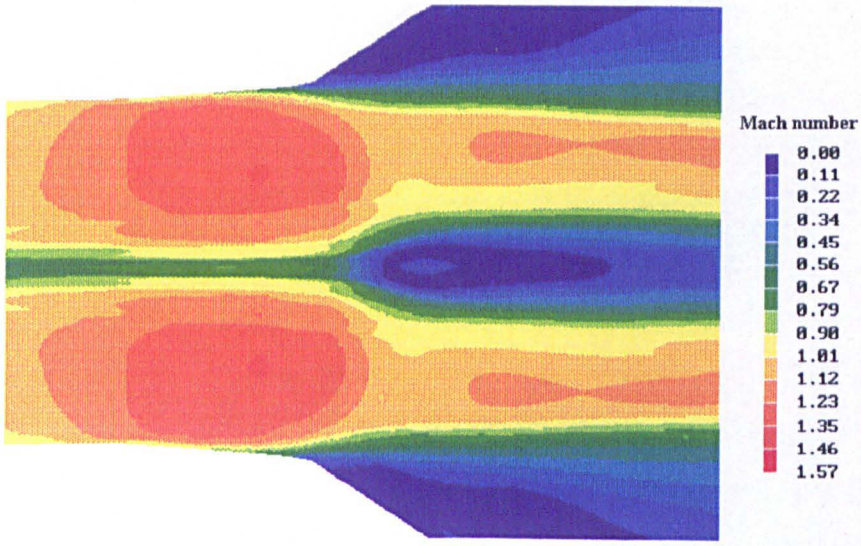

Figure 4.69 Mach number field at the downstream end of the cylindrical nozzle throat at current zero.

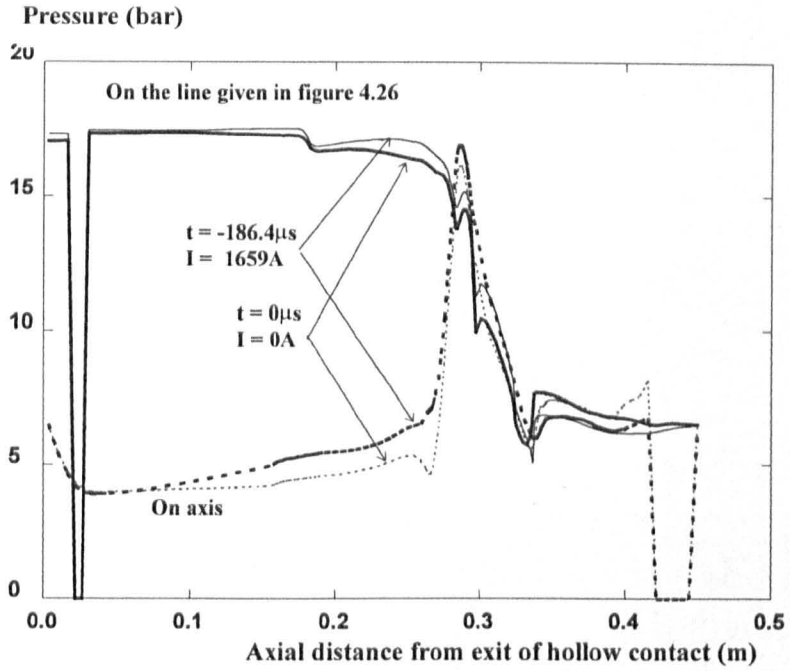

Figure 4.70 Change of axis pressure before current zero. See figure 4.6 for the position of the solid contact and current waveform.

4.9 Thermal Recovery Process

The hot plasma left between the contacts after current zero is electrically stressed by the recovery voltage from the power system. The race between electrical power input due to post-zero current and energy removal by convection and turbulent cooling determines whether the plasma will thermally recover or be re-ignited. The parameter which is used to quantitatively describe the interruption capability of an arcing chamber is the critical rate of rise of recovery voltage (RRRV). The residual plasma will be re-ignited under the stress of a RRRV above the critical value, otherwise its temperature will continuously decay towards the ambient temperature. The time scale for the thermal recovery process is usually a few microseconds from current zero.

Arc extinction depends largely on the turbulent cooling. The turbulence parameter in the Prandtl mixing length model must be calibrated by test results. Since we have used a value of 0.2 for C_1 in equation (3.15) which is obtained by fitting radial temperature measurement in

a supersonic nozzle of two pressure system, results given in this section form a qualitative account of the thermal recovery process in the auto-expansion circuit breaker.

For the geometry of the arcing chamber under simulation, the plasma downstream of the nozzle throat has a temperature around 12000K (figure 4.52). Thus most of the recovery voltage from the power system will be imposed upon the plasma section upstream of the nozzle throat (including the nozzle section), which leads to an unfavourable situation for the thermal recovery process. The critical RRRV is therefore expected to be low. Our model predicts a critical RRRV between 0.2 and 0.5kV/μs (figure 4.71) which is much lower than the applied recovery voltage of 2kV/μs in the short circuit test. Thermal failure was recorded in the short circuit test for the arcing chamber under investigation.

Figure 4.72 shows the decay of axis temperature for a recovery voltage of 0.2kV/μs at which our model predicts thermal recovery. The residual plasma has a very high rate of temperature decay in the nozzle throat (figure 4.73) and upstream of it (figure 4.74). The fastest decay takes place at the tip of the hollow contact where strong radial flow rapidly cools down the plasma. The temperature decay is slow at the stagnation point between the hollow contact and the nozzle throat (figure 4.72). However, axis temperature in the hollow contact does not decay in the first five 5μs after current zero (figure 4.72) since the cold gas from the storage volume has yet negligible cooling on the axis (figure 4.75). Thermal recovery downstream the nozzle throat is extremely slow. The decrease of axis temperature is less than 1000K in the first 5μs after current zero (figure 4.76).

Since the plasma downstream of the nozzle throat has attained a temperature around 12000K at current zero, most of the applied recovery voltage will be distributed across the upstream section of the plasma. With a recovery voltage of 1kV/μs which is above the predicted critical RRRV, the high axial electric field results in strong Ohmic heating around the upstream stagnant point and the plasma in this region is heated up quickly (figure 4.77) despite the continuous decay of axis temperature in the down stream region of the nozzle throat.

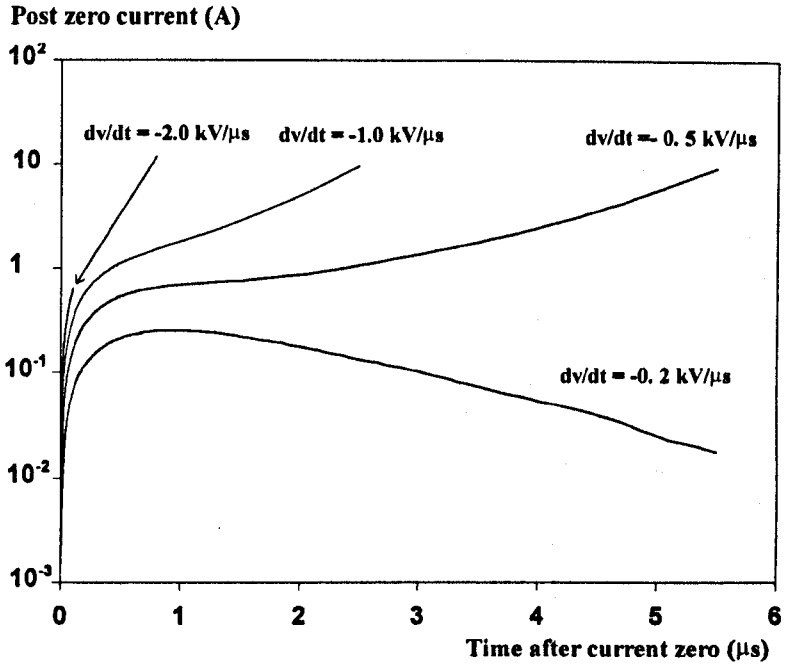

Figure 4.71 Discharge current after current zero under different rate of rise of recovery voltage.

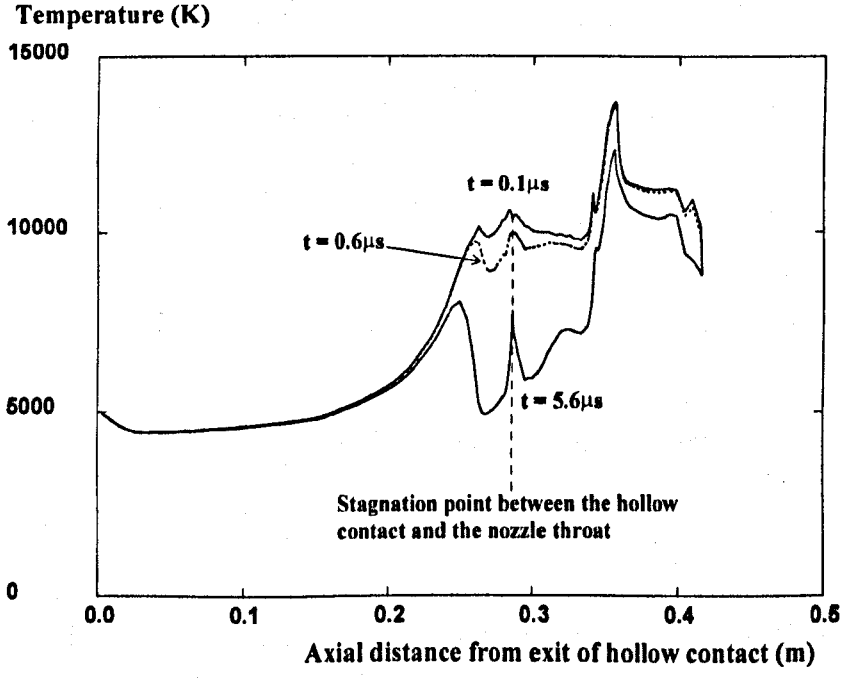

Figure 4.72 Predicted axis temperature decay for an RRRV of 0.2kV/μs. Time in this figure is relative to the instant at current zero.

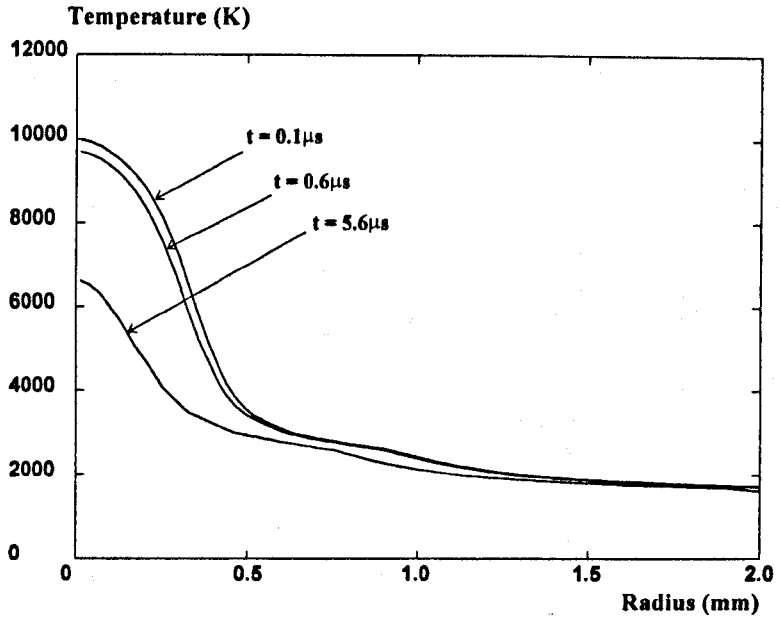

Figure 4.73 Radial temperature distribution at 312mm from the exit of hollow contact which is at the middle of the cylindrical nozzle throat. See figure 4.6 for the position. Recovery voltage = 0.2kV/μs. Time in this figure is relative to the instant at current zero.

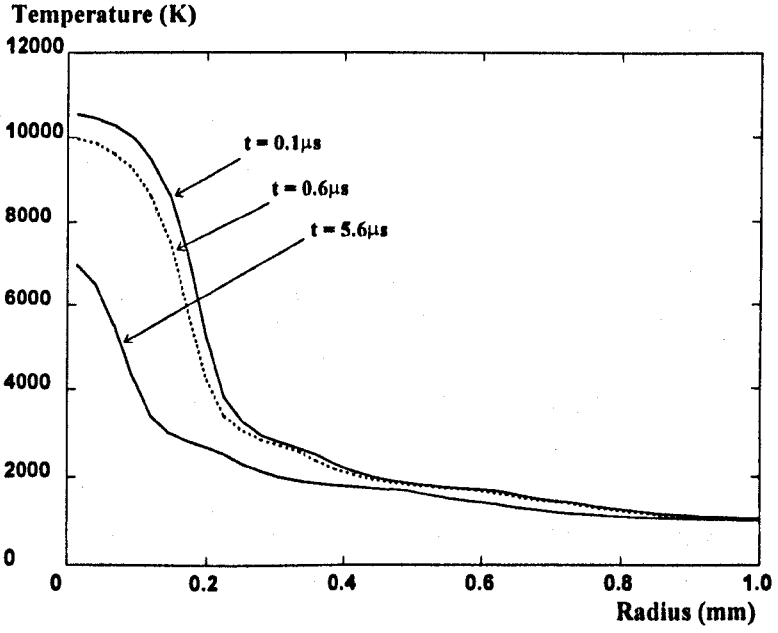

Figure 4.74 Radial temperature distribution at 284 mm from the exit of hollow contact which is at the upstream stagnant point. See figure 4.6 for position. Recovery voltage = 0.2kV/μs. Time in this figure is relative to the instant at current zero.

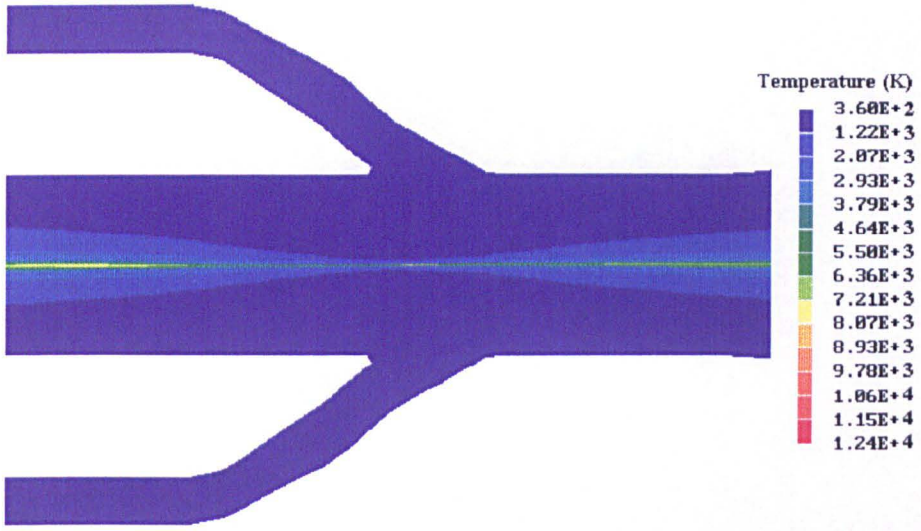

Figure 4.75 Temperature field of the residual plasma upstream of the nozzle throat at 5.6μs after current zero.

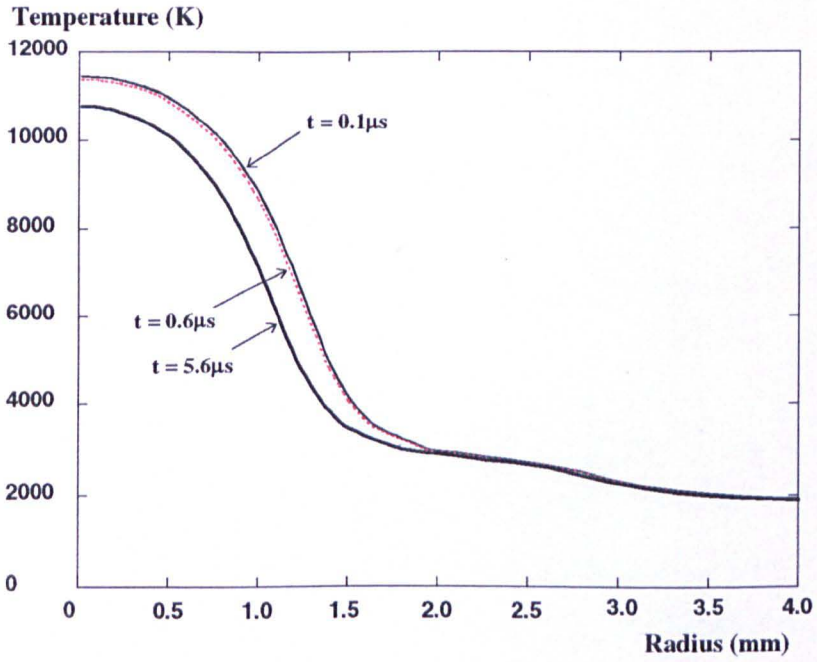

Figure 4.76 Radial temperature distribution at 366 mm from the exit of hollow contact which is located downstream of the flow reversal region. See figure 4.6 for position. Recovery voltage = 0.2kV/μs. Time in this figure is relative to the instant at current zero.

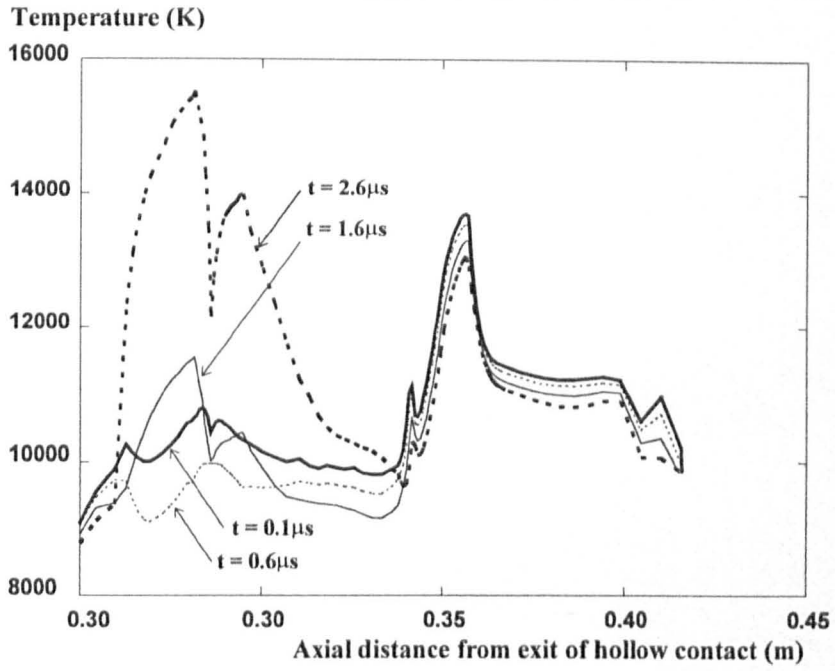

Figure 4.77 Predicted axis temperature variation after current zero with an recovery voltage = 1kV/μs. Time in this figure is relative to the instant at current zero.

4.10 Conclusions

The whole arcing process in a 245kV auto-expansion circuit breaker is computationally investigated. The moving part in a real circuit breaker is the hollow contact and nozzle assembly. To avoid the computational complexity of moving the assembly, we assume in our simulation that the hollow contact and the nozzle (including the storage volume) remain stationary and the other contact moves away from the hollow contact. The arc column is assumed to be axisymmetric and a transparent contact (to gas flow) is placed in the hollow contact to collect the arcing current. There is no Ohmic heating in the transparent contact region. Turbulent momentum and energy exchange is modelled by Prandtl mixing length theory and ablation of the nozzle material by arc radiation is accounted for by a quasi-steady model where the properties of the PTFE vapour are approximated by those of SF_6 . Body fitted grid system is used in the computation.

Arc initiation by contact separation is a very complicated, non-equilibrium process, the mechanisms of which are beyond the scope of the present work. For the case which we have simulated, the current at contact separation is 27kA (Positive current is defined as it flows from the hollow contact to the solid contact). A free burning arc at 2kA is used to

initiate the arcing. The current is then ramped up to 26.32kA in 0.2ms. The initial contact separation is simply given a value of 8mm which is much smaller than the contact separation of 150mm when the circuit breaker is at its fully opened position.

At the initial arcing stage when we run a free burning arc from 2kA to 26.32kA in just 0.2ms, expansion of the hot column in the hollow contact which is blocked at one end by the solid contact causes shock waves which travel towards the exit of the hollow contact at a speed faster than the sound speed of SF_6 at room temperature. The shock waves die out after the current reaches its first peak and the axis pressure in the hollow contact settles down to a smooth distribution.

Flow reversal in the arc column can considerably influence the arc voltage. Shortly before the solid contact clears the hollow contact and the cylindrical nozzle throat, flow reversal in front of the solid contact causes abrupt widening of the arc column and a rapid drop in arc voltage.

For the geometry of the arcing chamber under investigation, arc in the nozzle throat section becomes ablation dominated when a stagnation point is formed in the nozzle throat region when the current is higher than 15kA. For currents below 15kA, no stagnation point can be formed in the nozzle throat region and the arc is subsequently burning in a normal nozzle flow. The axial electric field is much higher than that of an ablation dominated arc.

The storage volume plays an important role in the arcing process. Pressure in the storage volume starts to rise rapidly when the arc is burning in the nozzle throat region. Hot gas is forced to flow into the storage volume at high currents. Hot gas on the inner side of the flow guide travels faster than that on the other side. The cold gas originally in the storage volume mixes with the incoming hot gas and is compressed due to pressure rise in the storage volume. The cold patch on the outer side of the flow guide moves slowly towards the flow passage between the storage volume and the nozzle. When the current approaches its final zero, the cold patch moves into the flow passage and supplies cold flow to the nozzle. Gas in the storage volume moves around the flow guide clockwise for most of the time in the high current phase. Predicted pressure variation in the storage volume agrees well with measurement.

Flow reversal on the axis occurs at the downstream end of the nozzle throat region when the arcing current approaches its final zero. Gas around the arc column leaves the nozzle throat region with a supersonic speed. However the pressure downstream of the nozzle throat

cannot support this supersonic flow and a shock is developed. The steep pressure rise in the shock region raises the pressure in the arc column. Flow in the arc from the nozzle throat region cannot overcome this adverse pressure gradient and reverse flow is subsequently developed on the axis. As a result, flow in the arc column further downstream is rather stagnant and the plasma in the downstream region has a extremely low thermal recovery rate after current zero and its temperature remains around 12000K. The recovery voltage after current zero has to be carried by the upstream section of the residual plasma, which leads to an unfavourable situation in the thermal recovery process in terms of post-zero current.

Thermal recovery of arc plasma in an arcing chamber critically depends on the turbulent cooling. The turbulence parameter in the Prandtl mixing length model must be calibrated by test results. Since we have used a value of 0.2 for C_t in equation (3.15) which is obtained by fitting radial temperature measurement in a supersonic nozzle, results for the current zero period (immediately before current zero and the thermal recovery process) represent a qualitative account of the behaviour of the arcing chamber.

The properties of the PTFE vapour are approximated by those of SF_6 in the present model. This restriction can be eliminated by solving a conservation equation of mass fraction for the PTFE vapour at the cost of computer memory and computing time. In addition, a method has to be found to calculate the electrical and thermal properties of the gas-vapour mixture.

CHAPTER FIVE SUMMARY AND FUTURE WORK

5.1 Summary of the Work

Computational and experimental investigation of the behaviour of an arc burning in a self-generated flow has been carried out. The work, which has been supported by Rolls-Royce Reyrolle, a major switchgear manufacturer in the United Kingdom, is closely related to high voltage auto-expansion circuit breakers, a new generation of high voltage switching devices. By self-generated flow we mean that the gas flow in the arc and its surroundings is generated as a result of the presence of the arc itself in a gaseous environment.

An auto-expansion circuit breaker uses much less operating energy than a puffer circuit breaker. The energy dissipated in the arc column is advantageously used to aid the arc quenching process in an auto-expansion circuit breaker. The flow which is required to cool the arc at a natural current zero is driven by a high pressure source in the storage volume which is built up during the high current phase. Results show that pressure in the storage volume starts to rise quickly shortly after the moving contact withdraws into the nozzle throat region. Ablation of nozzle material by arc radiation at high current forms a high pressure region in the nozzle throat. Hot gas is then forced to flow into the storage volume. The flow guide in the storage volume plays an important role in the arcing process. It has been shown that the hot gas entering the storage volume mixes with the cold gas and forces a cold patch to move slowly towards the exit of the storage volume. When the arcing current approaches its final zero, the cold patch moves into the passage between the storage volume and the nozzle and maintains a cold flow around the arc column. The performance of an auto-expansion circuit breaker at current zero depends on the whole arcing process in the arcing chamber, which is essentially of a transient nature.

Electromagnetic force generated by the interaction of the arcing current with its magnetic field plays an important role at the early stage of the arcing process. Since the arc column at the contact surface, especially at the cathode, is restricted by cathode spot

phenomenon, electric current density at the arc root is extremely high. Flow in the arc column is thus controlled by the electromagnetic force. When the size of the arc column is small in comparison with the arcing chamber, gas flow in the surrounding region of the arc column is rather stagnant with negligible pressure and temperature differences. Ablation of the wall of the arcing chamber by arc radiation is also negligible at the early stage of the arcing process in an auto-expansion circuit breaker. Under such circumstances, the arc can be adequately described by a simplified model for free burning arc.

The simplified model assumes a top-hat radial temperature profile for the arc. It uses a assumed radial distribution of the axial velocity in the arc column. The confining space is divided into two regions, namely the arc column and the surrounding cold region. The thermal properties in the surrounding region are assumed to be uniform. The governing equations are integrated radially from the axis to the arc radius and the dimensionality of the problem is thus reduced to one. The average current density and temperature at the arc root are required as upstream boundary conditions. Arc voltage and pressure measurements have been carried out in a device which simulated the initial arcing in an auto-expansion circuit breaker. Different electrode separations and filling pressures have been investigated. The predicted arc voltage and pressure variation in the confining space agree reasonably well with the measurements. Large discrepancies in arc voltage occur at the low current ends (below 1.5kA), which are attributed to the assumption of the top-hat radial temperature profile for the arc because a top hat temperature profile is not suitable at low currents. The simplified model should therefore be used for currents above 1.5kA. The advantage of such a simplified model is the low computing cost. It can also easily be used for preliminary optimisation studies of the gas discharge parameters, such as the dimensions of the various parts of the arcing chamber.

The condition for the application of such a simplified model is that the size of the arc column must be much smaller than that of the arcing chamber. In a modern auto-expansion circuit breaker, the arc size during the high current phase is comparable with the flow cross section and the simplified model is no longer applicable. Detailed information on thermal interruption capability of an auto-expansion circuit breaker can only be obtained by simulating the whole arcing period. When the currant approached zero, the simplified model is obviously invalid due to the assumption of a top-hat radial temperature profile for the arc column. Application of a two dimensional differential model therefore becomes necessary.

The differential model developed in Chapter Three is for turbulent arcs in axisymmetric flow which could be self-generated or externally maintained, such as by a high pressure reservoir. The governing equations for the turbulent flow are written in their conservative form. Boundary conditions with nozzle ablation of the arcing chamber are specified as source terms. Full closure of the governing equations requires a knowledge of the electric and magnetic fields in the flow domain, the calculation of which is based on the relevant Maxwell equations. The effects of a moving contact are represented by special surface sources of mass, momentum and energy at the interface between the arcing gas and the contact surface. The model is implemented by PHOENICS version 2.0. The results obtained by PHOENICS have been verified in a previous investigation[44]. The effects of the electromagnetic force on high current nozzle arcs, the influence of arc-shock interaction, and the role of turbulence have been investigated.

We first studied the effects of the electromagnetic force on high current arcs burning in a supersonic flow. Results show that the pressure on the nozzle axis is influenced by the $\vec{J} \times \vec{B}$ force induced by the arcing current. The predicted pressure difference on the axis with and without the $\vec{J} \times \vec{B}$ force could reach 2bar for a 30kA arc in SF_6 . Gas is strongly accelerated by the $\vec{J} \times \vec{B}$ force at the upstream electrode. However the arc voltage is not sensitive to the $\vec{J} \times \vec{B}$ force.

Shocks cannot be avoided during the operation of a puffer or auto-expansion circuit breaker. Results based on the differential model show that the presence of a shock in the diverging section of a supersonic nozzle causes flow separation and hence broadens the arc column. The shock has a very complicated structure and the centre is moved slightly upstream towards the nozzle wall in the current range investigated (200A-1500A). The shock strength reduces when current is increased. Compared with the shock free case, the arc voltage is reduced and the V-I characteristic has a minimum. Flow separation creates a very stagnant region which is expected to recover very slowly during the current zero period. It is therefore expected that the presence of a shock will have adverse effects on the thermal as well as dielectric recovery capability.

Turbulence is a very complicated phenomenon and so far there is no universal model, even for ordinary fluid. Most existing turbulence models are based on the concept of turbulent eddy viscosity and they assume negligible density fluctuation. It has been found that one of

the five turbulence parameters in the K-epsilon model has to be adjusted according to the value of the current in order to achieve agreement with the measured radial temperature profile. However, the turbulence parameter in the Prandtl mixing length model is not sensitive to the absolute value of the current for a given flow (nozzle) geometry. Thus for turbulent SF_6 arcs, consideration of the range of applicability of the turbulence parameters and the cost of computation has made the Prandtl mixing length model preferable to the K-epsilon model.

The whole arcing process in a 245kV auto-expansion circuit breaker is investigated in Chapter Four. The moving part in a real circuit breaker is the hollow contact and nozzle assembly. In view of the extreme computational complexity of moving the whole nozzle and the hollow contact assembly, we move the solid contact instead. The arc column is assumed to be axisymmetric and a transparent contact (to gas flow) is placed in the hollow contact to collect the arcing current. There is no Ohmic heating in the transparent contact region. Turbulent momentum and energy exchange is modelled by the Prandtl mixing length theory and ablation of the nozzle material by arc radiation is accounted for by a quasi-steady model. A body fitted grid system is used in the computation.

Arc initiation by contact separation is a very complicated, non-equilibrium process. We initiated the arc in an artificial manner. A low current free burning arc is used to initiate the arcing. The current is then ramped up to the required value in a very short time.

The predicted pressure variation in the storage volume agrees well with measurements for the high current phase. The storage volume plays a very important role in the arcing process of an auto-expansion circuit breaker. The pressure in the storage volume starts to rise rapidly as soon as the solid contact withdraws into the cylindrical nozzle throat, which occurs in the second loop. Ablation of the nozzle material by arc radiation at high currents generates a high pressure region in the nozzle throat region and hot gas is forced to flow into the storage volume. Results show that the geometry of the storage volume has a significant influence on the flow inside it. The incoming hot gas quickly fills up the inner part of the storage volume and forces the gas to form a pressurised cold patch in the outer part of the storage volume which is separated from the inner part by the flow guide. The cold patch moves slowly towards the flow passage in the high current phase. Flow reversal in the gas passage occurs at 20.35ms with a current of 20kA (the whole arcing period is 23ms). The cold patch then moves into the passage and maintains the gas flow in the nozzle in the current zero period.

For the geometry of the arcing chamber under investigation, arcs burning in the nozzle throat become ablation dominated when the current is higher than 15kA. When the current is below 15kA, no stagnation point can be formed in the nozzle throat region and the arc subsequently burns in a normal nozzle flow.

Flow reversal on the axis occurs at the downstream end of the cylindrical nozzle throat when the arcing current approaches its final zero. Results show that it is caused by the adverse axial pressure gradient in the arc column due to shocks in the ambient flow. As a result, flow in the arc column further downstream is rather stagnant and the plasma section downstream of the nozzle throat has a extremely slow thermal recovery rate. The recovery voltage from the power system has thus to be carried by the upstream section of the residual plasma, which leads to an unfavourable situation in the thermal recovery process.

5.2 Future Work

The computational investigation of the behaviour of a high voltage auto-expansion circuit breaker in Chapter Four is limited to only one test case. Future work is necessary to cover a wider range of discharge conditions.

Radiation transfer is a very important process in auto-expansion circuit breakers. Radiation which leaves the arc column is calculated by an approximate model in the present work. Empirical parameters have to be introduced. Recent investigation shows that for arcs in simple nozzle flow, results of radiative flux and its divergence obtained by an approximate method, the "Partial Characteristics" method developed by Sevast'yanenko[50,51], agree very well with the results of exact calculations. It will be of great benefit if this method could be adapted to arcs in auto-expansion circuit breakers.

The arc column in the arcing chamber is assumed to be axisymmetric. Arc rooting at the contact surface is an extremely complicated and three dimensional phenomenon. It has so far been poorly understood. Computer modelling of arc rooting needs to consider the interaction between the current and its magnetic field and the physical mechanisms involved in the sheath-electrode layer.

The properties of PTFE vapour are approximated by those of SF_6 in the present work. This restriction can be removed by solving a conservation equation of mass fraction for the PTFE vapour at the cost of computer memory and computing time. In doing so, a method has

to be found to calculate the electrical and thermal properties of the gas-vapour mixture at various temperatures, pressures and mass fractions.

Arc cooling by turbulent energy exchange has a significant influence on the thermal recovery process in an auto-expansion circuit breaker and so far there is no rigorous model even for ordinary fluid. An electric arc differs from an ordinary fluid in that there is strong heat source in the arc column and the arcing gas is highly compressible. Density fluctuation must be taken into account if an improvement in modelling of turbulence is to be made.

Local Thermal Equilibrium (LTE) is assumed for the arcing gas. However, doubts exist over the assumption of LTE in the plasma after current zero. Further investigation is required to examine the plasma state under a fast rising recovery voltage.

REFERENCES

[1] R.T. Lythall, The J&P Switchgear Book (7th Edition), Newnes-Butterworths, London, 1972

[2] C.H. Flurscheim, Power Circuit Breaker Theory and Design (IEE Power Engineering Series), Peter Peregrinus Ltd, 1982

[3] T.H. Li, Physics and Engineering of High Power Switching Devices, The MIT Press, 1975

[4] R.W. Blower, Distribution Switchgear, Collins, 1986

[5] H.J. Lingal, A.P. Strom and T.E. Browne, "An investigation of the arc-quenching behaviour of sulfur hexafluoride", AIEE Trans. Vol. PAS-72, 1963, Pp. 242-246

[6] G.J. Easley and J.M. Telford, "A new design 34.5 to 69kV intermediate capacity SF_6 circuit breakers", IEEE Trans., Vol. PAS-83, 1964, Pp. 1172-1173

[7] K. Suzuki, T. Toda, A. Aoyagi, H. Ikeda, A. Kobayashi, I. Ohshima and S. Yanabu, "Development of 550kV 1-break GCB (Part I): investigation of interrupting chamber performance", IEEE Trans. on Power Delivery, Vol. 8, 1993, Pp. 1184-1191

[8] Reyrolle Research Report, RD&C/TL/75/9/R, 1975

[9] Y.Ueda, H. Sasso, Y. Murai, K. Yoshinaga, T. Miyamoto and S. Tominaga, "Self-flow generation in a gas circuit breaker without puffer action", IEEE Trans. on Power Apparatus and Systems, Vol. PAS-100, Pp. 3888-3898, 1981

[10]T. Ushio, S. Tominaga,H. Kuwahara, T. Miyamoto, Y.Ueda and H. Sasao, "SLF interruption by a gas circuit breaker without puffer action", IEEE Trans. on Power Apparatus and Systems, Vol. PAS-100, Pp. 3801-3810, 1981

[11]Y. Murai, S. Yamaji, T. Miyamoto, H. Sasao and Y. Ueda, "An improvement of low current interrupting capability in self-interruption GCB", IEEE Trans. on Power Apparatus and Systems, Vol. PAS-101, Pp. 448-453, 1982

[12]H. Sasao, S. Hamano, T. Oomori, Y. Ueda and Y. Murai, "mixing process of arced gas with cold gas in the cylinder of gas circuit breaker", IEEE Trans. on Power Apparatus and Systems, Vol. PAS-101, Pp. 1115-1121, 1982

[13]Y. Ueda, y. Murai, A. Ohno and T. Tsutsumi, "Development of 7.2 kV - 63 kA advanced puffer gas circuit breaker", IEEE Trans. on Power Apparatus and Systems, Vol. PAS-101, Pp. 1504-1510, 1982

[14]T. Oomori, S. Hamano, H. Sasao, Y. Ueda and Y. Murai, "Optical observation of self-gas-flow in GCB", IEEE Trans. on Power Apparatus and Systems, Vol. PAS-102, Pp. 1408-1413, 1983

[15]H. Sasao, S. Hamano, Y. Wada, H. Hasegawa and N. Kobayashi, "Development of a magnet-assisted autopuffer GCB", IEEE Trans. on Power Delivery, Vol. 5, Pp. 1355-1361, 1990

[16]G. Bernard, P. Malkin and W. Legros, "An SF_6 circuit breaker using auto-expansion principle", IEEE Trans. on Power Delivery, Vol. 3, Pp. 1739-1744, 1988

[17]G. Bernard, A. Girard, P. Malkin and P. Scarpa, "An auto-expansion circuit breaker: the correlation between magnetic arc control and critical current", IEEE Trans. on Power Delivery, Vol. 5, Pp. 196-201, 1990

[18]P. Scarpa, B. Dauby, J.M. Defise, M. Barrault, and G. Bernard, "SF_6 auto-expansion circuit breaker design: numerical and experimental investigations of arc-gas interactions", IEEE Trans. on Power Delivery, Vol. 7, Pp. 339-349, 1992

[19]W. Hofbauer and J. Stechbarth, "Strategic tools-application for the development of a 300kV/50kA GIS self-blast circuit breaker", CIGRE 94, 13-110, Paris, 1994
[20]Dipl. -ing. Andreas Schiemann, "Third-generation SF_6 circuit breakers", Electricity International, Pp. 18-24, September 1990.
[21]D. Dufournet, "Evolution of the SF_6 thermal blast interruption in high voltage up to 245 kV", GEC Alsthom Technical Review, No. 6, Pp. 47-58, 1991
[22]M.N. Hirsh and H.J. Oskam, Gaseous electronics, Vol. 1, Academic Press, New York, 1978
[23]E. Lewis, A.N. Prasad and G.R. Jones, "Current zero spectroscopy of a high power SF_6 circuit breaker arc", Proc. of gas discharge and their applications, Oxford, Pp. 31-34, 1985
[24]A. Gleizes, A.A.M. Habib, M. Razafinimanana, M. Sabsabi and S. Vacquie, "Departures from Saha equilibrium in SF_6 arc plasmas", Spactrochemic Acta, Vol. 45B, No. 7, Pp. 789-797, 1990
[25]E.J. Robinson and S. Geltman, "Single- and double-quantum photo-detachment of negative Ions", Phys. Rev., Vol. 153, No. 1, Pp. 4-8, 1967
[26]W. Lochte-holtgreven, Plasma Diagnostics, North-Holland Publishing Company, 1968
[27]J.D. Anderson, Modern compressible flow, McGraw-Hill, 1982
[28]H. Schichting, Boundary layer theory, McGraw-Hill, 1979
[29]M. Mitchnner and C.H. Kruger, Partially ionised gases, John Wiley&Sons, New York, 1973
[30]R.H. Sabersky, A.J. Acosta and E.G. Hauptmann, Fluid flow, Macmillan Publishing Company, New York, 1978
[31]G.R. Jones and M.T.C. Fang, "The physics of high power arcs", Rep. Prog. Phys., Vol. 43, Pp. 1415-1465, 1980
[32]E. schade, "Recovery of switching arcs", Proc. XVIIth Int. Conf. Phenomena Ionised Gases, Pp. 277-297, 1985
[33]B.W. Swanson, and R.M. Roidt, "Boundary layer analysis of an SF6 circuit breaker arc", IEEE Trans., PAS-90, Pp. 1086-1903, 1970
[34]B.W. Swanson, R.M. Roidt and T.E. Browne, "Arc cooling and short line fault interruption", IEEE Trans. PAS-90, Pp. 1094-1102, 1970
[35]B.W. Swanson, and R.M. Roidt, "Thermal analysis of an SF6 circuit breaker arc", IEEE Trans. PAS-91, Pp. 381-389, 1972
[36]B.W. Swanson, and R.M. Roidt, "Some numerical solutions of the boundary layer equations for an SF6 arc", Proc. IEEE., Vol. 59, Pp. 493-501, 1971
[37]B.W. Swanson, R.M. Roidt and T.E. Browne, "A thermal arc model for short line fault interruption", ET-Z-A, Bd.93, Pp. 375-380, 1972
[38]B.W. Swanson, "A thermal analysis of short line fault interruption", IEE Winter Power Meeting, Paper C-47, 1974
[39]B.W. Swanson,, "Nozzle arc interruption in supersonic flow", IEEE Trans., PAS-96, 1977
[40]K. Ragaller, W. Egli and K.P. Brand, "Dielectric recovery of an axially blown SF_6-arc after current zero, Part II theoretical investigation", IEEE Trans. on Plasma Science, Vol. PS-10, Pp. 154-162, 1982
[41]R.R. Mitchell, D.T. Tuma and J.F. Osterle, "Transient two dimensional calculations of properties of forced convection stabilised electric arcs", IEEE Trans. on Plasma Science, Vol. PS-13, Pp. 207-213, 1985
[42]M.T.C. Fang, Q. Zhuang and X.J. Guo, "Current zero behaviour of an SF6 gas-blast arc. Part II: Turbulent flow", J. Phys. D: Appl. Phys., Vol. 27, Pp. 74-83, 1994

[43]G. Frind and J.A. Rich, "Recovery speed of axial flow gas-blast interrupter: dependence on pressure and di/dt for air and SF6", IEEE Trans. Power Appar. Syst., Vol. 93, Pp 1675-1684, 1974

[44]S. Kwan, Ph.D Thesis, Department of Electrical Engineering and Electronics, The University of Liverpool, 1996

[45]D. Leseberg and G. Pietsch, "Interferometrische Unterschungen Von Schaltichtbogen in Stromendem SF6 ", Proc. Of the 4th Int. Symp. On switching arc phenomena", Lodz, Polen, Pp. 236-240, 1981

[46]R.W. Liebermann and J.J. Lowke, "Radiation emission coefficients for sulphur hexafluoride arc plasmas", JQSRT, Vol. 17, Pp. 253-264, 1976

[47]D.C. Strachan, D. Lidgate, and G.R. Gones, "Radiative energy losses from a high current air-blast arc", Journal of Applied Physics, Vol. 48, Pp. 2324-2330, 1977

[48]P. Kovitya and J.J. Lowke, "Two-dimensional analysis of free-burning arcs in argon", J. Phys. D: Appl. Phys., 18, Pp. 53-70, 1985

[49]J.F. Zhang, D.B. Newland and M.T.C. Fang, "Radiation dominated arcs in gas flow and their current zero behaviour", Proc. of Gas Discharges and Their Application, Oxford, Pp. 57-60, 1982

[50]V.G. Sevast'yanenko, "Radiation transfer in a real spectrum: integration over frequency", J. Eng. Phys., Vol. 36, Pp. 138-149, 1979

[51]V.G. Sevast'yanenko, "Radiation transfer in a real spectrum: integration with respect to the frequency and angle", J. Eng. Phys., Vol. 38, Pp. 173-179, 1980

[52]G. Raynal and A. Gleizes, "calculation of thermal radiation transfer in SF_6 arcs", High Temp. Chem. Processes, Vol. 3, Pp. 389-397, 1994

[53]G. Raynal, P.J. Vergne and A Gleizes, "Radiative transfer in SF_6 and SF_6-Cu arcs", J. Phys. D: Appl. Phys., 28, Pp. 508-515, 1995

[54]G. Raynal and A. Gleizes, "Radiation transfer calculation in SF_6 arc plasmas using partial characteristics", Plasma Source Sci. Technol. Vol. 4, Pp. 152-160, 1995

[55]V. Aubrecht and J.J. Lowke, "Calculation of radiation transfer in SF_6 plasmas using the method of partial characteristics", J. Phys. D: Appl. Phys., 27, Pp. 2066-2073, 1994

[56]J. Slepian, "Extinction of an a.c. arc", AIEE Trans. vol. 47, Pp. 1398-1402, 1928

[57]A.M. Cassie, "Arc rupture and circuit severity: a new theory", CIGRE, Paper 102, Pp. 1-14, 1939

[58]O. Mayr, "Beitrage zur theorie des statischen und des dynamischen lichtbogens (contribution to the theory of static and dynamic arcs", Arch. Elect., 37, Pp. 588-608, 1943

[59]T.E. Browne Jnr, "A study of ac arc behaviour near current zero by means of mathematical models", AIEE Trans., Vol. 67, Pt. 1, Pp. 147-153, 1948

[60]W. Elenbaas, Phillips Research Report, Vol. 1, No. 5, 1946

[61]G. Frind, "time constant of flat arcs cooled by thermal conduction", IEEE Trans. on Power Apparatus and Systems, Vol. 84, Pp. 1125-1131, 1965

[62]R.L. Phillips, "The behaviour of dynamic electric arcs", ARL Report 64-150, 1964

[63]H.E. Weber, "Growth of an arc column in flow and pressure fields", Agardograph 84, Pp. 845-887, 1964

[64]D.T. Topham, "The electric arc in a constant pressure axial gas flow", J. Phys. D., Vol. 4, Pp. 114-1125, 1971

[65]M.T.C. Fang, "A review of gas-blast circuit breaker arc modelling", ULAP-T75, Dept. of Ele. Eng. And Electronics, University of Liverpool, 1983

[66]J.J. Lowke and H.C. Ludwig, "A simple model for high current arcs stabilised by forced convection", J.Appl. Phys., Vol. 46, Pp. 3361-3367, 1975

[67]D.T. Tuma and J.J. Lowke, "Prediction of properties of arcs stabilised by forced convection", ", J.Appl. Phys., Vol. 46, Pp. 3352-3360, 1975

[68]W. Hermann and E. Schade, "Radiation energy balance in cylindrical nitrogen arc", JQSRT, Vol. 12, Pp. 1257-1263, 1972

[69]F.R. EI-Akkari and D.T. Tuma, "Simulation of transient and zero current behaviour of arcs stabilised by forced convection", IEEE Trans., PAS, Vol. PAS-96, Pp. 1784-1788, 1977

[70]W. Hermann, U. Kogelschatz, L. Niemeyer, K. Ragaler and E. Schade, "Experimental and theoretical study of a stationary high current arc in a supersonic nozzle flow", J. Phys. D., Vol. 7, Pp. 1703-1722, 1974

[71]W. Hermann, K. Ragaller, "Theoretical description of the current interruption in high voltage gas blast circuit breakers", IEEE Trans. PAS, Vol. PAS-96, Pp. 1546-1555, 1977

[72]W. Hermann, U. Kogelschatz, L. Niemeyer, K. Ragaler and E. Schade, "Investigation of the physical phenomena around current zero in HV gas blast breakers", IEEE Trans. PAS, Vol. PAS-95, Pp. 1165-1176, 1976

[73]L. Niemeyer and K. Ragaller, "Development of turbulence by the interaction of gas flow with plasmas", Z. Naturfosch, Vol. 28a, Pp. 1281-1289, 1973

[74]W. Hermann, K. Ragaller and W. Schneider, "Theory of high pressure arc in a strong axial gas flow", Proc. 10th Int. Conf. on Phenomena in Ionised Gases, Pp. 199-201, 1971

[75]E. Richley and D. Tuma, "Free recovery of the gas blast arc column", IEEE Trans. on Plasma Science, Vol. PS-8, Pp. 405-410, 1980

[76]D.T. Tuma, "A comparison of the behaviour of SF6 and N2 gas blast arcs around current zero", ", IEEE Trans., PAS, Vol. PAS-99, pp. 2129-2137, 1980

[77]M.D. Cowley, "Integrated methods of analysing electric arcs : I. formulation", J. Phys. D. , Vol. 7, pp. 2218-2231, 1974

[78]Chan, S.K., Cowley, M.D. and Fang, M.T.C., "Integral methods of analysing electric arcs: III shape factor correlation for low radiation and laminar flow", J. Phys. D., Vol. 9, pp. 1085-1099, 1976

[79]V.R. Malghan, M.T.C. Fang, and G.R. Jones, "Investigation of quasi-steady state high current arcs in an orifice air flow", J. Appl. Phys., Vol. 48, Pp. 2331-2337, 1977

[80]I.R. Bothwell, M.D. Cowley and b. Grycz, IEE Conf. Publication, no. 118, Pp. 474-477, 1974

[81]A. Chapman and G.R. Jones, "The local electrical properties of gas blast arc near current zero", IEEE Trans. Plasma Science, vol. PS-6, Pp. 300-313, 1978

[82]Chan, S.K., Fang, M.T.C. and Cowley, M.D., "The DC Arc in a Supersonic Flow", IEEE Trans., Plasma Science, Vol. PS-6, pp. 394-405, 1978

[83]M.T.C. Fang, S.K. Chan and M.D. Cowley, "Transient behaviour of interrupted arcs in laminar flow", J. Phys. D., vol. 9, Pp. 1757-1770, 1976

[84]W.H. Bu, M.T.C. Fang and Z.Y. Guo, "The behaviour of ablation-dominated DC nozzle arcs", J. Phys. D: Appl. Phys. 23, Pp. 175-183, 1990

[85]M.T.C. Fang and W.H. Bu, "Investigation of ablation dominated AC nozzle arcs", IEE Proc.-A, Vol. 138, Pp. 71-77, 1991

[86]M.T.C. Fang and D.B. Newland, "DC nozzle arcs with mild wall ablation", J. Phys. D: Appl. Phys. 16, Pp. 793-810, 1983

[87]S.V. Pantankar, Numerical Heat Transfer and Fluid Flow, Hemisphere, New York, 1984

[88]K. Ragaller, W. Egli and K.P. Brand, "Dielectric recovery of an axially blown SF_6-arc after current zero, Part I experimental investigation", IEEE Trans. on Plasma Science, Vol. PS-10, Pp. 141-153, 1982

[89]J.J. Lowke and H.E. Lee, "A numerical study of a two dimensional circuit breaker arc during current interruption", Proc. of gas discharge and their applications, Oxford, Pp. 54-56, 1985

[90]M.T.C. Fang and W.Y. Lin, "Current zero behaviour of a gas blast arc, Part I: nitrogen", IEE Proc., Vol. 137, Pt. A, No 4, Pp. 175-183, 1990

[91]M.T.C. Fang and Q. Zhuang, "Current zero behaviour of an SF_6 gas-blast arc. Part I: Laminar flow". J. Phys. D: Appl. Phys., Vol. 25, Pp. 1197-1204, 1992

[92]M.T.C. Fang, S. Kwan and W. Hall, "Arc-shock interaction inside a supersonic nozzle", IEEE Trans. on Plasma Science, Vol.24, No.1, Pp.85-86, 1996

[93]H.Z. Maecker, H., Z. Phys., 141, Pp. 198-216, 1955

[94]S. Ramakrishnan, A.D. Strokes and J.J. Lowke, "An approximate model for high-current free-burning arcs", J. Phys. D: App. Phys., 11, Pp. 2267-2280, 1978

[95]K.C. Hsu, K. Etemadi and E. Pfender, "Study of the free-burning high-intensity argon arc", J. Appl. Phys. 54 (3), Pp. 1293-1301, 1983

[96]P. Kovitya and L.E. Cram, "A two-dimensional model of gas-tungsten welding arcs", Welding Journal, Pp. 34-39, 1986

[97]J.J. Lowke, P. Kovitya and H.P. Schmidt, "Theory of free-burning arc columns including the influence of the cathode", J. Phys. D: Appl. Phys. 25, Pp. 1600-1606, 1992

[98]Peiyuan Zhu, J.J. Lowke and R. Morrow, "A unified theory of free burning arcs, cathode sheaths and cathodes", J. Phys. D: Appl. Phys. 25, Pp. 1221-1230, 1992

[99]A. Kaddani, S. Zahrai, C. Delalondre and O. Simonin, "Three-dimensional modelling of unsteady high-pressure arcs in argon", J. Phys. D: Appl. Phys. 28, Pp. 2294-2305, 1995

[100]G.R. Jones, N.Y. Shammas and A.N. Prasad, "Radiatively induced nozzle ablation in high-power circuit interrupters", IEEE Trans. on Plasma Sci., Vol. PS-14, No.4, Pp. 413-422, 1986

[101]M.T.C. Fang and D.B. Newland, "DC nozzle arcs with mild wall ablation", J. Phys. D: Appl. Phys. 16, Pp. 793-810, 1983

[102]C.B. Ruchti and L. Niemyer, "Ablation controlled arcs", IEEE Trans. on Plasma Science, Vol. PS-14, Pp. 423-434, 1986

[103]B. Holzknecht, "An analytical model of the transient ablation of Polytetrafluoroethylene layers", Int. J. Heat Mass Transfer, Vol. 20, Pp. 661-668, 1977

[104]L. Muller, "Modelling of an ablation controlled arc", J. Phys. D: Appl. Phys. 26, Pp. 1253-1259, 1993

[105]M. Claessens, K. Moller and H.G. Thiel, "A computational fluid dynamics simulation of high- and low-current arcs in selfblast circuit breakers", J. Phys. D: Appl. Phys. 30, Pp. 1899-1907, 1997

[106]H.G. Thiel, "Modelling of pressure build-up and temperature distribution in SF_6 circuit breakers", 6th Int. Symp. Switching Arc Phenomena, Lodz, poland, 1989

[107]P. Kovitya and J.J. Lowke, "Theoretical prediction of ablation stablised arcs confined in cylindrical tubes", J. Phys. D: Appl. Phys. 17, Pp. 1197-1212, 1984

[108]P. Kirchesch and Niemeyer, "Arc behaviour in an ablating nozzle", 5th Int. Symp. Switching Arc Phenomena, Lodz, Poland, 1985

[109]L. Niemeyer, "Evaporation dominated high current arcs in narrow channel", IEEE Trans. Power App. Syst. PAS-97, Pp. 950-958, 1987

[110]Rutten,U., Proc. Gas Discharges and Their Applications, Pp. 140-143, 1992
[111]PHOENICS is the name of a commercial CFD package supplied by CHAM which is based at Bakery House, 40 High Street, Wimbledon Village, London, SW19 5AU, UK
[112]B. Bowman, "measurements of plasma velocity distributions in free burning dc arcs up to 2160A", J. Phys. D: Appl. Phys., 5, Pp. 1422-1432, 1972
[113]H. Edel, "The arc discharge: part I steady state properties", Proc. of Invited Lectures given at the VI Yugoslav Symposium and Summer School on the Physics of Ionised Gases, Miljevac by Split, Yugoslavis, Pp. 389-418, 1972
[114]L.S. Frost and R.W. Liebermann, "Composition and transport properties of SF6 and their use in a simplified enthalpy flow arc model", Proc. of the IEEE, Vol.59, Pp. 474-485, 1971
[115]A. Gleizes, J.J. Gonzalez, M. Razafinimanana, and T. Robert, "Influence of radiation on temperature field calculation in SF_6 arcs", Plasma Sources Sci. Technol., 1, Pp. 135-140, 1992
[116]M.S. Benilov and A. Marotta, "A model of the cathode region of atmospheric pressure arcs", J. Phys. D: Appl. Phys. 28, Pp. 1869-1882, 1995
[117]A. Gleizes, A. mahieddin Rahal, H. Delacroix, and Pham Van Doan, "Study of a circuit breaker arc with self-generated flow: Part I - energy transfer in the high current phase", IEEE Trans. on Plasma Sci., Vol. 16, No. 6, Pp. 606-614, 1988
[118]D.C. Strachan, "Radiation losses from high current free burning arcs between copper electrodes", J. Phys. D: Appl. Phys. 6, Pp. 1712-1723, 1973
[119]M. Bouaziz, G. Raynal, M. Razafinimanana and A. Gleizes, "An experimental and theoretical study of the absorption of SF_6 arc plasma radiation by cold SF_6 gas", J. Phys. D: Appl. Phys. 29, Pp. 2885-2891, 1996
[120]S.M.G. Ali, H.M. Ryan, D. Lightle, D.W. Shimmin, S. Taylor, and G.R. Jones, "High power short circuit studies on a commercial 420 kV puffer circuit breakers", IEEE Transactions on Power Apparatus and Systems, Vol. PAS-104, Pp. 459-466, 1985
[121]H.O. Noeske, "Investigation of dynamic nozzle parameters for various nozzle geometries and test conditions of an experimental half-size SF6 puffer breaker, IEEE Transactions on Power Apparatus and Systems, Vol. PAS-96, Pp. 896-906, 1977
[122]D.W. Shimmin, G.R. Jones and S.M.G. Ali, "Transient pressure variations in SF6 puffer circuit Breakers, J. Phys. D: Appl. Phys. 23, Pp. 533-541, 1990
[123]J.H. Huang, J.R. Zhang, P. Bazerque, M.B. Tavakoli-Juibari and G.R. Jones, "Free burning SF_6 arc", Experimental Report, Department of Electrical Engineering and Electronics, the University of Liverpool, UK
[124]J.R. Zhang, M.B. Tavakoli-Juibari, B. Nevin, J.H. Huang and G.R. Jones, "Experimental investigation of the dielectric recovery of SF_6 following very high current arcing", Experimental Report ULAP-T86, Department of Electrical Engineering and Electronics, the University of Liverpool, UK, 1988
[125]Y. Yokomizu, T. Matsumura, R. Henmi and Y. Kito, "Total voltage drops in electrode fall regions of SF_6 , argon and air in current range from 10 to 20000A", J. Phys. D: Appl. Phys. 29, Pp. 1260-1267, 1996
[126]H. Schlichting, "Boundary-layer theory", 7th Edition, McGraw-Hill, Inc., 1979
[127]N.C. Markatos, "The mathematical modelling of turbulent flows", Appl. Math. Modelling, Vol. 10, Pp. 190-220, 1986
[128]Kovitya, Private communications

[129]D.M. Benenson, G. Frind, R.E. Kinsinger, H.T. Nagamatsu, H.O. Noeske and R.E. Sheer, Jr., EPRI Report, EL-1455, Research Project 246-2, Pp.2-6 to 2-7, 1980

[130]K.P. Brand and J. Kopainsky, "Particle densities in a decaying SF_6 plasma", Appl. Phys. 16, Pp. 425-432, 1978

[131]K.Y.Park and M.T.C.Fang, "Mathematical modelling of SF_6 puffer circuit breaker I: High current phase", IEEE Trans. on Plasma Science, vol.24, Pp.490-502, 1996

[132]R. Reinhardt Sturzenegger and H.J. Schoetzau, "Influence of a shock on the electrical field distribution", IEEE Trans. on Power Apparatus and Systems, Vol.PAS-99, No.5, Pp.1957-1963, 1980

[133]L.C.Campbell, J.F.Perkins and J.L.Dallachy, "Effect of nozzle pressure ratio on SF_6 arc interruption", 4th Int. Conf. on Gas Discharges" , Swansea, Pp.44-47, 1976

[134]J.F. Zhang, M.T.C. Fang, and D.B. Newland, "Theoretical Investigation of a 2ka arc in a supersonic nozzle", J. Phys. D: Appl. Phys., Vol. 20, Pp. 368-79, 1987

[135]E Schade, "Recovery of switching arcs", Proc. Xviith Int. Conf. on Phenomena Ionised Gases, Pp. 277-297, 1985

[136]R.E. Blundell and M.T.C. Fang, "Stability of DC SF_6 arc in accelerating flow", Special Issue of IEEE Trans. on Plasma Science, 1997

[137]C.H. Huang and J.D. Ramshaw, Plasma Chem. Plasma Process., Vol. 13, Pp. 189-209, 1993

[138]M.T.C. Fang and J.D. Yan, "Common problems encountered in computer simulation of gas blast arcs", Proc. of 3rd Int. Conf. on Electrical Contacts, Arcs, Apparatus and Their Applications (IC-ECAAA), Vol. 1, Pp. 1-7, 1997

[139]D. Lesberg, "Holographische interferometrie und optische spektroskopie an einem SF_6-schaltlichtbogen", Ph.D thesis, RWTH Aachen, 1982

APPENDIX 1

Typical Input and Output Files in the Fortran 77 Program to Simulate Free Burning Arcs in a Confined Space with a Simplified Model

The execution of the program, which requires Salford FTN77 compiler, is controlled by the data file "CONTROL.DDD". The initial conditions, the arcing conditions and the adjustable parameters in the simplified model are specified in two data files named "GEOMETRY.DDD" and "CONDITIO.DDD".

The control file "CONTROL.DDD" has the following structure:

data	*comments*
0	integer, steady case =1, transient case =0
1	integer, first time step. Set at 1 for transient case
1	integer, last time step in transient case. set at 1 for steady case
200	integer, interval of time step at which pressure in the confining space is written to file "file0001.dat"
1000	integer, interval of time step at which field values in arc column written to file "file0002.dat" and "file0003.dat"
1	integer, interval of time step at which monitored values are displayed on screen
5	integer, position to be monitored
7	integer, number of data files for output, see the last five lines
+1.0000e-02	real E11.4, total computation time
+5.0000e-07	real E11.4, maximum time step
+5.0000e-01	real E11.4, factor to control time step length, 0.0-1.0
+1.0000e-06	real E11.4, accuracy for velocity iteration
+1.0000e-07	real E11.4, accuracy for arc radius iteration
geometry.ddd	data file for arcing condition
conditio.ddd	data file for initial condition
file0001.dat	to store pressure variation in the confining space
file0002.dat	to store temperature, electric field ,arc radius, velocity and n for arc column
file0003.dat	to store pressure, mass flow rate and density in arc column
file0004.dat	to store energy balance results
file0005.dat	to store steady state results as initial conditions for transient case

Arcing conditions are specified in the input data file "GEOMETRY.DDD" which has the following structure:

data	*comments*
+3.0000e-02	electrode gap length in meter
+9.0620e-04	inner volume of the confining space, V1 in cubic meter
+8.8889e-03	outer volume of the confining space, V2 in cubic meter
+3.0000e+02	initial gas temperature in Volume V1 for steady case, K
+3.0000e+02	initial gas temperature in Volume V2 for steady case, K
+5.1000e+05	initial gas pressure in Volume V1 for steady case, Pa
+5.1000e+05	initial gas pressure in Volume V2 for steady case, Pa

+0.3500e+00	energy loss factor to downstream electrode
+0.2500e+00	factor for radiation absorption in volume V1
+0.0120e+00	turbulent parameter
+5.0000e+02	peak current, A
+5.0000e+02	electrical current at time zero, A
+5.0000e+01	frequency of current waveform, Hz
+1.0000e+08	electric current density at upstream electrode
+5.7750e-04	area of flow passage between V1 and V2
+1.0000e+00	factor to multiply the above area
+1.0000e+00	factor controlling grid distribution in arc column

Initial conditions for steady state calculation are specified in the input data file "CONDITIO.DDD" which has the following structure:

+5.1000E+05	initial pressure at upstream end of arc column, Pa
+5.1000E+05	initial pressure at downstream end of arc column, Pa
+4.2000E+07	initial enthalpy at upstream end of arc column, J/kg
+4.2000E+07	initial enthalpy at downstream end of arc column, J/kg
+0.0000E+00	fixed initial velocity at upstream end of arc column, m/s
+5.0000E+02	initial velocity at downstream end of arc column, m/s
+5.0000E-01	variable n at upstream end of arc column
+1.0000E+00	variable n at downstream end of arc column
+0.4000E+00	percentage of radiation from axis which leaves the arc column, upstream end
+0.4000e+00	percentage of radiation from axis which leaves the arc column, downstream end

The above three files give the arcing conditions for a steady state 500A SF_6 arc in an open space at pressure of 5.1bar and temperature of 300K. The electrode separation is 30mm and the current density at the upstream electrode is 10^8 A/m^2 . The temperature at the upstream boundary of the arc column is 15000K (enthalpy is 4.2×10^7 J/kg). 35% of the energy flux hitting the downstream electrode will be lost to it. 40% of the net radiation emission from the arc centre is lost to the cold surroundings.

The computational results are stored in five data files. "file0001.dat" is used to store the pressure in the confining space and the arcing current as a function of time in a transient case:

time step	time(s)	current(A)	arc voltage(V)	Pv1(Pa)	Pv2(Pa)	Tv1(K)	Tv2(K)	mass in V1(kg)	Mass in V2(Kg)
1	0.5000E-06	0.5011E+03	0.7436E+02	0.5114E+06	0.5100E+06	0.3000E+03	0.3000E+03	0.2703E-01	0.2651E+00
200	0.1000E-03	0.7191E+03	0.8455E+02	0.5114E+06	0.5100E+06	0.3001E+03	0.3000E+03	0.2701E-01	0.2651E+00
400	0.2000E-03	0.9374E+03	0.8859E+02	0.5115E+06	0.5100E+06	0.3002E+03	0.3000E+03	0.2700E-01	0.2651E+00
600	0.3000E-03	0.1155E+04	0.9226E+02	0.5116E+06	0.5101E+06	0.3003E+03	0.3000E+03	0.2698E-01	0.2652E+00
800	0.4000E-03	0.1371E+04	0.9571E+02	0.5118E+06	0.5101E+06	0.3005E+03	0.3000E+03	0.2697E-01	0.2652E+00
1000	0.5000E-03	0.1586E+04	0.9888E+02	0.5120E+06	0.5102E+06	0.3007E+03	0.3000E+03	0.2695E-01	0.2652E+00
1200	0.6000E-03	0.1799E+04	0.1018E+03	0.5124E+06	0.5102E+06	0.3011E+03	0.3000E+03	0.2693E-01	0.2652E+00
1400	0.7000E-03	0.2011E+04	0.1046E+03	0.5129E+06	0.5102E+06	0.3015E+03	0.3000E+03	0.2691E-01	0.2652E+00
1600	0.7998E-03	0.2220E+04	0.1071E+03	0.5134E+06	0.5103E+06	0.3020E+03	0.3000E+03	0.2689E-01	0.2652E+00
1800	0.8957E-03	0.2419E+04	0.1093E+03	0.5138E+06	0.5103E+06	0.3025E+03	0.3000E+03	0.2687E-01	0.2653E+00
2000	0.9872E-03	0.2607E+04	0.1113E+03	0.5143E+06	0.5104E+06	0.3030E+03	0.3000E+03	0.2685E-01	0.2653E+00
2200	0.1075E-02	0.2786E+04	0.1131E+03	0.5150E+06	0.5104E+06	0.3036E+03	0.3000E+03	0.2683E-01	0.2653E+00
2400	0.1160E-02	0.2956E+04	0.1147E+03	0.5158E+06	0.5104E+06	0.3042E+03	0.3000E+03	0.2680E-01	0.2653E+00
2600	0.1242E-02	0.3119E+04	0.1162E+03	0.5164E+06	0.5105E+06	0.3049E+03	0.3000E+03	0.2678E-01	0.2654E+00
2800	0.1322E-02	0.3275E+04	0.1176E+03	0.5171E+06	0.5105E+06	0.3055E+03	0.3000E+03	0.2676E-01	0.2654E+00
3000	0.1400E-02	0.3426E+04	0.1188E+03	0.5178E+06	0.5106E+06	0.3062E+03	0.3000E+03	0.2673E-01	0.2654E+00

3200	0.1476E-02	0.3570E+04	0.1200E+03	0.5187E+06	0.5106E+06	0.3070E+03	0.3000E+03	0.2671E-01	0.2654E+00
3400	0.1551E-02	0.3710E+04	0.1211E+03	0.5195E+06	0.5107E+06	0.3077E+03	0.3000E+03	0.2668E-01	0.2655E+00
3600	0.1624E-02	0.3845E+04	0.1222E+03	0.5203E+06	0.5108E+06	0.3085E+03	0.3000E+03	0.2665E-01	0.2655E+00
3800	0.1695E-02	0.3976E+04	0.1232E+03	0.5212E+06	0.5108E+06	0.3093E+03	0.3000E+03	0.2662E-01	0.2655E+00
4000	0.1766E-02	0.4102E+04	0.1241E+03	0.5220E+06	0.5109E+06	0.3101E+03	0.3000E+03	0.2660E-01	0.2655E+00

"file0002.dat" keeps following results in the arc column as a function of axial position at a specified time step in a transient case :

time step= 1000 time= 0.5000E-03 (s) current= 0.1586E+04 (A)

axial position (m)	axis temperature (K)	E field(V/m)	arc radius (m)	axial velocity (m/s)	variable n
0.0000E+00	0.1503E+05	0.1577E+05	0.2246E-02	0.1000E+01	0.5000E+00
0.6000E-03	0.1757E+05	0.1124E+05	0.2419E-02	0.1922E+03	0.4957E+00
0.1200E-02	0.1779E+05	0.8989E+04	0.2692E-02	0.3246E+03	0.9071E+00
0.1800E-02	0.1762E+05	0.7460E+04	0.2966E-02	0.4006E+03	0.1230E+01
0.2400E-02	0.1734E+05	0.6410E+04	0.3221E-02	0.4453E+03	0.1515E+01
0.3000E-02	0.1704E+05	0.5673E+04	0.3451E-02	0.4718E+03	0.1775E+01
0.3600E-02	0.1673E+05	0.5145E+04	0.3656E-02	0.4872E+03	0.2014E+01
0.4200E-02	0.1642E+05	0.4761E+04	0.3842E-02	0.4956E+03	0.2235E+01
0.4800E-02	0.1611E+05	0.4475E+04	0.4011E-02	0.4995E+03	0.2438E+01
0.5400E-02	0.1579E+05	0.4255E+04	0.4169E-02	0.5003E+03	0.2623E+01
0.6000E-02	0.1547E+05	0.4079E+04	0.4320E-02	0.4991E+03	0.2791E+01
0.6600E-02	0.1517E+05	0.3931E+04	0.4468E-02	0.4965E+03	0.2943E+01
0.7200E-02	0.1487E+05	0.3801E+04	0.4614E-02	0.4929E+03	0.3080E+01
0.7800E-02	0.1459E+05	0.3683E+04	0.4760E-02	0.4886E+03	0.3203E+01
0.8400E-02	0.1433E+05	0.3572E+04	0.4906E-02	0.4838E+03	0.3314E+01
0.9000E-02	0.1409E+05	0.3467E+04	0.5052E-02	0.4786E+03	0.3418E+01
0.9600E-02	0.1386E+05	0.3370E+04	0.5196E-02	0.4729E+03	0.3524E+01
0.1020E-01	0.1365E+05	0.3278E+04	0.5340E-02	0.4670E+03	0.3610E+01
0.1080E-01	0.1346E+05	0.3188E+04	0.5483E-02	0.4610E+03	0.3679E+01
0.1140E-01	0.1328E+05	0.3103E+04	0.5626E-02	0.4549E+03	0.3740E+01
0.1200E-01	0.1311E+05	0.3021E+04	0.5768E-02	0.4487E+03	0.3795E+01
0.1260E-01	0.1296E+05	0.2944E+04	0.5909E-02	0.4425E+03	0.3844E+01
0.1320E-01	0.1281E+05	0.2871E+04	0.6047E-02	0.4363E+03	0.3889E+01
0.1380E-01	0.1268E+05	0.2801E+04	0.6183E-02	0.4301E+03	0.3928E+01
0.1440E-01	0.1255E+05	0.2736E+04	0.6317E-02	0.4239E+03	0.3963E+01
0.1500E-01	0.1243E+05	0.2674E+04	0.6448E-02	0.4177E+03	0.3991E+01
0.1560E-01	0.1232E+05	0.2615E+04	0.6577E-02	0.4117E+03	0.4015E+01
0.1620E-01	0.1222E+05	0.2560E+04	0.6703E-02	0.4056E+03	0.4034E+01
0.1680E-01	0.1212E+05	0.2507E+04	0.6827E-02	0.3997E+03	0.4047E+01
0.1740E-01	0.1203E+05	0.2458E+04	0.6948E-02	0.3939E+03	0.4057E+01
0.1800E-01	0.1195E+05	0.2411E+04	0.7066E-02	0.3881E+03	0.4062E+01
0.1860E-01	0.1186E+05	0.2367E+04	0.7182E-02	0.3825E+03	0.4064E+01
0.1920E-01	0.1179E+05	0.2325E+04	0.7295E-02	0.3770E+03	0.4062E+01
0.1980E-01	0.1171E+05	0.2285E+04	0.7406E-02	0.3716E+03	0.4057E+01
0.2040E-01	0.1164E+05	0.2248E+04	0.7515E-02	0.3662E+03	0.4049E+01
0.2100E-01	0.1158E+05	0.2212E+04	0.7621E-02	0.3610E+03	0.4039E+01
0.2160E-01	0.1151E+05	0.2178E+04	0.7725E-02	0.3559E+03	0.4026E+01
0.2220E-01	0.1145E+05	0.2146E+04	0.7826E-02	0.3509E+03	0.4011E+01
0.2280E-01	0.1140E+05	0.2115E+04	0.7925E-02	0.3460E+03	0.3995E+01
0.2340E-01	0.1134E+05	0.2086E+04	0.8022E-02	0.3412E+03	0.3976E+01
0.2400E-01	0.1129E+05	0.2058E+04	0.8117E-02	0.3366E+03	0.3957E+01
0.2460E-01	0.1124E+05	0.2032E+04	0.8210E-02	0.3320E+03	0.3936E+01
0.2520E-01	0.1119E+05	0.2006E+04	0.8302E-02	0.3275E+03	0.3914E+01
0.2580E-01	0.1114E+05	0.1982E+04	0.8391E-02	0.3231E+03	0.3891E+01
0.2640E-01	0.1110E+05	0.1959E+04	0.8478E-02	0.3188E+03	0.3867E+01
0.2700E-01	0.1105E+05	0.1936E+04	0.8564E-02	0.3146E+03	0.3843E+01
0.2760E-01	0.1101E+05	0.1915E+04	0.8649E-02	0.3105E+03	0.3819E+01
0.2820E-01	0.1097E+05	0.1894E+04	0.8732E-02	0.3064E+03	0.3794E+01

0.2880E-01	0.1093E+05	0.1874E+04	0.8814E-02	0.3025E+03	0.3769E+01
0.2940E-01	0.1089E+05	0.1855E+04	0.8894E-02	0.2986E+03	0.3744E+01
0.3000E-01	0.1089E+05	0.1855E+04	0.8894E-02	0.2986E+03	0.3744E+01

"file0003.dat" keeps part of the results in the arc column for a transient case:

time step= 1000 time= 0.5000E-03 (s) current= 0.1586E+04 (A)

axial position (m)	axis pressure (Pa)	axis enthalpy (J/kg)	electrical conduc	mass flow rate(kg/m)	axis density (kg/m3)
0.0000E+00	0.5100E+06	0.4200E+08	0.6344E+04	0.0000E+00	0.7311E-01
0.6000E-03	0.5257E+06	0.6808E+08	0.7676E+04	0.2044E+00	0.5256E-01
0.1200E-02	0.5230E+06	0.7105E+08	0.7751E+04	0.1202E+00	0.5088E-01
0.1800E-02	0.5211E+06	0.6869E+08	0.7691E+04	0.9898E-01	0.5181E-01
0.2400E-02	0.5197E+06	0.6483E+08	0.7592E+04	0.8608E-01	0.5366E-01
0.3000E-02	0.5187E+06	0.6069E+08	0.7475E+04	0.7653E-01	0.5600E-01
0.3600E-02	0.5180E+06	0.5673E+08	0.7340E+04	0.6918E-01	0.5864E-01
0.4200E-02	0.5174E+06	0.5314E+08	0.7186E+04	0.6367E-01	0.6147E-01
0.4800E-02	0.5170E+06	0.4997E+08	0.7014E+04	0.5981E-01	0.6439E-01
0.5400E-02	0.5166E+06	0.4721E+08	0.6826E+04	0.5738E-01	0.6729E-01
0.6000E-02	0.5163E+06	0.4485E+08	0.6631E+04	0.5610E-01	0.7011E-01
0.6600E-02	0.5160E+06	0.4283E+08	0.6434E+04	0.5563E-01	0.7278E-01
0.7200E-02	0.5157E+06	0.4109E+08	0.6239E+04	0.5569E-01	0.7528E-01
0.7800E-02	0.5155E+06	0.3961E+08	0.6052E+04	0.5604E-01	0.7758E-01
0.8400E-02	0.5153E+06	0.3833E+08	0.5873E+04	0.5650E-01	0.7970E-01
0.9000E-02	0.5151E+06	0.3723E+08	0.5705E+04	0.5688E-01	0.8176E-01
0.9600E-02	0.5150E+06	0.3627E+08	0.5548E+04	0.5725E-01	0.8398E-01
0.1020E-01	0.5148E+06	0.3544E+08	0.5403E+04	0.5762E-01	0.8588E-01
0.1080E-01	0.5146E+06	0.3470E+08	0.5267E+04	0.5787E-01	0.8747E-01
0.1140E-01	0.5145E+06	0.3404E+08	0.5140E+04	0.5800E-01	0.8891E-01
0.1200E-01	0.5144E+06	0.3346E+08	0.5022E+04	0.5803E-01	0.9030E-01
0.1260E-01	0.5143E+06	0.3293E+08	0.4912E+04	0.5797E-01	0.9164E-01
0.1320E-01	0.5142E+06	0.3246E+08	0.4810E+04	0.5786E-01	0.9293E-01
0.1380E-01	0.5141E+06	0.3203E+08	0.4715E+04	0.5770E-01	0.9419E-01
0.1440E-01	0.5140E+06	0.3164E+08	0.4625E+04	0.5750E-01	0.9540E-01
0.1500E-01	0.5139E+06	0.3128E+08	0.4542E+04	0.5728E-01	0.9655E-01
0.1560E-01	0.5138E+06	0.3095E+08	0.4464E+04	0.5703E-01	0.9766E-01
0.1620E-01	0.5138E+06	0.3065E+08	0.4390E+04	0.5679E-01	0.9872E-01
0.1680E-01	0.5137E+06	0.3038E+08	0.4321E+04	0.5653E-01	0.9972E-01
0.1740E-01	0.5136E+06	0.3012E+08	0.4255E+04	0.5627E-01	0.1007E+00
0.1800E-01	0.5136E+06	0.2988E+08	0.4194E+04	0.5601E-01	0.1016E+00
0.1860E-01	0.5135E+06	0.2966E+08	0.4135E+04	0.5576E-01	0.1025E+00
0.1920E-01	0.5135E+06	0.2945E+08	0.4080E+04	0.5550E-01	0.1033E+00
0.1980E-01	0.5134E+06	0.2925E+08	0.4028E+04	0.5525E-01	0.1041E+00
0.2040E-01	0.5134E+06	0.2907E+08	0.3978E+04	0.5500E-01	0.1048E+00
0.2100E-01	0.5134E+06	0.2890E+08	0.3930E+04	0.5476E-01	0.1055E+00
0.2160E-01	0.5133E+06	0.2873E+08	0.3885E+04	0.5452E-01	0.1062E+00
0.2220E-01	0.5133E+06	0.2858E+08	0.3842E+04	0.5429E-01	0.1069E+00
0.2280E-01	0.5133E+06	0.2843E+08	0.3800E+04	0.5407E-01	0.1075E+00
0.2340E-01	0.5132E+06	0.2829E+08	0.3761E+04	0.5387E-01	0.1081E+00
0.2400E-01	0.5132E+06	0.2816E+08	0.3723E+04	0.5365E-01	0.1087E+00
0.2460E-01	0.5132E+06	0.2804E+08	0.3686E+04	0.5345E-01	0.1092E+00
0.2520E-01	0.5131E+06	0.2792E+08	0.3651E+04	0.5324E-01	0.1098E+00
0.2580E-01	0.5131E+06	0.2780E+08	0.3618E+04	0.5305E-01	0.1103E+00
0.2640E-01	0.5131E+06	0.2770E+08	0.3586E+04	0.5285E-01	0.1108E+00
0.2700E-01	0.5131E+06	0.2759E+08	0.3555E+04	0.5264E-01	0.1113E+00
0.2760E-01	0.5131E+06	0.2749E+08	0.3525E+04	0.5244E-01	0.1117E+00
0.2820E-01	0.5130E+06	0.2740E+08	0.3496E+04	0.5225E-01	0.1122E+00

0.2880E-01	0.5130E+06	0.2730E+08	0.3468E+04	0.5205E-01	0.1126E+00
0.2940E-01	0.5130E+06	0.2722E+08	0.3441E+04	0.5184E-01	0.1131E+00
0.3000E-01	0.5130E+06	0.2722E+08	0.3441E+04	0.5184E-01	0.1131E+00

"file0004.dat" stores the results of energy balance for a steady case.

A: axial position, m
B: electrical power input in a slab, W
C: radiation loss in a slab, W
D: energy brought in by axial convection, W
E: energy taken away by axial convection, W
F: energy brought in by radial mass inflow, W
G: column A*1000
H: power input per unit arc length, W/m
I: radiation loss per unit length, w/m
J: energy loss by convection, W/m
K: energy brought in by radial mass inflow per unit arc length

The structure of the file is

1000	time step
5.000025E-04	time
1586.09	current
98.8850	arc voltage
161698.	Total power input in the whole arc column
0.605960	energy loss by radiation
0.297776	energy loss by convection
1.959119E-03	energy brought in by radial mass inflow

```
write(26,800)z(k),powerin(k),radout(k),hfluxin(k),hfluxout(k),
  /  hbymin(k),z(k)*1000.,powerin(k)/dz,radout(k)/dz,
  /  (hfluxout(k)-hfluxin(k))/dz,hbymin(k)/dz
```

A	B	C	D	E	F	G	H	I	J	K
0.6000E-03	0.1286E+05	0.2194E+04	0.0000E+00	0.8364E+04	0.2120E+02	0.6000E+00	0.2143E+08	0.3657E+07	0.1394E+08	0.3534E+05
0.1200E-02	0.9627E+04	0.2710E+04	0.8364E+04	0.1391E+05	0.1248E+02	0.1200E+01	0.1604E+08	0.4516E+07	0.9243E+07	0.2079E+05
0.1800E-02	0.7827E+04	0.3107E+04	0.1391E+05	0.1759E+05	0.1027E+02	0.1800E+01	0.1304E+08	0.5178E+07	0.6130E+07	0.1712E+05
0.2400E-02	0.6600E+04	0.3387E+04	0.1759E+05	0.2000E+05	0.8931E+01	0.2400E+01	0.1100E+08	0.5646E+07	0.4021E+07	0.1488E+05
0.3000E-02	0.5750E+04	0.3568E+04	0.2000E+05	0.2155E+05	0.7940E+01	0.3000E+01	0.9583E+07	0.5947E+07	0.2588E+07	0.1323E+05
0.3600E-02	0.5147E+04	0.3659E+04	0.2155E+05	0.2254E+05	0.7178E+01	0.3600E+01	0.8579E+07	0.6099E+07	0.1639E+07	0.1196E+05
0.4200E-02	0.4713E+04	0.3670E+04	0.2254E+05	0.2317E+05	0.6606E+01	0.4200E+01	0.7856E+07	0.6117E+07	0.1047E+07	0.1101E+05
0.4800E-02	0.4395E+04	0.3615E+04	0.2317E+05	0.2360E+05	0.6206E+01	0.4800E+01	0.7324E+07	0.6025E+07	0.7167E+06	0.1034E+05
0.5400E-02	0.4154E+04	0.3511E+04	0.2360E+05	0.2394E+05	0.5954E+01	0.5400E+01	0.6924E+07	0.5851E+07	0.5679E+06	0.9923E+04
0.6000E-02	0.3966E+04	0.3374E+04	0.2394E+05	0.2426E+05	0.5820E+01	0.6000E+01	0.6610E+07	0.5623E+07	0.5364E+06	0.9700E+04
0.6600E-02	0.3812E+04	0.3221E+04	0.2426E+05	0.2460E+05	0.5772E+01	0.6600E+01	0.6353E+07	0.5369E+07	0.5729E+06	0.9619E+04
0.7200E-02	0.3679E+04	0.3064E+04	0.2460E+05	0.2499E+05	0.5778E+01	0.7200E+01	0.6132E+07	0.5107E+07	0.6430E+06	0.9630E+04
0.7800E-02	0.3561E+04	0.2910E+04	0.2499E+05	0.2542E+05	0.5814E+01	0.7800E+01	0.5935E+07	0.4849E+07	0.7249E+06	0.9690E+04
0.8400E-02	0.3452E+04	0.2762E+04	0.2542E+05	0.2591E+05	0.5862E+01	0.8400E+01	0.5753E+07	0.4604E+07	0.8058E+06	0.9770E+04
0.9000E-02	0.3349E+04	0.2625E+04	0.2591E+05	0.2644E+05	0.5902E+01	0.9000E+01	0.5582E+07	0.4375E+07	0.8942E+06	0.9836E+04
0.9600E-02	0.3253E+04	0.2498E+04	0.2644E+05	0.2702E+05	0.5940E+01	0.9600E+01	0.5422E+07	0.4163E+07	0.9608E+06	0.9900E+04

0.1020E-01 0.3163E+04 0.2381E+04 0.2702E+05 0.2762E+05 0.5978E+01 0.1020E+02 0.5272E+07 0.3968E+07 0.1003E+07 0.9964E+04
0.1080E-01 0.3077E+04 0.2273E+04 0.2762E+05 0.2825E+05 0.6004E+01 0.1080E+02 0.5128E+07 0.3788E+07 0.1044E+07 0.1001E+05
0.1140E-01 0.2994E+04 0.2174E+04 0.2825E+05 0.2890E+05 0.6017E+01 0.1140E+02 0.4989E+07 0.3623E+07 0.1081E+07 0.1003E+05
0.1200E-01 0.2914E+04 0.2083E+04 0.2890E+05 0.2956E+05 0.6021E+01 0.1200E+02 0.4857E+07 0.3471E+07 0.1110E+07 0.1003E+05
0.1260E-01 0.2838E+04 0.1999E+04 0.2956E+05 0.3024E+05 0.6015E+01 0.1260E+02 0.4731E+07 0.3332E+07 0.1133E+07 0.1002E+05
0.1320E-01 0.2767E+04 0.1922E+04 0.3024E+05 0.3093E+05 0.6003E+01 0.1320E+02 0.4611E+07 0.3203E+07 0.1150E+07 0.1000E+05
0.1380E-01 0.2699E+04 0.1850E+04 0.3093E+05 0.3163E+05 0.5986E+01 0.1380E+02 0.4498E+07 0.3083E+07 0.1162E+07 0.9977E+04
0.1440E-01 0.2634E+04 0.1783E+04 0.3163E+05 0.3233E+05 0.5966E+01 0.1440E+02 0.4391E+07 0.2972E+07 0.1169E+07 0.9943E+04
0.1500E-01 0.2574E+04 0.1722E+04 0.3233E+05 0.3303E+05 0.5943E+01 0.1500E+02 0.4290E+07 0.2870E+07 0.1172E+07 0.9905E+04
0.1560E-01 0.2516E+04 0.1664E+04 0.3303E+05 0.3374E+05 0.5917E+01 0.1560E+02 0.4194E+07 0.2774E+07 0.1173E+07 0.9862E+04
0.1620E-01 0.2462E+04 0.1611E+04 0.3374E+05 0.3444E+05 0.5892E+01 0.1620E+02 0.4104E+07 0.2684E+07 0.1170E+07 0.9820E+04
0.1680E-01 0.2411E+04 0.1560E+04 0.3444E+05 0.3514E+05 0.5865E+01 0.1680E+02 0.4018E+07 0.2601E+07 0.1165E+07 0.9776E+04
0.1740E-01 0.2363E+04 0.1513E+04 0.3514E+05 0.3583E+05 0.5839E+01 0.1740E+02 0.3938E+07 0.2522E+07 0.1159E+07 0.9731E+04
0.1800E-01 0.2317E+04 0.1469E+04 0.3583E+05 0.3652E+05 0.5812E+01 0.1800E+02 0.3861E+07 0.2449E+07 0.1151E+07 0.9686E+04
0.1860E-01 0.2274E+04 0.1428E+04 0.3652E+05 0.3721E+05 0.5785E+01 0.1860E+02 0.3789E+07 0.2380E+07 0.1142E+07 0.9641E+04
0.1920E-01 0.2233E+04 0.1389E+04 0.3721E+05 0.3789E+05 0.5758E+01 0.1920E+02 0.3721E+07 0.2315E+07 0.1132E+07 0.9597E+04
0.1980E-01 0.2194E+04 0.1352E+04 0.3789E+05 0.3856E+05 0.5732E+01 0.1980E+02 0.3656E+07 0.2253E+07 0.1121E+07 0.9553E+04
0.2040E-01 0.2157E+04 0.1317E+04 0.3856E+05 0.3923E+05 0.5707E+01 0.2040E+02 0.3595E+07 0.2196E+07 0.1109E+07 0.9511E+04
0.2100E-01 0.2122E+04 0.1285E+04 0.3923E+05 0.3988E+05 0.5681E+01 0.2100E+02 0.3537E+07 0.2141E+07 0.1096E+07 0.9468E+04
0.2160E-01 0.2089E+04 0.1253E+04 0.3988E+05 0.4053E+05 0.5657E+01 0.2160E+02 0.3481E+07 0.2089E+07 0.1082E+07 0.9428E+04
0.2220E-01 0.2057E+04 0.1224E+04 0.4053E+05 0.4117E+05 0.5633E+01 0.2220E+02 0.3429E+07 0.2040E+07 0.1068E+07 0.9389E+04
0.2280E-01 0.2027E+04 0.1196E+04 0.4117E+05 0.4180E+05 0.5610E+01 0.2280E+02 0.3379E+07 0.1994E+07 0.1053E+07 0.9350E+04
0.2340E-01 0.1999E+04 0.1170E+04 0.4180E+05 0.4243E+05 0.5589E+01 0.2340E+02 0.3332E+07 0.1949E+07 0.1038E+07 0.9314E+04
0.2400E-01 0.1972E+04 0.1144E+04 0.4243E+05 0.4304E+05 0.5567E+01 0.2400E+02 0.3286E+07 0.1907E+07 0.1022E+07 0.9278E+04
0.2460E-01 0.1946E+04 0.1120E+04 0.4304E+05 0.4364E+05 0.5546E+01 0.2460E+02 0.3243E+07 0.1867E+07 0.1007E+07 0.9243E+04
0.2520E-01 0.1921E+04 0.1098E+04 0.4364E+05 0.4424E+05 0.5524E+01 0.2520E+02 0.3202E+07 0.1829E+07 0.9909E+06 0.9207E+04
0.2580E-01 0.1898E+04 0.1076E+04 0.4424E+05 0.4482E+05 0.5504E+01 0.2580E+02 0.3163E+07 0.1793E+07 0.9755E+06 0.9174E+04
0.2640E-01 0.1875E+04 0.1055E+04 0.4482E+05 0.4540E+05 0.5483E+01 0.2640E+02 0.3125E+07 0.1759E+07 0.9602E+06 0.9138E+04
0.2700E-01 0.1853E+04 0.1035E+04 0.4540E+05 0.4597E+05 0.5462E+01 0.2700E+02 0.3089E+07 0.1726E+07 0.9453E+06 0.9103E+04
0.2760E-01 0.1833E+04 0.1017E+04 0.4597E+05 0.4653E+05 0.5441E+01 0.2760E+02 0.3054E+07 0.1694E+07 0.9306E+06 0.9069E+04
0.2820E-01 0.1813E+04 0.9985E+03 0.4653E+05 0.4708E+05 0.5421E+01 0.2820E+02 0.3021E+07 0.1664E+07 0.9162E+06 0.9035E+04
0.2880E-01 0.1793E+04 0.9812E+03 0.4708E+05 0.4762E+05 0.5400E+01 0.2880E+02 0.2989E+07 0.1635E+07 0.9021E+06 0.9000E+04
0.2940E-01 0.1775E+04 0.9647E+03 0.4762E+05 0.4815E+05 0.5379E+01 0.2940E+02 0.2958E+07 0.1608E+07 0.8882E+06 0.8964E+04

"file0005.dat" stores all the results from a steady case. It is used to initiate a corresponding transient case. The structure of the file is defined in the program.

APPENDIX 2

INDEX OF PARAMETERS AND VARIABLES USED IN THE ARC MODELS

S.M. : Simplified arc model
D.M. : Differential arc model

Name	Physical Meaning	Description
	Ablation of nozzle material (D.M.)	The solution is sensitive to it
	Current density at the arc root (S.M)	The flow field is sensitive to it but the energy balance is not.
	Enthalpy at the arc root, one of the upstream boundary conditions (S.M.)	The solution is not sensitive to it.
	Radiation absorption in cold gas (S.M)	The solution is not sensitive to it
	Radiation re-absorption at the arc edge (S.M. and D.M.)	Solutions are sensitive to it
	Turbulence parameter in Prandtl mixing length model (D.M.)	The solution in the high current phase is not sensitive to it but that in the thermal recovery process is
$\vec{V}$	gas velocity, vector	m/s
$\vec{E}$	electric field, vector	V/m
$\vec{B}$	magnetic flux density, vector	Weber/m^2
ρ	density of gas	Kg/m^3
μ	dynamic viscosity of gas	μ_l , μ: laminar viscosity, N.s/m^2 μ_t : turbulent eddy viscosity
ε	permettivity of vacuum	=8.854×10^{-12} F/m
σ	electrical conductivity	1/(Ω.m)
ϕ	dependent variables solved by PHOENICS, electrostatic potential	
γ	ratio of specific heat at constant pressure to that at constant volume	
θ		used in equation (2.45)
Φ	viscous dissipation term in the energy equation	W/m^3
δ	thermal radius of an arc column	m
ξ_ρ	shape factor to calculate the mass storage (S.M)	$\xi_\rho = 1 - \frac{\xi_0}{2}$
$\sigma_{\varepsilon 3}$	Prandtl number for turbulence dissipation rate	=1.3
μ_0	permeability of vacuum	=$4\pi\times10^{-7}$ H/m
ξ_{θ}	parameter	$\xi_\theta = (1 + \frac{4\pi^2 P_{vl} R^2}{\mu_0 I^2})^{-1}$
ρ_c	density of space charge	C/m^3
σ_k	Prandtl number for turbulence kinetic energy	=1.0
ν_L	Larmor frequency of an electron	1/s
υ_t	turbulence kinematic viscosity	m^2/s
ξ_{v1}	shape factor to calculate the mass flux and momentum storage (S.M)	$\xi_{v1} = \frac{1}{n+1}(1 - \frac{\xi_0}{n+2})$
ξ_{v2}	shape factor to calculate the momentum flux and the kinetic energy storage (S.M)	$\xi_{v2} = \frac{1}{2n+1}(1 - \frac{\xi_0}{2n+2})$
ξ_{v3}	shape factor to calculate the kinetic energy flux (S.M)	$\xi_{v3} = \frac{1}{3n+1}(1 - \frac{\xi_0}{3n+2})$
τ_w	shear stress imposed on the gas by a solid wall	N/m^2
Δz	cell width in the axial direction	m

A_m	area through which volume V_1 exchanges mass with volume V_2 in the S.M.	m^2
c_μ	parameter in K-epsilon turbulence model	=0.09
c_l	turbulence parameter in the Prandtl mixing length model	to be determined by experimental results.
c_{1e}	parameter in K-epsilon turbulence model	=1.44
c_{2e}	parameter in K-epsilon turbulence model	=1.92
c_a	parameter indicating radiation absorption by cold SF_6	The solution is not sensitive to it.
c_e	percentage of the energy flux hitting the downstream electrode which is lost to the electrode (S.M.)	The solution is not sensitive to it.
c_f	skin friction coefficient	
c_p	specific heat at constant pressure	J/(Kg.K)
c_t	percentage of net radiation emission by an isothermal plasma column which is lost to its surrounding (S.M.)	The solution is sensitive to it.
c_v	specific heat at constant volume	=530 J/(Kg.K) for SF_6
e	electronic charge	$=1.602\times10^{-19}$C
E_r	radial electric field	V/m
E_z	axial electric field	V/m
F_m	mass exchange rate between V_1 and V_2 (S.M.); mass flux density of the nozzle vapour (D.M.)	Kg/s $Kg/(m^2.s)$
h	enthalpy Planck's constant	J/Kg $=6.63\times10^{-34}$ J.s
H_v	total energy which is used to break the chains in the PTFE molecules and to raise the vapour temperature to about 3400K	$=1.19\times10^7$ J/kg. The solution of the D.M. is sensitive to this parameter.
I	current	A
I_n	incident radiation flux density on the nozzle wall which can cause ablation of the nozzle material (D.M.)	W/m^2. The solution of the D.M. is sensitive to this parameter.
J_c	current density at the arc root (S.M. and D.M)	The flow field in a free burning arc case is sensitive to it but the energy balance is not. $=10^8 A/m^2$
J_r	radial current density component	A/m^2
J_z	axial current density component	A/m^2
k	thermal conductivity Boltzmann constant	W/(m.K) $=1.38\times10^{-23}$ J/K
L_s	turbulence length scale	m
m	mass flow rate across per unit length of the arc column (S.M.)	Kg/(m.s)
m_e	mass of an electron	$=9.108\times10^{-31}$Kg
M_{v1}	mass storage in volume V_1 (S.M.)	Kg
M_{v2}	mass storage in volume V_2 (S.M.)	Kg
n	parameter shaping the radial profile of the axial velocity (S.M.); the normal direction to a surface	
N	number of slabs (S.M.)	
P	pressure	Pa
P_{v1}	pressure in volume V_1 (S.M.)	Pa
P_{v2}	pressure in volume V_2 (S.M.)	Pa
q	radiation transfer as a volumetric energy source term	W/m^3
R	arc radius	m
R_c	arc radius at its upstream root	m
R_e	Reynolds number	
R_g	gas constant of an ideal gas	=56 J/(Kg.K) for SF_6
S_ϕ , ϕ=v,w,P,h,ρ	source term	

T_0	axis temperature or stagnation temperature	K
T_{v1}	temperature in volume V_1 (S.M.)	K
T_{v2}	temperature in volume V_2 (S.M.)	K
u	net radiation emission coefficient from an isothermal plasma column	W/m^3
u_i , u_j	velocity component in Cartesian coordinate system	m/s
v	radial velocity component in a cylindrical polar system	m/s
V_s	turbulence velocity scale	m/s
w	axial velocity component in a cylindrical polar system	m/s
w_*	shear velocity, see Eq. (3.8)	m/s
w_0, h_0, P_0, ρ_0	variables on axis (S.M.)	
w_e	speed of the moving contact (D.M.)	m/s